Università degli studi di Padova
Dipartimento di Ingegneria dell'Informazione

Dottorato in Ingegneria dell'Informazione
Indirizzo in Scienza e Tecnologia dell'Informazione

XXXII Ciclo

Accurate Modeling and Simulation in mmWave Cellular Networks for Spectrum Sharing and Antenna Designs

Supervisore

Chiar.mo Prof. Michele Zorzi

Candidato

Mattia Rebato

Coordinatore

Chiar.mo Prof. Andrea Neviani

Academic Year 2018/2019

Alla mia famiglia, e a tutti coloro che mi hanno sostenuto in questo lungo percorso...

Abstract

With the increasing demand for data and the growth of the connections between devices, a new generation of mobile networks, denominated 5G, has been defined to reach the high data rates required. Its deployment has already begun all around the world. The new standard presents many challenges due to its complexity, ranging from the concerns about its feasibility to the issues related to the new features introduced. In this thesis, after investigating how an accurate modeling of both the channel environment and the antenna propagation pattern strongly affect the simulated millimeter-wave scenario, some of the new issues are studied. We will present innovative solutions that will be examined in depth though figures and graphs which will be used to compare the performance of all the considered procedures. In this respect, we examine (*i*) different spectrum sharing approaches, (*ii*) some antenna array designs aspects and (*iii*) a stochastic geometry mmWave analysis.

Sommario

Con l'aumentare del traffico dati e la crescita delle connessioni tra dispositivi, un nuovo standard per reti cellulari, chiamato 5G, è stato definito in modo da soddisfare i flussi dati richiesti. L'installazione del nuovo standard è già iniziata in molti paesi del mondo. Il nuovo standard introduce molte sfide dovute alla sua complessità. Tali sfide riguardano la sua fattibilità, e vengono introdotte anche problematiche dovute alle nuove tecnologie adottate. In questa tesi, dopo un primo studio che mette in evidenza come le prestazioni di uno scenario *millimeter-wave* siano molto correlate ai modelli di canale e di propagazione dell'antenna usati, ci focalizzeremo su alcune nuove problematiche. Presenteremo soluzioni innovative con scenari simulati che saranno esaminati a fondo con l'uso di figure e grafici in modo da confrontare le prestazioni delle varie procedure. In particolare, investigheremo (*i*) diversi approcci di condivisione della banda, (*ii*) aspetti relativi al design dell'array di antenne e (*iii*) un'analisi stocastica per scenari che usano onde millimetriche.

Contents

List of Figures

List of Tables

Acronyms

3GPP	3rd Generation Partnership Project
5G	5th generation
ACIR	Adjacent Channel Interference Ratio
ACLR	Adjacent Channel Leakage Ratio
ACS	Adjacent Channel Selectivity
AoA	Angles of Arrival
AoD	Angles of Departure
BRAN	Broadband Radio Access Networks
CCDF	Complementary Cumulative Distribution Function
CDF	Cumulative Distribution Function
CSI	Channel State Information
DFT	Discrete Fourier Transform
DL	Downlink
ECDF	Empirical Cumulative Distribution Function
EIRP	Equivalent Isotropically Radiated Power
eMBB	evolved Mobile BroadBand
eNB	evolved Node Base
EPC	Evolved Packet Core
ETSI	European Telecommunications Standards Institute
FSS	Fixed-Satellite Service
gNB	Next Generation Node Base
GoB	Grid of Beams
HFSS	High-Frequency Structural Simulator
HPBW	Half Power BeamWidth
HPPP	Homogeneous Poisson Point Process
i.i.d.	independent and identically distributed
INR	Interference to Noise Ratio
IoT	Internet of Things
IP	Internet Protocol
ISD	Inter-Site Distance
ISO	Isotropic
ITU	International Telecommunication Union
LAA	Licensed Assisted Access

LBT	Listen-Before-Talk
LoS	Line of Sight
LSA	Licensed Spectrum Access
LTE	Long Term Evolution
LWA	LTE-WiFi Link Aggregation
MAC	Media Access Control
MF	Matched Filtering
MIMO	Multiple Input, Multiple Output
ML	Machine Learning
MMSE	Minimum Mean Square Error
mMTC	massive Machine-Type Communications
mmWave	millimeter wave
MU	Multi-User
NLoS	Non Line of Sight
NN	Neural Network
NR	New Radio
nRMSE	normalized Root Mean Square Error
NSA	Non Stand Alone
NYU	New York University
PDCP	Packet Data Convergence Protocol
PDF	Probability Density Function
PGFL	Probability Generating Functional
PHY	Physical
PPP	Poisson Point Process
PU	Primary User
QoS	Quality of Service
RAN	Radio Access Network
RAT	Radio Access Technologies
RLAN	Radio Local Area Network
RLC	Radio Link Control
RMSE	Root Mean Square Error
RR	Round Robin
RSRP	Reference Signal Received Power
RX	Receiver
SINR	Signal to Interference plus Noise Ratio
SIR	Signal to Interference Ratio
SISO	Single Input, Single Output
SLNR	Signal to Leakage plus Noise Ratio
SNR	Signal to Noise Ratio
SU	Secondary User
SVM	Support Vector Machine
SVR	Support Vector Regressor
TDD	Time Division Duplex
TX	Transmitter
UDP	User Datagram Protocol
UE	User Equipment
UL	Uplink

ULA	Uniform Linear Array
UMa	Urban Macro
UMi	Urban Micro
UPA	Uniform Planar Array
URLLC	Ultra-Reliable and Low-Latency Communication
V2V	Vehicle-to-Vehicle
V2X	Vehicle-to-Everything
VN	Vehicular Node
WLAN	Wireless Local Area Network
WPAN	Wireless Personal Area Network
WRC	World Radio Conference
ZF	Zero Forcing

Chapter 1

Introduction

The continuing growth in demand from subscribers for better mobile broadband experiences is encouraging the industry to look ahead at how networks can be readied to meet future extreme capacity and performance demands. It appears visible that a new generation of mobile networks will be necessary to reach the challenges required.

In the past, cellular networks were originally designed for voice-only applications, using analog transmission channels. When the digital technology evolved and more voice channels were required, 2G systems emerged in the 1990s. Digital transmission enabled new services such as text messaging and circuit switched data access. Then, with the arrival of the Internet, the low data rate services provided by 2G systems did not fulfill the need for mobile Internet access. This led to a demand for new 3G standards, which evolved to provide fast data services and more capacity for voice. After that, the 4G mobile communications system, commonly identified as Long Term Evolution (LTE), was developed to provide high capacity and high data rate service for mobile multimedia.

The demand for cellular data has continued to increase and a new standard was required to satisfy all the users' needs. For this purpose, a new standard for wireless communications, commonly defined as 5th generation (5G),[1] is starting to operate over the mobile network environment during this year all around the world, although it will not fully replace previous mobile generations immediately. Differently from the earlier standards, 5G will be able to connect a really large number of devices. Not only will mobile phones be connected to the grid, but also Internet of Things (IoT) devices will gather access to the network generating a huge number of simultaneous connection requests. Combining cutting-edge network technology and the very latest research, 5G is able to deliver vastly increased capacity, lower latency, and faster speeds. It brings a network that is much faster than the current one, with average download speeds of around 1 Gbps expected to soon be the norm.

[1]The 3rd Generation Partnership Project (3GPP), an industry association which has the responsibility of delineating the standard, defines any system using "5G NR" (5G New Radio) software as "5G".

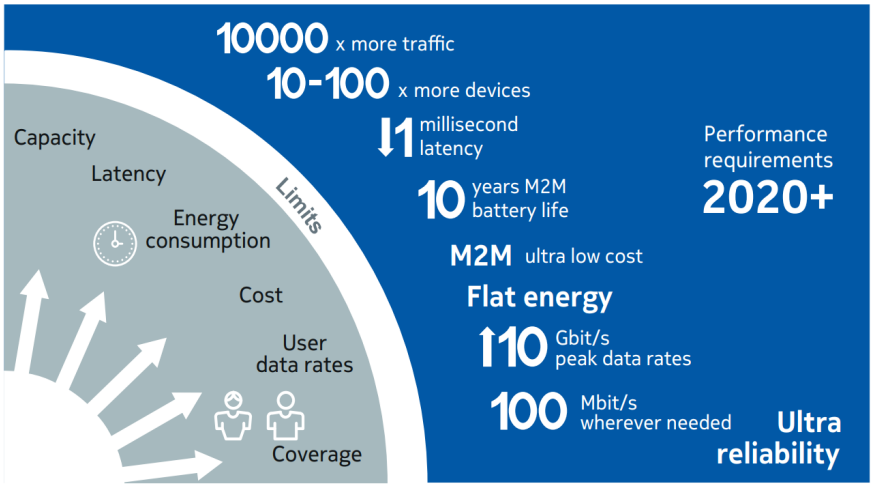

Figure 1.1: Overall summary of key requirements for 5G demands: higher capacity, lowest latency and more consistent experience [1].

Another important aspect which must be properly considered is the reliability of the data exchanged. In some *critical conditions* such as those of latency sensitive devices (e.g., applications like factory automation, autonomous driving, and remote surgery), the connection must be extremely reliable to ensure the safety of the users [1]. Differently from the new standard, the previous 4G specification was designed for smartphones only and not for critical network services. In critical scenarios, speed, capacity and reduced latency are clearly important, but not fundamental as the reliability which is the main driver in these critical cases.

All the new requirements are collected and reported in Figure 1.1, which highlights the required improvements in all the metrics in order to meet the 5G demands. For clarification in the understanding of the meaning of the requirements, three main generic services have been defined, which, according to teh International Telecommunication Union (ITU)-R, are classified as evolved Mobile BroadBand (eMBB), massive Machine-Type Communications (mMTC), and Ultra-Reliable and Low-Latency Communication (URLLC) (also referred to as mission-critical communications) [2, 3]. This generalization emphasizes that not all the requirements must be verified in every instance of a future network. Instead, a particular set of requirements must be adopted according to the generic service considered. A succinct characterization of these services can be given as follows:

(i) **eMBB** supports stable connections with very high peak data rates, which means high bandwidth Internet access suitable for web browsing, video streaming, and virtual reality. This is equivalent to the common Internet access service we use in our smartphones. Similarly, it supports also stable connections with moderate rates for cell-edge users;

(*ii*) **mMTC** supports a massive number of IoT devices (e.g., about 10^5 nodes/km^2), which are only sporadically active and send small data payloads. The data rates for these services are usually quite small, but the coverage range can be very large;

(*iii*) **URLLC** supports low-latency transmission of small payloads with very high reliability from a limited set of terminals, which are active according to patterns typically determined by outside events, such as alarms. Differently from eMBB, URLLC becomes relevant when a small amount of data needs to be transferred extremely fast and with a small packet loss rate. Clearly, due to the fact that the transmitted information in this scenario is ultra-reliable and with low latency, the data rate cannot achieve very high values.

These generic services are crucial to satisfy all the requirements of the 5G cellular standard. To develop these services and satisfy all the requirements, new technology tools are envisioned for the new cellular standard. Some of those are the use of millimeter wave (mmWave) bands, massive Multiple Input, Multiple Output (MIMO) systems, network slicing and a flexible frame structure. It is the first time that such new approaches are all used in a mobile standard thus a lot of research is required to jointly optimaize them.

One of the main ways to obtain high performance is the use of a large portion of bands in the mmWave spectrum. To be precise, 5G networks are designed to operate in a high-frequency band of the wireless spectrum, between 28 GHz and 60 GHz, and also in the sub-6 GHz range where current mobile communication standards are working. Together with directional transmission (achieved applying beamforming and MIMO antenna arrays), mmWave bands are of interest in developing wireless systems that can exploit the large amount of spectrum available in this frequency range.[2]

The research activities of this thesis are focused on the accurate and realistic modeling of simulators in order to be able to precisely study network protocols, spectrum sharing approaches and antenna designs for 5G networks. In contrast with a lot of studies present in the literature, where simplified models were used to simulate typical 5G scenarios, we believe that a proper evaluation study must be done considering realistic assumptions and models.

Entering into details, in this thesis we aim to find solutions to use the available resources in the best possible way. Even if, with the use of mmWave frequencies, the spectrum of resources accessible is large, still the amount is limited and efficient mechanism must be adopted for its use. The same concept applies to antenna design aspects: even if directional transmission can be performed providing a boost in the signal power, particular attention should be paid to the channel characterization and the interference which is generated in future networks. We remark also that in 5G networks the density of nodes will be much

[2]From a theoretical point of view, mmWave communications are defined with frequencies in the range 30–300 GHz, though the frequencies 6–30 GHz are also often referred to as mmWave.

higher with respect to the previous generation of networks. Therefore, particular focus must be given to interference related aspects. As highlighted in one of our previous works [4], using directional beams, the amount of interference received is not uniform and varies greatly at any time instant according to the location of scheduled users and access nodes.

In our research, we do not consider all the new features that will be available in 5G networks but, instead, focus our research on those relevant to the use of mmWave spectrum and the design of MIMO antenna arrays. Therefore, to accomplish these research goals, it appears extremely important to precisely characterize the mmWave environment and all the details of 5G cellular scenarios in a way to precisely study algorithms and protocols for the new standard. In line with the goals just described, the three main topics that will be covered in the thesis are:

- **Spectrum Sharing.** Sharing of the resource is a key dimension in mmWave network design in which spectrum, access and/or network infrastructure resources can be shared by multiple operators. It is argued that this sharing paradigm will be essential to fully exploit the tremendous amounts of bandwidth and the large number of antenna degrees of freedom available in these bands, and to provide statistical multiplexing to accommodate the highly variable nature of the traffic. Regulators all around the world have already identified the portions of the spectrum that will be used for the next generation of cellular networks. In this respect, in response to the very high expected traffic demand, a sharing mechanism may make it possible to use the spectrum more efficiently. Therefore, we investigate and compare various sharing configurations in order to capture the enhanced potential of mmWave communications. We deliver a number of key insights, corroborated by detailed simulations, which include several analyses of the effects of the distinctive propagation characteristics of the mmWave channel, along with a rigorous multi-antenna characterization. Our results reflect both the technical and the economical aspects of the various sharing paradigms.

- **Antenna Design and Evaluation.** Large antenna arrays and mmWave frequencies have been attracting growing attention as possible candidates to meet the strict requirements of future 5G mobile networks. In view of the large path loss attenuation in these bands, beamforming techniques that create a beam in the direction of the user equipment are essential to perform the transmission. For this purpose, it is extremely important to correctly model and consider the propagation antenna effects in any transmission. Therefore, it is fundamental to characterize realistic antenna radiation patterns, motivated by the need to properly capture mmWave propagation behaviors and understand the achievable performance in 5G cellular scenarios. With the use of a realistic characterization, antenna design and optimization phases can be done. Many are the parameters of the antenna array which can be optimized also considering the optimization of network metrics. We propose in our research a Machine Learning

(ML) approach which can be used to identify the optimal antenna configuration according to any given objective function (e.g., maximization of average throughput or maximization of worst users received power).

- **Stochastic Geometry Analysis.** Together with simulations, the system performance can be also assessed by using models from stochastic geometry that cater for the directivity in the desired signal transmissions as well as the interference, and by calculating the Signal to Interference plus Noise Ratio (SINR) coverage. Nonetheless, the accuracy of the state of the art coverage expressions derived through stochastic geometry may be questioned, as it is not clear whether they capture the impact of the detailed mmWave channel and antenna features. Through several studies, we propose an SINR coverage analysis framework that includes realistic channel models and antenna element radiation patterns. The proposed analytical framework has been validated and used as an evaluation tool for dense mobile and vehicular networks.

1.1 Organization of the Thesis

This thesis is organized in six chapters. In Chapter 2 where we will introduce the relationship between mmWave frequencies and 5G cellular networks, providing challenges and benefits of this portion of spectrum. Furthermore, we will present some general concepts related to the bands and we will conclude the chapter with a channel characterization useful for the remaining chapters of the thesis.

After the preliminary introduction on the mmWave frequencies for 5G cellular networks, the thesis is organize into two main parts.

Part I deals with the spectrum sharing paradigm for 5G mmWave cellular networks.

- In Chapter 3 we will study the spectrum sharing paradigm and protocols to provide an efficient use of the resources available in 5G networks. The original research contributions of this chapter can be found starting from Section 3.2, which is taken from works [5, 6], then in Section 3.3, which is taken from **[C5]**, and finally in Sections 3.4, which are taken from works [7] and **[J1]**.

Part II deals, instead, with the antenna design and evaluation.

- In Chapter 4 we will discuss all the research activities related to the antenna array evaluation and design with a particular focus on mmWave cellular networks. A preliminary evaluation of the antenna array can be found in Section 4.1, which is taken from **[C3]**, then also in Section 4.4, which is taken from **[C4]**. Research activities tailored to the design of antenna arrays are discussed in Section 4.5 which is specific

for MIMO scenarios and taken from **[C6]**, in Section 4.6 which is taken from **[J4]** and will discuss antenna tilting optimization, and finally in Sections 3.4, which are taken from **[C7]** and will present an innovative optimization framework that uses ML techniques.

- In Chapter 5 we will present a stochastic geometry analysis which can be used for the coverage analysis in mmWave networks. The contribution can be found starting from Section 5.1, which is taken from works **[C1]** and **[J3]**. Furthermore, in Section 5.6 we will provide additional details to analyze mmWave vehicular networks, which are taken from works **[C2]** and **[J2]**.

Finally, in Chapter 6 we will report the conclusions of this thesis.

1.2 Notation

In this thesis, column vectors and matrices are respectively denoted by boldface lowercase and uppercase letters. We identify with $\mathbf{X}^H$ the conjugate transpose of $\mathbf{X}$, and the Frobenius norm is denoted $\|\cdot\|_{\mathrm{F}}$ while the Euclidean norm is denoted as $\|\cdot\|$. The set of all complex numbers is denoted by $\mathbb{C}$, with $\mathbb{C}^{N\times 1}$ and $\mathbb{C}^{N\times M}$ being the generalizations to vectors and matrices, respectively. The $M \times M$ identity matrix is written as $\mathbf{I}_M$ and the zero matrix of size $N_{\mathrm{T}} \times M$ is denoted as $\mathbf{0}_{N_{\mathrm{T}}\times M}$. Finally, we generally indicate with $\widehat{\mathbf{X}}$ the Frobenius normalized matrix of $\mathbf{X}$.

As a general rule, the symbols and the acronyms are self-contained and self-explained in each chapter, while the mathematical notation just provided is common to all chapters.

Chapter 2

Millimeter-Waves in 5G Cellular Networks

With the rapidly growing demand for cellular data services, conventional frequencies below 3 GHz are now highly congested. At the same time, probably due to the shortage of traditional spectrum, millimeter wave (mmWave) frequencies, roughly corresponding to bands above 6 GHz, have been attracting growing attention and have been widely cited as one of the most promising technologies for 5G and *Beyond 5G* cellular evolution.

In this chapter we introduce and present some general concepts related to mmWave that will be used in the remainder of the thesis. We conclude the chapter with a basic channel characterization which will be used in Chapters 3, 4 and 5, possibly with some minor changes according to the aspects being analyzed.

2.1 5G Cellular Networks

5G is the next step in the evolution of mobile communication. Even if a lot of research has been done for this new paradigm, its deployment is just at the beginning and much more is still required to gather the best from the standard. It will be a key component of the society and will help realize the vision of essentially unlimited access to information and sharing of data anywhere and anytime for anyone and anything [8].

5G will therefore not only be about mobile connectivity for people. Rather, the aim of 5G is to provide ubiquitous connectivity for any kind of device and any kind of application that may benefit from being connected. Mobile broadband will continue to be important and will drive the need for higher system capacity and higher data rates. This new generation will also provide wireless connectivity for a wide range of new applications and use cases, including wearables, smart homes, traffic safety control, and critical infrastructure and industry applications, as well as for very-high-speed media delivery.

In contrast to earlier generations, 5G wireless access should not be seen as a specific radio-access technology. Rather, it is an overall wireless-access solution addressing the demands

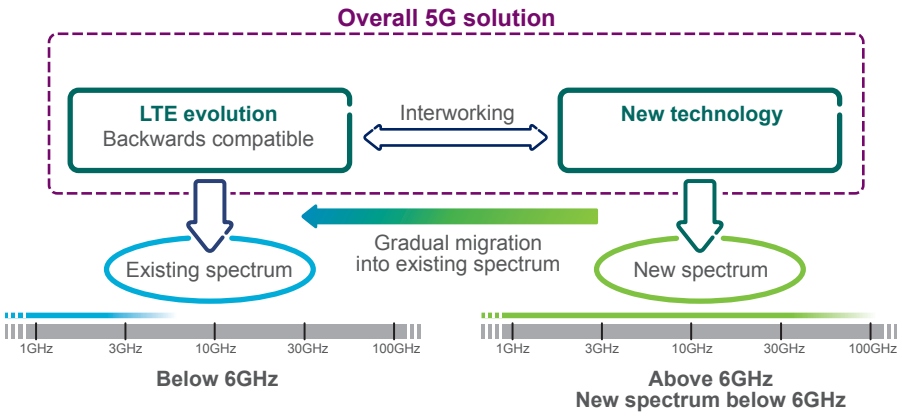

Figure 2.1: Overall 5G wireless-access solution consisting of LTE evolution and new technologies. Figure from [8].

and requirements of mobile communication beyond 2020. The previous standard Long Term Evolution (LTE) will continue to develop in a backwards-compatible way and will be an important part of the 5G wireless-access solution for frequency bands below 6 GHz [8]. Figure 2.1 shows an overall 5G wireless-access solution consisting of LTE evolution and new technology working at mmWave frequencies.

Due to the spectrum scarcity in microwave bands used by legacy communication technologies, mmWave bands are considered as a promising enabler for 5G cellular networks to provide multi-gigabit wireless access. The available spectrum at these higher frequencies can easily be 200 times greater than all cellular allocations today.

2.2 Millimeter Waves (mmWave)

Although mmWave frequencies can be used, mmWave communications exhibit high attenuation, vulnerability to obstacles and sparse-scattering environments, which are not taken into account in the existing cellular wireless design approaches [9, 10].

In a different way, the small wavelengths of mmWave signals make it possible to incorporate a large number of antenna elements both at the Next Generation Node Base (gNB) and at the User Equipment (UE), which in turn lead to high directivity gains and fully-directional communications. This level of directionality can result in a network that is noise-limited as opposed to interference-limited.

The significant differences between mmWave networks and traditional ones challenge the classical design constraints, objectives, and available degrees of freedom. An example of this can be a Non Line of Sight (NLoS) scenario, where the communication between transmitter and receiver can not be achieved due to the high attenuations [9]. This demands a reconsideration of almost all design aspects in mmWave systems.

2.2.1 Challenges of mmWave

Despite the potential of mmWave cellular systems, there are a number of key challenges to realize the vision of cellular networks in these bands [10]:

- **Range and directional communication**: Friis' transmission law, in the equation below

$$P_{\mathrm{RX}} = P_{\mathrm{TX}} G_{\mathrm{TX}} G_{\mathrm{RX}} \left(\frac{\lambda}{4\pi d} \right)^2 \tag{2.1}$$

  states that the free space omnidirectional path loss grows with the square of the frequency. In the equation: P_{RX} and P_{TX} are respectively the received and the transmitted powers, G_{TX} and G_{RX} are the gains of the Transmitter (TX) and Receiver (RX) antennas, d is the distance between the receiver and transmitter and λ is the wavelength. However, the smaller wavelength of mmWave signals also enables proportionally greater antenna gains (knowing that the gain is given by: $G = \frac{4\pi}{\lambda^2} A_{\mathrm{eff}}$) for the same physical antenna size. Consequently, the higher frequencies of mmWave signals do not in themselves result in any increased free space propagation loss, provided the antenna area remains fixed and suitable directional transmissions are used. This is also confirmed from measurements in [10].

- **Atmospheric gaseous losses**: This kind of attenuation is typically less than a few dB per kilometer excluding particular absorption bands like those of oxygen (i.e., near 60 GHz) and water vapor (i.e., near 20 and 200 GHz). In the particular case of small cells/areas, some hundreds of meters, this attenuation is not so relevant.

- **Shadowing**: A more significant concern for range is that mmWave signals are extremely susceptible to shadowing. For example, materials such as brick can attenuate signals by as much as 40 to 80 dB and the human body itself can result in a 20 to 35 dB loss. On the other hand, humidity and rain fades (common problems for long range mmWave backhaul links) are not an issue in cellular systems. Even in a very heavy rainfall, rain fades are typically less than a dB per 100 meters meaning they will have minimal impact in cellular systems with cell radii smaller than 200 meters. Also, the human body and many outdoor materials are very reflective, and therefore are important scatterers for mmWave propagation.

- **Rapid channel fluctuations and intermittent connectivity**: For a given mobile velocity, channel coherence time is linear in the carrier frequency, meaning that it will be very small in the mmWave range. In addition, high levels of shadowing imply that the appearance of obstacles will lead to much more dramatic swings in path loss, although beamsteering may overcome this. Also, mmWave systems will be inherently built of small cells, meaning that relative path losses and cell association

also change rapidly. From a system perspective, this implies that connectivity will be highly intermittent and communication will need to be rapidly adaptable.

In conclusion, after excluding some sub-bands with severe atmospheric absorption and assuming 40% of the remaining spectrum potentially becomes available over time, a possible 100 GHz new spectrum among the mmWave band could be opened up for future mobile communication use [10, 11].

2.2.2 Benefits of mmWave

Despite all the challenges listed above, the use of mmWave also provides some advantages. Due to the small wavelength, the use of Multiple Input, Multiple Output (MIMO) is easily implementable and this is already a key technology in supporting high data rates in 4G systems. MIMO enables multi-stream transmission for high spectrum efficiency, improved link quality and adaptation of radiation patterns for signal gain and interference mitigation via adaptive beamforming using antenna arrays [12], [13].

Since the tiny wavelengths allow for dozens to hundreds of antenna elements to be placed in an array on a relatively small physical platform at the gNB, or access point, massive MIMO can be used. Extra antennas help by focusing energy into ever smaller regions of space to bring huge improvements in throughput and radiated energy efficiency. Other benefits of massive MIMO include extensive use of inexpensive low-power components, reduced latency, simplification of the Media Access Control (MAC) layer, and robustness against intentional jamming [13, 14].

All these aspects are perfect for scenarios of mmWave communications. In addition, MIMO systems allow to use beamforming and so obtain a directional signal transmission or reception. This is achieved by combining elements in a phased array in such a way that signals at particular angles experience constructive interference while others experience destructive interference. Beamforming can be used at both the transmitting and receiving ends in order to achieve spatial selectivity [15].

After the list of pros and cons, all the studies and in-the-field simulations have identified mmWave frequencies as the means to carry communication in the systems of fifth generation.

2.3 mmWave Spectrum Characterization

mmWave propagation is characterized by three main challenges, namely (*i*) *directionality*, obtained from the combination of multiple antennas to increase the intrinsically low transmission range, (*ii*) *severe shadowing*, because mmWave signals are extremely sensitive to objects, including foliage and the human body, and (*iii*) *intermittency*, where obstacles can lead to much more dramatic fluctuations of the channel gain, resulting in frequent and sudden drops (e.g., people passing through the area of coverage) [10, 16, 17].

Table 2.1: Path loss model parameters derived from real measurements made in the Manhattan scenario [21]. Values for both the 28 and 73 GHz bands, and for both LoS and NLoS conditions.

Frequency	State	α	β	σ
28 GHz	NLoS	72	2.9	8.7 dB
	LoS	61.4	2	5.8 dB
73 GHz	NLoS	86.6	2.45	8.0 dB
	LoS	69.8	2	5.8 dB

Since these effects play a key role in determining the performance in a mmWave scenario, it is particularly important to carefully characterize the propagation phenomena, and the directional gains introduced by multi-antenna schemes. In the remainder of the chapter we report some basic aspects of the mmWave environment characterization which will be useful for the entire thesis.

We start with the traditional definition of link budget

$$P_{\mathrm{RX}} = P_{\mathrm{TX}} + G_{\mathrm{BF}} - \ell - \xi \tag{2.2}$$

where P_{RX} and P_{TX} are the received and transmitted power in dBm, respectively. G_{BF}, ℓ and ξ are the beamforming gain, path loss and shadowing in dB, respectively [17].

2.3.1 mmWave Propagation

From the measurement campaign carried out in a real dense urban environment and reported in [18–20], path loss can be modeled with three states: Line of Sight (LoS), NLoS and outage (out). Each link is characterized by the channel state probabilities p_{LoS}, p_{NLoS} and p_{out}, which are expressed in terms of the distance d between the UE and the gNB as follows

$$\begin{aligned} p_{\mathrm{out}}(d) &= \max(0, 1 - e^{-a_{\mathrm{out}}d + b_{\mathrm{out}}}) \\ p_{\mathrm{LoS}}(d) &= (1 - p_{\mathrm{out}}(d))e^{-a_{\mathrm{LoS}}d} \\ p_{\mathrm{NLoS}}(d) &= 1 - p_{\mathrm{out}}(d) - p_{\mathrm{LoS}}(d) \end{aligned} \tag{2.3}$$

where $a_{\mathrm{out}} = 0.0334$ m^{-1}, $b_{\mathrm{out}} = 5.2$ and $a_{\mathrm{LoS}} = 0.0149$ m^{-1} (all these values are taken from [21] assuming a carrier frequency of 28 GHz). On the other hand, the path loss is given by:

$$\ell(d)[\mathrm{dB}] = \alpha + \beta 10 \log_{10}(d) \tag{2.4}$$

where $\xi \sim N(0, \sigma^2)$ is the log-normal shadowing, and the parameters α, β, σ, derived in [21], are reported in Table 2.1 and depend on the carrier and the LoS or NLoS link state.

2.3.2 mmWave MIMO Channel

The channel, which is based on a WINNER II model [22], is assumed to be composed of a random number K of clusters, each corresponding to a macro-level scattering path. The models for the large-scale parameters are also carrier and link-state dependent. At the receiver, the number of estimated clusters is given as the maximum value between 1 and a Poisson random variable whose mean λ is related to the carrier frequency as explained in [21]. For each cluster k, the number of sub-paths is modeled as an integer random variable L_k uniformly distributed in $\{1, \ldots, 10\}$. Given a set of clusters and of sub-paths for a channel, we can compute the channel matrix as

$$\mathbf{H}(t,f) = \sum_{k=1}^{K} \sum_{l=1}^{L_k} g_{kl}(t,f) \mathbf{u}_{Rx}(\theta_{kl}^{Rx}, \phi_{kl}^{Rx}) \mathbf{u}_{Tx}^{*}(\theta_{kl}^{Tx}, \phi_{kl}^{Tx}) \tag{2.5}$$

where L_k is the number of sub-paths in cluster k, $g_{kl}(t,f)$ is the small-scale fading over time and frequency and $\mathbf{u}_{Rx}(\cdot)$ and $\mathbf{u}_{Tx}(\cdot)$ are the spatial signature vector of the receiver and transmitter, respectively. Spatial signatures are computed with horizontal and vertical Angles of Arrival (AoA) $\theta_{kl}^{Rx}, \phi_{kl}^{Rx}$, and horizontal and vertical Angles of Departure (AoD) $\theta_{kl}^{Tx}, \phi_{kl}^{Tx}$, where $k = 1, \ldots, K$ is the cluster index and $l = 1, \ldots, L_k$ is the sub-path index within the cluster.

The small-scale fading is generated based on the number of clusters, the number of sub-paths in each cluster, the Doppler shift, the power spread, and the delay spread, as

$$g_{kl}(t,f) = \sqrt{P_{lk}} e^{j2\pi f_d cos(\omega_{kl})t} e^{-j2\pi\tau_{kl}f} \tag{2.6}$$

where P_{kl} is the power spread of sub-path l in cluster k, f_d is the maximum Doppler shift, ω_{kl} is the angle of arrival of sub-path l in cluster k with respect to the direction of motion, τ_{kl} is the delay spread of sub-path l in cluster k and finally, f is the carrier frequency.

The power spread P_{kl} is obtained by following [23] as

$$\begin{aligned} P_{kl} &= \frac{P'_{kl}}{\sum P'_{kl}} \\ P'_k &= \frac{U_k^{r_\tau - 1} 10^{-0.1 Z_k + V_k}}{L_k} \end{aligned} \tag{2.7}$$

where $U_k \sim U[0,1]$, $V_k \sim U[0, 0.6]$ and $Z_k \sim N(0, \zeta^2)$, while parameters r_τ and ζ are found in [21].

Part I

Spectrum Sharing

Chapter 3

Spectrum Sharing Specifications

In this chapter, we discuss resource sharing, a key dimension in mmWave network design in which spectrum, access and/or network infrastructure resources can be shared by multiple operators. It is argued that this sharing paradigm will be essential to fully exploit the tremendous amounts of bandwidth and the large number of antenna degrees of freedom available in these bands, and to provide statistical multiplexing to accommodate the highly variable nature of the traffic. Regulators all around the world have started identifying the portions of the spectrum that will be used for the next generation of cellular networks. In this respect, a band in the mmWave spectrum will be exploited to increase the available capacity. In response to the very high expected traffic demand, a sharing mechanism may make it possible to use the spectrum more efficiently.

In our works [5–7, 24, 25], we investigate and compare various sharing configurations in order to capture the enhanced potential of mmWave communications. Our results reflect both the technical and the economical aspects of the various sharing paradigms. We deliver a number of key insights, corroborated by detailed simulations, which include an analysis of the effects of the distinctive propagation characteristics of the mmWave channel, along with a rigorous multi-antenna characterization.

3.1 Introduction

With the severe spectrum shortage in conventional cellular bands, mmWave frequencies between 10 and 300 GHz have been attracting growing attention as a possible candidate for next-generation micro- and pico-cellular wireless networks. The mmWave bands offer orders of magnitude greater spectrum than current cellular allocations and enable very high-dimensional antenna arrays for further gains via beamforming and spatial multiplexing. However, due to the unique nature of propagation in these bands, cellular systems will need to be significantly redesigned [9]. Resource sharing is among the most promising approaches

to better leverage the potential of mmWave-based frequencies in cellular communications.

Resource sharing has common challenges with heterogeneous networks. Although densification has observable limits for microwave frequencies, it is shown in both [26] and [27] that denser deployments are advantageous for mmWave bands because of their different propagation characteristics for LoS and NLoS environments [21].

3.1.1 Related Works

In the recent literature, we can find severals contributions that relate to *spectrum* and *infrastructure* sharing in both the microwave and the mmWave bands. Here described in the following the most relevant.

3.1.1.1 Spectrum sharing

In the microwave bands, where interference is the main limiting factor, competitive and greedy sharing methods might result in severe underutilization of the spectrum, as shown in [28]. A viable sensing approach for dynamic inter-operator spectrum sharing for an LTE-A system with carrier aggregation is proposed in [29]. Under the assumption of partial interference suppression, the optimality of full-spectrum sharing is validated by means of simulations in [30]. In the mmWave bands, interference avoidance has been shown to give optimum results for WiGig under dense deployments [31], [32]. However, the directional transmissions typically used at these frequencies allow considerable throughput gains even with blind reuse of frequency bands, e.g., as shown in [33], where a ray-tracing model is used to characterize the channel. The authors in [34] propose an interference sensing beamforming mechanism in Wireless Personal Area Networks (WPANs) that outperforms blind selection algorithms by $15\% - 31\%$. In [35], based on a simplified channel and antenna model and on a stochastic geometry approach, the authors show that sharing spectrum licenses increases the per-user rate when antennas have narrow beams, and that if network operators share their licenses, they can achieve the same per-user median rate as if each had an exclusive license with more bandwidth.

3.1.1.2 Infrastructure sharing

Load-aware strategies for the microwave bands are proposed in [36], through an approach based on cognitive spectrum sensing capabilities. In [37], the authors investigate the current technological, regulatory, and business landscape from the perspective of sharing network resources, and propose several different approaches and technical solutions for network sharing. In [35], co-location of base stations in the mmWave bands is considered. Through a simplified analytical approach, the authors document the potential benefits of infrastructure sharing, although the sensitivity of such results to more accurate channel and antenna

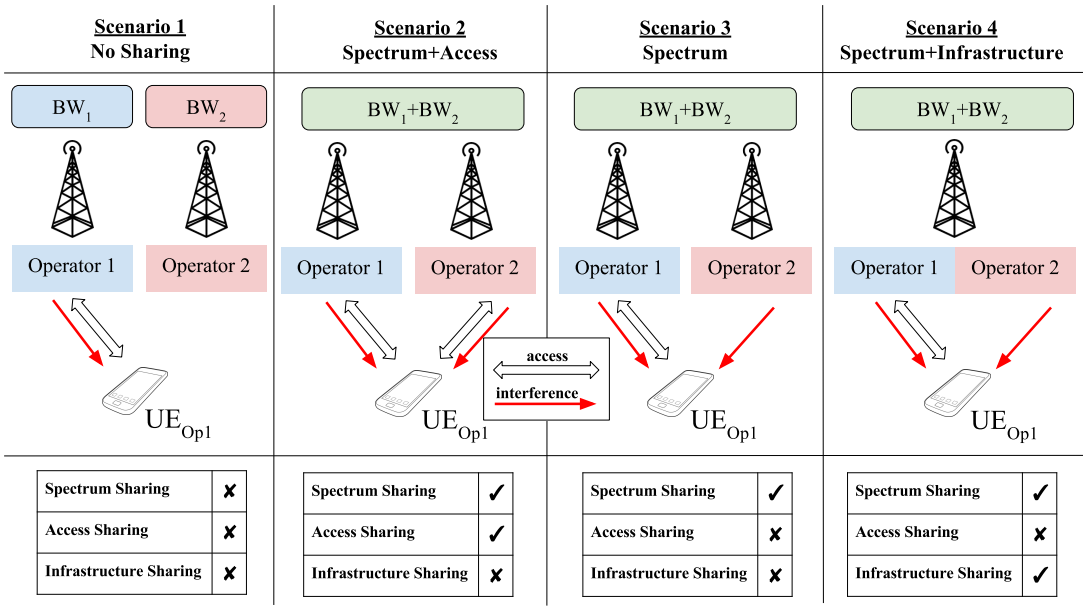

Figure 3.1: Considered {spectrum, access, infrastructure} sharing configurations.

models is not discussed.

3.2 Preliminary Evaluation

3.2.1 Sharing Configurations

As in both [6, 35], in this first analysis we want to compare different sharing configurations, and to derive some insights about the feasibility and performance benefits of resource sharing in mmWave networks. The scenarios considered in this evaluation are reported in Figure 3.1, and described in the following.[1]

Scenario 1 (No Sharing): This is our benchmark, where operators transmit in their own bands, which are orthogonal to each other, and utilize their own network infrastructures. Moreover, users can only connect to the operator they subscribe to. This is a traditional network architecture, used to assess the performance improvements obtained by the various sharing options.

Scenario 2 (Spectrum plus Access): Network providers share the same spectrum, and thus have a wider available bandwidth. They operate on separate infrastructures, but users can be associated to any operator. Due to the intrinsic complexity of this scenario, where full coordination is needed among the service providers to enable access sharing, it serves as an upper bound for the more realistic scenarios illustrated below. From a

[1] In this evaluation, we implicitly refer to the common case of two operators. Extension to the case of more than two operators is straightforward.

Table 3.1: Simulation parameters used in the preliminary spectrum sharing evaluation.

Value	Description (Notation)
2	Number of operators (M)
200 UE/km^2	UE density (λ_{UE})
30 gNB/km^2	gNB density (λ_{gNB})
1 km^2	Area of the simulations (A)
30 dBm	Transmitting power (P_{TX})
28 GHz	Carrier frequency (f)
1 GHz	Total bandwidth (W)
7 dB	Noise figure (NF)
64 elements	$[8 \times 8]$ UPA TX antennas (n_{TX})
16 elements	$[4 \times 4]$ UPA RX antennas (n_{RX})

mathematical point of view, this case corresponds to the previous one with twice the densities of UEs and gNBs and a double amount of bandwidth.

Scenario 3 (Spectrum): Network providers share the same spectrum but operate on separate infrastructures. Unlike in the previous scenario, users can only connect to their associated operator.

Scenario 4 (Spectrum plus Infrastructure): This is similar to Scenario 3, but with co-located gNBs, so that, besides sharing their spectrum, the operators also use a common network infrastructure. More precisely, each gNB site hosts one antenna for each operator. Note that this can be achieved if each of the two operators acquires half as many gNB sites and shares them with the other, thereby obtaining a dense infrastructure (with improved Signal to Interference plus Noise Ratio (SINR) and rate coverage) at a reduced cost compared to the case of separate infrastructures.

3.2.2 Evaluation Results

All our simulation parameters are reported in Table 3.1, where we assume that each of the two networks own a license for 500 MHz. In Scenarios 2, 3 and 4, both networks share their spectrum licenses, so that the same 1 GHz of total bandwidth is available to both operators.

Our simulations follow a Monte Carlo approach, in which many independent experiments are repeated to empirically derive statistical quantities of interest. Each experiment consists in (*i*) deploying UEs and gNBs according to two Poisson Point Process (PPP), as done in [6, 35] and [36], (*ii*) establishing UE-gNB associations according to a minimum path loss criterion, and (*iii*) computing the SINR of the user at the center of the area. The SINR statistics are estimated based on 10^4 repetitions of this procedure.

For a detailed comparison of the performance of the various sharing options, we compare all scenarios in Figures 3.2 and 3.3, focusing on a realistic channel and antenna representation. In terms of SINR coverage, a full-spectrum and access sharing configuration, i.e., Scenario 2, outperforms any other configuration. This, as explained in the previous section,

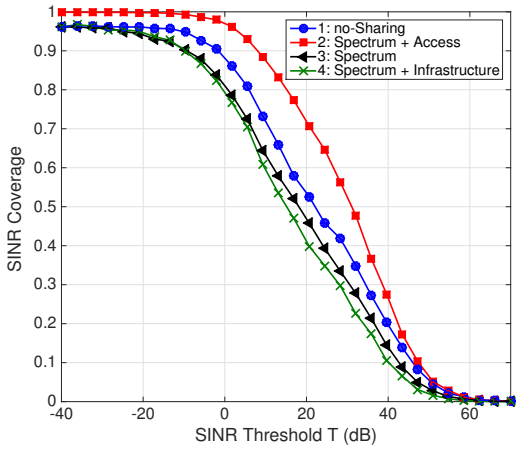

Figure 3.2: SINR coverage comparison for all scenarios.

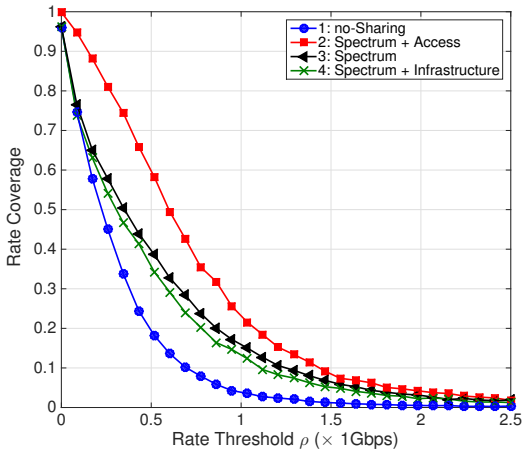

Figure 3.3: Rate coverage comparison for all scenarios.

serves as an upper bound because of the access sharing complexity, and is due to the fact that each user has more association opportunities and therefore better signal quality. Configurations with spectrum sharing and closed access, like Scenarios 3 and 4, show less SINR coverage than the no-sharing case of Scenario 1 (see Figure 3.2), because of the increased interference, but outperform it in terms of rate coverage (see Figure 3.3), because of the increased available bandwidth. Finally, we can note that Scenario 4, which is the most favorable setting for the operators from an economic perspective[2], presents only a slight degradation compared to Scenario 3. While this degradation was expected because of the constraints on gNB placement imposed by infrastructure sharing, it is interesting to observe that the performance loss is actually quite limited, especially in terms of rate. This shows that infrastructure sharing has the potential to provide an economical means to densify the

[2]This is due to the fact that network providers share the infrastructure costs of deployment.

network, achieving a performance level similar to what could be obtained with separate infrastructures, while using only half as many gNB sites.

3.2.3 Final Remarks

Based on the results shown in this section, we can draw the following key conclusions:

- Operators that share their licenses (frequency bands) can access more resources, thus providing higher rate for the average user of both providers.
- Full-spectrum and access sharing outperforms any other sharing scheme, in terms of both SINR and rate coverage, as users have more opportunities to find a gNB in-range (because of the increased gNB density) and can achieve higher data rates (because of the increased bandwidth).
- Scenarios with co-located antennas, namely infrastructure sharing, can obtain the performance gains achievable by network densification while incurring a significantly reduced deployment cost.

In this evaluation, we showed how resource sharing represents a solution to better leverage the potential of mmWave technology for cellular networks, where very large bandwidths and many antenna degrees of freedom are available. Through some detailed simulation results based on accurate channel and antenna models, we have characterized the benefits of resource sharing in these bands. In particular, the desirability of a full-spectrum and infrastructure sharing configuration, which results in increased user rate as well as in economical advantages for both service providers.

3.3 Dynamic Spectrum Sharing

In study [25], moving within the European and Italian regulatory conditions, we evaluate and then propose the use of Licensed Spectrum Access (LSA) to coordinate sharing among cellular operators. Additionally, we show some preliminary results on our research activities which are focused on a dynamic spectrum sharing approach applied in simulated 5G cellular scenarios.

3.3.1 Motivations

The next generation of cellular networks will need to cope with a very high mobile traffic demand, due to the expected increase in the number of connected devices and of the traffic they produce [38]. We have already discussed in the previous chapter that, as an enabler for these capacity-intensive applications, the mmWave band has been identified as a promising candidate for communication, thanks to the availability of wide portions of free spectrum [10].

Therefore, the fifth generation of cellular networks (5G), which is currently being standardized by the 3rd Generation Partnership Project (3GPP), will introduce carrier frequencies in the mmWave bands.

In the meantime, in addition to the 3GPP specification, spectrum regulators are providing indications on the mmWave bands they plan to release, and on the authorization mechanisms they plan to use in these frequencies. In the European spectrum specifications [39], each *Member State* should indicatively consider the range of frequencies between 24.25 and 27.5 GHz in a way to uniformly spread the use of 5G frequencies throughout Europe. Furthermore, each *Member State* is required to be flexible in the mix of authorization approaches to use. Alternative authorization approaches may include general authorization regimes (license exemption), exclusive license, licensed shared use between different UEs, geographical sharing (comprising sub-national, regional and site-specific licensing, including at the local level directly to businesses), or more dynamic approaches to spectrum sharing in time and space, possibly using geolocation databases [39].

Another important aspect, which should be properly settled, regards the coexistence of 5G systems around the 26 GHz band (or equivalent mmWave bands) with other services such as wireless fixed links and also Fixed-Satellite Services (FSSs) [40]. Depending on the location of the fixed links, the demand for 5G small cells, and the extent to which interference can be mitigated using new technologies, it may be possible to deploy 5G small cells within the same frequency range as some of these existing fixed links.

Even if the mmWave spectrum is large, in order to fit multiple operators in the available band, high 5G performance will only be possible with intelligent spectrum management mechanisms. For this reason, there arises a question from the regulators on how to efficiently use the available spectrum. According to regulatory rules which impose the full use of the band, and in order to address the question of how to properly use the available spectrum, in this work we propose a spectrum sharing solution for the mmWave band in 5G cellular scenarios. This requires an adaptive technology which can control and coordinate the sharing between operators. This technology must operate with a known language so that it can be used by all the entities in the network. To be precise, in this work we suggest the use of either a LSA approach or similarly the use of a third-party spectrum broker, both with the role to control and dynamically coordinate the sharing of licensed spectrum and efficiently use the resources according to operators needs. For example, if in a particular spatial and time instance the traffic grows faster and traditional exclusive spectrum is not enough, LSA allows for sharing while meeting the requirements of mobile operators and incumbents for predictable conditions of spectrum use and Quality of Service (QoS). The accessible band of any operator can be dynamically adjusted according to the needs of each network in the environment at any particular instant. Efficient spectrum sharing is necessary to provide fairness in the allocation as well as service satisfaction across multiple UEs while maximizing

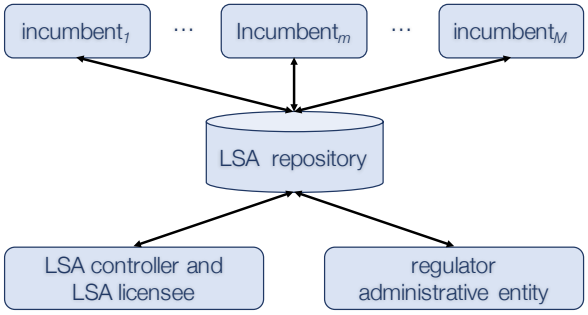

Figure 3.4: The LSA architecture reference model [41].

the spectral efficiency and the utilization of the total available bandwidth. In order to use the available spectrum in an efficient way, there should not be any unused resources. LSA may be a proper approach to avoid this issue, as it facilitates access to additional licensees in bands which are already in use by one or more incumbents[3]. We note that this should not be confused with the Licensed Assisted Access (LAA) approach, a technology which involves the sharing and aggregation of different bands (e.g., unlicensed spectrum) or also different Radio Access Technologies (RAT). Instead, LSA is a concept which permits to dynamically share the band, whenever and wherever it is unused by the incumbent users, i.e., Primary Users (PUs). The shared use of the spectrum is only allowed on the basis of an individual authorization (i.e., operators holding an LSA license or registered to use the band). As shown in Figure 3.4, each operator (i.e., incumbent) can request an LSA license through the LSA repository [41]. Then, the LSA controller, in agreement with the administrative entity, has the task to address all the license requests. LSA is defined within the framework of the European Union as: *"a regulatory approach aiming to facilitate the introduction of radiocommunication systems operated by a limited number of licensees under an individual licensing regime in a frequency band already assigned or expected to be assigned to one or more incumbent users"* [39]. Under this approach, the additional users are authorized to use the spectrum (or part of the spectrum) in accordance with sharing rules included in their rights of use of the spectrum, thereby allowing all the authorized users, including incumbents, to provide a certain QoS [39].

3.3.1.1 Related Works

Works [42,43] and [44] discuss possible sharing approaches that can be used for future mobile scenarios. However, in all these survey works simulation results are missing and a detailed mmWave environment was not considered. Some simulations and numerical evaluations were presented in [6, 24] and [45]. In both [6] and [45] it is shown that spectrum sharing at

[3]For example, such an incumbent may be a telephone service provider (i.e., an operator) that owns the license for the band.

mmWave has the potential for a more efficient spectrum use than a traditional exclusive spectrum allocation to a single operator. Work [24] introduces a hybrid spectrum access scheme for mmWave networks, where data packets are scheduled through two mmWave carriers with different characteristics. In particular, the authors combined a lower mmWave band with exclusive access and a higher mmWave band where spectrum is pooled between multiple operators. As a result, the investigation shows that this approach provides advantages for the average UE with respect to traditional fully licensed or fully pooled spectrum access schemes. The approach in [24] is dynamic, but cannot change during transmission, which means that the spectrum allocation is done only once, e.g., before starting the transmission. Differently, work in [46] reports a comparison between fixed and dynamic spectrum sharing and shows that dynamic spectrum sharing can benefit from spectrum handoff to enhance the rate performance by switching from the unavailable channels to the available ones, thereby maximizing the utilization of the total available bandwidth. Generally, dynamic spectrum sharing can benefit from spectrum handoff. On the other hand, static spectrum sharing can avoid the impacts of spectrum handoff delay by allowing Secondary Users (SUs) to back off and wait if any PU is using the same channel. In [47], the authors proposed a spectrum market mechanism where sharing is promoted explicitly by the government which regulated the use of the spectrum. The frequency regulator offers subsidy support to the wireless operators and requires a performance metric to be reported. Therefore, the spectrum is better exploited and all the entities benefit from this approach. Finally, work [48] proposed the use of a geolocation database together with a spectrum broker to control the time and spatial allocation of the band.

None of the above-related works have discussed the possibility to apply an LSA approach or a third-party spectrum broker as a controller which helps to improve the spectral efficiency of the networks in mmWave bands. For this reason, in our study we are suggesting the use of such approaches for mmWave bands in a way to improve the spectral efficiency and the QoS that operators can ensure to the customers.

3.3.2 Spectrum Use

3.3.2.1 Sharing Mechanisms

Before entering into the details about the Italian spectrum specifications[4], we discuss in this first part the two possible mechanisms that can be used to dynamically allocate spectrum. On one hand, we can consider an LSA approach where the administrative entity has direct control of the licensed band and also the temporal LSA licenses which are distributed to the other operators, i.e., the secondary users (SUs). On the other hand, a spectrum broker can also be considered which is not directly controlled by an administrative entity, but rather

[4]We are considering the Italian spectrum regulator because it was one of the first agencies setting conditions on the use of mmWave bands for 5G [49].

by a third-party company. In this second approach, only an agreement between operators is required, so that more complex business models become possible. It is clear that both these allocation procedures depend on the spatial region considered. Therefore, a geolocation database will be needed to store information about which portion of the band is shared and in which region.

Furthermore, an additional economic study is required, in order to understand if operators have business advantages to dynamically share the spectrum. In this preliminary analysis, we are not focusing on any economic aspects. Therefore, we reserve as a future work the study of how to optimize the use of spectrum considering also a cost model for sharing the band.

In the following section, we will analyze in detail the Italian spectrum specifications for the 5G mmWave band. However, similar procedure and considerations can be applied to other bands according to their corresponding regulatory specifications.

3.3.2.2 Italian regulatory conditions

AGCOM, the Italian spectrum regulator, provides a plan in [49], where 1 GHz of bandwidth at 26 GHz is designated for 5G applications and allocated for a future auction[5]. Furthermore, the entire bandwidth is slotted in five chunks with fixed sizes of 200 MHz each. Each operator can buy the license for at most two chunks and, if a band is not used, other operators or services in the area can use the portion of unused spectrum. This last rule is fundamental in order to efficiently use all the spectrum and avoid waste of resources. This restriction is valid in relation with the area considered, and therefore the use of the spectrum may vary in different regions. For this reason, an approach such as LSA combined with geo-location databases appears to be a proper solution to address the use of resources. A display of the portion of the band in question can be seen in Figure 3.5. The figure exhibits also the current use of the frequencies below 26.5 GHz and above 27.5 GHz (e.g., the broadband satellite communications designated for frequencies between 27.5 and 29.5 GHz). The detailed values here reported are taken from [49] and are valid for the Italian territory. Even if the concept proposed in this work is studied focusing on those values, it can be identically considered in others portion of the spectrum for the other European Member States and likewise other countries outside Europe.

As a possible result of the auction, five operators can buy a chunk of band each or, differently, four operators can buy the license of a chunk each, while the last unsold chunk can be shared among all the operators. Another possible outcome of the auction can see a single operator owning two chunks (i.e., 400 MHz of band) and the other three owning only a single chunk each. These are all possible outcomes of the auction. In the next part of

[5]Even though the document refers to this portion of spectrum as the 26 GHz band, the precise portion of spectrum is between 26.5 and 27.5 GHz.

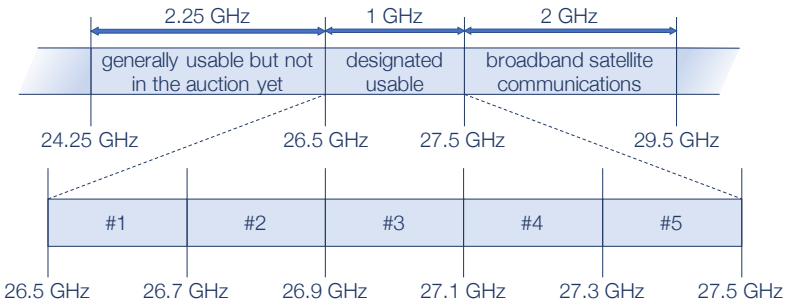

Figure 3.5: View of the spectrum around 27 GHz. The top part shows the designated use for each band, while in the bottom we show the five chunks of 200 MHz each, which will be auctioned in the Italian territory as specified in [49].

the research activity we will focus on the evaluation of just the first case, which is the most appropriate choice. Thus, we are considering five operators assigned a chunk of 200 MHz each.

Following these preliminary assumptions, we examine here a scenario with $M = 5$ operators indexed by $m \in \{1, \ldots, M\}$. Each operator owns distinct gNBs with no particular infrastructure sharing between operators, and the only iterations take place through the LSA controller. If $W_{tot} = 1$ GHz is the total system bandwidth available in the portion of spectrum accessible for auction (i.e., band around 26 GHz), initially we assume that each of the five operators is auctioned a $W_m = 200$ MHz chunk of licensed bandwidth, in which the m-th operator is the PU and has priority access. Therefore, bands assigned to different operators are disjoint. In this exploratory study, the effective allocation is dynamically adjusted according to the instantaneous traffic. In particular, an operator whose traffic is below a certain threshold must release part of its resources to other operators on a secondary basis.

As previously mentioned, in this study we propose and evaluate an approach where the spectrum is dynamically allocated. The use of the dynamic access scheme is motivated by the fact that in some cases an operator may need more resources with respect to the other operators in a particular area. Thus, a dynamic allocation of the resources can help to improve the QoS experience of the UEs in a particular time and space instance. The dynamic approach offers also better balancing of the available resources with respect to the baseline case, resulting in higher fairness. By adding the dynamic component, the average throughput and spectral efficiency are further improved thanks to the dynamic allocation of resources among operators. We note that this approach is reminiscent of the LSA framework, in fact, the dynamic component of the approach is achieved thanks to the LSA procedure, which permits to share the unused PU resources with others operators (i.e., SUs) as a way to better use the entire bands. Similarly, as previously mentioned, this dynamic sharing can be managed by a third-party broker which has the same distributed role of controlling the use of resources as in the LSA mechanism. In order to reproduce this behavior, we model a

scenario where the allocated band for each operator is proportional to its traffic.

3.3.3 System Model and Evaluation Methodology

In order to provide a proof-of-concept evaluation of the proposed dynamic hybrid spectrum access approach under realistic scenarios for mmWave cellular systems, we study it through a simulation methodology, where detailed models are used for all important effects and variables (including in particular channel characteristics and association policies), as described below. To do this, we simulate a dense area where multiple operators are co-located, and compare the performance of a baseline configuration with one based on dynamic sharing.

3.3.3.1 Deployment Model

For each operator $m \in \{1, \ldots, M\}$, the positions of the UEs and of the gNBs are modeled according to two PPPs, with densities λ_{UE} and λ_{gNB} in area A. This corresponds to considering an unplanned deployment, where gNBs are not optimally located.

3.3.3.2 Channel Model

The MIMO channel matrices are generated according to a statistical channel model derived from a set of extensive measurement campaigns in New York City [21]. We capture the metric of interest from the typical user located in the center of the area. With this method, we remove the border effects by considering all the interfering terms, thereby correctly evaluating the statistics of interest for the typical user.

3.3.3.3 Beamforming

We model the antennas as a Uniform Planar Array (UPA) with $\lambda/2$ spacing at both the gNB and the UE. Furthermore, we precisely model the antenna radiation pattern following the 3GPP specifications, as done in [50]. This permits to carefully characterize the steering beams, and therefore to have a precise knowledge of the amount of power irradiated by the antenna arrays in all directions, thus accurately computing the desired and interfering signals. Among other simplifications, this model assumes perfect beam tracking and the ability to form an arbitrary beamforming vector. Therefore, we can generate a beamforming vector for any possible angle and we also assume perfect alignment between the beams of each UE and its serving gNB.

3.3.3.4 Rate and Scheduling Model

For simplicity, in this initial study we assume that the channel gain is flat across time and frequency. We consider beamforming with single-stream transmissions (i.e., we do not consider spatial multiplexing) to any one UE. Thus, we define with term G_{ij} the desired gain

between gNB i and UE j. Similarly, we consider the gain G_{ijk} from an interfering gNB k from the same operator m. In this case, the UE will experience a time-varying interference as the interfering gNB directs its transmissions to the different UEs it is serving[6]. The SINR is then given by

$$\gamma_{ij} = \frac{\frac{P_{\mathrm{TX}}}{\ell_{ij}} G_{ij}}{\sum_{k \neq i} \frac{P_{\mathrm{TX}}}{\ell_{kj}} G_{ijk} + W_m N_0} \tag{3.1}$$

where P_{TX} is the total transmit power from the gNB, N_0 is the thermal noise power spectral density and ℓ_{ij} is the path loss between gNB i and UE j and is computed considering LoS, NLoS and outage states [21]. The summation in the denominator of (3.7) is over all gNBs k in the band, including gNBs of the same operator. Note that, within the cell, we assume that UEs are scheduled on orthogonal resources (e.g., in time or frequency) and hence there is no intra-cell interference.

Using the SINR expression in (3.7) we approximate the throughput for the j-th user (B_j) as follows

$$B_j = \frac{W_m}{N_i^{(m)}} \log_2 \left(1 + \gamma_{ij}\right) \tag{3.2}$$

where the total available resources, which are identified by the band W_m, are split among all the $N_i^{(m)}$ users of operator m associated to the i-th gNB. The ratio between the total bandwidth W_m and the number of users $N_i^{(m)}$ associated to the specific carrier provides the average amount of resources allocated to the j-th user over time.

We are also interested in the evaluation of the achievable performance in the case in which the transmission is performed with a coordination mechanism which permits to properly avoid inter-cell interference. In this last particular case, the interference can be neglected and the SINR formula in (3.7) can be approximated with the Signal to Noise Ratio (SNR) expression as follows

$$\hat{\gamma}_{ij} = \frac{\frac{P_{\mathrm{TX}}}{\ell_{ij}} G_{ij}}{W_m N_0} \tag{3.3}$$

3.3.3.5 Carrier Association

In cell and carrier association, each UE j must be assigned a serving gNB cell i. To be precise, each UE is associated with the gNB that provides the smallest path loss among all the available gNBs of the operator. Multiple UEs can be associated with a single gNB, while the gNB serves only a single UE per unit time slot according to a uniformly random scheduler.

[6]Detailed explanations of the channel, antenna and gain characterizations and calculations can be found later in this thesis in Sections 4.2 and 4.3.1, but also in works [21, 24] and [50].

3.3.3.6 Evaluation Approach

In order to evaluate the benefit of a dynamic sharing approach, we present a preliminary analysis of two different scenarios. As the baseline case, we consider a scenario where all the operators are serving the associated UEs using only the licensed chunk of band they own. As an alternative scenario, we consider a dynamic case where the resources are split among the operators according to the number of associated UEs in the area.

This simulation tool permits to understand the benefit and the achievable throughput of a system with a dynamic use of the resources. To be precise, defining as the typical gNB the gNB to which the typical UE is associated, we compare the number of associated UEs to the typical gNB with respect to all the other gNBs in the area. We then split the total band W_{tot} according to the need of each operator in the considered area. For instance, if the typical gNB of operator m has fewer associated UEs with respect to the other gNBs in the area, the allocated band W_m used for the transmission of the typical gNB will be smaller with respect to the licensed chunk operator m has licensed. Thus, the remaining part of the chunk will be shared and then allocated to other operators in the area with a larger number of associated UEs. Conversely, if the typical gNB has more associated UEs with respect to the other gNBs in the area, the allocated band used for its transmission will be larger than the licensed chunk, therefore the use of some portions of bands licensed to other operators will be necessary.

We use the *Jain* fairness measures to determine whether users are receiving a fair share of the system resources [51]. The fairness for a set of n throughput values is computed as

$$\mathcal{J}(B_1, B_2, \ldots, B_n) = \frac{(\sum_{i=1}^{n} B_i)^2}{n \sum_{i=1}^{n} B_i^2} \tag{3.4}$$

The metric $\mathcal{J}$ ranges from $\frac{1}{n}$, which represents the worst case, to 1 (best case), and it is maximum when all UEs have the same throughput.

3.3.4 Numerical Results

We report in this section results obtained from the analysis we have done in order to understand the advantages that an efficient use of the spectrum can bring. As previously explained, we are comparing two different simulation scenarios: (*i*) the baseline where the chunks of the band are equally and exclusively split among five operators; (*ii*) a scenario where operator bands are shared and dynamically adjusted in relation to the needs of the operators in a particular region.

We report in Figure 3.6 the empirical CDF of the throughput for the typical UE in all the compared configurations. As we can see, the procedure in which the band is dynamically adjusted according to the area results in better fairness among the UEs. In fact, the throughput is reduced for the best users (i.e., upper right part of the curve) while at the

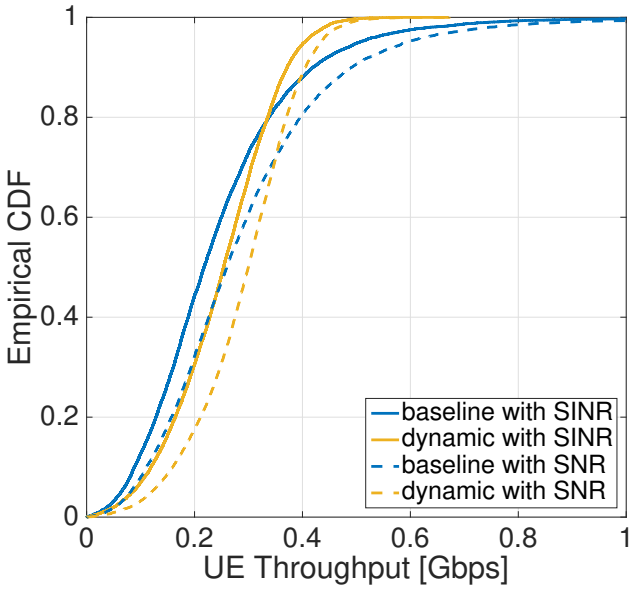

Figure 3.6: Empirical Cumulative Distribution Function (CDF) of the throughput (B) per UE in the two configurations evaluated. In particular, the dashed lines are used for throughput representations when interference is neglected, thus SNR is considered instead of SINR. Figure obtained considering a gNB density of 75 gNB/km^2 for each operator.

same time, passing from the blue curve to the yellow one, the throughput is improved for all the other users (e.g., worst and medium UEs). This means that the users in the dynamic procedure experience better fairness and the overall spectral efficiency increases. Similar behavior is achieved when the term $\hat{\gamma}_{ij}$ (i.e., SNR) is considered. As expected, the throughput is bigger if an interference avoidance mechanism is adopted (as shown by the dashed curves). Furthermore, this last set of curves (i.e., when SNR is considered in place of the SINR) allows us to understand the upper bound that can be reached in the case in which all the interference conditions can be mitigated in the system.

Moreover, in Table 3.2 we report the Jain fairness measure and the average UE throughput varying the gNB density, which is considered equal for all the operators in the area. We recall that, even if the densities of UEs and gNBs are fixed and equal for all the operators, the precise number of nodes deployed is random and follows two independent PPPs. As the table reports, with the dynamic use of the spectrum, the average throughput is slightly bigger than the baseline, but more importantly, the fairness increases, which means that resources are better assigned among all the UEs. Other spectrum sharing techniques (i.e., the ones studied in [6, 24, 45]) can further improve the average throughput and the spectral efficiency, although drastically reducing the fairness among the UEs. Moreover, such schemes would require accurate coordination, which may be costly in dense networks.

Table 3.2: Comparison of the Jain fairness measure and the average UE throughput $\bar{B}$ [Gbps] varying the gNB density per operator.

		50 gNBs/km^2	75 gNBs/km^2	100 gNBs/km^2
baseline	$\mathcal{J}$	0.6798	0.7384	0.7584
	$\bar{B}$	0.2333	0.2422	0.2475
dynamic	$\mathcal{J}$	0.8406	0.8719	0.8834
	$\bar{B}$	0.2359	0.2510	0.2527

3.3.5 Remarks and Future Directions

With this evaluation we suggest the use of an LSA or a third-party spectrum broker approach to dynamically share the total system band among operators in 5G mmWave cellular networks. In the context of the Italian regulator, which in turn follows the European directives, we suggest the use of a dynamic allocation of resources among operators. It appears useful to use a dynamic sharing approach for these frequencies in a way to better manage the spectrum and improve UE fairness. Our preliminary results show that dynamically sharing the spectrum according to the number of UEs associated to each operator results in better fairness among the UEs and also in the improvement of both spectral efficiency and user QoS.

As a future extension of this study, it appears interesting to further research spectrum sharing approaches in line with the specifications of the regulators. An improvement of the preliminary analysis is required, focusing also on other specific outcomes of the auctions between operators. Moreover, as previously mentioned, an economic study is needed in order to optimize the use of spectrum considering also a cost model for the network operators that use the shared bands.

3.4 Hybrid Spectrum Sharing

While spectrum at mmWave frequencies is less scarce than at traditional frequencies below 6 GHz, still it is not unlimited, in particular if we consider the requirements from other services using the same band and the need to license mmWave bands to multiple mobile operators. Therefore, an efficient spectrum access scheme is critical to harvest the maximum benefit from emerging mmWave technologies. In this last section, we introduce a new hybrid spectrum access scheme for mmWave networks, where data packets are scheduled through two mmWave carriers with different characteristics. In particular, we consider the case of a hybrid spectrum scheme between a mmWave band with exclusive access and a mmWave band where spectrum is pooled between multiple operators [7, 24]. To the best of our knowledge, this is the first study proposing hybrid spectrum access for mmWave networks and providing a quantitative assessment of its benefits. Our results show that this approach provides

advantages with respect to traditional fully licensed or fully pooled spectrum access schemes, though further work is needed to achieve a more complete understanding of both technical and non-technical implications.

3.4.1 Motivations

mmWave communications has emerged as a key disruptive technology for both cellular networks (5G and beyond) [10,11,52–54] and Wireless Local Area Network (WLAN) (802.11ad and beyond) [55,56]. While spectrum is extremely limited in traditional bands below 6 GHz, mmWave frequencies offer potentially orders of magnitude greater bandwidths. In addition, thanks to the small wavelength, mmWave communication is typically characterized by transmission and reception with very narrow beams, enabling further gains from directional isolation between mobiles [17, 57].

This combination of massive bandwidth and spatial degrees of freedom may make it possible for mmWave to meet some of the boldest 5G requirements, including higher peak per-user data rate, high traffic density, and very low latency [58,59]. However, even spectrum at mmWave is obviously not unlimited, in particular if we consider the requirements from other services (e.g., satellite and fixed services [40]) and the need to license mmWave bands to multiple mobile operators. Therefore, an efficient spectrum access scheme is critical to harvest the maximum benefit from emerging mmWave technologies [45].

As regulatory authorities are considering opening up some mmWave bands for cellular use, the licensing and usage models for these bands require some studies. At root, the mmWave bands present three unique features not present at lower frequencies. First, due to the massive bandwidth and spatial degrees of freedom, the mmWave bands could be highly under-utilized if large bandwidths are allocated exclusively to a single operator. For example, a scaling law analysis in [60], as well as simulations in [4], demonstrate that links may become power-limited in wide bandwidth regimes, thereby forgoing the benefits of the large numbers of degrees of freedom. Second, mmWave communications are typically characterized by transmissions with very narrow beams. Third, mmWave signals suffer from major propagation-related shortcomings, such as a relatively short range and the difficulty of providing a robust connection, which makes it challenging to provide a consistent user experience. To overcome these shortcomings, mmWave networks have been usually envisioned in the context of heterogeneous deployments [61–64], where part of the connection is carried out with an anchor over a traditional sub-6 GHz carrier and part via a mmWave carrier.

More recent results have shown that even stand-alone mmWave systems can be deployed, and in this case it becomes of interest to study systems where the use of different bands in the very wide mmWave spectrum (e.g., at lower frequencies – around 30 GHz – and at higher frequencies – around 70 GHz) may provide complementary features, thereby enabling a more efficient use of the spectrum resources, especially in the context of a spectrum sharing

paradigm [45]. Such a *heterogeneous mmWave deployment* paradigm is consistent with the choice made by the 2015 World Radio Conference (WRC), where different bands, ranging from about 24 GHz to 86 GHz, were selected for further studies on their use in future 5G systems [65].

These features raise some broad questions that are the main motivation for this study, e.g., how the mmWave spectrum should be utilized amongst multiple operators and, specifically, to what extent spectrum should be shared and how the optimal spectrum sharing arrangement varies with the different frequency bands. The main goal of this research activity is to provide some initial answers to these important questions, with focus on technical and network performance issues.

3.4.1.1 Traditional spectrum access models for mobile communications

Traditionally, wireless data services have been delivered mainly by using two different spectrum access models. Under the *exclusive* model, each mobile operator is granted the exclusive right of use of a spectrum band to provide mobile services. Exclusive spectrum access has been one of the key factors for the successful deployment of cellular systems since their inception, and it is by far the default model to provide mobile services. Under the *license-exempt* (also referred to as *unlicensed*) model, spectrum is allowed to be used by several users/mobile operators. While there is no guaranteed access to an instantaneously fixed amount of spectrum, politeness rules (e.g., based on a Listen-Before-Talk (LBT) principle) are in place to promote a fair use of the spectrum. The license-exempt spectrum model has been one of the key factors for the successful deployment of WiFi as a ubiquitous way of connecting devices to the Internet. The *spectrum pooling* model has also been considered as an intermediate paradigm, where a small number of operators are granted access to the same spectrum resources, with rules that are known a priori [66]. Although spectrum pooling still does not provide guarantees for the access to an instantaneously fixed amount of spectrum, it does ensure some level of predictability and of short-term and long-term fairness [67]. We note that spectrum pooling is a subcase of co-primary spectrum sharing, where an operator is authorized to share a band with a limited number of other spectrum users (for example sharing between fixed links and satellite services licensed on the same band) [67, 68].

Many other sharing paradigms have been considered in addition to co-primary sharing, like sharing between a primary and a secondary user (vertical sharing) [69], sharing on a geographic basis [70], licensed shared access (e.g., via databases) [71], and sharing via license-exemption [43]. However, herein we mainly consider spectrum pooling, although our results can be extended also to the case of license-exemption.

3.4.1.2 The emergence of hybrid spectrum access for sub-6 GHz wireless communications

Recently, new technologies have emerged that aggregate spectrum in both exclusive and license-exempt bands, routing packets to the carrier frequency that best matches their requirements. Aggregation is implemented in a way to permit a very rapid switch between exclusive and license-exempt carriers, effectively realizing a *hybrid spectrum access regime*. Examples of these technologies are LTE-LAA, LTE-WiFi Link Aggregation (LWA) and LTE-WiFi integration at the IP layer (LWIP) [72–76]. LAA is an extension of carrier aggregation that allows aggregating licensed carriers with license-exempt spectrum at 5 GHz, in the same bands used for WiFi. In particular, it uses licensed spectrum for control-related transmissions while sending data over either licensed or licence-exempt spectrum via MAC-layer switching[7]. LWA is a framework standardized by 3GPP aiming at providing a tight radio-level interaction between LTE and WiFi. Using LWA, aggregation between LTE and WiFi is implemented at the base station at the Packet Data Convergence Protocol (PDCP) layer, where scheduling decisions can be made based on real-time channel conditions. LWIP is similar to LWA, but aggregates traffic at the Internet Protocol (IP) layer in a way to route IP packets to either an LTE base station or a WiFi access point via an IPSec tunnel.

3.4.1.3 Which spectrum access for mmWave networks?

As discussed above, an efficient spectrum access scheme is a key requirement to maximally benefit from emerging mmWave technologies [45]. Recent works compared exclusive spectrum allocation with different types of spectrum pooling or unlicensed models, showing different results as a function of the assumptions used. Reference [33] introduced a new signaling report among mobile operators, to establish an interference database to support scheduling decisions, with both a centralized and a distributed supporting architecture. In the centralized case, a new architectural entity receives information about the interference measured by each network and determines which links cannot be scheduled simultaneously. In the decentralized case, the victim network sends a message to the interfering network with a proposed coordination pattern. The two networks can further refine the coordination pattern via multiple stages. Reference [35] studied the feasibility of spectrum pooling in mmWave networks under the assumption of ideal antenna patterns and showed that spectrum pooling might be beneficial even without any coordination between the different operators. In particular, [35] showed that uncoordinated pooling provides gains at both 28 GHz and 73 GHz. Reference [45] further developed the results in [33] and [35], focusing on the effect of coordination and of inaccurate beamforming, and showed that, while coordination may

[7] An equitable coexistence between LAA and WiFi is guaranteed by mandating that both LAA and WiFi implement a set of politeness protocols, whose details have been recently defined by the European Telecommunications Standards Institute (ETSI) Broadband Radio Access Networks (BRAN) committee.

not be needed under ideal assumptions, it does provide substantial gains when considering more realistic channel and interference models and antenna patterns. Moreover, it showed that, under realistic assumptions, spectrum pooling without coordination might be more feasible at high mmWave frequencies (e.g., 70 GHz) than at low mmWave frequencies (e.g., 28 or 32 GHz), due to the higher directionality of the beams.

Reference [6] compares different resource sharing paradigms and shows that a full-spectrum and infrastructure sharing configuration provides significant advantages, even without resorting to complex signaling protocols for the exchange of information between multiple operators' networks. Reference [77] investigates the use of spectrum sharing as a function of cell association and beamforming, through the formulation of various optimization problems for different levels of inter-operator coordination, and characterizes the performance gains achievable in different scenarios. Finally, reference [78] studies both technical and economic implications of resource sharing in mmWave networks. The work shows that open deployments of neutral small cells that serve subscribers of any service provider encourage market entry. In fact, neutral small cells make it easier for networks to reach a sufficient number of subscribers than unlicensed spectrum would.

3.4.1.4 The contribution of this study: hybrid spectrum access for mmWave networks

This study extends the previous results in [6, 7, 45] and [77] to the case of hybrid spectrum allocation. In other words, differently from the previous works, where exclusive access and spectrum pooling were compared, in this work we propose a spectrum access paradigm that builds on both exclusive access and spectrum pooling. We introduce the use of an iterative algorithm that permits to evaluate the equilibrium point of the system, and therefore to precisely appraise our hybrid spectrum sharing procedure. Note that this algorithm is not meant to represent how a real system would work but is just one possible tool to evaluate the system. Moreover, with the use of this algorithm we can easily test different allocation procedures (such as joint carrier and cell or carrier-only), thus we can further show the benefit of the hybrid procedure suggested under different parameters and different power constraints. In particular, motivated by the results in [45] where pooling was proved to be more feasible at high mmWave frequencies, we study the performance of a hybrid spectrum scheme where exclusive access is used at frequencies in the 20/30 GHz range while pooling is used at frequencies around 70 GHz[8]. The two bands are aggregated at the MAC layer as illustrated in Figure 3.7, and users are allocated to one or the other band to maximize the

[8]In the following we will refer to the 28 GHz and 73 GHz bands, for which many measurements are available in the literature (e.g., see [11, 18–21]). However, we note that the results herein, possibly with some minor modifications, would apply to adjacent bands as well. In particular, the results obtained for the 28 GHz band apply also to the two bands selected by the 2015 WRC [65] for sharing and compatibility studies for 5G, i.e., 24.25 – 27 GHz and 31.8 – 33.5 GHz. The results obtained for 73 GHz apply to the 66 – 76 GHz band, again selected by WRC-15 for sharing and compatibility studies for 5G.

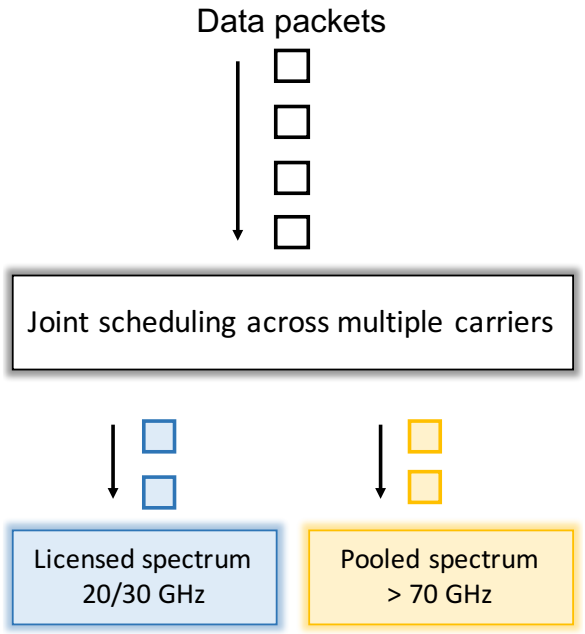

Figure 3.7: Block diagram of the joint scheduling that allocates user packets in the different bands.

rate, based on cell load and interference.

Differently from the LAA case, in this study we assume that all the operators sharing the pooled band have access to an anchor in the licensed spectrum. Moreover, differently from LAA, that includes politeness techniques based on a LBT protocol permitting co-existence with WiFi within the same 5 GHz bands, here we investigate the possibility of providing politeness between different operators sharing the pooled mmWave band by exploiting mmWave directional characteristics (narrower beams and shorter range) through load information and an interference-aware scheduler[9].

Finally, we note that we consider aggregation between a licensed and a pooled carrier rather that between a licensed and a license-exempt carrier. Overall, the different spectrum sharing assumptions (pooled and unlicensed, with and without an anchor in licensed spectrum) and the very different directional characteristics lead us to designing a different solution for hybrid spectrum access at mmWave, compared to the solutions already available for sub-6 GHz spectrum.

We compare our proposal with two baselines, one relying on exclusive spectrum access at both 28 GHz and 73 GHz and the other relying on pooling at both 28 GHz and 73 GHz. Our initial assessment shows that this approach provides advantages for the average user with respect to traditional fully licensed or fully pooled spectrum access schemes, in terms of increased throughput, spectral efficiency, and better balancing of the available resources,

[9]Note that with this term we generically indicate a scheduler that is able to choose the less interfered carrier. However, this work does not aim to analyze in depth any particular kind of scheduler.

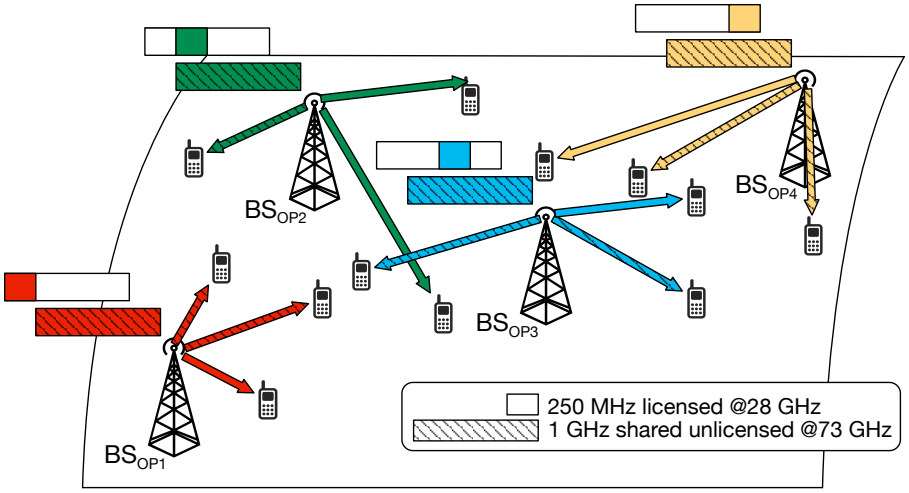

Figure 3.8: Example of the hybrid spectrum paradigm where four different operators share 1 GHz in the 70 GHz range, while having each exclusive access to 250 MHz in the 20/30 GHz range.

which results in higher fairness. These results motivate further work towards achieving a more complete understanding of both technical and non-technical implications of different sharing paradigms.

3.4.2 Spectrum Access Modes: Exclusive, Pooled and Hybrid

We begin by more precisely defining the various modes for spectrum access. We consider a scenario with M operators indexed by $m \in \{1, \ldots, M\}$. Each operator owns distinct gNBs with no infrastructure sharing between operators. Each gNB supports two mmWave bands: one at a low carrier c_ℓ and one at a high carrier c_h. In each carrier c, a gNB can radiate a maximum total power $P_{\mathrm{TX}}^{(c)}$ over the available bandwidth $W^{(c)}$.

Each carrier can be pooled or exclusive. Let $W_{tot}^{(c)}$ be the total system bandwidth available at carrier c. Exclusive access means that each operator is assigned a bandwidth $W^{(c)} = W_{tot}^{(c)}/M$, such that bands assigned to different operators are disjoint. As a result, in the exclusive case, there is no co-channel interference between different operators. A carrier being pooled instead means that it is shared by all M operators, so that in this case all operators use the same bandwidth and $W^{(c)} = W_{tot}^{(c)}$. Hence, in this case there is co-channel interference between operators.

In this section, we propose and evaluate the following novel hybrid spectrum access model for systems with two carriers:

- *Hybrid:* The low frequency carrier c_ℓ is exclusive while the high frequency carrier c_h is pooled (see Figure 3.8 for an example),

which will be compared with the following two baseline approaches:

- *Exclusive only:* Both carriers are licensed for exclusive use for all operators;
- *Pooled only:* Both carriers are pooled for all operators.

The use of the hybrid access scheme is motivated by the results in [45] that showed that while at "low" c_ℓ mmWave frequencies (e.g., 20/30 GHz) spectrum pooling requires coordination between different operators, at higher c_h mmWave frequencies (e.g., 70 GHz) pooling works well even in an uncoordinated setup. As an example of a possible use of this paradigm, data requiring higher reliability (e.g., control signaling) is routed through exclusive mmWave spectrum while best-effort data uses pooled mmWave spectrum.

We note that this approach is reminiscent of the LAA framework, recently standardized by 3GPP [72]. LAA is an extension of carrier aggregation that allows aggregating licensed carriers with license-exempt spectrum at 5 GHz. The main differences between LAA and the approach we propose is that here we consider aggregation between a licensed and pooled carrier rather than between a licensed and a license-exempt carrier[10]. Moreover, differently from LAA, that includes politeness techniques to allow coexistence with WiFi within the same 5 GHz bands, here we investigate the possibility of aggregating licensed and pooled carriers, by exploiting the directional characteristics (narrower beams and shorter range) of mmWave bands via an interference-aware scheduler.

From a spectrum authorization perspective, the difference between LAA and the scheme we propose here is that LAA is built to work on a shared band that is license exempt, i.e., where everyone can have an access point compliant with the Radio Local Area Network (RLAN) standard and deploy it. Some of these access points might be LAA access points (and therefore exploit an exclusively licensed carrier in a different frequency), while others might be WiFi access points (and therefore only use license-exempt spectrum). The way regulators ensure that LAA and WiFi access points equitably share the spectrum is by mandating the use of a set of politeness protocols. In this study we consider the case where the spectrum is shared (pooled) by a limited number of users, all of which have access to an exclusively-licensed band at a different frequency. From a technical perspective, there is a significant difference related to the use of politeness protocols. Due to the specific authorization assumption we make, we do not consider politeness protocols, and design our proposed user/carrier allocation technique accordingly.

3.4.3 System Model and Evaluation Methodology

A precise mathematical analysis of the capacity under different spectrum access models is difficult due to the inter-relations among interfering operators, the coupling introduced

[10]We highlight that the main difference between pooled and license-exempt frequencies is that if we enable a licence-exempt use of the band, we ought to consider mechanisms to ensure an equitable use of the spectrum. From a technical perspective, this would require further steps compared to what we have proposed up to now. At lower frequencies (5 GHz) this is already done, but mechanisms used there (e.g., listen-before-talk) might not apply or might not be optimized for mmWave frequencies.

by load-aware association policies, and the complex characterization of the MIMO channel model. Such an analysis requires careful modeling and the use of approximations, and will be part of our future work. Here, in order to provide a proof-of-concept evaluation for the proposed hybrid spectrum access approach under realistic scenarios for mmWave cellular systems, we study the different spectrum access schemes through a careful simulation methodology, where detailed models are used for all important effects and variables (including in particular channel characteristics and association policies), as described below.

3.4.3.1 Deployment model

For each operator $m \in \{1, \ldots, M\}$, the positions of the UEs and of the gNBs are modeled according to two PPPs, with densities λ_{UE} and λ_{gNB} in some area A. This corresponds to considering an unplanned deployment, where base stations (i.e., gNB) are not optimally located.

3.4.3.2 Rate and scheduling model

We let $\mathbf{H}_{ij}^{(c)}$ denote the MIMO channel matrix from gNB i to UE j at carrier c. For simplicity, in this initial study we assume that the channel gain is flat across time and frequency. We assume beamforming with single-stream transmissions (i.e., no spatial multiplexing) to any one UE. We let $\mathbf{w}_{\text{RX}_{ij}}^{(c)}$ and $\mathbf{w}_{\text{TX}_{ij}}^{(c)}$ denote the RX and TX beamforming vectors that would be used if gNB i were serving UE j. The generation of the channel matrices and selection of the beamforming vectors is discussed below.

With single-stream beamforming, the effective Single Input, Single Output (SISO) channel gain along the serving link is given by

$$G_{ij}^{(c)} = \left| \mathbf{w}_{\text{RX}_{ij}}^{(c)H} \mathbf{H}_{ij}^{(c)} \mathbf{w}_{\text{TX}_{ij}}^{(c)} \right|^2 \tag{3.5}$$

Now, consider the gain from an interfering gNB k. An interfering gNB may be from the same operator as that of the UE or a different operator within a common pooled band. In either case, the UE will experience a time-varying interference as the interfering gNB directs its transmissions to the different UEs it is serving. We let $\bar{G}_{ijk}^{(c)}$ be the average channel gain from the interfering gNB k to user j of gNB i, defined as

$$\bar{G}_{ijk}^{(c)} = \frac{1}{N_k^{(c)}} \sum_{j'} \left| \mathbf{w}_{\text{RX}_{ij}}^{(c)H} \mathbf{H}_{kj}^{(c)} \mathbf{w}_{\text{TX}_{kj'}}^{(c)} \right|^2 \tag{3.6}$$

$$\mathbf{w}^{(c)}_{\mathrm{TX}_{mij}}(\theta,\phi) = \frac{1}{\sqrt{n_{\mathrm{TX}}}} \begin{bmatrix} 1 \\ \exp(0)\exp(-j2\pi\Delta\phi) \\ \exp(0)\exp(-j2\pi\Delta 2\phi) \\ \vdots \\ \exp\left(-j2\pi(\sqrt{n_{\mathrm{TX}}}-1)\Delta\theta\right)\exp(-j2\pi(\sqrt{n_{\mathrm{TX}}}-2)\Delta\phi) \\ \exp\left(-j2\pi(\sqrt{n_{\mathrm{TX}}}-1)\Delta\theta\right)\exp(-j2\pi(\sqrt{n_{\mathrm{TX}}}-1)\Delta\phi) \end{bmatrix} \tag{3.8}$$

where the averaging is over all UEs j' served by gNB k. The SINR is then given by

$$\gamma^{(c)}_{ij} = \frac{\frac{P^{(c)}_{\mathrm{TX}_i}}{\ell^{(c)}_{ij}} G^{(c)}_{ij}}{\sum_{k\neq i} \frac{P^{(c)}_{\mathrm{TX}_k}}{\ell^{(c)}_{kj}} \bar{G}^{(c)}_{ijk} + W^{(c)} N_0} \tag{3.7}$$

where $P^{(c)}_{\mathrm{TX}_i}$ is the total transmit power from the gNB in the available bandwidth $W^{(c)}$ at carrier c, N_0 is the thermal noise power spectral density and $\ell^{(c)}_{ij}$ is the path loss between gNB i and UE j and is computed as described in the following paragraphs. The summation in the denominator of (3.7) is over all gNBs k in the band, including gNBs of both the same operator and other operators. Note that, within the cell, we assume that UEs are scheduled on orthogonal resources (e.g., in time or frequency) and hence there is no intra-cell interference.

3.4.3.3 MIMO Channel Model

The MIMO channel matrices are generated according to a statistical channel model derived from a set of extensive measurement campaigns in New York City [18–20, 23]. Details of this model are given in [21] and were previously described in Section 2.3. In addition to our basic channel characterization, we consider in this study, a wrap-around procedure that replicates each transmitting gNB in eight different additional areas all around the main area. With this method, we remove the cell-edge effects by considering all the interfering terms, thereby correctly evaluating the statistics of interest for all the users.

We model the antennas as a UPA with $\lambda/2$ spacing at both the gNB and the UE. Once the large-scale parameters are randomly generated, a random matrix $\mathbf{H}^{(c)}_{ij}$ can be generated from the UPA array and random small-scale complex fading applied to each sub-path in the path cluster. Further details regarding the channel characterization can be found in Section 2.3.

3.4.3.4 Beamforming

For each channel matrix $\mathbf{H}_{ij}^{(c)}$ we compute the beamforming vectors at the transmitter (or receiver) as reported in (3.8), where Δ is the spacing between the elements of the array, (θ, ϕ) are the horizontal and vertical angles of the direction of transmission (or reception in the RX case), and n_{TX} is the normalization factor, which corresponds to the total number of elements in the antenna array [79]. Note that the only difference between RX and TX is the number of antenna elements. Among other simplifications, this model assumes perfect beam tracking and the ability to form an arbitrary beamforming vector. Therefore, we can generate a beamforming vector for any possible angle between 0 and 360 degrees. We also assume perfect alignment between the beams of each UE and its serving gNB.

3.4.3.5 Antenna configuration and Power Limits

We consider three different transmitter and receiver configurations:

i) Both bands use the same number of antenna elements: $n_{\mathrm{TX}} = 64$ and $n_{\mathrm{RX}} = 16$. We consider the same constraint on the Equivalent Isotropically Radiated Power (EIRP) on both bands, i.e.

$$E\left[|\mathbf{x}^{(c)H}_{mij}\mathbf{x}^{(c)}{}_{mij}|^2\right] \leq P_{\mathrm{TX}}, \quad c \in \{c_\ell, c_h\} \tag{3.9}$$

where $\mathbf{x}_{mij}^{(c)}$ is the symbol exchanged between gNB i and UE j of operator m using carrier c.

ii) We double the number of antenna elements per dimension for the higher band[11]. Moreover, we normalize the beamforming coefficients in a way to satisfy the same EIRP constraint for both bands as in *i)*.

iii) As in *ii)*, we double the number of antenna elements per dimension for the higher band. However, we consider different EIRP constraints for the different bands:

$$E\left[|\mathbf{x}^{(c)H}_{mij}\mathbf{x}^{(c)}{}_{mij}|^2\right] \leq P_{\mathrm{TX}}^{(c)}, \quad c \in \{c_\ell, c_h\} \tag{3.10}$$

Under the assumption of $n_{\mathrm{TX}} = 64$ and $n_{\mathrm{RX}} = 16$ for c_ℓ and $n_{\mathrm{TX}} = 256$ and $n_{\mathrm{RX}} = 64$ for c_h, we can assume the following values for the antenna array gains:

$$\begin{aligned} G^{(c_\ell)} &= 10\log_{10}(64) \simeq 18\,\mathrm{dB} \\ G^{(c_h)} &= 10\log_{10}(265) \simeq 24\,\mathrm{dB} \end{aligned} \tag{3.11}$$

[11] For example, due to the reduced wavelength, with the same antenna array dimension at 73 GHz we can fit about 2.6 times more elements per dimension than at 28 GHz.

Table 3.3: Antenna element sizes and transmit power limits for the various power constraints.

	# UE antenna elements		# gNB antenna elements		gNB power limit P_{TX} [dBm]	
	28 GHz	73 GHz	28 GHz	73 GHz	28 GHz	73 GHz
i)	16	16	64	64	30	30
ii)	16	64	64	256	30	24
iii)	16	64	64	256	30	30

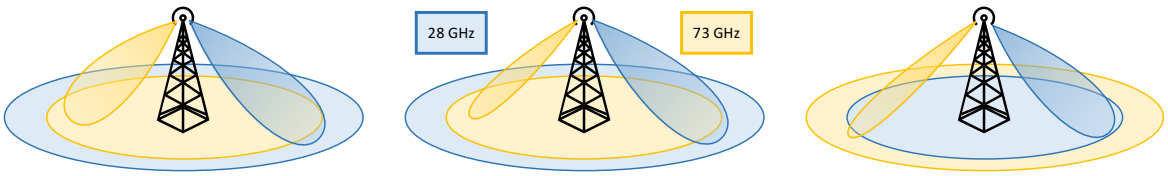

Figure 3.9: Examples of beamforming and coverage in the two bands for the three power constraint scenarios. The left drawing is case *i)*, the one in the middle is constraint *ii)* and finally, the right drawing is case *iii)*.

Then:

$$\begin{aligned} P_{\text{TX}}^{(c_h)}[dB] &= P_{\text{TX}}^{(c_\ell)}[dB] + G^{(c_h)} - G^{(c_\ell)} \\ &= P_{\text{TX}}^{(c_\ell)}[dB] + 6 \end{aligned} \tag{3.12}$$

We provide a graphical representation of the implications of the different configurations on the transmit beams in Figure 3.9, and summarize the parameters for the different configurations in Table 3.3. Configuration *i)* implies that the same beamwidth is used for the two bands. Moreover, due to the increased path loss at higher frequencies, the higher band provides a reduced coverage area. Configuration *ii)* implies that a narrower beam is used for the higher frequency. However, EIRP normalization at the higher frequency implies that also in this case the higher frequency might provide a reduced coverage area. Configuration *iii)* implies that a narrower beam is used for the higher frequency. Allowing a higher EIRP for the higher band allows an increased the coverage area (which becomes similar to that of the lower band), although the drawback is an increased interference to the other cells.

3.4.4 Distributed Cell and Carrier Association

The network performance under any spectrum access model (exclusive, pooled or hybrid) will depend on how a UE is assigned a serving gNB and a carrier. This problem is called cell and carrier association and can be formalized as follows. Indexing the set of all gNBs by i and all UEs by j. Let $\mathcal{I}_m$ and $\mathcal{J}_m$ be the subsets of gNBs and UEs for operator m.[12] In cell

[12]Note that $\mathcal{J}_m$ represents the set of users for operator m, while J_m stands for their number, so $J_m = |\mathcal{J}_m|$, $\forall m \in \mathcal{M}$. The same concept is also used for operators and gNBs, thus $I_m = |\mathcal{I}_m|$ and $M = |\mathcal{M}|$.

and carrier association, each UE j must be assigned a serving gNB cell $i^*(j)$ and a carrier $c^*(j)$. The selection $(i^*(j), c^*(j))$ will be called the cell-carrier assignment. Importantly, we assume that the UE can only be assigned a cell from its own operator's network.

Although joint cell and carrier assignment has been discussed extensively in the past, most works in this area have focused on macro/pico user association [80–82], whereas reference [83] considers user association in multi-carrier settings. All these works perform a "one-shot" optimization where all UEs are reallocated together.

Unlike in these related papers, here we consider the following simple distributed method: each new UE decides an initial cell-carrier assignment when it enters connected mode in the network. We consider an uncoordinated approach where each UE that joins the network receives status information from the gNBs that it can reach and then makes the association decision. We observe that the proposed distributed schemes do not require any major changes to the signaling procedures of today's systems. Moreover, they do not require the exchange of information among the gNBs. The amount of information exchanged is limited to the load of the carrier's gNB and the channel of the link for the two carriers. The downlink SINR values $\gamma_{ij}^{(c)}$ can be determined from measurement reports exchanged (assuming they account for the beamforming gain) and the load information is received from the pool of candidate base stations. Then, the cell-carrier assignment is chosen to ensure the desired rate and provide load balancing in the network.

To perform the cell-carrier assignment, we consider two possible greedy heuristic approaches:

- *Load-aware joint carrier and cell association.* In this case, the UE *jointly* selects the serving gNB and the carrier so as to maximize its rate without considering the effect of this choice on the other UEs. Specifically, the UE selects the cell-carrier assignment via the maximization.

$$(c^*, i^*) = \underset{i \in \mathcal{I}_m, c \in \mathcal{C}}{\arg\max} \left(\frac{W^{(c)}}{1 + N_i^{(c)}} \log_2 \left(1 + \gamma_{ij}^{(c)} \right) \right) \tag{3.13}$$

  where $N_i^{(c)}$ is the number of UEs already associated to the c-th carrier of the i-th base station; $W^{(c)}$ is the bandwidth of the c-th carrier, and $\gamma_{ij}^{(c)}$ is the SINR between UE j and gNB i if allocated in the carrier c, given in Equation (3.7) which includes the spatial channel characteristics and beamforming directions. For pooled carriers, it will also include the interference from other operators in the same band. We let B_j denote the resulting maximum rate for the UE

$$B_j = \frac{W^{(c^*)}}{1 + N_{i^*}^{(c^*)}} \log_2 \left(1 + \gamma_{i^* j}^{(c^*)} \right) \tag{3.14}$$

  When computing the rate B_j, we are splitting the bandwidth among all the users

associated to the gNB even if during the simulation we allocate the entire bandwidth to a single UE at a time. Furthermore, with this procedure, the ratio between the total bandwidth $W^{(c)}$ and the number of users $(1 + N_{mi}^{(c)})$ associated to the specific carrier provides the average amount of resources allocated to the j-th user over time.

- *Load-aware carrier-only association.* gNB and carrier selection are decoupled, i.e., the UE allocation to the serving gNB is kept fixed for the entire simulation, while the UE is allowed to select only the carrier as a function of the load and of the SINR. That is, the carrier is updated via

$$(c^*) = \arg\max_{c \in \mathcal{C}} \left(\frac{W^{(c)}}{1 + N_{i^*}^{(c)}} \log_2 \left(1 + \gamma_{i^* j}^{(c)} \right) \right) \tag{3.15}$$

  where, instead of trying all the possible gNBs $i \in \mathcal{I}_m$, the algorithm is constrained to keep the current gNB i, i.e., $i \equiv i^*$, and only optimizes the choice of the carrier $c \in \mathcal{C}$.

Both these greedy procedures are computable with the knowledge of load and channel state conditions that are obtained from $N_i^{(c)}$ and $\gamma_{i^* j}^{(c)}$ respectively.

3.4.4.1 Observations and Extensions

The distributed approach described above results in a lightweight implementation that enables responsiveness to rapid fluctuations of the channel state and traffic conditions. Nonetheless, relying on distributed rate optimization may lead to sub-optimal solutions. Conversely, a centralized framework can generate optimal solutions, but the excessive control signaling may affect the responsiveness to channel and traffic dynamics. The performance gap between distributed approaches and a centralized implementation may be the objective of our future work.

We also note that the approaches in Equations (3.13) and (3.15) assume a Round Robin (RR) scheduling. However, the results can be easily extended to a proportionally fair scheduler, by capturing the effect of different UE rates.

3.4.4.2 Cell and carrier selection simulation

In the simulation, we use a methodology to evaluate the steady-state behavior of the network. More precisely, we implement an iterative procedure (described in the following) which converges to the long-term load distribution between the two carriers achieved in the hybrid scheme.

In the first phase of the simulation, conditioned on all channel gains, each UE $j \in \mathcal{J}_m$ in the area is associated to the gNB $i \in \mathcal{I}_m$ with the highest signal strength. Note, that the choice of gNB i is not random but instead based on minimum path loss and so, given the shadowing conditions, deterministic. After the selection of the best gNB, we randomly

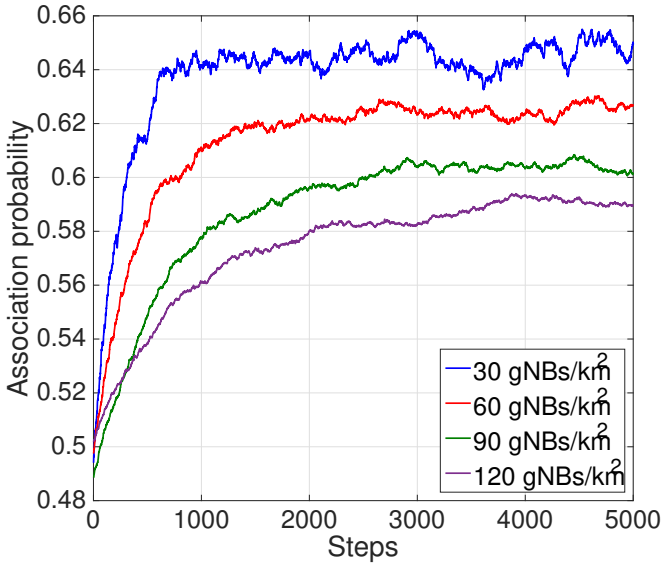

Figure 3.10: Example of the convergence for the probability of a user to be associated to the c_ℓ = 28 GHz carrier. Here reported is the run for hybrid case *i)*. The algorithm is initialized with a 0.5 value for each carrier and converges to a stable value.

associate the UE to the gNB band at c_ℓ or c_h, according to the probabilities $\mathcal{P}_{c_\ell}$ and $\mathcal{P}_{c_h} = 1 - \mathcal{P}_{c_\ell}$. In this study, these initial assignment probabilities are taken equal to $\frac{1}{2}$.

In the second phase of the simulation, we iteratively update the cell-carrier assignment by randomly picking one UE at a time (referred to in the following as UE j). For the selected UE j, we update its cell and carrier using (3.13) or only its carrier using (3.15). We repeat this iterative procedure by re-allocating a random UE at each step, until convergence to a point is reached. We use the numerical results of Figure 3.10 to quantify the convergence point and, using this method, we can identify the percentage of users that are connected to c_ℓ or c_h. We note that (cf. Figure 3.10) the probability that a user is associated to either the c_ℓ or the c_h carrier converges to a stable value, not necessarily equal to the one assumed in the initial phase. We summarize this iterative procedure in Algorithm 1.

It is important to highlight that the convergence values depend on the different propagation characteristics, bandwidth and amount of interference in the two bands. Moreover, Figure 3.10 shows how the number of iterations required increases as the density of UEs in the area increases.

3.4.5 Simulation Results

We start by simulating our proposed hybrid spectrum access scheme for the case of joint carrier and cell association. We consider 4 operators sharing 1 GHz of spectrum at c_h = 73 GHz, while having exclusive access to 250 MHz each at c_ℓ = 28 GHz (see Figure 3.8). We also consider two baselines for comparison. The first is the "fully licensed" case where

Algorithm 1 Pseudo-code of the simulation methodology

$\forall m \in \mathcal{M}$ deploy in the area A J_m UEs and I_m gNBs following a PPP;
N: matrix initialized to zeros used to count # of UEs $\forall i \in \mathcal{I}_m$ and $\forall c \in \mathcal{C}$;
$\overline{M}$: vector that stores for each UE the *index* of the associated gNB;
for $\forall m \in \mathcal{M}$ and $\forall$ user $j \in \mathcal{J}_m$ **do**
    Associate user j to the gNB i^* with minimum PL_{mij};
    $p \leftarrow$ randomly pick a value $\in [0, 1]$;
    if $p < \mathcal{P}_{c_\ell}$ **then**
        $c^* \leftarrow$ 28 GHz band;
    else
        $c^* \leftarrow$ 73 GHz band;
    end if
    $N(i^*, c^*) \leftarrow N(i^*, c^*) + 1$;
    $\overline{M}(j) \leftarrow (i^*, c^*)$;
end for
$P_{\mathrm{TX}_{ic}}$: power set $\forall i \in \mathcal{I}_m$ and $\forall c \in \mathcal{C}$;
G_c: computed following Equation (3.11) $\forall c \in \mathcal{C}$;
$W^{(c)}$: bandwidth set $\forall c \in \mathcal{C}$;
n: number of times iterative procedure is repeated;
for n times **do**
    $j \leftarrow$ pick random UE in the system;
    $(i, c) \leftarrow \overline{M}(j)$
    $N(i, c) \leftarrow N(i, c) - 1$;
    $\overline{\gamma}^{(c)}_{mij} \leftarrow$ compute matrix of SINRs $\forall i \in \mathcal{I}_m$, $\forall c \in \mathcal{C}$ as in (3.7);
    $B_{mj} \leftarrow$ compute matrix of rates using $\overline{\gamma}^{(c)}_{mij}$, W_c, and $N(i, c)$;
    $(c^*, i^*) \leftarrow \arg\max_{i \in \mathcal{I}_m, c \in \mathcal{C}} (B_{mj})$;
    $N(i^*, c^*) \leftarrow N(i^*, c^*) + 1$;
    $\overline{M}(j) \leftarrow i^*$;
end for

the four operators have each exclusive access to 250 MHz at c_ℓ and 250 MHz at c_h. The second one is the "fully pooled" case, where the four operators share 1 GHz at both c_ℓ and c_h. For simplicity, we consider the same UE and gNB densities for each operator, although extension to non-homogeneous scenarios would be possible. Moreover, the results have been averaged over a sufficient number of repetitions in order to obtain the desired accuracy, thus precisely evaluating the proposed hybrid scheme with respect to the baselines.

In the first set of results (Figure 3.11), we provide a comparison between the three schemes in terms of 5th, 50th and 95th percentile user rate, for gNB densities of 30 and 60 gNB/km^2. We assume that there are on average ten UEs per gNB, so that UE densities of 300 and 600 UEs/km^2 have been considered for gNB densities of 30 and 60 gNBs/km^2, respectively. For these results, we consider the power constraint with an equivalent isotropic radiated power fixed to 48 dBm for both carriers, and we assume twice the number of antenna elements per dimension at 73 GHz with respect to 28 GHz (this model corresponds to power

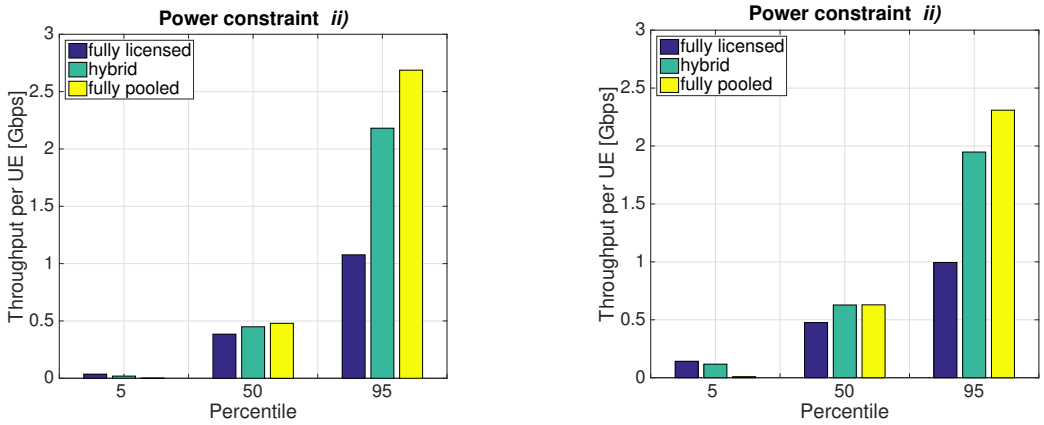

(a) Case with gNB density equal to 30 gNBs/km^2. **(b)** Case with gNB density equal to 60 gNBs/km^2.

Figure 3.11: Comparison of the throughput measured for the hybrid case and the two baselines. Empirical CDF values of the throughput for the 5th, 50th and 95th percentiles in the power constraint case *ii)*.

scenario *ii)* above).

First of all, we can observe how the 95th percentile throughput slightly decreases with the increase of the gNB density, since denser topologies result in more interference, thus affecting the performance of the best users. This effect is decreased, and in fact almost vanishes, in the fully licensed case due to the reduced number of interfering sources. For the 5th and 50th percentiles, increasing the density results in a throughput increase, because the average coverage area is reduced and the gNBs are closer to the UEs. Unlike in the 95th percentile case, here the gain from the closeness of the gNB outweighs the loss due to the increased interference. Especially in the fully pooled case, considering also multiple operators, the amount of interference is very large, and as a result an increased node density does not lead to increased performance. In fact, the gap between hybrid and fully pooled decreases as the system becomes more interference-limited, i.e., denser.

Our proposed hybrid approach also treats the worst users more fairly, as shown by the 5th percentile throughput results in which the hybrid scheme does essentially as well as fully licensed and much better than fully pooled. Conversely, the best users (95th percentile) in the hybrid scheme achieve a throughput that is not much worse than in fully pooled while being significantly better than in fully licensed.

Comparing the throughput of the worst (5th percentile) users with that of the best (95th percentile) users, we see that they are very different. This finds an explanation in the fact that, due to directionality, the amount of interference may greatly differ depending on the number and the alignment of the interferers [84]. More detailed performance results are reported in the Empirical Cumulative Distribution Function (ECDF) plots in Figure 3.12. The green curve of the hybrid access is close to the total licensed (blue curve) for the worst users (bottom left), while the curve approaches the total pooled (yellow curve) for the best

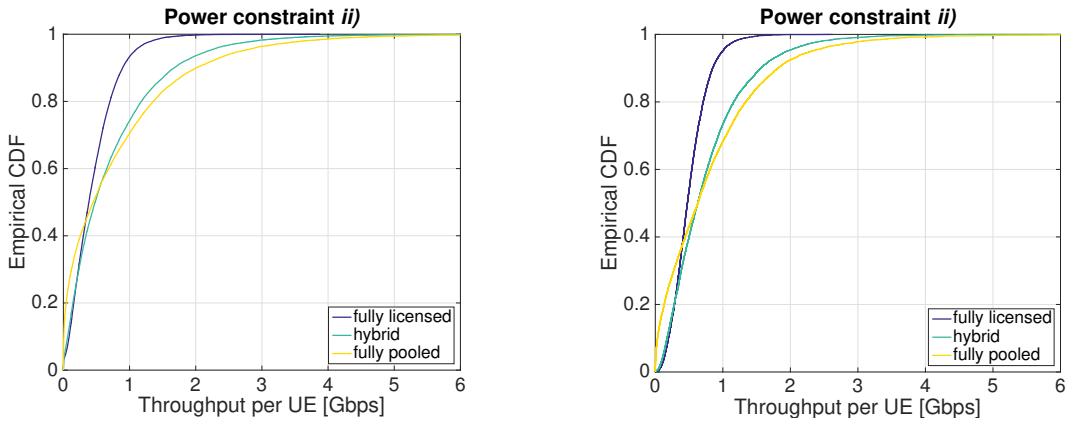

(a) Case with gNB density equal to 30 gNBs/km^2. **(b)** Case with gNB density equal to 60 gNBs/km^2.

Figure 3.12: Comparison of the throughput measured for the hybrid case and the two baselines. Empirical CDF curves of the throughput for the power constraint case *ii)*.

Table 3.4: Values of the throughput (measured in Gbps) for the hybrid case and the two baselines. Rates for the 5th, 50th and 95th percentiles and all the power constraints, simulations with a gNB density of 30 gNBs/km^2. The ratio values are computed as the throughput of the hybrid or total pooled cases divided by that of the total licensed case, which is taken as the baseline.

	Power constraint *i)*		Power constraint *ii)*		Power constraint *iii)*	
	Value	Ratio	Value	Ratio	Value	Ratio
Fully licensed 5%	0.0328	1.00	0.0362	1.00	0.0674	1.00
Hybrid 5%	0.0147	0.45	0.0190	0.52	0.0265	0.39
Fully pooled 5%	0.0003	0.0091	0.0007	0.019	0.0007	0.010
Fully licensed 50%	0.3455	1.00	0.3848	1.00	0.4176	1.00
Hybrid 50%	0.3736	1.08	0.4492	1.17	0.5081	1.22
Fully pooled 50%	0.3143	0.91	0.4795	1.25	0.4878	1.17
Fully licensed 95%	0.9188	1.00	1.0770	1.00	1.0218	1.00
Hybrid 95%	1.9194	2.09	2.1810	2.03	2.0252	1.98
Fully pooled 95%	2.1926	2.39	2.6970	2.49	2.5461	2.49

users (top right), as expected. This behavior shows that the proposed hybrid scheme is almost able to approach the best performance in various conditions.

In Table 3.4, which reflects the results shown in Figure 3.12a, we provide a comparison for all the different antenna setups and power constraints. We report the 5th, 50th and 95th percentile values of the user throughput measured in Gbps along with a ratio value, which is computed as the throughput of the hybrid or total pooled cases divided by that of the total licensed case (taken here as the baseline). It is interesting to note how the throughput varies, at each power constraint.

We recall from Section 3.4.3 that in case *i*) we consider the same number of antenna

elements at 28 GHz and 73 GHz, in case *ii*) we double the number of antenna elements per dimension at 73 GHz with an equal constraint on the EIRP, and, finally, in case *iii*) we use the configuration of case *ii*) but with different EIRP constraints for the two bands. Constraint *ii)* represents a trade-off for the available throughput between the number of antenna elements usable for a fixed area and the power radiated in the environment.

From Table 3.4, we can note that a large number of antenna elements has a positive impact on the 95th percentile user rate for both the hybrid and the fully pooled case. This relates to coverage, along with the amount of interference generated within the cell: using more antennas results in narrower beams, and hence reduced interference, which in turn leads to higher throughput. Further, by looking at the ratio values reported in Table 3.4, we can better understand the performance gains obtained with a hybrid scheme vs. a total pooled spectrum access. In the more realistic scenario, i.e., power constraint *ii)*, the 5% user throughput of the hybrid case is smaller than that obtained via a *fully licensed* scheme (about 50% smaller), and on the other hand much higher than the rate achieved with a *total pooled* approach (about 32 times higher). A similar behavior is observed for all the power configurations at the 5th percentile, while the opposite occurs if we consider the 95% user throughput. This last behavior is less pronounced and for this reason we can conclude that our hybrid procedure exhibits desirable performance, and represents a trade-off between the two baselines. This is due to the fairness that originates from our opportunistic carrier selection.

As another result, we report in Figure 3.13 a comparison between the different association algorithms, where each UE either jointly selects the serving gNB and the frequency band (left plot), or can only choose the optimal carrier while keeping the gNB association fixed (right plot). From these results, we can observe that the throughput provided by *carrier-only* association is higher than the *joint* association for the best users (95th percentile), while the opposite occurs for the median and worst (5th percentile) users. This can be explained by observing that in the carrier-only association, it is not possible to redistribute users to balance the load among gNBs, and therefore the best users are likely to be those that happen to be associated to lightly loaded gNBs, enjoying a higher rate compared to what they would achieve under the joint cell and carrier association. For the same reason, the worst users (likely associated to highly loaded gNBs) experience very poor performance. On the contrary, the joint cell and carrier association tends to distribute users among gNBs and carriers more equitably, and results in a fairer system.

3.4.6 Final Remarks

In this study, we have introduced a new hybrid spectrum access scheme for mmWave networks, where data packets are scheduled through two mmWave carriers with different characteristics. In particular, we have proposed a spectrum sharing scheme which combines a

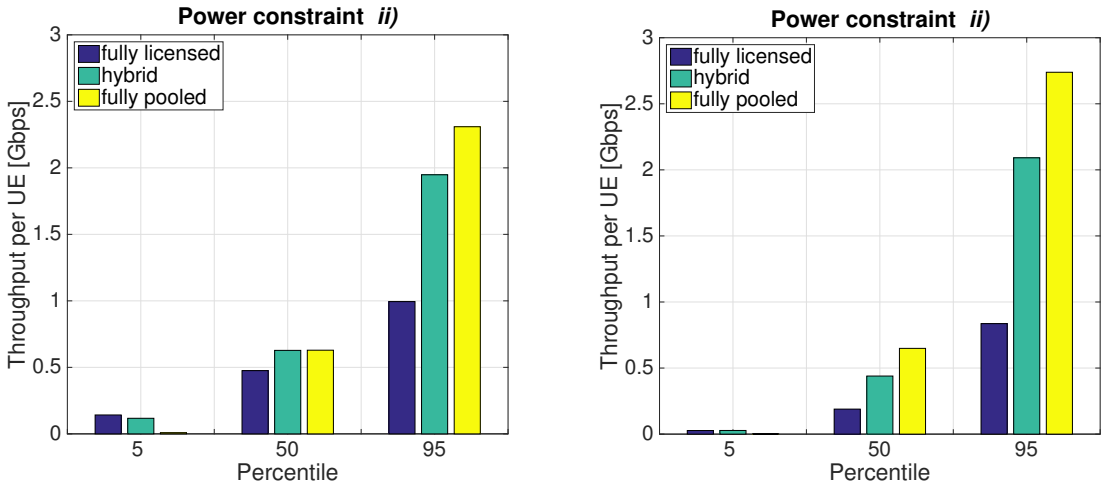

(a) Load-aware joint carrier and cell association.

(b) Load-aware carrier association.

Figure 3.13: Comparison of the throughput measured for the hybrid case and the two baselines and for the two different association algorithms. Values of simulations of the power constraint *ii)* with a gNB density of 60 gNBs/km^2.

lower mmWave band with exclusive access and a higher mmWave band where spectrum is pooled between multiple operators. Our investigation shows that this approach provides advantages for the average user with respect to traditional fully licensed or fully pooled spectrum access schemes, in terms of increased throughput and spectral efficiency. The approach offers also better balancing of the available resources with respect to the fully pooled case, resulting in higher fairness. This work opens a promising line of research towards a more flexible and efficient use of the radio spectrum, and will provide useful input and insights to standardization and spectrum policy.

However, further work is needed to reach a more complete understanding of different aspects. First, the study in this evaluation considers the case where the higher mmWave band is pooled between multiple operators all having a licensed anchor in another mmWave band at a lower frequency. It would be interesting to study a more general spectrum arrangement where the higher mmWave band is entirely license-exempt, i.e., can be accessed by heterogeneous users with and without an anchor at a lower frequency. The main challenge, in this case, is how to design politeness mechanisms in a very directional propagation environment. On one side traditional LBT techniques would not provide a reliable solution. On the other side, more recent directional MAC approaches introduced for 802.11ad (that is based on fully unlicensed spectrum access) would be suboptimal in a hybrid mmWave spectrum context. Second, our study is based on a distributed uncoordinated algorithm. We chose this approach because it allows an initial assessment based on a practical mechanism that has a low impact on signaling and architecture design. On the other hand, we believe that centralized approaches could also provide a realistic solution, in particular in networks where

infrastructure sharing is used. Third, while this study provides an initial, proof-of-concept assessment based on simulation, we believe that a mathematical analysis could lead to a more fundamental understanding of the different factors underlying hybrid spectrum access. Finally, it would also be interesting to evaluate our cell and carrier selection methods under time-varying traffic, where users come and go according to some statistics. In this case, the dynamics of traffic and interference will interact with the user allocation strategies and will accordingly lead to a time-varying throughput performance, whose characterization is an interesting item of future study.

Part II

Antenna Design and Evaluation

Chapter 4

Antenna Radiation Modeling

As previously mentioned, large antenna arrays and mmWave frequencies have been attracting growing attention as possible candidates to meet the high requirements of future 5th generation (5G) mobile networks. In view of the large path loss attenuation in these bands, beamforming techniques that create a beam in the direction of the user equipment are essential to perform the transmission.

For this purpose, it is extremely important to correctly model and consider the propagation antenna effects in any transmission. Therefore, we aim at characterizing realistic antenna radiation patterns, motivated by the need to properly capture mmWave propagation behaviors and understand the achievable performance in 5G cellular scenarios. Entering into details, this chapter highlights all the research and evaluation activities which are related to the antenna design precisely explaining how all the antenna components have been computed [50, 85–88].

4.1 Importance of Accurate Antenna Modeling

Due to high path loss attenuations, MIMO systems with beamforming techniques are essential to ensure an acceptable range of communication in mmWave networks [10]. In particular, the use of antenna arrays for future mobile scenarios is fundamental in order to create a beam in the direction of the UE, thus increasing the gain of the transmission. Among the possible antenna array designs, the most suitable approach is the use of Uniform Planar Array (UPA) where the antenna elements are evenly spaced on a two-dimensional plane and a 3D beam can be synthesized [89]. Several are the other possible antenna configurations such as Uniform Linear Array (ULA), circular array or any other array with irregular lattice. However, our research activities are primarily focused on UPA only.

We have already stressed the concept that in order to precisely evaluate 5G mmWave cellular scenarios, it is important to consider realistic and accurate radiation models. Related

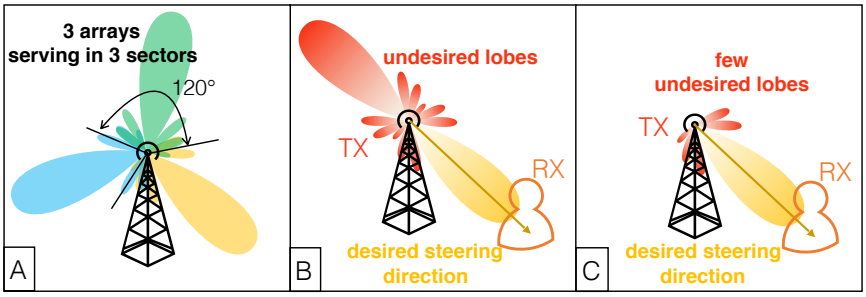

Figure 4.1: Illustration of the different antenna configurations. **Scheme A**: Configuration with three arrays serving three sectors with the single-element 3GPP antenna radiation pattern [90]. **Scheme B**: Antenna radiation pattern using beamforming with *isotropic* radiation elements. **Scheme C**: Single sector antenna with radiation pattern obtained using beamforming from 3GPP radiation elements.

works in the literature characterize the antenna array either over-simplifying its gain with piece-wise functions, or modeling it as an array of isotropic transmitting sources. Considering precise antenna pattern for each angle is critical (computationally speaking), especially for configurations where the interference is measured in directions that are different from those of the served UE. At high frequencies (e.g., mmWave bands), where high attenuations are present, quantifying the actual antenna gain obtained due to the radiation pattern is fundamental in order to precisely evaluate any mmWave system.

The radiation model proposed by the 3GPP in [90] can be used to address this issue. This model precisely simulates the radiation pattern of a patch antenna element assuming large attenuation for lobes in the opposite plane of transmission. In addition, as illustrated in Scheme A of Figure 4.1, the 3GPP specifications suggest modeling each gNB site with three sectors, thus three arrays placed with central angles shifted by 120° each. The configuration with multiple sectors already used in traditional 4G LTE systems seem to be appropriate also for future cellular scenarios, and permits a better control in the design of both desired and undesired lobes (e.g., using arrays of patches that perform the steering within the interval $[-60°, +60°]$).

In this research activity, motivated by the need to properly capture mmWave propagation behaviors and understand the achievable performance (e.g., capacity or interference studies) in 5G cellular scenarios, we spend some effort into accurately characterizing the antenna radiation pattern. In addition to a realistic antenna pattern, we also incorporate mmWave channel characteristics as derived from a measurement-based mmWave channel model operating at 28 GHz provided by the New York University (NYU) Wireless Group. This model is described in [21, 23], and was adopted in works [4, 6] from the previous chapters[1].

Our study leads to several observations. First, we highlight how the radiation pattern

[1]Even if in this study we have adopted the NYU channel, any other WINNER II based channel models can be used for the channel characterization.

significantly influences the performance evaluation of cellular scenarios. Results obtained with a simplified pattern appear to be significantly different from those obtained using realistic radiation models. Specifically, we try to quantify the interference perceived by a generic user in a way to identify the working regime (e.g., noise or interference-limited) of mmWave networks. Second, we compare different realistic antenna patterns in order to evaluate how the design choices influence the entire network performance.

4.1.1 Related Works

For tractability of analysis or ease of computation, most of the works in the literature approximate the actual beamforming patterns by a sector model. An example of this approximation can be found in [91], where a piece-wise beamforming gain function is used to characterize key features of an antenna pattern such as directivity gain, half-power beamwidth, and front-back ratio. This model is too generic and cannot be compared with a realistic pattern because design parameters like gain, beamwidth and front-back ratio change according to the steering direction. It is therefore challenging to compare this model with a realistic pattern since it uses fixed parameters for all the steerable directions.

A more precise antenna pattern can be obtained combining together the array factor expression, which provides information on the directivity equation of an antenna array, with the single element radiation pattern [79]. In [6], the array directivity equation with *isotropic* antenna elements was applied. As a result, each transmitting source (i.e., antenna element) radiates equal power in all directions, while a detailed lobe-shaped radiation pattern is used to capture the beamforming gain. When considering beamforming with isotropic transmitting sources, undesired lobes are generated as shown in Scheme B of Figure 4.1. Since gNBs in real cellular systems do not transmit omnidirectionally but, instead, in sectors, it appears essential to consider antenna radiation models that avoid the generation of undesired lobes. In this respect, a more realistic antenna pattern (e.g., the one shown in Scheme C of Figure 4.1) should be used when modeling UPA radiation.

4.2 Antenna Array Radiation Patterns Definition

We describe in this section how to compute and replicate the realistic antenna array patterns considered in this study and report expressions for the diverse field factors. The radiation pattern of the entire array (called array radiation pattern) is obtained by the superposition of its array factor, which provides information on the directivity equation of an antenna array, and the element radiation pattern. This last term takes into account how power is radiated by each single antenna element.

We precisely describe in the following sub-sections how to obtain the pattern expressions for all the different antenna radiation models used in this comparison.

4.2.1 Element Radiation Pattern

The element radiation pattern indicated as A_E and expressed in decibel (dB) is a term used to characterize how the power of a single antenna element is radiated in all directions, and thus is defined for any pair of vertical and horizontal angles (θ, ϕ). This parameter is extremely important in scenarios where directional transmission is used because it allows to precisely understand where the antenna transmits or receives power.

For the purpose of evaluating the differences between the realistic patterns and those already available in the literature, we compare three different antenna radiation configurations.

4.2.1.1 ISO

The *isotropic* radiation pattern used in the literature is achieved using a single array of isotropic transmitting sources. Hence, each element of the array redistributes equally the transmitted power in all directions, and beamforming is obtained considering only the array factor. We use this radiation pattern for comparison, knowing that it is the least realistic. It assumes that any antenna element irradiates an equal amount of power in each direction, thus: $A_E^{(\mathsf{ISO})} = 0$ dB, $\forall\theta \in [0, \pi], \forall\phi \in [-\pi, \pi]$.

4.2.1.2 3GPP

The 3GPP model is realized following the specifications in [90,92,93]. First, differently from the ISO configuration, it implies the use of three sectors, thus three arrays, placed as in traditional mobile networks. Second, the single element radiation pattern presents a high directivity with maximum gain in the main-lobe direction of about 8 dBi. The 3GPP A_E of each single antenna element is composed of horizontal and vertical radiation patterns. Specifically, this last pattern $A_{E,V}(\theta)$ is obtained as

$$A_{E,V}(\theta) = -\min\left\{12\left(\frac{\theta - 90}{\theta_{3\text{dB}}}\right)^2, SLA_V\right\} \tag{4.1}$$

where $\theta_{3\text{dB}} = 65°$ is the vertical 3 dB beamwidth, and $SLA_V = 30$ dB is the side-lobe level limit. Similarly, the horizontal pattern is computed as

$$A_{E,H}(\phi) = -\min\left\{12\left(\frac{\phi}{\phi_{3\text{dB}}}\right)^2, A_m\right\} \tag{4.2}$$

where $\phi_{3\text{dB}} = 65°$ is the horizontal 3 dB beamwidth, and $A_m = 30$ dB is the front-back ratio. Bringing together the previously computed vertical and horizontal patterns we can

obtain the 3D antenna element gain for each pair of angles as

$$A_E^{(\mathsf{3GPP})}(\theta,\phi) = G_{\max} - \min\left\{-\left[A_{E,V}(\theta) + A_{E,H}(\phi)\right], A_m\right\} \tag{4.3}$$

where $G_{\max} = 8$ dBi is the maximum directional gain of the antenna element [90]. The expression in (4.3) provides the dB gain experienced by a ray with angle pair (θ, ϕ) due to the effect of the element radiation pattern.

4.2.1.3 HFSS

In addition to the 3GPP pattern, we consider also a realistic pattern obtained reproducing a real patch antenna with a finite element simulator called High-Frequency Structural Simulator (HFSS) [94]. This last model is the most realistic among the models studied, but is also the most computationally intensive. As in the 3GPP model, it considers a three-sector cell, while the element radiation pattern is modeled as a real patch antenna element working at 29.5 GHz with horizontal and vertical spacing equal to 0.55λ and 0.77λ, respectively. The A_E of this last model is obtained by the HFSS finite element simulator by setting the antenna element parameters (e.g., working frequency and size of the element), and exhibits a maximum gain of about 5.71 dBi.

4.2.2 Array Radiation Pattern

In order to study the pattern of a UPA, we must focus on the radiation of the entire array, i.e., taking into account the effect of all the elements.

The relation between the array radiation pattern and a single element radiation pattern is defined, following [92], as

$$A_A^{(i)}(\theta,\phi) = A_E^{(i)}(\theta,\phi) + \mathsf{AF}(\theta,\phi) \tag{4.4}$$

The expression in (4.4) is valid for all three array radiation patterns, where the single-element term $A_E^{(i)}$ depends on the selected model. More specifically, $i \in \{\mathsf{ISO}, \mathsf{3GPP}, \mathsf{HFSS}\}$ corresponds to the element radiation functions described in the previous sub-section. The relation in (4.4) considers the effect of the element radiation pattern in combination with the array factor $\mathsf{AF}(\theta,\phi)$ defined for an array of n elements as

$$\mathsf{AF}(\theta,\phi) = 10\log_{10}\left[1 + \rho\left(\left|\mathbf{a}\cdot\mathbf{w}^T\right|^2 - 1\right)\right] \tag{4.5}$$

where ρ is the correlation coefficient, assumed equal to unity, $\mathbf{a} \in \mathbb{C}^n$ is the amplitude vector and $\mathbf{w} \in \mathbb{C}^n$ is the beamforming vector. We assume to use an equal and fixed amplitude for all the antenna elements[2], thus $\mathbf{a}$ is a constant normalized vector with all elements equal to

[2]The array radiation pattern can be further refined adjusting the amplitude of each single element with a

$\frac{1}{\sqrt{n}}$. The beamforming vector contains information about the main lobe steering direction (θ_s, ϕ_s), and is obtained as

$$\begin{aligned} \mathbf{w} &= [w_{1,1}, w_{1,2}, \ldots, w_{m,m}], \text{ where } m = \sqrt{n} \\ w_{p,r} &= e^{j2\pi\left((p-1)\frac{\Delta_V}{\lambda}\Psi_p + (r-1)\frac{\Delta_H}{\lambda}\Psi_r\right)} \\ &\begin{cases} \Psi_p = \cos(\theta) - \cos(\theta_s) \\ \Psi_r = \sin(\theta)\sin(\phi) - \sin(\theta_s)\sin(\phi_s) \end{cases} \end{aligned} \tag{4.6}$$

where Δ_V and Δ_H are the spacing distances between the vertical and horizontal elements of the array, respectively[3]. A detailed explanation of the relation between array and element patterns can be found in [50] and [92]. We highlight that the pair of angles (θ, ϕ) must not be confused with the steering pair (θ_s, ϕ_s) where the main beam is steered due to beamforming.

Moreover, we note that the radiation pattern of an array should consider also the mutual coupling effect. In fact, the radiation pattern of a single antenna element is modified by the absorption of the nearby antennas. For ease of computation, we are not considering mutual coupling[4] effects in our comparison study.

4.2.3 Field Pattern

In order to integrate the array radiation pattern into the channel model, we must compute the field pattern [93], which comprises both vertical and horizontal polarization terms as

$$\begin{cases} F_\theta^{(i)}(\theta, \phi) = \sqrt{A_A^{(i)}(\theta, \phi)}\cos(\zeta) \\ F_\phi^{(i)}(\theta, \phi) = \sqrt{A_A^{(i)}(\theta, \phi)}\sin(\zeta) \end{cases} \tag{4.7}$$

respectively, where ζ is the polarization slant angle and $A_A^{(i)}(\theta, \phi)$ is the 3D antenna array gain pattern previously obtained in (4.4). Note that, for simplicity, in most cases a purely vertically polarized antenna, thus $\zeta = 0$ and

$$\begin{cases} F_\theta^{(i)}(\theta, \phi) = \sqrt{A_A^{(i)}(\theta, \phi)} = F^{(i)}(\theta, \phi) \\ F_\phi^{(i)}(\theta, \phi) = 0 \end{cases} \tag{4.8}$$

weighing factor. This can provide both control of the side lobe levels and electrical steering. For simplicity, in this study we consider an equal and fixed amplitude for each radiation element, and leave as future work the study of beamforming design optimizing the weight factor of each antenna element.

[3]Except for the HFSS configuration, we always assume all elements to be evenly spaced on a two-dimensional plane, thus $\Delta_V = \Delta_H = \lambda/2$.

[4]Mutual coupling describes energy absorbed by one antenna's receiver when another nearby antenna is operating. This effect is typically undesirable because the energy that should be radiated away is absorbed by a nearby antenna. Similarly, the energy that could have been captured by one antenna is instead absorbed by a nearby antenna. Hence, mutual coupling reduces the antenna efficiency and performance of antennas in both the transmit and receive mode.

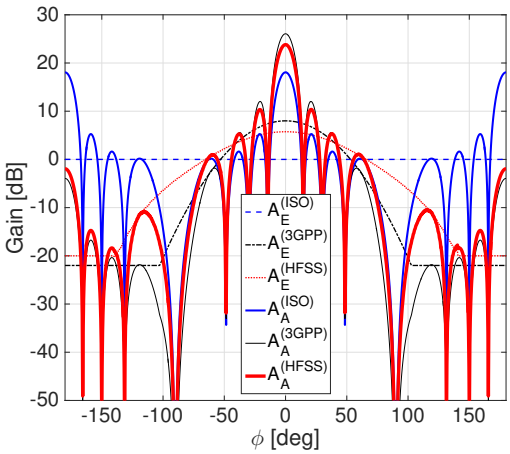

(a) Configuration with $\phi_s = 0°$.

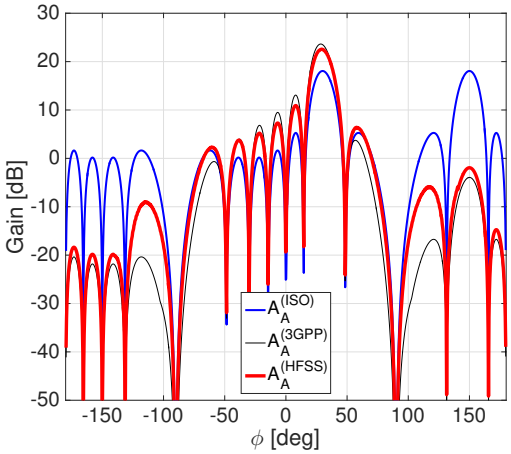

(b) Configuration with $\phi_s = 30°$.

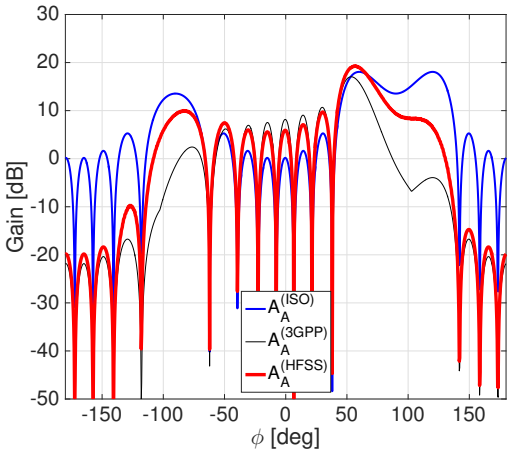

(c) Configuration with $\phi_s = 60°$.

Figure 4.2: Representation of the array radiation pattern $A_A(\theta, \phi)$ in relation with the element radiation pattern $A_E(\theta, \phi)$ varying horizontal angle ϕ, while vertical angles θ and θ_s are kept fixed to 90°. Examples obtained using a UPA with 64 antenna elements and performing the steering in different directions ϕ_s.

In Figure 4.2 we report examples of the three array radiation patterns for different steering directions ϕ_s. More importantly, in Figure 4.2a we are overlapping the element radiation pattern with the resulting array radiation pattern for all the configurations. The figures highlight two important aspects. Firstly, they show the reduction of the undesired side lobes when considering beamforming with 3GPP and HFSS antenna models. An accurate evaluation of the interference can be done only knowing the precise gain in all directions: unrealistic side lobes must be removed from the pattern while, at the same time, realistic lobes must be properly considered. Secondly, as we can see in Figure 4.2c, the maximum gain is affected by the scan loss[5] when the main lobe is steered from the broadside direction:

[5]A problem associated with beam scanning is the beam distortion with the scan angle. Steering at the

due to the directivity of the single antenna element radiation pattern, the main lobe obtained with beamforming has beamwidth and maximum gain that depend on the steering angle. In fact, $\phi_s = 60°$ is the maximum angle allowed with the 3-sector configuration[6] and in this particular case the main beam presents a gain that is lower if compared to the other smaller steering angles in Figures 4.2a and 4.2b. Moreover, this can also be observed in the element radiation pattern A_E in Figure 4.2a, where the 3GPP configuration exhibits an attenuation of 10 dB for $\phi = 60°$ with respect to the central angle $\phi = 0°$. On the contrary, the HFSS configuration presents a smaller attenuation of around 6 dB. Indeed, we notice that the HFSS element radiation pattern is less directive compared to the 3GPP model, being the maximum gain of the single-element radiation pattern around 5.7 dBi for the former and 8 dBi for the latter. Such a difference in directivity results in higher gain for the 3GPP model when a central steering is performed, while on the contrary higher gain is exhibited by the HFSS configuration when steered broadside (e.g., around 60°).

4.3 MATLAB Simulator

4.3.1 System Model

4.3.1.1 Channel Characterization

We adopt the NYU channel model presented in [21,23] and Section 2.3, which is derived from the WINNER II model [22] and is based on real-world measurements at 28 GHz. According to the channel model, each wireless link comprises K clusters, corresponding to macro-level scattering paths, in turn composed of L_k subpaths.

Given a set of clusters and subpaths, each element of the channel matrix $\mathbf{H} \in \mathbb{C}^{n_{\mathrm{TX}} \times n_{\mathrm{RX}}}$, which characterizes a communication link, is represented as

$$h_{r,t} = \sum_{k=1}^{K} \sum_{l=1}^{L_k} g_{kl} F_r\left(\Omega_{kl}^r\right) u_r\left(\Omega_{kl}^r\right) F_t\left(\Omega_{kl}^t\right) u_t^*\left(\Omega_{kl}^t\right), \tag{4.9}$$

where t and r are the indices of the t-th and r-th elements of the transmitter and receiver array respectively, g_{kl} is the small-scale fading gain of subpath l in cluster k, F_r and F_t are the receiver and transmitter field patterns previously computed, and $u_r(\cdot)$ and $u_t(\cdot)$ indicate the 3D spatial signature element of the receiver and transmitter, respectively. Moreover, $\Omega_{kl}^r = (\theta_{kl}^r, \phi_{kl}^r)$ are the angular spread of vertical and horizontal angles of arrival and $\Omega_{kl}^t = \left(\theta_{kl}^t, \phi_{kl}^t\right)$ are the angular spread of vertical and horizontal angles of departure, both for subpath l in cluster k [21]. Note that even if we consider channels with UPA antennas, in our simulations we neglect for ease of computation the vertical signatures by setting their

side of the array results in the spread of the beam shape and a consequent reduction in gain known as *scan loss*.

[6] Using three sectors each array can perform the steering within the interval $[-60°, +60°]$.

Table 4.1: List of all the notation terms and channel parameters used in the radiation pattern comparison.

Notation	Meaning
A_E	Element radiation pattern
AF	Array factor
A_A	Array radiation pattern
F	Field pattern
f	Carrier frequency
$\ell(r)$	Path loss at distance r in LoS/NLoS/out states
n_{TX}, n_{RX}	# antennas of a gNB and a UE
K	# clusters $\sim \max\{\mathsf{Poiss}(1.8), 1\}$
L_k	# subpaths in the k-th cluster $\sim \mathsf{DiscreteUni}[1, 10]$
ϕ^r_{kl}, ϕ^t_{kl}	Angular spread of subpath l in cluster k [21]: $\phi_k^{(\cdot)} \sim \mathsf{Uni}[0, 2\pi]$, $s_{kl} \sim \max\{\mathsf{Exp}(0.178), 0.0122\}$, $\phi_{kl}^{(\cdot)} = \phi_k^{(\cdot)} + (-1)^l s_{kl}/2$
P_{kl}	Power gain of subpath l in cluster k [23]: $U_k \sim \mathsf{Uni}[0, 1]$, $Z_k \sim \mathcal{N}(0, 4^2)$, $V_{kl} \sim \mathsf{Uni}[0, 0.6]$, $\tau_{kl} = 2.8, P_{kl} = \frac{P'_{kl}}{\sum P'_{kl}}$, $P'_{kl} = \frac{U_k^{\tau_{kl}-1} 10^{-0.1 Z_k + V_{kl}}}{L_k}$

angles $\theta_{(\cdot)}$ equal to 90°. As defined herein, the channel matrix $\mathbf{H}$ contains information on the channel conditions along with beamforming and antenna radiation pattern. Then, we recall that the small-scale fading gain g_{kl} is obtain as previously defined in Equation 2.6 of Section 2.3. Moreover, specific parameters are provided in Table 4.1.

Consider a directional beamforming where the main lobe center of a gNB's transmit beam points at its associated UE, while the main lobe center of a UE's receive beam aims at the serving gNB. Unless stated otherwise, we assume that both beams can be steered in any direction. Therefore, in each sector, we can generate a beamforming vector $\mathbf{w}$ for any possible angle in the interval $[-60°, +60°]$.[7] At a typical UE j, the aligned gain G_{ij} (considering also the channel) is its beamforming gain towards the serving gNB i. With a slight abuse of notation, we represent it as

$$G_{ij} = \left| \sum_{r=1}^{n_{\mathrm{RX}}} \sum_{t=1}^{n_{\mathrm{TX}}} h_{r,t} \right|^2 \tag{4.10}$$

[7] We recall that, among the different configuration, only the ISO model uses a single sector. Therefore, the ISO beam can be generated in any direction.

4.3.1.2 INR and SINR definitions

Thanks to a detailed channel and antenna characterization, we can compute the SINR between transmitter i and receiver j as

$$\mathrm{SINR}_{ij} = \frac{\frac{P_{\mathrm{TX}}}{\ell_{ij}} G_{ij}}{\sum_{y \neq i} \frac{P_{\mathrm{TX}}}{\ell_{yj}} G_{yj} + W \times N_0} \tag{4.11}$$

where y represents the y-th interfering link, W is the total bandwidth, N_0 is the thermal noise, P_{TX} is the transmitted power, G is the beamforming gain, and ℓ is the path loss. This last quantity is modeled with three states, as reported in Section 2.3: LoS, NLoS and outage, as a function of the distance d between transmitter and receiver. Furthermore, in our simulations, we associate each UE to the gNB that provides the smallest path loss (maximum average received power).

Similarly to the SINR, we can compute the Interference to Noise Ratio (INR), which is defined following [4] as

$$\mathrm{INR}_{ij} = \frac{\sum_{y \neq i} \frac{P_{\mathrm{TX}}}{\ell_{yj}} G_{yj}}{W \times N_0} \tag{4.12}$$

where, as previously explained, at the numerator we sum all the interfering links by multiplying their transmit powers P_{TX}, beamforming gains G and respective path loss values ℓ. The denominator represents the thermal noise power.

4.3.2 Framework Test and Evaluation

In this section, we report simulation results to show the achievable performance of the three different antenna configurations previously introduced. We consider scenarios using UPAs with 64 antenna elements $[8 \times 8]$ at the gNB, while at the receiver side we model UPAs with 16 elements $[4 \times 4]$. In our simulation campaign, we have adopted a 7 dB noise figure, a 500 MHz total bandwidth, and a transmit power $P_{\mathrm{TX}} = 30$ dBm, which are in line with the specifications envisioned for downlink transmission in 5G mmWave mobile networks [10].

The first result we report is a study on the level of interference experienced by a generic user in a 5G cellular network. In order to quantify the amount of interference, we compute the INR as in (4.12) for a large number of independent simulations and then derive its ECDF. With the ECDF we identify the point that satisfies the condition INR = 1 as the transitional point that determines the shift from a noise-limited to an interference-limited regime. In this manner, we obtain the user noise-limited probability $\mathsf{P_{nl}}$, defined as the probability for a generic user to have the noise power bigger than the interference power. This metric allows to better understand the behavior of a network for different gNB densities.

In Figure 4.3 we show the evolution of $\mathsf{P_{nl}}$ for the different radiation pattern configurations and varying the gNB density of the network. We can notice immediately that $\mathsf{P_{nl}}$ is

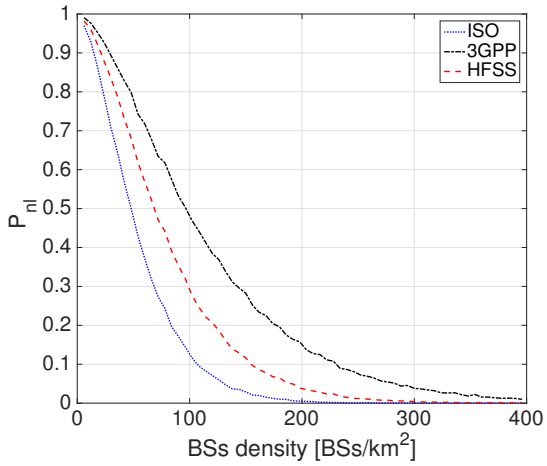

Figure 4.3: Noise-limited probability (P_{nl}) varying the gNB density in the three different configurations.

bigger in both 3GPP and HFSS with respect to the ISO configuration. This is due to the attenuation of the interference in both 3GPP and HFSS configurations caused by the use of directive elements which attenuate the side lobes. Furthermore, the interference is larger in the ISO configuration due to the use of a single sector that operates in all directions. We recall that both 3GPP and HFSS configurations use three sectors (i.e., three arrays) that are orientated with a mechanical phase-shift of 120° each as in traditional cellular networks. As we can see from Figure 4.3, for densities around 100 gNBs/km^2 and using an ISO antenna configuration, about 90% of the users can be considered in an interference-limited regime. This is not verified when adopting the HFSS or 3GPP antenna configurations, in fact, for the same density, only 70% and 50% of the users are in an interference-limited regime for the HFSS and 3GPP pattern, respectively. More precisely, using the 3GPP antenna model only half of the users are in an interference-limited scenario with a density of 100 gNBs/km^2. This corresponds to a dense scenario where the average cell radius is about 60 meters.

Differently from prior INR studies in [4, 10, 95] and [96], where antenna patterns were modeled with simplified functions for tractability, here we can precisely evaluate the operating regime of mmWave networks as a function of the gNB density. We also highlight how the interference results change with the adopted radiation pattern, which confirms the importance of using a precise radiation model when evaluating the network performance.

In Figure 4.4, we show the ECDF of the downlink SINR, for each antenna configuration, varying the gNB density. Firstly, as per the result in the interference study, also in this SINR evaluation we can see how the performance of a typical network drastically changes with the different antenna patterns. The diverse behavior can easily be seen starting from Figure 4.4a where, with 25 gNB/km^2, the median value of the ISO configuration is around 10 dB, while in the 3GPP or HFSS configuration it is above 20 dB. Moreover, with a small

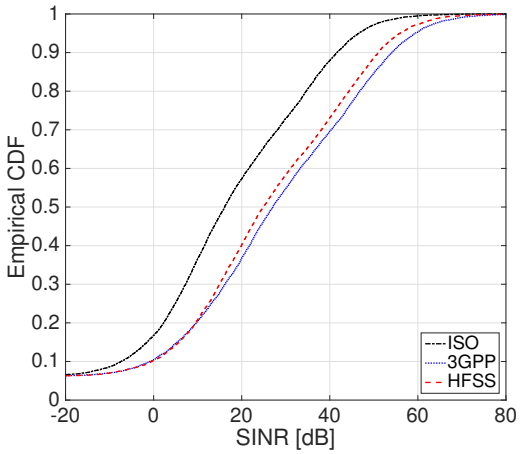

(a) Example of varying pattern with density equal to 25 gNBs/km^2.

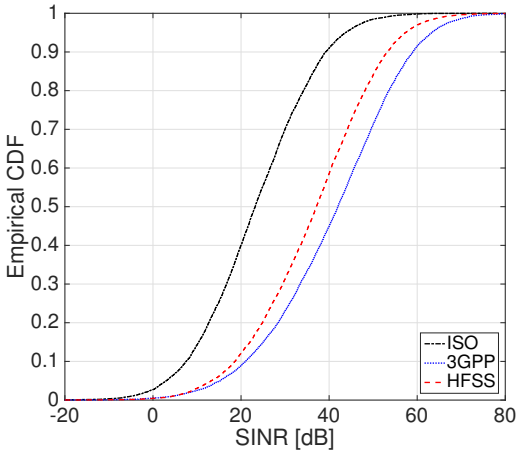

(b) Example of varying pattern with density equal to 100 gNBs/km^2.

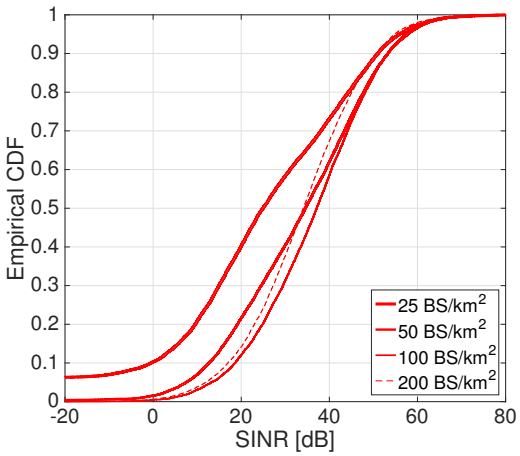

(c) Example of varying gNB density with HFSS radiation pattern.

Figure 4.4: Representation of Empirical CDF of the downlink SINR, for different antenna configuration and varying the gNB density.

density of 25 gNB/km^2, all curves show the presence of users in an *outage* condition, which is revealed by the SINR ECDF not starting from zero. Increasing the gNB density from Figure 4.4a to Figure 4.4b we can see how the SINR improves while maintaining different outcomes for the different pattern configurations. Also, with the larger density, no users are in an *outage* condition.

Contrary to the performance improvement for the smaller density case, with 200 gNB/km^2 the reduced distance between UE and gNB provides less improvement with respect to the growth of the interference. A similar behavior has been observed also in the ISO and 3GPP models.

Table 4.2 reflects the results shown in Figure 4.4 and provides a comparison among all

Table 4.2: Summarizing table reporting the 5-th ECDF percentile of the SINR for different configurations and densities. Values are expressed in decibel.

	gNB/km^2		
	50	100	200
ISO	0.00	3.02	1.74
3GPP	8.11	15.31	14.03
HFSS	7.54	13.22	11.94

the different antenna setups and gNB densities. Specifically, we report the 5-th percentile values of the user SINR in dB, which represents the performance of the worst users and is typically used to classify network performance. Note that SINR values for the density of 25 gNB/km^2 are not reported in the table because more than 5% of the users are in an *outage* condition with such a small gNB density. In general, our results show that different antenna models may provide quite different SINR performance. Also, we observe a performance gain passing from 50 to 100 gNB/km^2. Instead, as already discussed for Figure 4.4c, in extremely dense networks (e.g., with 200 gNB/km^2) the interference is really large and we observe SINR values that are smaller than in the case with 100 gNB/km^2. This behavior is the same for all the radiation patterns used.

4.4 ns-3 Framework

From the previous section we have understood the importance of precisely model the antenna propagation in mmWave communication for the next generation of cellular networks. We remark that communication at such high frequencies, suffers from high path loss and blockage, therefore directional transmissions using antenna arrays and dense deployments are needed. Thus, when evaluating the performance of mmWave mobile networks, it is necessary to accurately model the complex channel, the directionality of the transmission, but also the interplay that these elements can have with the whole protocol stack, both in the radio access and in the higher layers.

In this section, we report a study which improves the channel model abstraction of the mmWave module for ns-3, by introducing the support of a more realistic antenna array model, compliant with 3GPP NR requirements, and of multiple antenna arrays at the base stations and mobile handsets [85]. We then study the end-to-end performance of a mmWave cellular network by varying the channel and antenna array configurations, and show that increasing the number of antenna arrays and, consequently, the number of sectors is beneficial for both throughput and latency.

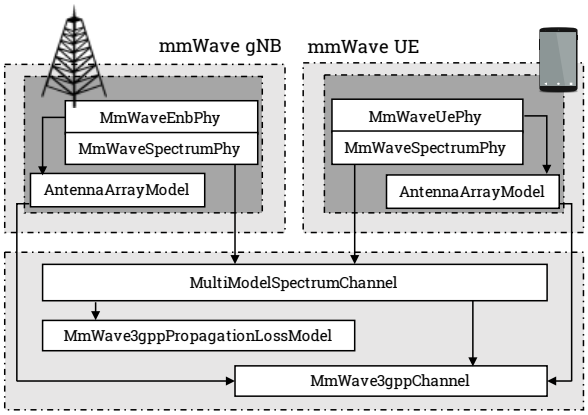

Figure 4.5: Block scheme of the Physical (PHY) layer and channel modeling in the ns-3 mmWave framework.

4.4.1 ns-3 Modules Integration

In this work we extend the ns-3 framework in [97] by incorporating the possibility to simulate the realistic antenna patterns and configurations described in the previous section.

As shown in Figure 4.5, the channel model implementation in the ns-3 mmWave module depends on a number of classes, with different functionalities. The propagation loss is computed by the `MmWave3gppPropagationLossModel` class, which implements also a probabilistic model for the LoS and NLoS condition according to [90]. The `MmWave3gppChannel`, instead, computes the channel matrix $\mathbf{H}$ (i.e., Equation (4.9))for each single transmitter-receiver pair, and applies the beamforming vectors to get the beamformed received power spectral density. Moreover, the `AntennaArrayModel` class models the antenna arrays at the gNB and the UE. Finally, in each terminal, an instance of the `MmWaveSpectrumPhy` handles the interaction between the PHY layer implementation, the error model and the channel abstraction.

In order to implement the 3GPP antenna array model, the `AntennaArrayModel` class has been extended to properly handle the presence of multiple antenna arrays, allowing each terminal to transmit and receive with the proper sector (or panel) according to the angular direction of the other transceiver in the link. In the same class, we introduce the possibility of modeling accurate antenna radiation patterns, providing the field patterns F (previously explained in Section 4.2.3) to the `MmWave3gppChannel`, which applies them to the channel matrix. In this first version, we consider the LoS direction to compute the beamforming vector pair for the link. Future extensions of the ns-3 simulator will include the possibility of performing a codebook-based beamforming, with a realistic cell scan.

We highlight that all the introduced antenna settings are tunable using the ns-3 *attributes* system, therefore the framework can be adjusted to simulate 3GPP NR specifications (i.e., with the settings in Table 4.3), but also other configurations, resulting in a useful tool for

Table 4.3: gNB and UE suggested settings from [3]. Moreover, vertical and horizontal spacing of antenna elements (dy, dz) is kept equal and fixed to 0.5λ for both gNB and UE. The Half Power BeamWidth (HPBW) is the angular separation in which the magnitude of the radiation pattern decrease by 50% (or -3 dB) from the peak of the main beam.

	directivity $G_{\max}$	HPBW $(\theta_{3\text{dB}}, \phi_{3\text{dB}})$	# sectors/panels
gNB	8 dBi	$(65°, 65°)$	3
UE	5 dBi	$(90°, 90°)$	2

the evaluation of realistic end-to-end mmWave networks.

4.4.2 Framework Test and Evaluation

4.4.2.1 Scenario

In this work, we study the performance in terms of end-to-end user throughput and latency in a multi-site deployment, using User Datagram Protocol (UDP) as the transport protocol. We consider a scenario with 4 gNBs at the vertices of a square of distance d and a gNB at the center. In this setup, the 5G network is deployed in a Non Stand Alone (NSA) mode, i.e., it uses a 4G Evolved Packet Core (EPC) network, and the UEs are configured with multi-connectivity between an LTE evolved Node Base (eNB) (co-deployed with the central gNB) and an NR gNB [98]. The end-to-end flows are configured as split bearers, i.e., the LTE eNB acts as a local traffic anchor with respect to the core network, and data packets are forwarded to and from the mmWave gNBs, according to the configuration described in [99]. All the base stations are interconnected with X2 links, which are realistically simulated in terms of data rate limit and additional latency, as shown by the parameters in Tabble 4.4.

There are N_{UE} users in the scenario, and they move randomly according to a two-dimensional random walk model. They can freely hand over between the different mmWave gNBs, or switch to the LTE eNB if all the mmWave links are in the outage condition (i.e., with an SINR below -5 dB). The handover procedure is coordinated by the central LTE unit, and avoids latency-consuming interactions with the core network. The users consume content from a remote server (e.g., for video streaming), with a constant bitrate $R_{\text{UE}} = 100$ Mbit/s. We test a different number of sectors for each mmWave gNB, ranging from 3 to 4. In this first evaluation, we do not consider the single-sector setup with isotropic antenna elements that is still available in the ns-3 mmWave module, since it would be less realistic. The antenna directivity in our simulations is configured as described in previous Section 4.2. The UEs are equipped with 2 panels [3]. We also compare the results for two different 3GPP channel model configurations, namely the Urban Macro (UMa) and the Urban Micro (UMi) scenarios. The channel condition between each user and each gNB is randomly assigned according to the 3GPP model [90].

Table 4.4: Additional simulation parameters used for the ns-3 simulation.

Parameter	Value
mmWave carrier frequency	28 GHz
mmWave bandwidth	1 GHz
3GPP Channel Scenario	UMi, UMa
mmWave outage threshold Ω	-5 dB
mmWave max PHY rate	3.2 Gbit/s
X2 link latency D_{X2}	1 ms
S1 link latency D_{S1}	10 ms
RLC buffer size B_{RLC}	5 MB
RLC AM reordering timer	1 ms
S1-MME link latency D_{MME}	10 ms
UE speed v	$\mathcal{U}[2, 4]$ m/s
UDP source rate R_{UE}	100 Mbit/s

The metrics we consider are the end-to-end throughput, measured above the transport layer for each user, and the latency in the Radio Access Network (RAN). In particular, in our simulation setup, the end-to-end latency is given by a fixed component in the wired part of the connection, and by a variable one in the RAN (i.e., the PDCP layer latency), which depends on the different configurations we examine. Therefore, in the following section we will only report the PDCP layer latency.

4.4.2.2 Evaluation Results

Figure. 4.6 shows the average UDP end-to-end throughput and RAN latency, respectively, for different numbers of sectors at the gNBs and numbers of panels at the UEs. The numbers of users N_{UE} and distances d are fixed to 25 and 100 m, respectively.

The first notable result, which holds for both UMa and UMi scenarios, is that the throughput increases when increasing the number of sectors in each gNB from 3 to 4, while the average latency decreases. This is due to a combination of two factors. First, with more sectors it is possible to limit the angular coverage area of each sector, thus beams with a better shape and a higher gain are selected. Second, the interference decreases, since the usage of a multi-sector deployment limits the back and side lobes that generate undesired interference. The end result is an increase in the SINR, which translates into higher throughput and lower latency, given that fewer retransmissions are needed and less buffering occurs. Notice that, on average, the throughput gain is less remarkable than the latency reduction. This is due to the fact that the source rate is limited to $R_{\mathrm{UE}} = 100$ Mbit/s, and most of the users experience an average good channel condition and can reach this throughput. The improvement is more relevant for the worst users, i.e., those who generally need a larger number of retransmissions, as we will show in the next paragraphs. Finally, we highlight that increasing the number of sectors has a cost related to the gNB hardware.

The second observation is that the UMi channel condition yields higher throughput and

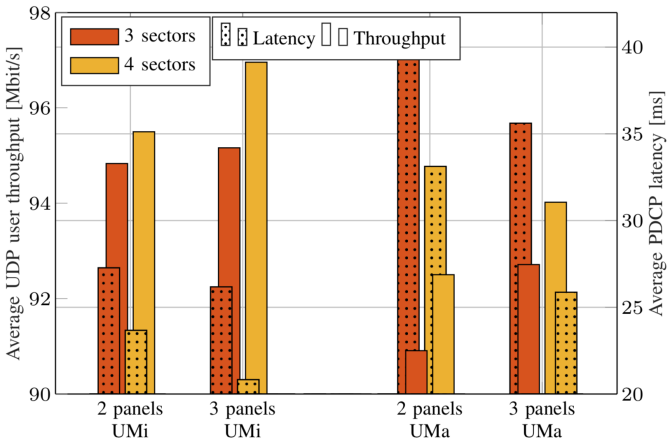

Figure 4.6: Average user throughput and latency for different configurations of the UE panels and gNB sectors, for distance $d = 100$ m and $N_{\text{UE}} = 25$ users. The 3GPP channel is either UMi or UMa.

lower latency than UMa. The latter, indeed, generates a larger amount of interference across neighboring cells, thus decreasing the SINR. The UMi scenario, instead, models a street canyon deployment, thus the inter-cell interference is much more limited. In fact, interference affect the performance of the transmission reducing the average throughput and increasing the number of Radio Link Control (RLC) retransmission, thus increasing average user latency.

We have shown in the previous result how the multi-sector gNB deployment improves the link budget performance thanks to the possibility to better control the design of both desired and undesired beams. As reported in Table 4.3, the 3GPP suggests the use of 2 panels for each UE. However, given the importance of handset design in 5G mmWave networks [100, 101], our result permits to evaluate the end-to-end performance by also configuring two different numbers of panels (i.e., 2 or 3) at the UE.

Similar to the multi-sector deployment, the performance improves when installing 3 instead of 2 panels at the UEs, for the throughput but more remarkably for the latency. In particular, for the UMi configuration with 3 panels and 4 sectors, it is possible to nearly reach (on average) the maximum throughput R_{UE} without increasing the latency, which has the smallest value with this configuration (i.e., 20.83 ms). However, even if the use of 3 panels at the UE node results in an improvement of the performance, from a practical implementation point of view, the design of a UE with these many panels must be studied carefully, since it may not be easy to physically place all the panels in the handset. Some preliminary designs and considerations are given in [100, 101].

As a future extension of this work, it appears interesting to further evaluate the end-to-end performance of networks with different multi-sector and multi-panel configurations, to clearly outline the trade-offs related to the antenna array configurations and their modeling. For example, analyze larger simulation scenarios, i.e., with more gNBs and UEs deployed

and consequently a higher interference, other antenna array factor components, such as the spacing of the elements and the amplitude and the phase vectors of each antenna element, and network configurations.

4.5 MIMO Precoding

The volume of mobile data is continuously increasing, especially with high capacity applications that are emerging together with the next generation of cellular communications [38]. As an enabler for these capacity-intensive applications, in addition to the use of mmWave frequencies, another major aspect of the new mobile generation is the densification of the network applying small cells in large numbers. Furthermore, Multi-User (MU) massive MIMO systems became of high interest as they contribute to reaching the 5G high demands (e.g., in terms of rates and densities), due to their ability to greatly increase network capacity [13]. For this reason, it is important to study and evaluate MU massive MIMO systems over 5G mmWave propagation channels. By exploiting such technologies, data transmission rates are expected to increase in the RAN, and a more efficient use of the radio spectrum can be achieved.

The purpose of MU MIMO systems is to account for channel scattering and reflections, thus exploiting the spatial dimension and creating multiple beams of the signal in the direction of the UEs, so that each user can benefit from the whole allowed bandwidth at any time instant. This can be achieved by precoding the information at the gNB side. Using a precoder, data is distributed on the different antenna elements of the gNB in order to perform beamforming of information toward the served UEs.

4.5.1 Related Works

Many works in the literature focused on the evaluation of precoding techniques for MU mmWave systems with massive MIMO. The closest works to ours are [102–105]. In [102], massive MIMO was proposed and studied under the ideal condition of almost infinite antennas. In [103], precoding techniques such as Minimum Mean Square Error (MMSE), Matched Filtering (MF) and Zero Forcing (ZF) were studied under the assumption of a Rayleigh channel model and under the condition of perfect Channel State Information (CSI) acquisition. In [104], channel estimation errors were introduced to estimate the implementation loss in terms of precoding gain, whereas in [105] the authors link the precoding performance with channel correlation. Finally, a recent piece of work [106] uses a realistic channel model to perform an evaluation of a MU system in terms of bit error rate as a function of the number of antenna elements used at the transmitter side, while however overlooking the effect of different precoding strategies and channel estimation errors.

From the literature, it emerges that linear precoding schemes can be used to reach

high performance under ideal assumptions. Less known is however their performance when realistic channel models are considered. To be precise, under a Rayleigh fading model, it is known that MMSE performs appreciably better in terms of balancing the resources among the UEs acting as a trade-off between MF and ZF approaches. However, the Rayleigh fading model oversimplifies the channel characterization, resulting in a channel model that does not reflect the real mmWave propagation specifics.

In 3GPP NR systems, the exploitation of mmWave frequency bands (both at 28 GHz and at 60 GHz) for the next generation of mobile communications is currently defined [107]. Within the standard, different types of CSI feedback mechanisms have been included to support MIMO transmissions. In particular, release 15 includes Type-I and Type-II codebook CSI feedback, enabling different trade-offs between CSI resolutions and feedback overhead [108]. Both codebooks attempt to reduce the CSI overhead by approximating the channel matrix dominant eigenvector by a predefined Discrete Fourier Transform (DFT) codebook. More precisely, when a Type-I CSI feedback scheme is adopted, the UE feeds back the index of a vector taken from a suitable oversampled DFT codebook that best approximates the dominant eigenvector of the channel matrix; conversely, when Type-II CSI is adopted, the feedback is composed of a linear combination of two or more (up to 4 per polarization) vectors taken from the oversampled DFT codebook. In this latter case, both the indices of the chosen vectors and the linear combination coefficients are fed back to gNB. Finally, it is worth observing that the accuracy of a Type-II CSI feedback scheme is larger, and so is the resulting overhead [109]. The reason behind such mechanisms is to be found in the attempt to reduce the amount of CSI acquisition overhead while exploiting MIMO advantages, such as spatial multiplexing and beamforming. Although at the moment full CSI[8] is not included in the standard, ongoing discussions are attempting to assess the trade-off between precoding gain and overhead cost.

Differently from the prior art, the objective of this study is twofold. First, we aim at evaluating the performance of diverse precoders when a realistic channel is considered, where "realistic" denotes both the adoption of a channel model supported by experimental evidence and the inclusion of CSI imperfections. Second, we compare the aforementioned linear precoders against Grid of Beams (GoB) optimization approaches, with the goal of assessing the gain of linear precoders over simpler (and less demanding in term of CSI) GoB approaches.

4.5.2 System Model

As reported in Figure 4.7, we consider a scenario with both a realistic sectorization and an antenna array radiation pattern, as suggested by the 3GPP specifications in [92]. Moreover, two measurement-based realistic channel models are considered, one from NYU [21] and one

[8] According to the 3GPP terminology, the term full CSI is known as explicit CSI.

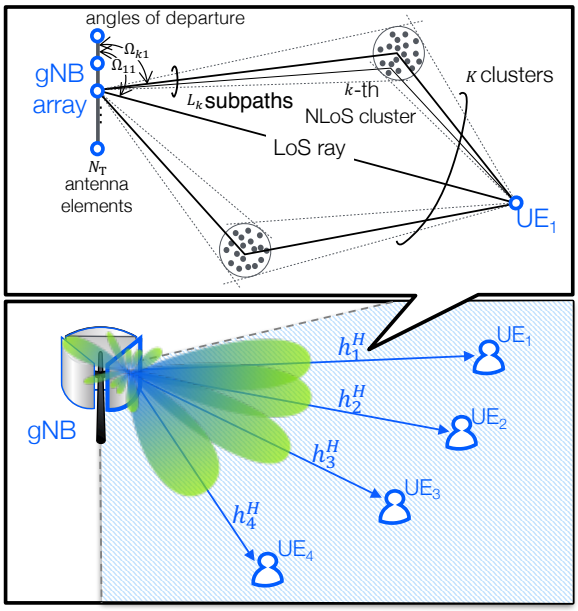

Figure 4.7: Illustration of the mmWave system model considered (bottom) and representation of the channel model used for each link in the framework (top).

from 3GPP as suggested in [90], both used to evaluate and compare the performance of different precoders.

We consider a narrowband single-cell downlink MU MIMO mmWave system where a single gNB sector with N_T transmit antennas is serving M single-antenna UEs.[9] The channel to the m-th user is assumed narrowband and is described by the vector of coefficients $\mathbf{h}_m \in \mathbb{C}^{N_\mathrm{T}\times 1}$, and its j-th element describes the channel response between the j-th transmitting antenna element and the receive antenna. This input-output relationship can be described as

$$y_m = \mathbf{h}_m^H \mathbf{x} + n_m, \quad m \in \{1, 2, \ldots, M\} \tag{4.13}$$

where $\mathbf{x}$ is the $N_\mathrm{T} \times 1$ transmitted vector signal, $y_m \in \mathbb{C}$ is the received signal, and n_m is the noise term. Assuming to use a precoder, the transmitted vector signal is $\mathbf{x} = \sum_{i=1}^{M} \mathbf{w}_i s_i$, where s_i is the data symbol and $\mathbf{w}_i$ is the $N_\mathrm{T} \times 1$ linear precoding vector.

Aggregating together the precoding vectors of all the M UEs we can define the precoding matrix $\mathbf{W} = [\mathbf{w}_1, \ldots, \mathbf{w}_M] \in \mathbb{C}^{N_\mathrm{T}\times M}$. We note that, in order to respect the power constraint $\mathbb{E}\left[\|\mathbf{W}\mathbf{s}\|^2\right] = 1$, we normalize the precoding matrix with the Frobenius norm as follows $\widehat{\mathbf{W}} = \frac{\mathbf{W}}{\|\mathbf{W}\|_\mathrm{F}}$. Using this notation, it is possible to write the system input-output equation as

$$\mathbf{y} = \mathbf{H}^H \widehat{\mathbf{W}} \mathbf{s} + \mathbf{n} \tag{4.14}$$

[9] We note that the number of UEs that can be simultaneously supported by the gNB sector is less than or equal to the number of antenna elements, i.e., $M \leq N_\mathrm{T}$.

where $\mathbf{y}, \mathbf{s}$ and $\mathbf{n}$ are vectors with dimension $M \times 1$, while channel matrix $\mathbf{H}$ is defined in $\mathbb{C}^{N_T \times M}$.

Finally, we define $\bar{\mathbf{H}}^{(p)}$ as the $M \times M$ equivalent matrix obtained with the product

$$\bar{\mathbf{H}}^{(p)} = \mathbf{H}^H \widehat{\mathbf{W}}^{(p)} \tag{4.15}$$

where superscript p is used to identify the different precoding approaches evaluated as described in the following.

4.5.3 Precoders Considered

With the intent to perform a study of the different precoding techniques while realistically modeling the channel, we discuss in the following paragraphs all the approaches evaluated and provide details on how they are computed.

4.5.3.1 Grid of beams (power optimization)

This approach consists in the use of a codebook $\mathcal{Z}$ of precomputed precoders that will be tested with the aim to choose the one that maximizes a specific metric. Each precoder vector in the codebook represents a DFT beam pointing towards a direction. According to this principle, the entire codebook spans the whole effective area[10].

Two different GoB metrics and thus optimization criteria are considered in this study. First, for each active UE, we identify the precoder $\mathbf{w}_m^{(\mathsf{GoB_P})}$ which maximizes the received power among all possible precoder vectors z in the codebook $\mathcal{Z}$, thus

$$\mathbf{w}_m^{(\mathsf{GoB_P})} = \arg\max_{z \in \mathcal{Z}} |\mathbf{h}_m^H \mathbf{w}_z|^2 \tag{4.16}$$

We identify it with the acronym $\mathsf{GoB_P}$, and the respective precoding matrix is derived as

$$\mathbf{W}^{(\mathsf{GoB_P})} = \left[\mathbf{w}_1^{(\mathsf{GoB_P})}, \ldots, \mathbf{w}_M^{(\mathsf{GoB_P})}\right] \tag{4.17}$$

4.5.3.2 Grid of beams (SLNR optimization)

Similarly, we study an alternative in which the precoder is chosen by maximizing the Signal to Leakage plus Noise Ratio (SLNR) for each single UE m. We define it as $\mathsf{GoB_{SLNR}}$ and the optimization expression becomes

$$\mathbf{w}_m^{(\mathsf{GoB_{SLNR}})} = \arg\max_{z \in \mathcal{Z}} \left(\frac{|\mathbf{h}_{m,m}^H \mathbf{w}_z|^2}{\sigma^2 + \sum_{i \neq m} |\mathbf{h}_{m,i}^H \mathbf{w}_z|^2} \right) \tag{4.18}$$

[10]This principle is an assumption adopted for this evaluation. Different codebook designs can also be applied in our optimization.

then, the precoder matrix $\mathbf{W}^{(\mathsf{GoB}_{\mathsf{SLNR}})}$ is derived as in (4.17).

The rationale behind this choice is that the sum of SLNRs is a close approximation of the sum of SINRs, with the advantage of being computationally much easier to perform. This stems mainly from the fact that whereas the sum SINR maximization would require an exhaustive search for all possible beams and all users in the cell, the sum SLNR can be maximized by simply maximizing the SLNR of each UE.

4.5.3.3 Matched filter precoder [110]

The MF, also known as conjugate beamforming, maximizes the power of the received signal, without any interference consideration. It is optimum when the noise power received by the UE is much stronger than the interference that would result from the transmitted signals intended to be received by the co-scheduled UEs. For this reason, it is optimum for noise-limited scenarios.[11] Its precoding matrix is expressed as

$$\mathbf{W}^{(\mathsf{MF})} = \widehat{\mathbf{H}} \tag{4.19}$$

The gNB computes the precoding matrix after estimating the channel so as to direct the useful energy in the direction of each UE. In our evaluation, we assume complete knowledge of the channel and we use this assumption for the calculation of this and the next precoders.

4.5.3.4 Zero-forcing precoder

An evolution of MF linear processing can be used to limit the detrimental effects of multi-user interference. The ZF precoder tries to cancel the power of the interference, and therefore is an optimal solution for interference-limited scenarios. This interference canceling property is obtained at the price of a slightly complex precoder computation and of a reduced received power. The precoding matrix is designed according to the ZF criterion [111] and is given by

$$\mathbf{W}^{(\mathsf{ZF})} = \widehat{\mathbf{H}}(\widehat{\mathbf{H}}^H\widehat{\mathbf{H}})^{-1} \tag{4.20}$$

which simply denotes the right pseudo-inverse of the matrix $\widehat{\mathbf{H}}^H$.

4.5.3.5 Minimum mean square error precoder

Differently from the last two precoders considered, the MMSE precoding strategy (also known as Kalman filter precoder) maximizes the sum of the SINR. Therefore, it optimizes the received power while minimizing the interference signal. It can be considered as a solution

[11] *Noise-limited* and *interference-limited* scenario refer, respectively, to the case in which the noise power is greater than the interference power and vice-versa.

in between the MF and the ZF precoders. The precoding matrix is expressed as

$$\mathbf{W}^{(\mathsf{MMSE})} = \widehat{\mathbf{H}} \left(\widehat{\mathbf{H}}^H \widehat{\mathbf{H}} + \frac{1}{\mathrm{SNR}} \mathbf{I}_M \right)^{-1} \tag{4.21}$$

and it is possible to prove that it can be expressed as a linear combination of MF and ZF precoders [112].

4.5.4 Imperfect Channel Estimate

Focusing on a realistic system, achieving a complete and correct knowledge of the CSI is not feasible in a practical framework. To be precise, typical mmWave implementation does not have direct access to the signals received on each gNB antenna, so learning the channel on each antenna element is currently extremely difficult and almost infeasible. For this reason, we consider the performance in case the transmitter has an imperfect channel estimate.

The channel estimation error is modeled following a Gauss-Markov formulation, where the imperfect channel $\mathbf{H}_e$ is obtained using the *true* channel $\mathbf{H}$ as follows

$$\mathbf{H}_e = \tau \mathbf{H} + \sqrt{1 - \tau^2} \mathbf{E} \tag{4.22}$$

where each term of the matrix $\mathbf{E}$ follows a circularly symmetric Normal distribution $\mathcal{CN}(0, 1)$. Moreover, the scalar parameter $\tau \in [0, 1]$ is used to indicate the quality of the channel estimation, where $\tau = 1$ corresponds to perfect estimation of the channel whereas $\tau = 0$ corresponds to having only the random channel $\mathbf{E}$ [113]. This parameter depends on factors such as the time/power spent on pilot-based channel estimation. As done in (4.15), and with the imperfect channel consideration, the equivalent matrix becomes

$$\bar{\mathbf{H}}_e = \widehat{\mathbf{H}}^H \widehat{\mathbf{W}}_e^{(p)} \tag{4.23}$$

where the precoder $\widehat{\mathbf{W}}_e^{(p)}$ has been calculated considering the imperfect channel $\mathbf{H}_e$.

4.5.5 Precoders Evaluation

In this section we provide some simulation results to compare the performance of the different precoders considered, which will be assessed in terms of SINR and achievable system capacity. Before examining in detail all the results, we briefly report here the SINR expression used in our evaluation. Furthermore, some important parameters of the study are the total number of antennas N_{T} at the gNB site which is 64 placed with a $[8 \times 8]$ vertical and horizontal UPA configuration and $\lambda[0.7, 0.5]$ vertical and horizontal as element spacing, respectively. Then, we have evaluate an imperfect channel considering using the imperfect channel metric

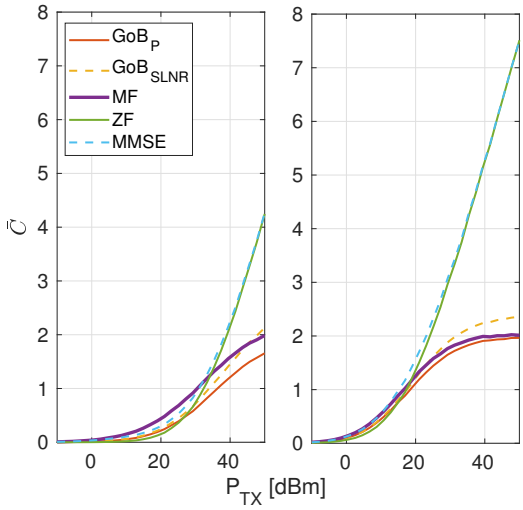

Figure 4.8: System capacity for the different precoders, varying the transmitted power P_{TX}. In this figure, $M = 4$, $\mathsf{NF} = 7$ dB, and the channel is modeled as NYU in the left plot and following the 3GPP characterization in the right plot.

$\tau = 0.99$.[12] The results have been collected over a sufficient number of repetitions in order to obtain the desired accuracy, thus precisely evaluating the different precoders. In fact, the figures are obtained with a Monte Carlo approach which generates random samples of channel and environment for all the UEs in each iteration.

The first metric considered in our evaluation is the SINR, we calculate it for each UE m as follows

$$\text{SINR}_m^{(p)} = \frac{|\bar{\mathbf{h}}_{m,m}^{(p)}|^2}{\frac{1}{\text{SNR}} + \sum_{i \neq m} |\bar{\mathbf{h}}_{m,i}^{(p)}|^2} \tag{4.24}$$

where SNR is computed using the transmitted power, the path loss ℓ, and the thermal noise σ^2 as $\frac{P_{\text{TX}}\ell^{-1}}{\sigma^2}$. We note that each UE's SINR is affected by the accurate antenna array radiation pattern that is computed considering the field factor term into the channel gains, as previously described in (5.4). Finally, superscript (p) is used to identify the $M \times 1$ vector of the equivalent matrix $\bar{\mathbf{H}}^{(p)}$ obtained with the corresponding precoder $\widehat{\mathbf{W}}^{(p)}$. We recall that the precoding matrix is included into the equivalent matrix as done in (4.15).

With the use of the SINR expression in (5.9), we can compute the channel capacity as follows

$$\text{C}_m^{(p)} = \log_2\left(1 + \text{SINR}_m^{(p)}\right). \tag{4.25}$$

This metric can be used to evaluate the spectral efficiency of each configuration, and we indicate its average value by $\bar{\text{C}}$. Figure 4.8 plots the average system capacity in the different configurations as a function of the transmit power P_{TX} used at the gNB side. The growing

[12] The value $\tau = 0.99$ identifies an optimistic channel imperfection. As discussed later in the results, even with a small error in the CSI the degradation is notable.

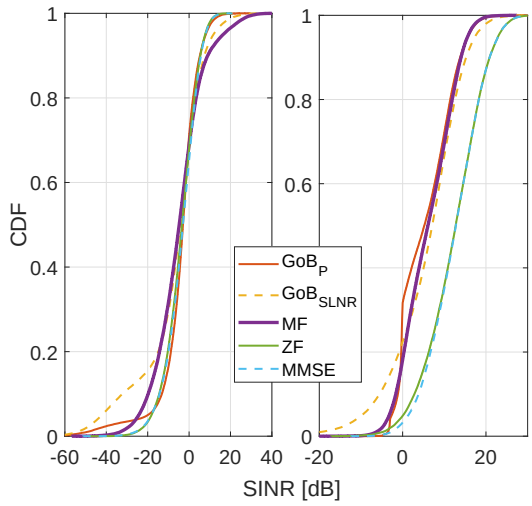

Figure 4.9: Empirical CDF of the SINR for the different precoders evaluated when an imperfect channel is considered. In this figure, $M = 4$, NF $= 7$ dB and $\tau = 0.99$, and the channel is modeled as NYU in the left plot and following the 3GPP characterization in the right plot.

transmit power increases at the same rate the received power and the interference levels for the interference-blind precoders (i.e., MF, GoB) hence resulting in a saturation of the performance. Conversely, interference-aware precoders such as ZF and MMSE can have indefinitely growing performance. The figures display the good performance of the GoB precoder when the SLNR is optimized. We remark that, even if the average MF SINR is higher with respect to the other configurations, it presents poor fairness among the UEs.

Comparing the two realistic models, we can notice also in this figure how the directivity of the NYU model results in good outcomes for the capacity in the two GoB approaches in the range of values around 20 dBm of transmitted power. Contrary to expectation, in this particular range, GoB procedures can perform appreciably better than ZF if high spectral efficiency is desired, while, if a more energy-efficient operating point is chosen, the performance gap narrows, and eventually MF outperforms all the other configurations.

As a final result, Figure 4.9 reports the empirical CDF of the SINR when an imperfect channel $\mathbf{H}_e$ is considered. As expected, the MMSE precoder outperforms all the other configurations for most of the UEs. Furthermore, due to the high directivity of the NYU channel, both GoB precoders are able to reach higher SINR values, with respect to the MF, for more than forty percent of the UEs. We note that for these plots we have used a 7 dB noise figure[13], which corresponds to a mostly interference-limited system [4].

We remind that in this evaluation we have used an error identified by the parameter $\tau = 0.99$. More importantly, when an error in the channel estimation is considered, the gap between GoB optimization approaches and linear precoders is strongly reduced and, in

[13]The noise figure term quantifies the degradation of the SNR due to the noise present in the system.

Table 4.5: Evaluation of the gaps in the 50-th percentile of the SINR expressed in dB for the different precoders considered in this evaluation. Table obtained with a fixed number of UEs $M = 4$, and $P_{\mathrm{TX}} = 30$ dBm.

	perfect CSI ($\tau = 1$)		imperfect CSI ($\tau = 0.99$)	
	NYU	3GPP	NYU	3GPP
MF – $\mathsf{GoB}_{\mathsf{SLNR}}$	+0.87	−0.80	−0.46	−1.03
ZF – $\mathsf{GoB}_{\mathsf{SLNR}}$	+1.40	+6.33	+0.89	+5.67
MMSE – $\mathsf{GoB}_{\mathsf{SLNR}}$	+4.05	+6.45	+1.36	+5.67

most cases, GoB is even able to outperform the linear precoders. We recall that gathering the CSI necessary to use MF, ZF and the MMSE precoders has a cost for the system that should be properly considered. Furthermore, given the small implementation loss of GoB precoding with respect to more refined systems, and considering the high level of complexity that gathering the necessary CSI would require, it seems that the additional complexity may not be justified by the modest (or even vanishing) performance improvement.

4.5.5.1 Remarks

We report in this subsection the main remarks raised in our evaluation study. Due to the directionality of mmWave channels, our results support GoB approaches as a good trade-off between CSI acquisition complexity and performance. Given the limited advantage (about +4 dB with MMSE and the NYU channel model), there is no strong motivation to use linear precoders in multi-user systems at mmWave frequencies. Table 4.5 summarizes our findings, reporting the SINR gaps for the 50-th percentile in the different approaches considered. Although linear precoders can exploit a larger amount of information on the channel matrix, requiring full CSI at the transmitter, the gain under imperfect CSI can be assessed as less than +1.36 dB with MMSE and the NYU channel model. If the inaccuracy of the channel estimation grows, it is possible to conjecture that the gap would close even more, eventually eliding any advantage. A similar trend, though with slightly higher gains, can be observed when the 3GPP channel model is considered.

4.6 Tilt Angle Optimization

In the next generation of cellular communications, in addition to the use of mmWave frequencies, several new features will be integrated into the cellular framework of the next generation. Among them, directional transmission, achieved by radio frequency beams and base-band precoding, is adopted to increase the spectral efficiency and coverage, whereas a dynamic Time Division Duplex (TDD) frame structure would allow a more efficient usage of the spectral resources. In particular, the latter is a promising way to improve the spectral

efficiency of the wireless communication networks, since a flexible traffic adaptation can be achieved by dynamically changing the slots of the frame structure between the Uplink (UL) and Downlink (DL) transmission directions. Briefly, this means that transmission slots are dynamically allocated in DL or UL by each gNB according to the needs at every time instant.

While such a feature is useful to dynamically meet the needs of the UEs, it raises new issues, such as the increase of interference levels in case an adjacent node is transmitting while the other one is receiving. Furthermore, even if the interfering source belongs to another operator and is using a different band, interference is not negligible due to the presence of out-of-band emissions and receiver selectivity [114]. For this reason, considering the large amount of interference perceived, a study of valid solutions is required in order to take complete advantage of the dynamic TDD transmission.

In this study, we are interested to consider the optimization of the mechanical tilt angle as an antenna parameter which can be useful to reduce the interference. Since *antenna tilting* can strongly influence the radiation pattern of both transmitter and receiver, both desired and interference directions are affected by this setting [87]. Eventually, we aim to highlight the relationship between performance and tilting angle.

4.6.1 Related Works

In the literature, while some works focus on tilting optimization approaches for past generations of mobile communication systems (e.g., LTE), in the academia there are no works that study the advantages of mechanical tilting when the directional transmission is applied in 5G mobile scenarios. The closest works to ours are [115] and [116]. Moreover, some 3GPP specifications[14] are relevant and they can be considered as state of the art for this study, such as [90] and [107]. Due to the lack of research on this aspect, we want to highlight with this work the importance and the benefits of the tilt consideration.

In [115], the authors investigate the use of dynamic TDD configurations in the application of outdoor LTE Pico-cell deployments. Performance benefits are evaluated and gains in packet throughput are displayed. However, new and complex considerations are required to adapt this approach to a 5G mmWave system (e.g., due to directional transmissions).

A preliminary analysis obtained through system-level simulations for next-generation cellular systems can be found in [116], where the use of a frequency domain interference coordination technique is proposed. However, this second work focuses on the study of the performance of the dynamic allocation approach only, without detailed scenario considerations or discussions.

[14]These technical reports are provided by the industry members of the 3GPP alliance, which have studied this aspect. However, except for suggesting some values, no particular details on the research activities are available.

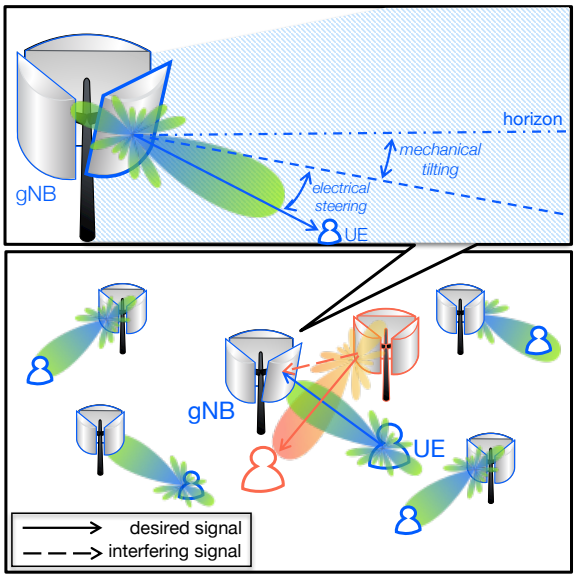

Figure 4.10: Example of steering obtained through both mechanical and electrical downtilts (top). Illustration of the dynamic TDD scenario considered (bottom). In the scenario, a UL transmission is performed by the central UE with the blue beam, while a DL and interfering transmission is operated by the gNB of another operator which is shown by the orange beam.

4.6.2 Scenario Considered

With respect to these prior studies, several are the assumptions we introduce in this work. As shown in Figure 4.10, we have considered a realistic mmWave environment operating in the 28 GHz band where two operators are dynamically controlling the frame structure, thereby generating a situation of adjacent interference. Furthermore, interference from other nodes of the same operators is also considered, thus representing a detailed 5G mobile system. Each transmitting link in the environment, either desired or interfering connection, is precisely characterized using realistic MIMO channel matrices generated according to NYU statistical channel model. We remind that, this model is based on the WINNER II channel characterization [22], and considers macro-level scattering paths and respective sub-paths. Precise details on channel aspects can be found in our previous analysis [117] and Section 2.3. Finally, an accurate antenna characterization has been used to model the array radiation pattern as done in our previous work [86].

We consider a cellular MIMO mmWave system in which a single gNB sector equipped with a panel composed of $[8 \times 8]$ antenna elements is receiving a UL communication signal from an associated UE. In order to precisely evaluate the performance of a dynamic TDD system, we deploy a realistic dense cellular network and compute the performance of the transmission. Thus, both the interfering gNBs and UEs are deployed in the area surrounding the receiving UE. All the UEs in the network are equipped with a $[4 \times 4]$ UPA antenna with element spacing set to $[0.5, 0.5]\lambda$ in the vertical and horizontal dimensions.

Table 4.6: List of ACLR and ACS parameters used in the evaluation.

Value	Meaning
28 dB	ACLR_{gNB}
17 dB	ACLR_{UE}
24 dB	ACS_{gNB}
23 dB	ACS_{UE}

Considering a UL connection, the desired communication link is affected by two main sources of interference. The first source of interference is composed of the other nodes of the same operator in the area: other gNBs in downlink and UEs in uplink. The second source of interference is composed of gNB of a different operator which may be closely located to the examined node. Although the interfering node is using a different portion of the band, the interference generated by out-of-band emissions is not negligible, especially when the two nodes are closely located. In the classic analysis, Adjacent Channel Interference Ratio (ACIR) effects are usually not considered, since they can be neglected if frames are synchronized and frequency-reuse mechanisms are applied. However, this is not the case here, since coordination between nodes of different operators is typically not feasible.

Also in this study, the channels linking all the devices are modeled according to the NYU channel model. Furthermore, the antenna array radiation model adopted follows the one established by 3GPP in [90] as previously explained in Section 4.2 and work [50]. Finally, each UE in the network is associated with the gNB which provides the strongest Reference Signal Received Power (RSRP), and transmission beams are aligned between transmitter and receiver.

4.6.3 Adjacent Channel Interference Ratio

To accurately evaluate the effect of interference originating from out-of-band emission in the adjacent band, the ACIR term must be properly treated. It is computed considering two parameters: Adjacent Channel Leakage Ratio (ACLR) and Adjacent Channel Selectivity (ACS). The former is related to the interfering system transmitter, and is specified as the ratio of the mean power centered on the assigned channel frequency to the mean power centered on an adjacent channel frequency. Conversely, the ACS term relates to the selectivity error of the victim system receiver [114, 118]. According to these definitions, the ACIR is calculated as

$$\text{ACIR} = \frac{1}{\frac{1}{\mathsf{ACLR}_s} + \frac{1}{\mathsf{ACS}_s}} \tag{4.26}$$

where both *leakage* and *selectivity* terms are specific for the node type, i.e., $s \in \{\text{gNB}, \text{UE}\}$. Values of the ACLR and ACS parameters have been computed according to documents [92, 107, 119] and are reported in Table 4.6.

Using the ACIR term, we can compute the SINR as

$$\text{SINR} = \frac{\frac{P_{\text{TX}}}{\ell_1} G_1}{\sum_y \frac{P_{\text{TX}}}{\ell_y} G_y + \mathsf{ACIR} \frac{P_{\text{TX}}}{\ell_2} G_2 + \sigma^2} \tag{4.27}$$

where in the numerator the received power is calculated considering the specific path loss ℓ_1 and gain G_1 computed examining the antenna radiations and channel characterizations of the desired link. The denominator is obtained summing three parts. First, the interference generated by all the active nodes $y \in Y$ of the same operator. Second, the interference generated by the gNB of the other operator attenuated by the ACIR value. Third, the thermal noise σ^2.

4.6.4 Comparison Results

This section reports the numerical simulation results that show the achievable performance when the mechanical tilt angle is properly considered.

In detail, a gNB with three sectors, each equipped with a UPA composed of 64 antenna elements, is considered. The UEs are modeled as 16 elements UPAs facing their attached gNB. In our evaluation, we display results for the $[8 \times 8]$ antenna elements configuration. However, we remark that similar behaviors can be observed also with different antenna configurations, e.g., with a diverse number of antenna elements or antenna spacing.

In this study, we account for the effect of interference to assess its impact on the optimal tilting angle. Figure 4.11 display these findings. The green solid line represents the variation of the SNR as a function of the tilting angle, and has it maximum at about 110 degrees, i.e., 20 degrees below the horizon[15]. This is not surprising since most UEs attached to the gNB are located in that zone. However, when the SINR (displayed by the solid yellow line) is considered, the optimal tilting angle increases to 140 degrees, which yields a 3 dB average performance gain. This is due to the reduction of the interference power that is obtained by further tilting towards the ground the panel direction. To display this effect, we report the level of the INR as a dashed blue line, which has its minimum at about 150 degrees.

In relation to our results, 3GPP specifications [90] recommend the usage of a tilting angle in the range 102–110 degrees. This is coherent with an analysis done for interference-free scenarios. However, when interference is accounted, such recommendation yields suboptimal results. Nonetheless, our results are strongly scenario-dependent and prone to vary with both the UE and the gNBs placement, the transmission power and the ISD. Although all the parameters have an impact on the value of the optimal tilt angle, the most relevant are linked to the topology of the environment: ISD and antenna heights. Therefore, we suggest that, in order to use a scenario in the optimal condition, this evaluation should be made on

[15]In this evaluation we consider the zero of the elevation (i.e., the z-axis) pointing towards the zenith. Consequently, a 90 degree elevation is oriented towards the horizon.

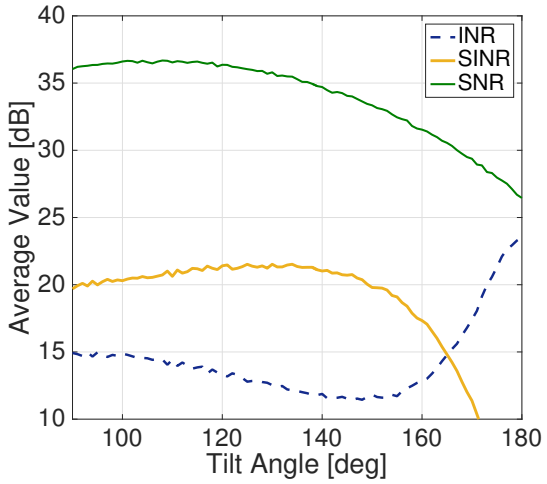

Figure 4.11: Average gain values of the INR, SINR, and SNR varying the tilt angle in the configuration with $[8 \times 8]$ antenna elements, vertically and horizontally spaced as $\lambda[0.7, 0.5]$, respectively. Furthermore, Inter-Site Distance (ISD) is considered fixed to 100 m.

a per placement basis. In other words, instead of using a fixed value, as suggested in 3GPP specifications [90], a proper evaluation should be done prior to the deployment of each gNB in a way to identify the optimal tilt angle according to the specific antenna, adjacent nodes and network settings.

4.6.4.1 Remarks

This research activity highlights the impact of the mechanical tilt angle on the mmWave communication performance when dynamic TDD is applied. Our study led to the following observations. First, due to the dynamic TDD frame structure, the tilting determined solely based on an interference-free assumption leads to suboptimal network performance. Second, it is possible to identify the optimal tilt angle to improve the SINR of both the average and the worst user. Third, the optimal angle depends on several scenario-dependent parameters and should be quantified on a network planning basis. Therefore, alongside to the industry tilt results in [90], our work aims to highlight the importance of precisely considering mechanical tilting to achieve performance improvements.

4.7 Antenna Optimization through Machine Learning

Complex phenomena are generally modeled in sophisticated simulators that, in order to be accurate, can be very demanding in terms of computational resources and simulation time. Their time-consuming nature together with a typically vast parameter space to be explored makes simulation-based optimization often unfeasible. In this last section, we present a method that, bypassing the simulator, enables the optimization of complex antenna systems

through Machine Learning (ML) techniques [88].

In details, we show how well-known learning algorithms are able to reliably emulate a complex simulator with a modest dataset obtained from it. The trained emulator is then able to yield values close to the simulated ones in virtually no time. Therefore, it is possible to perform a global numerical optimization over the vast multi-dimensional parameter space, in a fraction of the time that would be required by a simple brute-force search. After simulating a number of antenna configurations and collecting the relative network-level statistics, we feed it into our framework. Results show that, even with few data points, extrapolating a continuous model makes it possible to estimate the global optimum configuration almost instantaneously. The very same tool can then be used to achieve any further optimization goal on the same input parameters in negligible time.

Before proceeding with the manufacturing of antenna array, a careful design phase is required in order to optimize user performance. For an accurate analysis of 5G mmWave cellular scenarios, it is important to consider realistic antenna patterns combined with a rigorous channel model in order to simulate the wireless radiation environment.

Given the high prototyping cost, antenna designs are generally evaluated through simulators first. However, given the large number of parameters that need to be tuned, the optimization of an objective function (e.g., maximization of the SINR) is extremely time-consuming, or even infeasible. Gathering results from a realistic simulator can take a very long time, depending on the required level of detail and the accuracy of the employed antenna models. Therefore, an alternative way must be found to reach the optimization goal.

In order to address this problem, we propose and evaluate a ML framework able to emulate a complex simulator and to achieve the optimization in a reasonable amount of time. This last concept is represented in the diagram of Figure 4.12, where it is shown how the parameter optimization can be reached through the ML-based emulator, that only requires a relatively small dataset of simulated data. We highlight that the proposed framework can be used for optimization in a wide set of scenarios, when a complex environment is simulated.

4.7.1 Related Works

Researchers are eager to understand the possibilities that the ML techniques can offer when applied to communication problems. The new database proposed in [120] is a proof of this new trend, as it lays the premises for a common research ground.

One common application of ML is parameter estimation, where great results were achieved even when the most sophisticated classical techniques failed. This is the case in [121], where the authors try to estimate the DL channel starting from samples of the UL channel. While well-known signal processing techniques (e.g., the Wiener filter) were not able to perform a good estimate, the ML approach proposed by the authors yields great results.

Another common approach is the encoding of the channel representation through au-

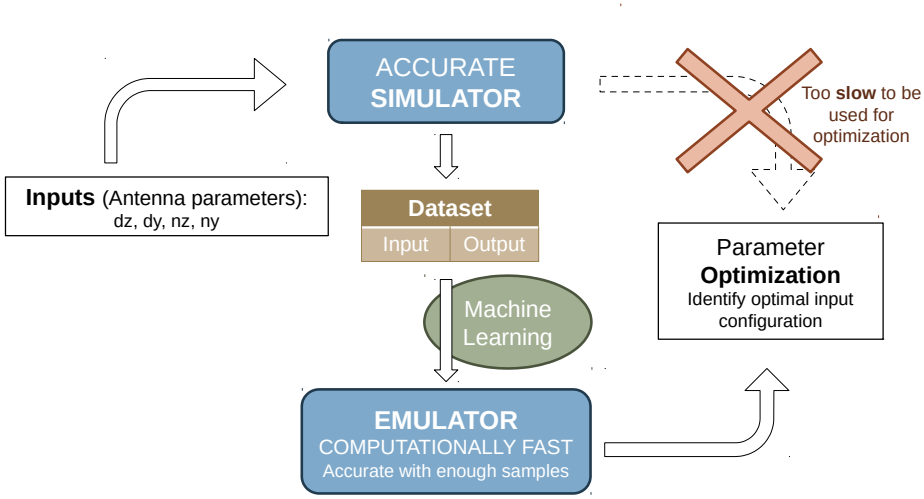

Figure 4.12: Workflow of the proposed framework. The diagram highlights how the parameter optimization is reached using a ML-based emulator.

toencoders [122]. Autoencoders are an unsupervised learning algorithm, and as such they do not need labeled data but can learn autonomously. The idea behind this technique is to train two Neural Networks (NNs), one performing the encoding of the input data, the second trying to decode it. The layer between the two should contain, in our case, a useful and extremely compressed representation of the channel. This can be applied at many levels, starting from the pure, physical channel model, to the entire transmitter-channel-receiver chain [123]. This allows obtaining either encoders/decoders, transmitter/receiver chains or channel models that have a much lower computational complexity.

Then, ML has been successfully applied also at the network layer. Innovative ideas and proposals have challenged even the most resilient classical paradigms such as the ISO/OSI architecture [124], as the evolution of the information infrastructures calls for a radical change. These new approaches started showing their potential in the increasingly heterogeneous network scenarios, e.g., when facing the high data load and quality of experience required for video streaming [125]. We believe that ML can play a central role in tackling highly complex problems in a data-rich environment.

Furthermore, the authors in [126] use Deep NNs to optimize the allocation algorithm in a wireless resource management problem. The proposed concept is similar to the one described in our work, as a learning tool is used to approximate a complex input-output function. However, the authors also include the optimization step into the learning process

and use many more training samples to accommodate the needs of their deep architecture. For our work, instead, it is crucial to use as few samples as possible as we aim to speed up the optimization process by approximating very slow simulators, making the data acquisition the main bottleneck.

In the literature, many research activities have been focusing on the study of mmWave mobile environments while in parallel a lot of works have studied in the past the problem of beamforming and antenna array optimization. However, there are no conclusive works focused on antenna optimization precisely for mmWave mobile scenarios.

In view of this goal, in the remainder of the section we report some related works on antenna characterization for mmWave bands which have been a guideline for the activity carried out in this study. Our previous work [4] has been considered as the baseline for the mobile network simulator. Starting from that, several changes have been made to adapt the cellular simulator to test all the antenna element and array settings. While, the actual antenna gain obtained due to the radiation pattern is precisely evaluated as described in Section 4.2 and previous work [50]. As it is customary, antenna patterns were modeled as the superposition between the single element radiation pattern and the array factor.

4.7.2 Framework Description

The objective of the proposed framework is to speed up simulation-based optimization in the presence of slow simulators. Optimization based on simulated data requires a number of iterations, each with a different input configuration, for the optimization strategy to steer toward the optimal value. The major constraint is the simulation time[16], which makes a brute-force approach unfeasible. The goal of our framework is to require a small number of simulations to learn the input-output relationship through ML algorithms, which are orders of magnitude faster to evaluate. A key advantage is that, after the preliminary database creation, the optimization of the selected antenna parameters can be achieved in a negligible amount of time, even when testing different optimization goals. In fact, we remark that once the emulator is trained, the optimization of multiple objective functions can be done instantaneously. Although the idea is broadly applicable, our focus here is antenna optimization over network-level metrics for mmWave systems.

4.7.2.1 Network Simulator

In order to test the framework, we need to emulate some data. A custom simulator was built in order to efficiently obtain results from such complex simulations. Simulation parameters are 3GPP standard-compliant [90, 127].

[16]Simulation times vary remarkably depending on the type of the simulation and the accuracy required. It is not unlikely for a single run to require hours or even days.

Variable parameters of the scenarios considered are antenna spacing d_z, d_y in the vertical and horizontal directions, respectively, and number of antenna elements $n_z, n_y \in 1, 2, \ldots, N$ in the vertical and horizontal directions, respectively. The total number of antenna elements is fixed to $N = 64$, in order to obtain a fair comparison between different configurations. Thus, n_z and n_y are the integer divisors of N and they are deterministically related through $n_z = \frac{N}{n_y}$.

For each configuration, we collect network-level metrics such as:

- average SINR ($\overline{\text{SINR}}$);
- 5-th percentile of the SINR (SINR_5).

4.7.2.2 Data Analysis and Machine Learning

The dataset was created with the simulator introduced in previous Section 4.7.2.1. Given that our goal is to show the capabilities of the framework and not the optimization itself, the simulator has been simplified to obtain a good number of samples in a reasonable amount of time. It should be clear that such a rich database would not be available in a complex, thus more realistic simulation.

The objective of the learning algorithm is to learn the underlying function mapping the input antenna configuration to the output network metrics, as an example

$$\begin{aligned} f : \mathbb{R}^n &\rightarrow \mathbb{R}^m \\ \mathbf{x} &\mapsto \mathbf{y} \end{aligned} \tag{4.28}$$

where $\mathbf{x}$ is the vector of the n input antenna parameters, f represents the simulator, computing the output network statistics from a given antenna configuration, and, finally, $\mathbf{y}$ is the vector of the m considered network metrics. Therefore, the learning algorithm (*emulator*) learns an approximation $\hat{f}$ of the *simulator*'s underlying function f, thus trying to mimic it.

Considering a scalar output y, the prediction or emulation error is then computed as the difference between the prediction of the emulator $\hat{y}$ and the corresponding simulator output y. In order to assess this, we define the normalized Root Mean Square Error (nRMSE) as

$$\text{nRMSE} = \sqrt{\frac{1}{N}\sum_{i=1}^{N}\left(\frac{y_i - \hat{y}_i}{y_i}\right)^2} \tag{4.29}$$

where N is the number of samples of the test set. This parameter allows for a fair comparison among metrics on different scales, as the normalization yields a percentage of standard error with respect to the simulated value. Note that SINR values are first converted to linear units.

In this preliminary study, results are validated using a test set of 300 samples, that was proved to be large enough for this setup to obtain good testing accuracy. In this work, the test set size is kept fixed, to allow a simplified presentation of the framework while guaranteeing a proper result validation.

Several learning techniques have been analyzed and tested [128]. However, only results for linear regression, random forests and RRs are hereby reported.

- **Linear Regression** is the most basic regression algorithms. Despite its simplicity, many versions and adaptations have been created, able to solve non-trivial problems. It is often considered as a baseline for more powerful algorithms;
- **Gaussian Processes** consider data as if it was sampled from a stochastic process, trying to minimize the log-marginal-likelihood during the fit;
- **Random Forests** are ensembles of decision trees, that approximate stepwise the target function;
- **Support Vector Regressors (SVRs)** are derived from the Support Vector Machine (SVM) classification algorithm. Among all the typical kernels, the Gaussian one performed best and is shown here.

One of the main advantages of the polynomial regression is that, due to its simplicity, it is fast to train and easily interpretable, i.e., the analysis of the coefficients leads to some insights on the importance of the different inputs and their correlation. On the other hand, random forests and SVRs are black-box algorithms, meaning that results are hardly interpretable.

In Figure 4.13, we evaluate the performance of the selected algorithms for increasing training sizes. We recall that increasing the number of training samples is always beneficial for learning, improving both emulation accuracy and stability. However, it affects the dataset creation time, going against the purpose of the framework.

Moreover, note that the performance of linear regression quickly saturate, while more complex algorithms achieve a lower error before converging. Saturation is expected even with the most powerful algorithms since data obtained from the simulator is inherently noisy (e.g., the number of Monte Carlo simulations is never infinite, thus statistics are not perfect). Instead, the reason why simpler algorithms tend to saturate earlier and with higher errors is because they are too simple to describe the inherent properties of the underlying function f. This concept can be easily seen in Figure 4.14, where we visually compare the emulator fit with the simulator samples.

As expected, the nRMSE decreases as the training size increases, but at different rates for different algorithms. The trade-off between the number of samples and the emulation precision has to be taken into account when selecting the algorithm. The achieved nRMSE can be extremely low, namely about 3.2% and 5.7% for $\overline{SINR}$ and SINR_5, respectively.

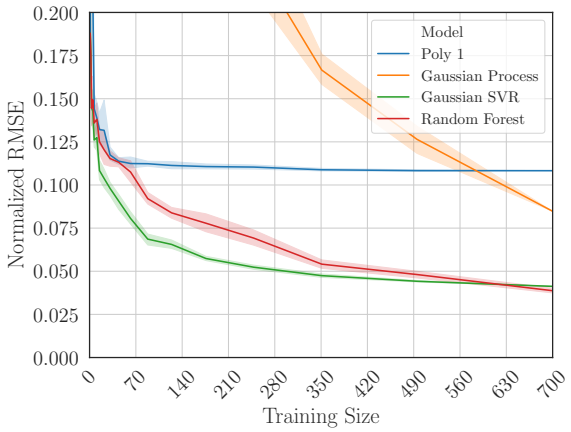

Figure 4.13: Plots show the nRMSE as a function of the number of training samples. Multiple runs are performed, showing mean (line) and 95 % confidence interval for each algorithm (shadowed area).

Finally, in general, we observed that it is not possible to have a universally valid list of best algorithms, as this is very much dependent on the simulator, the scenario, and even the considered metric. As a basic approach, once the error achieves a target threshold, the emulator can be used for the optimization and the simulator can be stopped. As an example, if our target is a 6% error, then for SINR_5 we would need 300 training samples, while for $\overline{SINR}$, 150 samples would suffice, much fewer than the 700 reported here. Thus, in a realistic deployment, the number of required samples could be decided on the fly.

4.7.2.3 Optimization

The proposed framework is optimization agnostic, meaning that most standard numerical optimization techniques can be equally used. Clearly, the learned representation is just an approximation of the real-world performance, as the simulator tries to reproduce the reality, the emulator approximates the simulator itself, adding a further level of abstraction that further distances it from the real-world.

Since in general our models are not required to be differentiable, nor would we have an explicit derivative for most of them, gradient-based techniques are hardly usable. Some of the inputs could also be categorical or discrete (e.g., the number of antennas in each dimension). Furthermore, we are not posing any constraint on the convexity (or concavity) of the underlying function. For these reasons, gradient-based optimization algorithms would not even be desirable.

On the other hand, since a global optimum is typically desired, gradient-free global optimization algorithms exist that satisfy all these requirements (e.g., genetic algorithms or simulated annealing). Nowadays most scientific-oriented programming languages have optimization libraries, implementing a number of algorithms. As briefly explained in 4.7.2,

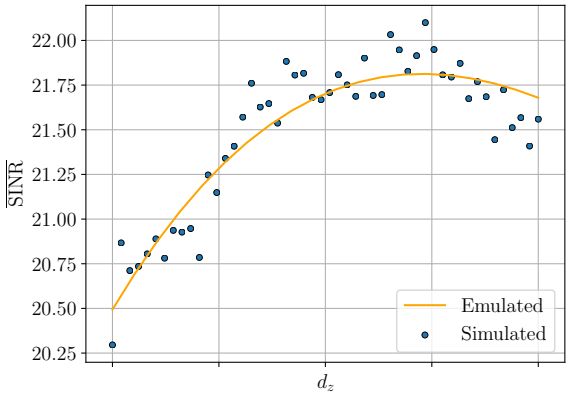

Figure 4.14: Representation of a one-dimensional plot obtained by fixing all the array parameters except one. The plot makes it possible to visually compare the emulator fit with the simulator samples. In this case, an $[8 \times 8]$ array was used with $d_y = 0.5\lambda$ spacing, while the vertical spacing d_z is varying. The emulator is still trained in all 4 inputs simultaneously, justifying the suboptimal fit towards higher values of d_z.

Figure 4.14 shows the noisiness of the training data. Thus, finding the maximum values over the raw data might not be the best choice, while numerically finding a global maximum over a smooth model might be a better choice, provided that the model is not underfitting. In the next part, we show the results obtained for the antenna optimization.

4.7.3 Optimization Results

The optimization phase shows the significant advantages of this framework. As previously stated, we remark that the proposed framework can be used for optimization in a wide set of scenarios, beyond that of cellular network design, used here as an example. As the optimization is done jointly on all the input parameters, the hyperspace where it operates can be extremely vast and complex. These features, along with the complexity of the search of the global maximum, require a very large number of evaluations. The gain of the framework can then be measured comparing the number of entries necessary for the database creation with the number of function evaluations needed by the optimization. This is because, due to the typical complexity of a simulator, the time required to obtain the database far exceeds that of the training and the optimization itself. In terms of time costs, the training itself is negligible and, once trained, the predictions are instantaneous.

Another aspect to take into account is that, although significant, the database creation in our framework is an overhead that is needed only once, as it does not depend on the optimization goal. The same emulator, providing almost instantaneous iterations, can be used with different optimization objectives, without requiring long simulator-based iterations.

For our example, given the data analysis initially done, we decided to use as the objective

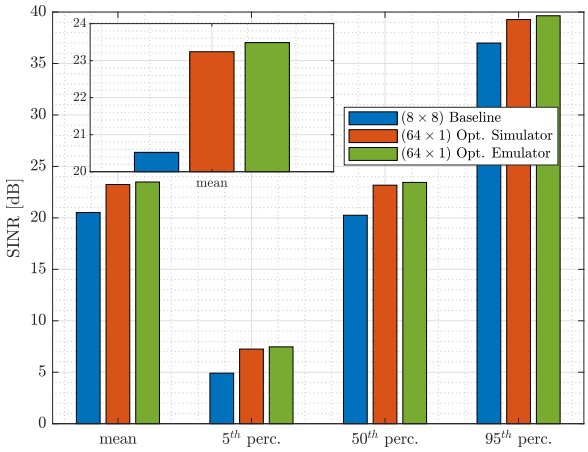

Figure 4.15: Comparison of the network performance obtained with the baseline configuration (blue bar), with the optimal configuration identified using the simulator samples (orange bar) and using the emulator (green bar).

function

$$\begin{aligned} &\text{maximize} && \overline{\text{SINR}} \\ &\text{s.t.} && \text{SINR}_5 > 6 \text{ dB} \end{aligned} \tag{4.30}$$

where the constraint on the worst UEs (identified with SINR_5) has been introduced in order to guarantee some degree of fairness and coverage to all the UEs in the network.

The optimization results obtained within the scenario described in the previous section are presented in Figure 4.15. Results show that in the proposed scenario, a baseline setup consisting of $[8 \times 8]$ arrays with $\lambda/2$ spacing in both directions performs significantly worse than the optimized ones. The other two configurations represent the optimum obtained over the collected dataset (*Opt. Simulator*, made of 1000 randomly sampled points in the four-dimensional space described in Section 4.7.2) and the global optimum obtained using our framework (*Opt. Emulator*). They both identified a 64×1 configuration (vertical ULA), but with 0.825λ and 0.734λ as vertical and horizontal spacing, respectively. Results show a ~ 3 dB improvement over the trivial baseline. Although in this case the results are really close (both inputs and outputs), two facts are important. First, we discussed in Section 4.7.2 that significantly fewer than 1000 samples would have been enough, a far lower number than required by a brute force optimization. Second, as more inputs are considered, the input space will not be sampled enough to find a good setup, making the emulation even more important.

Having computed 1000 samples while the optimization required more than 12000 function evaluations, we obtain a speedup factor of $12\times$ with respect to brute force evaluation. A key advantage of our approach is the possibility of changing the objective functions of the optimizer, which would be easily and quickly done with the emulator, without having to

retrain it.

4.7.3.1 Remarks

An innovative framework has been presented that makes the joint optimization of multiple parameters a reality, needing just a fraction of the time that is currently required when directly employing a simulator. As simulators are generally computationally complex and time-consuming, the key idea is to bypass them using a fast emulator, obtained through ML techniques. After a long, initial database creation, any objective function can be optimized in a matter of minutes or even seconds. The effectiveness of this methodology has been proved using a network simulator. Network simulators require a long time to compute the network metrics for specific antenna configurations, thus representing the perfect testbed for our framework. Future works call, in the first place, for further studies on how to reduce the number of required training samples and increase the accuracy of the emulators.

Chapter 5

Stochastic Geometry Analysis

It is well known already that mmWave bands will play an important role in 5G wireless systems. Together with simulations, the system performance can be also assessed by using models from stochastic geometry that cater for the directivity in the desired signal transmissions as well as the interference, and by calculating the SINR coverage. Nonetheless, the accuracy of the state of the art coverage expressions derived through stochastic geometry may be questioned, as it is not clear whether they capture the impact of the detailed mmWave channel and antenna features. Through several studies, we propose an SINR coverage analysis framework that includes realistic channel model and antenna element radiation patterns [84, 117, 129, 130].

We introduce and estimate two parameters, *aligned gain* and *misaligned gain*, associated with the desired signal beam and the interfering signal beam, respectively. We provide the distributions of the aligned and misaligned gains through curve fitting of system-simulation results. The distributions of these gains are used to determine the distribution of the SINR which is compared with the corresponding SINR coverage calculated via system-level simulations.

Among the results, we show that both aligned and misaligned gains can be modeled as *exponential-logarithmically* distributed random variables with the highest accuracy, and can further be approximated as *exponentially* distributed random variables with reasonable accuracy. These approximations are thus expected to be useful to evaluate the system performance under Ultra-Reliable and Low-Latency Communication (URLLC), evolved Mobile BroadBand (eMBB) scenarios and other 5G connectivity scenarios in the mmWave band.

5.1 mmWave and Stochastic Geometry

To enjoy this benefit in 5G cellular systems, the significant distance attenuation of the desired mmWave signals needs to be compensated by means of sharpened transmit/receive

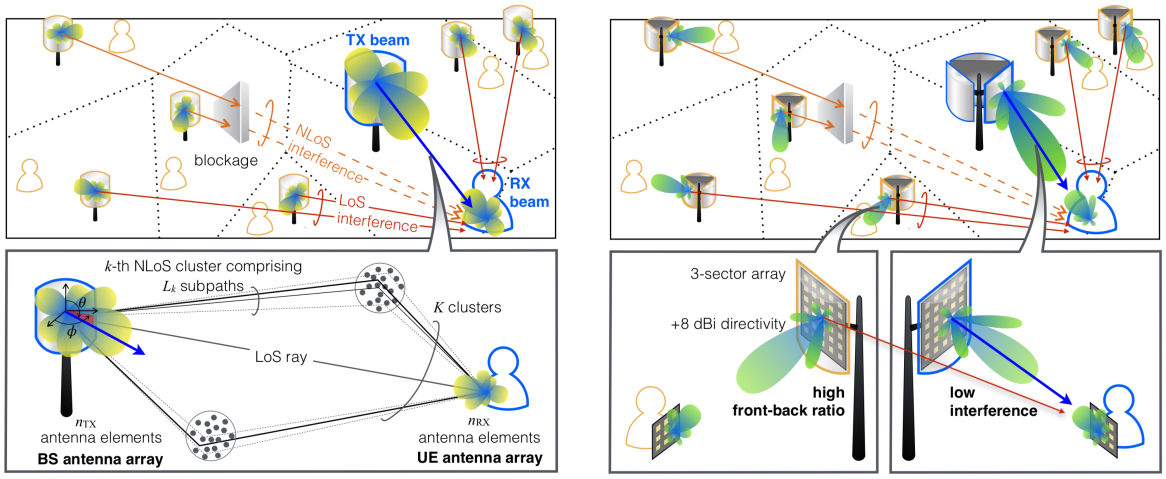

(a) With the ISO element pattern [84].

(b) With the 3GPP element pattern [90].

Figure 5.1: An illustration of our mmWave network model (top) and the channel model of each link with the transmitter/receiver antenna radiation model (bottom):
(a) With the Isotropic (ISO) element pattern, antenna gain parameters come from our previous work [84]; (b) With the 3GPP element pattern, antenna gain parameters follow from the 3GPP specifications [90]. For both element radiation patterns, channel parameters are obtained from a measurement-based mmWave channel model provided by the NYU Wireless Group [21].

beams [57, 131]. The directionality of mmWave transmissions can induce intermittent yet strong interference to the neighboring receivers. The sharpening of the directional beams reduces the probability of interference from the main lobe, while increasing the signal strength within the main lobe. This has a significant impact on the statistics of the SINR across the network.

In this work, we incorporate the experimental models for mmWave channels and antenna radiations into the tools of stochastic geometry. This results in a sufficiently realistic framework for system-level analysis of mmWave systems. Figure 5.1 illustrates the framework, which can be seen as a semi-heuristic, as it bridges the gap between a very theoretical study at a large scale (stochastic-geometric analysis), and practical measurements at a small scale. The novelty of our work compared to the existing works on mmWave SINR coverage analysis is summarized in the following.

5.1.1 Background and Related Works

The SINR coverage of a mmWave cellular network has been investigated in [35, 91, 132–137] using stochastic geometry, a mathematical tool able to capture the random interference behavior in a large-scale network. Compared to traditional cellular systems using sub-6 GHz frequencies, the major technical difficulty of mmWave SINR coverage analysis comes from incorporating their unique channel propagation and antenna radiation characteristics in a tractable way, as detailed next.

5.1.1.1 Channel gain model

mmWave signals are vulnerable to physical blockages, which can lead to significant distance attenuation under NLoS channel conditions as opposed to under LoS conditions. This is incorporated in the mmWave path loss models by using different path loss exponents for LoS and NLoS conditions. Besides this large-scale channel gain, there exists a small-scale fading due to reflections and occlusions by human bodies. In order to capture this, while maximizing the mathematical tractability, one can introduce an *exponentially* distributed gain as done in [35, 135–137]. This implies assuming Rayleigh fading, which is not always realistic, particularly when modeling the sparse scattering characteristics of mmWave signals [135].

At the cost of making analytical tractability more difficult, several works have detoured this problem by considering generalized small-scale channel gains that follow a *gamma* distribution (i.e., Nakagami-m fading) [91, 132, 133] or a *log-normal* distribution [134]. Nevertheless, such generic fading models have not been compared with real mmWave channel measurements, and may therefore either overestimate or underestimate the actual channel behaviors.

5.1.1.2 Antenna gain model

Both gNBs and UEs in 5G mmWave systems are envisaged to employ planar antenna arrays that enable directional transmissions and receptions. A UPA comprises a set of patch antenna elements placed in a two-dimensional plane. The radiation pattern of each single antenna element is either isotropic or directional, which are hereafter denoted as ISO and 3GPP element patterns, respectively. By superimposing the radiation of all the antenna elements, a planar antenna array is able to enhance its radiation in a target direction while suppressing the radiation in other directions.

The 3GPP element pattern is incorporated in the antenna gain model provided by the 3GPP [90]. Compared to the ISO element pattern, the directional antenna elements in the 3GPP element pattern enable element-wise beam steering, thereby yielding higher main lobe and lower side lobe gains, i.e., increased front-back ratio[1], as visualized in Figure 5.1b. Such benefit diminishes as the beam steering direction becomes closer to the plane of the antenna array. In order to solve this problem, the 3GPP suggests to equip each gNB with 3-sectored antenna arrays [90], thus restricting the beam steering angle to $\pm 60°$.

The said radiation characteristics and antenna structure of the 3GPP element pattern complicate the antenna gain analysis. For this reason, most of the existing approaches based on stochastic geometry [35, 84, 91, 133–138] still resort to the ISO element pattern. This underestimates the front-back ratio of the actual cellular system, degrading the accuracy in the mmWave SINR coverage analysis. Furthermore, the antenna gains are commonly ap-

[1]The front-back ratio is the difference expressed in decibels between the gain of the main lobe and the second maximum gain. This ratio increases with the number of antenna elements [50, 79].

proximated by using two constants obtained from the maximum and the second maximum lobe gains [35, 91, 133–137]. It is unclear whether such an approximation is still applicable for the mmWave SINR coverage analysis with realistic radiation patterns. By approximating the original system model with a simplified one, whose performance is determined by a mathematically convenient intensity measure, tractable yet accurate integral expressions for computing area spectral efficiency and potential throughput are provided in [139]. The considered system model accounts for many practical aspects which are typically neglected, e.g., LoS and NLoS propagation, antenna radiation patterns, traffic load, practical cell associations, and general fading channels. However, a measurement-based channel characterization is missing.

Recently, a few studies [140] and [141] incorporate the impact of directional antenna elements on the stochastic geometric SINR coverage analysis, by approximating the element radiation pattern as a cosine-shaped curve under a one-dimensional linear array structure. Compared to these works, we consider two-dimensional planar arrays, and approximate the combined array-and-channel gain as a single term, as detailed in the following subsection.

5.1.1.3 Aligned/misaligned gain model

In order to solve the aforementioned issue brought by inaccurate channel gains, one can use measurement-based channel gain models, such as the models provided by the NYU Wireless Group, which are operating at 28 GHz as described in [21, 23, 142, 143]. However, the NYU channel gain model requires a large number of parameters, and is thus applicable only to system-level simulators with high complexity, as done in our previous study [6].

In our works [84, 117], we simplified the NYU channel gain model via the following procedure so as to allow stochastic geometric SINR coverage analysis.

(i) We separated the path loss gains from the small-scale fading, and treated them independently in a stochastic geometric framework. The fading term can be considered as representative of propagation effects when the user moves locally, and is independent of the link distance.

(ii) For each downlink communication link, we combined the channel gain and the antenna gain into an aggregate gain. The aggregate gain is defined for the desired communication link as *aligned gain* and for an interfering link as *misaligned gain*, respectively.

(iii) We applied a curve fitting method to derive the distributions of the aligned/misaligned gains.

(iv) Finally, we derived the distribution of a reference user's SINR, which is a function of path loss gains and aligned/misaligned gains, by applying a stochastic geometric technique to the path loss gains and then by exploiting the aligned/misaligned gain distributions.

The limitation of our work [84] is its use of the ISO element pattern in step (ii). This results in excessive side lobe gains, particularly including backward propagation, which are unrealistic. To fix this problem, in our study (i.e., work [117] here reported) we also apply the 3GPP element pattern to the aforementioned aligned/misaligned gain model, thereby yielding a tractable mmWave coverage expression that ensures high accuracy, comparable to the results obtained from a system-level simulator. Moreover, instead of Signal to Interference Ratio (SIR) as considered in [84], we focus on the SINR evaluation by incorporating also the impact of the noise power.

A recent work [138] is relevant to this study. While neglecting interference, it firstly considers a simplified keyhole channel, and then introduces a correction factor. The aggregate channel gain thereby approximates the channel gain under the mmWave channel model provided by the 3GPP [90]. Compared to this, using the NYU channel model [21], we additionally consider a realistic antenna radiation pattern provided by the 3GPP [90]. In addition, we explicitly provide the SINR coverage probability expression using these realistic channel and antenna models, as well as its simplified expression.

5.1.2 Contributions of the Analysis

The contributions of this research activity are summarized below.

- Accurate distributions of aligned and misaligned gains are provided (see **Remarks 1-4**), which reflect the NYU mmWave channel model [21] and the 3GPP mmWave antenna radiation model [90].

- Considering the ISO element pattern, following from our preliminary study [84], the aligned gain is shown to follow an *exponential* distribution, despite the scarce multipath in mmWave channels (**Remark 1**). On the other hand, we show that the misaligned gain can be approximated with a *log-logistic* distribution (**Remark 3**) having a heavier tail than the exponential distribution, which can be lower and upper bounded by a *Burr* distribution and a *log-normal* distribution, respectively.

- In contrast, for the 3GPP element pattern, we show that both aligned and misaligned gains independently follow an *exponential-logarithmic* distribution (**Remarks 2** and **4**), which has a lighter tail compared to the exponential distribution.

- Applying these aligned and misaligned gain distributions, the downlink mmWave SINR coverage probabilities with the ISO and 3GPP element patterns are derived using stochastic geometry (**Propositions 1** and **2**, respectively).

In spite of the exponential-logarithmical distribution of the aligned/misaligned gains of the 3GPP element pattern, it is still possible, in the SINR calculation, to approximate both gains independently using *exponential* random variables with proper mean value adjustment

(**Remark 5** and Figure 5.12), yielding a further simplified (though slightly less accurate) SINR coverage probability expression (**Proposition 3**). The feasibility of the exponential approximation under the 3GPP element pattern comes from the identical tail behaviors of both aligned/misaligned gains, that cancel each other out during the SINR calculation. Following the same reasoning, this approach provides a similar approximation under the ISO element pattern that leads to the different tail behaviors of both the aligned/misaligned gains due to the low front-back ratio obtained with isotropic elements (see Figure 5.12 in Section 5.5).

5.2 System Model

In this study, we consider a downlink mmWave cellular network where both gNBs and UEs are independently and randomly distributed in a two-dimensional Euclidean plane. Each UE associates with the gNB that provides the maximum average received power, i.e., minimum path loss association. The UE density is assumed to be sufficiently large such that each gNB has at least one associated UE. Multiple UEs can be associated with a single gNB, while the gNB serves only a single UE per unit time slot according to a uniformly random scheduler, as assumed in [84, 135, 137] under stochastic geometric settings.

Out of these serving users in the network, we hereafter focus on a reference user that is located in the origin of the area considered, and is denoted as the typical UE. This typical UE's SINR is affected by the antenna array radiation patterns and channel gains, as described in the following subsections.

5.2.1 Antenna Gain

Each antenna array at both gNB and UE sides contributes to the received signal power, according to the radiation patterns of the antenna elements that comprise the antenna array. The amount is affected also by the vertical angle θ, horizontal angle ϕ, and polarization slant angle ζ, as described next.

For each antenna element in an antenna array, we consider two different radiation patterns: isotropic radiation and the radiation provided by the 3GPP [92]. We recall from Section 4.2.1 that the element radiation pattern $A_E^{(z)}(\theta, \phi)$ (dB) for superscript $z \in \{\mathsf{ISO}, \mathsf{3GPP}\}$ specifies how much power is radiated from each antenna element towards the direction (θ, ϕ).

The 3GPP element pattern is realized according to the specifications in [90, 92] and [93]. We remind that, differently from the isotropic configuration, it implies the use of three sectors, thus three arrays, placed as in traditional mobile networks[2]. The 3GPP A_E of each single antenna element is composed of horizontal and vertical radiation patterns and was

[2]We note that, even if three sectors are present in each gNB site, only a single sector is active and transmitting in each time instant.

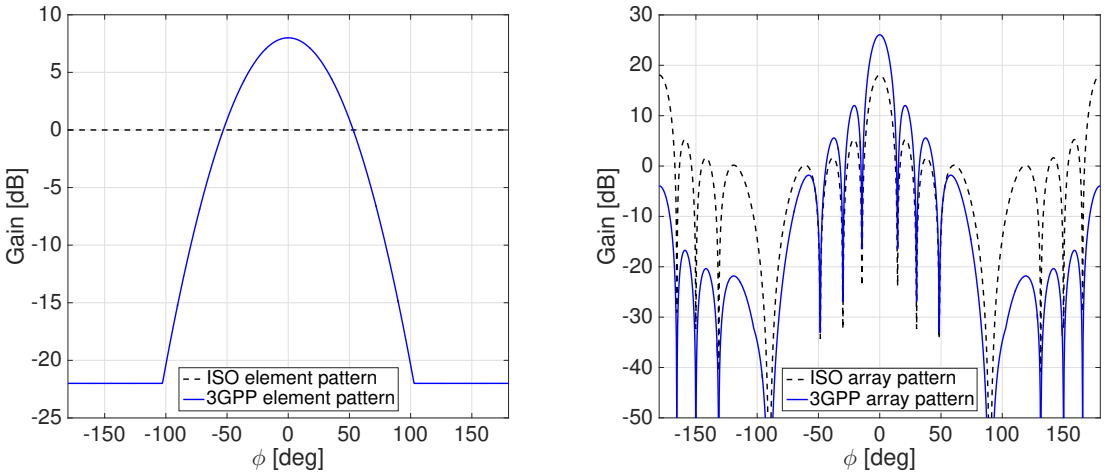

(a) Element radiation gain.

(b) 64 elements array radiation gain.

Figure 5.2: Illustrations of the element radiation gains and the array radiation gains for the ISO and 3GPP element patterns, with respect to the horizontal steering angle $\phi \in [-180°, 180°]$ while the vertical steering angle θ is fixed at 90°.

defined in previous Equation (4.3).

Then, we recall that the antenna array radiation pattern $A_A^{(z)}(\theta, \phi)$ determines how much power is radiated from an antenna array towards the steering direction (θ, ϕ) and was previously defined in (4.4). In Figure 5.2a we report a comparison of the two continuous element radiation patterns (i.e., A_E). The figure permits to understand the difference between the ISO element pattern showing a fixed gain and the 3GPP element pattern providing 8 dBi directivity. As a consequence of the element pattern used, we can see the respective shape of the array radiation pattern (i.e., A_A) in Figure 5.2b. The plot permits to see the reduction of undesired side lobes and backward propagation when considering the 3GPP curve with respect to the ISO element pattern. Furthermore, shape and position of the main and undesired lobes vary as a function of the steerable direction. Further definitions and accurate examples for these concepts can be found in [50].

Finally, with the given antenna array pattern $A_A^{(z)}(\theta, \phi)$, we can identify the antenna gain for the channel computations which was previously defined as field pattern in Subsection 4.2.3. Moreover, for simplicity in this study we consider a purely vertically polarized antenna, i.e., $\zeta = 0$. Following [93], the vertical and horizontal field patterns are thereby given as follows

$$F_\theta^{(z)}(\theta, \phi) = \sqrt{A_A^{(z)}(\theta, \phi)} \cos(\zeta) = \sqrt{A_A^{(z)}(\theta, \phi)} = F^{(z)} \tag{5.1}$$

$$F_\phi^{(z)}(\theta, \phi) = \sqrt{A_A^{(z)}(\theta, \phi)} \sin(\zeta) = 0 \tag{5.2}$$

5.2.2 Channel gain

Following the system-level simulator settings [21], we divide the channel gains into two parts: (i) *path loss* that depends on the link distance; and (ii) the channel gain multiplicative component. The latter gain is affected not only by the channel randomness but also by the antenna array directions. The following channel gain computation aspects are independent of the different radiation pattern considered, thus they are valid for both ISO and 3GPP.

The antenna array direction is determined by the gNB-UE association. To elaborate, for each associated gNB-UE link, denoted as the desired link, their beam directions are aligned, pointing their main-lobe centers towards each other. As a consequence, for all non-associated gNB-UE links, denoted as interfering links, the beam directions can be misaligned. In order to distinguish them in (ii), we define *aligned gain* and *misaligned gain* as the channel gain for the desired link and for an interfering link, respectively. The definitions of path loss and aligned/misaligned gains are specified in the following subsections.

5.2.2.1 Path loss

By definition, the set of gNB locations follows a Homogeneous Poisson Point Process (HPPP) Φ with density λ_b. At the typical UE, the desired/interfering links can be in either LoS or NLoS state. To be precise, from the perspective of the typical UE, the set Φ of all the gNBs is partitioned into a set of LoS gNBs Φ_L and a set of NLoS gNBs Φ_N. According to the minimum path loss association rule, the desired link can be either LoS or NLoS, specified by using the subscript $i \in \{L, N\}$. Likewise, the LoS/NLoS state of each interfering link is identified by using the subscript $j \in \{L, N\}$. Furthermore, we assume a sufficiently large UE density such that at least one UE is associated with each gNB. Then, each gNB serves only a single UE at a time.

For a given link distance r, the LoS and NLoS state probabilities are $p_L(r) = e^{-0.0149r}$ and $p_N(r) = 1 - p_L(r)$ [21, 23]. Here, compared to the system-level simulator settings in [21, 23], we neglect the outage link state induced by severe distance attenuation. This assumption does not incur a loss of generality for our SINR analysis, since the received signal powers that correspond to outage are typically negligibly small.

When a connection link has distance r and is in state $j \in \{L, N\}$, transmitted signals passing through this link experience the following path loss attenuation

$$\ell^j(r) = \beta_j r^{-\alpha_j} \tag{5.3}$$

where α_j indicates the path loss exponent and β_j is the path loss gain at unit distance [21, 144].

Table 5.1: List of notations and channel parameters considered in the NYU mmWave network simulator [142].

Notation	**Meaning**: Parameters
f	Carrier frequency: 28 GHz
Φ_b	gNB locations following a HPPP with density λ_b
$p_L(r)$	LoS state probability at distance r: $p_L = e^{-0.0149r}$
x_o, x	Serving and interfering gNBs or their coordinates
α_j	Path loss exponent, with $j \in \{L, N\}$: $\alpha_L = 2$, $\alpha_N = 2.92$
β_j	Path loss gain at unit distance: $\beta_L = 10^{-7.2}$, $\beta_N = 10^{-6.14}$
$\ell^j(r)$	Path loss at distance r in LoS/NLoS state
n_{TX}, n_{RX}	# of antennas of a gNB and a UE
σ^2	Normalized noise power
$G_o^{(z)}$, $G_x^{(z)}$	Aligned and misaligned gains, with $z \in \{\mathsf{ISO}, \mathsf{3GPP}\}$
$f_{G_o}^{(z)}, f_{G_x}^{(z)}$	Aligned and misaligned gain PDFs
K	# of clusters $\sim \max\{\mathsf{Poiss}(1.8), 1\}$
L_k	# of subpaths in the k-th cluster $\sim \mathsf{DiscreteUni}[1, 10]$
ϕ_{kl}^{RX}, ϕ_{kl}^{TX}	Angular spread of subpath l in cluster k [21]: $\phi_k^{(\cdot)} \sim \mathsf{Uni}[0, 2\pi], \forall k \neq 1$, $\phi_{kl}^{(\cdot)} = \phi_k^{(\cdot)} + (-1)^l s_{kl}/2$ $s_{kl} \sim \max\{\mathsf{Exp}(0.178), 0.0122\}$,
g_{kl}	Small-scale fading gain: $g_{kl} = \sqrt{P_{kl}} \exp(-j2\pi\tau_{kl} f)$
τ_{kl}	Delay spread induced by different subpath distances.
P_{kl}	Power gain of subpath l in cluster k [23]: $U_k \sim \mathsf{Uni}[0, 1]$, $Z_k \sim \mathcal{N}(0, 4^2)$, $V_{kl} \sim \mathsf{Uni}[0, 0.6]$, $P_{kl} = P'_{kl}/\sum P'_{kl}$, $P'_{kl} = U_k^{\tau_{kl}-1} 10^{-0.1Z_k + V_{kl}}/L_k$, $\tau_{kl} = 2.8$

5.2.2.2 Aligned and misaligned gains

In both ISO and 3GPP element patterns, for a given link, a random channel gain is determined by the NYU channel model that follows mmWave channel specific parameters [21, 23] based on the WINNER II model [22]. These parameters are summarized in Table 5.1, and discussed in the following subsections. In this model, each link comprises K clusters that correspond to macro-level scattering paths. For cluster $k \leq K$, there exist L_k subpaths, as visualized in Figure 5.1. Moreover, the first cluster angle (i.e., $\phi_k, k = 1$) exactly matches the LoS direction between transmitter and receiver in the simulated link.

Given a set of clusters and subpaths, the channel matrix of each link is represented as

$$\mathbf{H}^{(z)} = \sum_{k=1}^{K} \sum_{l=1}^{L_k} g_{kl} F_{\text{RX}}^{(z)}\left(\phi_{kl}^{\text{RX}}\right) \mathbf{u}_{\text{RX}}\left(\phi_{kl}^{\text{RX}}\right) F_{\text{TX}}^{(z)}\left(\phi_{kl}^{\text{TX}}\right) \mathbf{u}_{\text{TX}}^{*}\left(\phi_{kl}^{\text{TX}}\right) \tag{5.4}$$

where g_{kl} is the small-scale fading gain of subpath l in cluster k, and $\mathbf{u}_{\text{RX}}$ and $\mathbf{u}_{\text{TX}}$ are the 3D spatial signature vectors of the receiver and transmitter, respectively. Note that $\mathbf{u}_{\text{TX}}^{*}$ stands for the complex conjugate of vector $\mathbf{u}_{\text{TX}}$. Moreover, ϕ_{kl}^{RX} is the angular spread

of horizontal AoA and ϕ_{kl}^{TX} is the angular spread of horizontal AoD, both for subpath l in cluster k [21]. Note that, for ease of computation, we consider a planar network and channel, i.e., we neglect vertical signatures by setting their angles to 90° (i.e., $\pi/2$ radian). Finally, $F_{\mathrm{TX}}^{(z)}$ and $F_{\mathrm{RX}}^{(z)}$ are the field factor terms of transmitter and receiver antennas, respectively and they are computed as in (5.1) with $z \in \{\mathsf{ISO}, \mathsf{3GPP}\}$.

We consider directional beamforming where the main lobe center of a gNB's transmit beam points at its associated UE (we recall that ϕ_1 is the main lobe center angle as shown in the channel illustration of Figure 5.1), while the main lobe center of a UE's receive beam aims at the serving gNB. We assume that both beams can be steered in any directions. Therefore, considering the ISO element pattern, we can generate a beamforming vector for any possible angle in $[0, 360°]$. Instead, with the three-sectors consideration adopted in the 3GPP element pattern, the beamforming vectors for any possible angles are mapped within one of the three sectors, thus using an angle in the interval $[0, 120°]$.

At the typical UE, the aligned gain $G_o^{(z)}$ is its beamforming gain towards the serving gNB at x_o. With a slight abuse of notation for the subscript x_o, $G_o^{(z)}$ is represented as

$$G_o^{(z)} = |\mathbf{w}_{\mathrm{RX}_{x_o}}^T \mathbf{H}_{x_o}^{(z)} \mathbf{w}_{\mathrm{TX}_{x_o}}|^2 \tag{5.5}$$

$$= \left| \sum_{k=1}^{K} \sum_{l=1}^{L_k} g_{kl} F_{\mathrm{RX}}^{(z)} \left(\mathbf{w}_{\mathrm{RX}_{x_o}}^T \mathbf{u}_{\mathrm{RX}_{x_o}} \right) F_{\mathrm{TX}}^{(z)} \left(\mathbf{u}_{\mathrm{TX}_{x_o}}^* \mathbf{w}_{\mathrm{TX}_{x_o}} \right) \right|^2 \tag{5.6}$$

where $\mathbf{w}_{\mathrm{TX}_{x_o}} \in \mathbb{C}^{n_{\mathrm{TX}}}$ is the transmitter beamforming vector and $\mathbf{w}_{\mathrm{RX}_{x_o}}^T \in \mathbb{C}^{n_{\mathrm{RX}}}$ is the transposed receiver beamforming vector computed as in [50, 79]. Their values contain information about the main lobe steering direction and both are computed using the first cluster angle ϕ_1 as

$$\mathbf{w}_{\mathrm{TX}}^T = [w_{1,1}, w_{1,2}, \ldots, w_{\sqrt{n_{\mathrm{TX}}}, \sqrt{n_{\mathrm{TX}}}}] \tag{5.7}$$

where $w_{p,r} = \exp\left(j2\pi \left[(p-1)\Delta_V \Psi_p/\lambda + (r-1)\Delta_H \Psi_r/\lambda\right]\right)$, for all $p, r \in \{1, \ldots, \sqrt{n_{\mathrm{TX}}}\}$, $\Psi_p = \cos(\theta_s)$, and $\Psi_r = \sin(\theta_s)\sin(\phi_1)$. The terms Δ_V and Δ_H are the spacing distances between the vertical and horizontal elements of the array, respectively. Then, angles θ_s and ϕ_s are the steering angles and θ_s is kept fixed to 90°. We assume all elements to be evenly spaced on a two-dimensional plane, thus it equals $\Delta_V = \Delta_H = \lambda/2$. The same expression can be used to compute the receiver beamforming vector $\mathbf{w}_{\mathrm{RX}}$ with the exception that its dimension is n_{RX}.

Similarly, the typical UE's misaligned gain $G_x^{(z)}$ is its beamforming gain with an interfering gNB at x

$$G_x^{(z)} = |\mathbf{w}_{\mathrm{RX}_x}^T \mathbf{H}_x^{(z)} \mathbf{w}_{\mathrm{TX}_x}|^2 \tag{5.8}$$

where $\mathbf{w}_{\mathrm{TX}_x}$ and $\mathbf{w}_{\mathrm{RX}_x}$ respectively are the transmitter and receiver beamforming vectors. It is noted that both $G_o^{(z)}$ and $G_x^{(z)}$ incorporate the effects not only of the main lobes but also of all the other side lobes. We highlight that even if both aligned and misaligned gain definitions are valid for both the ISO and 3GPP configurations, the gains will have a different distribution in the two radiation patterns.

5.2.3 SINR Definition

The typical UE is regarded as being located at the origin, which does not affect its SINR behaviors thanks to Slivnyak's theorem [145] under the HPPP modeling of the gNB locations. At the typical UE, let x_o and all the $x \in \Phi_i$ respectively indicate the associated and interfering gNBs as well as their coordinates. We note that the set Φ_i represents gNB locations following a HPPP with density $\lambda_i, i \in \{L, N\}$.

Using equations (5.3), (5.6), and (5.8), we can represent SINR_i as the received SINR at the typical UE associated with $x_o \in \Phi_i, i \in \{L, N\}$, which is given by

$$\mathrm{SINR}_i = \frac{G_o^{(z)} \ell_i(r_{x_o}^i)}{\sum\limits_{x \in \Phi_L / x_o} G_x^{(z)} \ell_L(r_x^L) + \sum\limits_{x \in \Phi_N / x_o} G_x^{(z)} \ell_N(r_x^N) + \sigma^2} \tag{5.9}$$

where the term $r_{x_o}^i$ denotes the association distance of the typical UE associating with $x_o \in \Phi_i$ and along similar lines, r_x^i denotes the association distance of a generic UE associating with $x \in \Phi_i$ and $i \in \{L, N\}$. Knowing that the typical UE is located in the origin o, r_x is equals to $\|x\|$. Here, we assume that each gNB transmits signals with the maximum power P_{TX} through the bandwidth W. In (5.9), SINR_i is normalized by P_{TX}. The term σ^2 denotes the normalized noise power σ^2 that equals $\sigma^2 = WN_0/P_{\mathrm{TX}}$ where N_0 is the noise spectral density per unit bandwidth.

5.3 Aligned and Misaligned Gain Distributions

Starting from the expressions derives in the previous section, it is practically infeasible to further approximate aligned and misaligned gains using analytic methods, as analyzing each of their subordinate terms is a major task in itself, as shown by related works. Therefore, in this section we focus on the aligned gain $G_o^{(z)}$ in (5.6) and the misaligned gain $G_x^{(z)}$ in (5.8) with ISO and 3GPP element patterns, and aim at deriving their distributions.

Following the definitions in Section 5.2.2, the aligned gain $G_o^{(z)}$ is obtained for the desired received signal when the angles of the beamforming vectors $\mathbf{w}_{\mathrm{TX}_{x_o}}$ and $\mathbf{w}_{\mathrm{RX}_{x_o}}$ are aligned with the AoA and AoD of the spatial signatures $\mathbf{u}_{\mathrm{TX}_{x_o}}$ and $\mathbf{u}_{\mathrm{RX}_{x_o}}$ in the channel matrix $\mathbf{H}_{x_o}^{(z)}$. The misaligned gain $G_x^{(z)}$ is calculated for each interfering link with the beamforming vectors

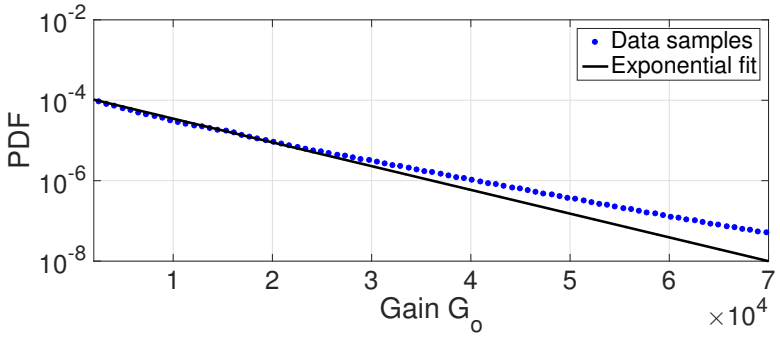

Figure 5.3: Fitting of the aligned gain $G_o^{(\mathsf{ISO})}$ with the ISO element pattern. The empirical Probability Density Function (PDF) of $G_o^{(\mathsf{ISO})}$ is obtained by the NYU mmWave network simulator [142], and is fit with the *exponential* distribution in Remark 1 ($n_{\mathrm{RX}} = 64$, $n_{\mathrm{TX}} = 256$).

and spatial signatures that are not aligned.[3] Figure 5.1 shows an example of misalignment between the beam of the desired signal (yellow or green colored beam) and the interfering gNBs beams (red-colored beams).

In the following subsections, using curve fitting with the system-level simulation, we derive the distributions of the aligned gain $G_o^{(z)}$ and the misaligned gain $G_x^{(z)}$.

5.3.1 Aligned Gain Distribution

Running a large number of independent runs of the NYU simulator we empirically evaluated the distribution of the aligned gain $G_o^{(z)}$. From the obtained data samples we have noticed that $G_o^{(z)}$ is roughly exponentially distributed $G_o^{(\mathsf{ISO})} \sim \mathsf{Exp}(\mu_o)$ when an ISO element pattern is used. Indeed, the signal's real and imaginary parts are approximately independent and identically distributed zero-mean Gaussian random variables. This exponential behavior finds an explanation in the small-scale fading effect implemented in the channel model using the power gain term P_{kl} computed as reported in Table 5.1. We report in Figure 5.3 an example of the exponential fit of the simulated distribution. The fit has been obtained using the *curve fitting toolbox* of MATLAB.

For the purpose of deriving an analytical expression, it is also interesting to evaluate the behavior of μ_o as a function of the number of antenna elements at both receiver and transmitter sides. For this reason, in our analysis we consider the term μ_o as a function of the number of elements. We show in Figure 5.4 the trend of the parameter μ_o versus the number of antenna elements at the transmitter side n_{TX} and at the receiver side n_{RX}.

[3] At the typical UE, the serving gNB's beamforming is aligned with the typical UE, whereas the beamforming vectors of interfering gNBs are determined by their own associated UEs that are uniformly distributed. For this reason, each interfering gNB's beamforming has a circularly uniform orientation. Consequently, in (5.8), the angles of the beamforming vectors $\mathbf{w}_{\mathrm{TX}_x}$ and $\mathbf{w}_{\mathrm{RX}_x}$ as well as the angles of the spatial signatures $\mathbf{u}_{\mathrm{TX}}$ and $\mathbf{u}_{\mathrm{RX}}$ are not aligned with the angles of $G_o^{(z)}$, which are independent and identically distributed (i.i.d.) across different interfering gNBs.

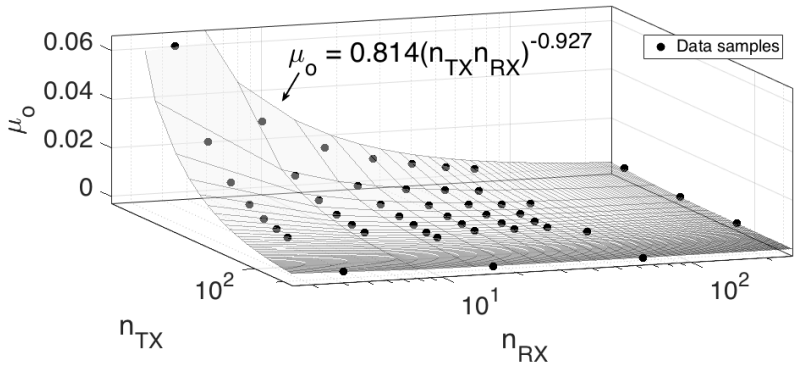

Figure 5.4: Fitting of the aligned gain distribution parameter μ_o with the ISO element pattern, with respect to the number of antenna elements n_{TX} and n_{RX}.

Again, using the MATLAB curve fitting toolbox, we have obtained a two-dimensional power fit where the value of μ_o can be obtained as in the following remark.

Remark 1 *(Aligned Gain, ISO)* At the typical UE, under the ISO antenna model, the aligned gain $G_o^{(\mathsf{ISO})}$ can be approximated by an *exponential* distribution with PDF

$$f_{G_o}^{(\mathsf{ISO})}(y;\mu_o) = \mu_o e^{-\mu_o y} \tag{5.10}$$

where $\mu_o = \frac{0.814}{(n_{TX}n_{RX})^{0.927}}$.

This result provides a fast tool for future calculations. Indeed, the expression found for the gain permits to avoid running a detailed simulation every time. We note that from a mathematical point of view the surface of the term $\mu_o(n_{\mathrm{TX}}, n_{\mathrm{RX}})$ is symmetric. In fact, the gain does not depend individually on the number of antennas at the transmitter or receiver sides, but rather on their product, so we can trade the complexity at the gNB for that at the UE if needed.

By contrast, using the 3GPP element pattern, we have noticed that the data samples of $G_o^{(\mathsf{3GPP})}$ can no longer be approximated as an exponentially distributed random variable. Instead, an *exponential-logarithmic* distribution provides the most accurate fitting result with the simulated desired gain, validated by simulation as shown in Figure 5.5.

Remark 2 *(Aligned Gain, 3GPP)* At the typical UE, and adopting the 3GPP element pattern, the aligned gain $G_o^{(\mathsf{3GPP})}$ can be approximated by an *exponential-logarithmic* distribution with PDF

$$f_{G_o}^{(\mathsf{3GPP})}(y;b_o,p_o) = \frac{1}{-\ln(p_o)} \frac{b_o(1-p_o e^{-b_o y})}{1-(1-p_o)e^{-b_o y}} \tag{5.11}$$

where the parameters b_o and p_o are specified in Table 5.2.

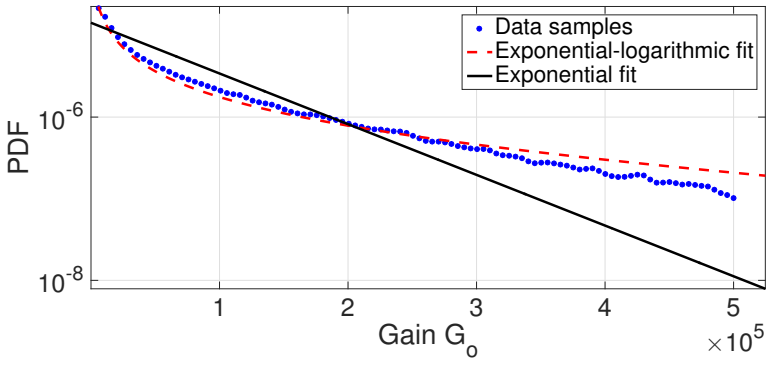

Figure 5.5: Fitting of the aligned gain $G_o^{(3GPP)}$ with the 3GPP element pattern. The empirical PDF of $G_o^{(3GPP)}$ fits with the *exponential-logarithmic* distribution in Remark 2. It no longer fits with an exponential distribution, as opposed to the ISO element pattern's ($n_{RX} = 64$, $n_{TX} = 256$).

Table 5.2: Aligned gain's *exponential-logarithmic* distribution parameters (b_o, p_o) with the 3GPP element pattern for different n_{TX} and n_{RX}. The table is symmetric, so we hereafter report only the upper triangular part.

(b_o, p_o)		n_{TX}			
		4	**16**	**64**	**256**
n_{RX}	**4**	(0.002, 0.112)	(4e-4, 0.075)	(0.0001, 0.0713)	(7.84e-5, 0.15)
	16	–	(2e-4, 0.15)	(8.24e-5, 0.511)	(1.93e-5, 0.1223)
	64	–	–	(1.84e-5, 0.15)	(4.83e-6, 0.089)
	256	–	–	–	(1.96e-6, 0.1126)

Exponential-logarithmic distributions are often used in the field of reliability engineering, particularly for describing the lifetime of a device with a decreasing failure rate over time [146]. Its tail is lighter than that of the exponential distribution, which is explained by the 3GPP element pattern's high directivity and side lobe attenuation that mostly yield a higher aligned gain than the ISO element pattern's aligned gain.

An exponential-logarithmic distribution is determined by using two parameters b_o and p_o, as opposed to the ISO element pattern's exponential distribution with a single parameter μ_o. Precisely, the distribution is given by a random variable that is the minimum of N independent realizations from $\text{Exp}(b_o)$, while N is a realization from a logarithmic distribution with parameter $1 - p_o$. Due to its generation procedure, the relationship between the two parameters and the number of antenna elements is not representable with a simple function in a way to be generalized as done in Remark 1 for the ISO element pattern. In particular, due to the extreme characteristics of the gain, even a small variation in the well-fitted parameters yields a significant change in the fitting accuracy. For this reason, obtaining a good-fit of the parameters that can be generalized requires an exhaustive search, with an extremely large number of combinations. Therefore, for 16 practically possible combinations of n_{TX} and n_{RX}, the appropriate values of b_o and p_o are provided in Table 5.2 by curve-fitting

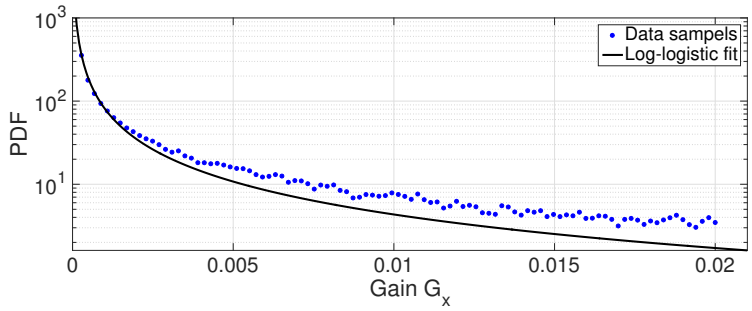

Figure 5.6: Fitting of the aligned gain $G_x^{(\mathsf{ISO})}$ with the ISO element pattern. The empirical PDF of $G_x^{(\mathsf{ISO})}$ is obtained by the NYU mmWave network simulator [142], and is fit with the *log-logistic* distribution in Remark 3 ($n_{\mathrm{RX}} = 64$, $n_{\mathrm{TX}} = 256$).

of the system-level simulation results.

5.3.2 Misaligned Gain Distribution

Following the same procedure as used for the aligned gain with the NYU simulator, we extract the distribution of the misaligned gain $G_x^{(z)}$ under the ISO and 3GPP element patterns. With the ISO element pattern, we found that the $G_x^{(\mathsf{ISO})}$ PDF displayed in Figure 5.6 has a steep decreasing slope in the vicinity of zero, while showing a heavier tail than the exponential distribution. This implies that the occurrence of strong interference is not frequent thanks to the sharpened main lobe beams, yet is still non-negligible due to the interference from side lobes that include the backward propagation. We examined possible distributions satisfying the aforementioned two characteristics, and conclude that a *log-logistic* distribution provides the most accurate fitting result with the simulated misaligned gain.

Remark 3 *(Misaligned Gain, ISO)* At the typical UE, and using ISO antenna elements, the misaligned gain $G_x^{(\mathsf{ISO})}$ can be approximated by a *log-logistic* distribution with PDF

$$f_{G_x}^{(\mathsf{ISO})}(y; a, b) = \frac{\left(\frac{b}{a}\right)\left(\frac{y}{a}\right)^{b-1}}{\left(1 + \left(\frac{y}{a}\right)^{b}\right)^{2}} \tag{5.12}$$

where the values of a and b are provided in Table 5.3.

A log-logistic distribution is given by a random variable whose logarithm has a logistic distribution. The shape is similar to a log-normal distribution, but has a heavier tail [147]. For a similar reason addressed after Remark 2, a log-logistic distribution is determined by two parameters a and b, and their relationship with the number of antenna elements is difficult to generalize. We instead report the appropriate values of a and b for 16 combinations of n_{TX} and n_{RX} in Table 5.3.

Table 5.3: Misaligned gain's *log-logistic* distribution parameters (a, b) with the ISO element patterns for different n_{TX} and n_{RX}.

(a,b)		n_{TX}			
		4	**16**	**64**	**256**
n_{RX}	**4**	$(3.28, 0.877)$	$(2.51, 0.743)$	$(2.11, 0.722)$	$(1.92, 0.709)$
	16	–	$(3.49, 0.656)$	$(3.28, 0.612)$	$(2.89, 0.589)$
	64	–	–	$(2.55, 0.57)$	$(1.98, 0.551)$
	256	–	–	–	$(1.45, 0.547)$

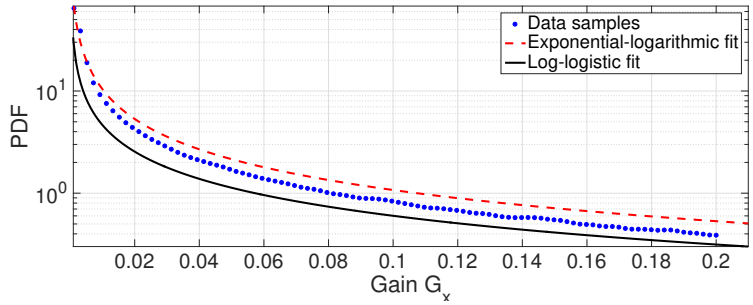

Figure 5.7: Fitting of the aligned gain $G_x^{(\mathsf{3GPP})}$ with the 3GPP element pattern. The empirical PDF of $G_x^{(\mathsf{3GPP})}$ fits with the *exponential-logarithmic* distribution in Remark 4. It no longer fits with a log-logistic distribution, as opposed to the ISO element pattern's ($n_{\mathrm{RX}} = 64$, $n_{\mathrm{TX}} = 256$).

Next, with the 3GPP element pattern, we identified the $G_x^{(\mathsf{3GPP})}$ PDF in Figure 5.7. Using the simulated data samples we have performed a test on the decay of the tail in order to understand if the behavior was heavy tailed. It turns out that the PDF of $G_x^{(\mathsf{3GPP})}$ has a lighter tail than the exponential distribution, which is far different from the heavy-tailed $G_x^{(\mathsf{ISO})}$ distribution. In this case, we found that the misaligned gain $G_x^{(\mathsf{3GPP})}$ fits well an exponential-logarithmic distribution, as also used for the aligned gain $G_o^{(\mathsf{3GPP})}$ in Remark 2.

Remark 4 *(Misaligned Gain, 3GPP)* At the typical UE, and adopting the 3GPP element pattern, the misaligned gain $G_x^{(\mathsf{3GPP})}$ can be approximated by an *exponential-logarithmic* distribution with PDF

$$f_{G_x}^{(\mathsf{3GPP})}(y; b_x, p_x) = \frac{1}{-\ln(p_x)} \frac{b_x(1 - p_x e^{-b_x y})}{1 - (1 - p_x)e^{-b_x y}} \tag{5.13}$$

where the values of parameters b_x and p_x are provided in Table 5.4.

Although both $G_o^{(\mathsf{3GPP})}$ and $G_x^{(\mathsf{3GPP})}$ can be described by using exponential-logarithmic distributions, these two results come from different reasons, respectively. For $G_o^{(\mathsf{3GPP})}$, it follows from the higher main lobe gains than under the ISO element pattern that yields the exponentially distributed $G_o^{(\mathsf{ISO})}$. For $G_x^{(\mathsf{3GPP})}$, on the contrary, its light-tailed distribution originates from attenuating side lobes, reducing the interfering probability. For these distinct reasons, the distribution parameters (b_o, p_o) for $G_o^{(\mathsf{3GPP})}$ and (b_x, p_x) for $G_x^{(\mathsf{3GPP})}$ are different,

Table 5.4: Misaligned gain's *exponential-logarithmic* distribution parameters (b_x, p_x) with the 3GPP element patterns for different n_{TX} and n_{RX}.

(b_x, p_x)		n_{TX}			
		4	**16**	**64**	**256**
n_{RX}	**4**	(4.428, 4.3e-5)	(0.7967, 3.7e-5)	(0.288, 6.8e-5)	(1.2e-04, 1.5e-9)
	16	–	(0.2873, 6.5e-5)	(0.024, 3.6e-5)	(0.075, 7.4e-7)
	64	–	–	(0.2316, 1.5e-4)	(0.0133, 2.34e-5)
	256	–	–	–	(0.2406, 2.7e-4)

Table 5.5: Minimized RMSE for aligned and misaligned gains under different fitting distributions (for the case when the fitted distribution shape was unable to match the data, we marked it as avoid).

Distribution Type	**Minimized RMSE** G_o	G_x
Exponential	1.99e-6	7.46
Exponential-logarithmic	**4.11e-7**	**0.51**
Burr	4.26e-6	1.74
Log-logistic	–	1.63
Log-normal	–	–
Log-Cauchy	–	0.56
Gamma	–	0.80
Weibull	4.27e-6	0.63
Rayleigh	–	–
Nakagami	–	1.04
Lévi	–	1.73

as shown in Table 5.2 and Table 5.4. Moreover, we note that in order to precisely fit both the distributions for the 3GPP case, due to the particular behavior of both tail and slope parts we have studied several well known distributions. We have evaluated the accuracy by measuring the Root Mean Square Error (RMSE) and obtained Table 5.5. By evaluating the RMSE, we have concluded that the exponential-logarithmic distribution was the most accurate distribution, among the ones evaluated, for both $G_o^{(\mathsf{3GPP})}$ and $G_x^{(\mathsf{3GPP})}$.

The fitting plots of both aligned and misaligned gains, respectively Figures 5.3–5.5 and Figures 5.6–5.7, permit to see the approximation error which is introduced due to the fitting procedure. However, we note that we are plotting the curves using a log-scale for the y-axis, thus when the PDF becomes smaller even if the error gap looks bigger, the real error may be smaller.

Note that $G_x^{(\mathsf{ISO})}$ is often considered as a *Nakagami-m* or a *log-normal* distributed random variable [91, 133, 134]. In Section 5.5, we will thus compare our proposed distributions for $G_x^{(z)}$ with them. For a fair comparison, for a Nakagami-m distribution with $n_{\mathrm{TX}} = 256$ and $n_{\mathrm{RX}} = 64$, we will use its best-fit distribution parameters obtained by curve-fitting with the

system-level simulation, which are given with the PDF as follows

$$f_{G_x}^{(\mathsf{ISO})}(y;m,g)=\frac{2m^m}{\Gamma(m)g^m}y^{2m-1}\exp\left(-\frac{m}{g}y^2\right),\begin{cases}m=0.099\\ g=50.53\end{cases} \tag{5.14}$$

With this PDF, we will observe in Section 5.5 that a Nakagami-m distribution underestimates the tail behavior of $G_x^{(\mathsf{ISO})}$ too much, thereby leading to a loose empirical upper bound for the SINR coverage probability.

Likewise, for a log-normal distribution with $n_{\mathrm{TX}}=256$ and $n_{\mathrm{RX}}=64$, we will consider the following PDF with the parameters

$$f_{G_x}^{(\mathsf{ISO})}(y;\sigma,\mu)=\tfrac{1}{y\sigma\sqrt{2\pi}}\exp\left(-\tfrac{(\log y-\mu)^2}{2\sigma^2}\right),\qquad\begin{cases}\sigma=2.962\\ \mu=0.908\end{cases} \tag{5.15}$$

Under the ISO element pattern, it will be shown in Section 5.5 that a log-normal distribution is a better fit than a Nakagami-m distribution, yet it still underestimates the interference, yielding an empirical upper bound to the SINR coverage probability.

As an auxiliary result, we will also provide the result with a *Burr* distribution [148]. This overestimates the tail behavior of $G_x^{(\mathsf{ISO})}$, leading to the empirical lower bound of the SINR coverage probability. For this, we will consider the following PDF under $n_{\mathrm{TX}}=256$ and $n_{\mathrm{RX}}=64$

$$f_{G_x}^{(\mathsf{ISO})}(y;c,k)=\tfrac{cky^{c-1}}{(1+y^c)^{k+1}},\qquad\begin{cases}c=0.692\\ k=0.518\end{cases} \tag{5.16}$$

5.4 mmWave SINR Coverage Probability

In this section, we aim at deriving the closed-form expression of the SINR coverage probability $C_{\mathrm{SINR}}(T)$, defined as the probability that the typical UE's SINR is no smaller than a target SINR threshold $T>0$, i.e., $C_{\mathrm{SINR}}(T):=\Pr(\mathrm{SINR}\geq T)$. In the first subsection, utilizing the aligned/misaligned gains provided in Section 5.3, we derive the exact SINR coverage expressions under ISO and 3GPP element patterns. In the following subsection, applying a first-moment approximation to aligned/misaligned gains, we further simplify the SINR coverage expressions.

5.4.1 SINR Coverage

Let $r^i_{x_o}$ denote the association distance of the typical UE associating with $x_o \in \Phi_i$. By using the law of total probability, C_{SINR} at the typical UE can be represented as

$$C_{\text{SINR}}(T) = \Pr\big(\underbrace{\text{SINR} \geq T, x_o \in \Phi_L}_{\text{SINR}_L \geq T}\big) + \Pr\big(\underbrace{\text{SINR} \geq T, x_o \in \Phi_N}_{\text{SINR}_N \geq T}\big) \tag{5.17}$$

$$= \mathbf{E}_{r^L_{x_0}}\left[\Pr\left(\text{SINR}_L \geq T | r^L_{x_o}\right)\right] + \mathbf{E}_{r^N_{x_o}}\left[\Pr\left(\text{SINR}_N \geq T | r^N_{x_o}\right)\right] \tag{5.18}$$

In (5.18), two expectations are taken over the typical UE's association distance $r^i_{x_o}$. The PDF of $r^i_{x_o}$ is given by [35] as

$$f_{r^i_{x_o}}(r) := f_{|x_o|,i}(r, x_o \in \Phi_i) \tag{5.19}$$

$$= 2\pi\lambda_i(r) r \exp\left(-2\pi\lambda_b\left[\int_0^r v p_i(v)\mathrm{d}v + \int_0^{(r^{\alpha_i}\beta_{i'}/\beta_i)^{\frac{1}{\alpha_{i'}}}} v p_{i'}(v)\mathrm{d}v\right]\right) \tag{5.20}$$

where $\lambda_i(r) = \lambda_b p_i(r)$, and i' indicates the opposite LoS/NLoS state with respect to i.

For the ISO element pattern, the typical UE's SINR coverage probability $C_{\text{SINR}}(T)$ in (5.18) is then derived by exploiting $f_{r^i_{x_o}}(r)$ while applying Campbell's theorem [145] and the $G_o^{(\mathsf{ISO})}$ distribution in Remark 1.

Proposition 1 *(Coverage, ISO)* At the typical UE, and considering arrays with ISO radiation elements, the SINR coverage probability $C_{\text{SINR}}(T)$ for a target SINR threshold $T > 0$ is given as

$$C_{\text{SINR}}(T) = \sum_{i\in\{L,N\}} \int_0^\infty f_{r_{x_o^i}}(r) \exp\left(\frac{-\mu_o T r^{\alpha_i}\sigma^2}{\beta_i}\right) \mathcal{L}_{I_i^L}\left(\frac{\mu_o T}{\ell^i(r)}\right) \mathcal{L}_{I_i^N}\left(\frac{\mu_o T}{\ell^i(r)}\right) \mathrm{d}r \tag{5.21}$$

where $\mathcal{L}_{I_i^j}(r)$ is the Laplace transform of the interference from gNBs $\in \phi_j$, for $j \in \{L, N\}$, to the typical UE and is given in (5.22) with $z = \mathsf{ISO}$ at the bottom of this page.

Sketch of the Proof: Starting from the SINR joint probability in (5.18) and applying the SINR definition we obtain an expression which depends on the Complementary Cumulative Distribution Function (CCDF) $F^{(\mathsf{ISO})}_{G_o}(y;\mu_o)$. Then, applying Remark 1, which provides a channel gain expression with specific distribution, together with Slyvnyak's theorem and the

---

$$\mathcal{L}_{I_i^j}(r) = \exp\left(-2\pi\lambda_b \int_0^\infty \left(\int_{\left(\frac{\beta_j r^{\alpha_i}}{\beta_i}\right)^{\frac{1}{\alpha_j}}}^\infty \left[1 - \exp\left(-\frac{\ell^j(v)\mu_o T g}{\ell^i(r)}\right)\right] v p_j(v)\mathrm{d}v\right) f^{(z)}_{G_x}(g)\mathrm{d}g\right) \tag{5.22}$$

mutual independence of PPPs Φ_i^L and Φ_i^N we obtain the final coverage expression. The detailed proof is provided in Appendix A.1. ■

Note that $1/\mu_o$ is the mean aligned gain in Remark 1. The misaligned gain PDF $f_{G_x}^{(\mathsf{ISO})}(y)$ and its corresponding parameters are provided in Remarks 3 and 4 as well as in Table 5.3. As opposed to the standard method where the exponential random variables can be found in both desired and interfering links, the misalignment gain in our interfering link follows a log-logistic distribution. This does not allow to further expand the expression as done in the standard method, yet the expression can easily be calculated numerically as done in [141], which is far simpler than the system-level simulation complexity. Then, the term p_i is the LoS/NLoS channel state probability defined in Section 5.2.2.

For the 3GPP element pattern, following the same procedure and $G_o^{(\mathsf{3GPP})}$ distribution in Remark 2, we obtain $C_{\mathrm{SINR}}(T)$ as shown in the following proposition.

Proposition 2 *(Coverage, 3GPP)* At the typical UE, and considering arrays with 3GPP radiation elements, the SINR coverage probability $C_{\mathrm{SINR}}(T)$ for a target SINR threshold $T > 0$ is upper bounded as

$$C_{\mathrm{SINR}}(T) \leq \sum_{i\in\{L,N\}} \int_0^\infty \frac{f_{r_{x_o^i}}(r)}{\ln(p_o)} \ln\left(1-(1-p_o)\exp\left(\frac{-b_o T r^{\alpha_i}\sigma^2}{\beta_i}\right)\right. \\ \left.\mathcal{L}_{I_i^L}\left(\frac{b_o T}{\ell^i(r)}\right)\mathcal{L}_{I_i^N}\left(\frac{b_o T}{\ell^i(r)}\right)\right)\mathrm{d}r \tag{5.23}$$

where the Laplace transform $\mathcal{L}_{I_i^j}(r)$ for $j \in \{L, N\}$ is given as before in (5.22) with $z = \mathsf{3GPP}$.
Sketch of the Proof: The first step of the demonstration is equivalent to the one in Proposition 1 with the only difference that $G_o^{(\mathsf{3GPP})}$ follows an exponential-logarithmic distribution with the CCDF $F(y; b_o, p_o) = \ln\left(1-(1-p_o)\,e^{-b_o y}\right)/\ln p_o$. Then, differently from the previous proposition, Jensen's inequality is used to obtain an upper bound of the SINR coverage probability. The remainder of the proof follows the Proof of Proposition 1. For completeness, the detailed derivation is provided in Appendix A.2. ■

It is worth noting that the Laplace transform expression in (5.22) is used for both ISO and 3GPP element patterns, i.e., in Propositions 1 and 2. Here, the element pattern is differentiated only by the distribution of the misaligned gain $f_{G_x}^{(z)}(g)$ contained therein. For different element patterns and their fitting results, we can thus change $f_{G_x}^{(z)}(g)$ accordingly while keeping the rest of the terms, thereby allowing us to quickly compare the resulting SINRs. This is an advantage of the analysis, that avoids redundant calculations. Similarly, we can substitute the distribution of $f_{G_x}^{(\mathsf{ISO})}(g)$ from log-logistic to Burr or log-normal (equations (5.16) and (5.15), respectively) to obtain a lower or upper bound of the SINR coverage probability assuming ISO antenna elements.

5.4.2 Simplified SINR Coverage

In this subsection, our goal is to further simplify the SINR coverage probability expressions in Propositions 1 and 2. To this end, we revisit a channel-antenna gain approximation approach that is commonly used with stochastic geometric analysis, as done in [35, 91, 133–137]. This approach relies on approximating the channel gain based on its first-moment value, and may therefore be less accurate compared to the simulated result.

Nevertheless, with a slight refinement, we conjecture that such a simple approach can still provide a tight approximation, also for the 3GPP element pattern. In fact, the only major difference, with respect to the ISO case is the presence of a high front-back ratio, which in turn is due to the directivity gain considered. With this purpose in mind, we elaborate the approximation procedures of the channel and antenna gains as follows. For the channel gain, instead of directly using the realistic channel model, we consider a first-order approximated Rayleigh fading channel with the mean value that is identically set as that of the realistic channel model. For the antenna gain, as illustrated in Figure 5.2b, we approximate the continuous array gain using only two constants, i.e., main lobe gain $M_s^{(z)}$ and side lobe gain $m_s^{(z)}$. The mean aligned gain $\Upsilon_o^{(z)}$ and the mean misaligned gain $\Upsilon_x^{(z)}$ are determined by these two antenna gain constants that are specified by the ISO and 3GPP element patterns, as detailed in the following remark.

Remark 5 *(Simplified Aligned/Misaligned Gains)* For a given antenna array radiation pattern $z \in \{\mathsf{ISO}, \mathsf{3GPP}\}$, we consider the following channel and array radiation approximations.

- *Rayleigh fading channel gain* – Both the aligned gain $G_o^{(z)}$ and the misaligned gain $G_x^{(z)}$ at the typical UE independently follow an *exponential* distribution, i.e.,

$$G_o^{(z)} \sim \mathsf{Exp}(1/\Upsilon_o^{(z)}) \quad \text{and} \quad G_x^{(z)} \sim \mathsf{Exp}(1/\Upsilon_x^{(z)}) \tag{5.24}$$

- *Piece-wise constant array gain* – The average channel gains $\Upsilon_o^{(z)}$ and $\Upsilon_x^{(z)}$, taken from [91], are given as

$$\Upsilon_o^{(z)} = \quad M_{\mathrm{TX}}^{(z)} M_{\mathrm{RX}}^{(z)} \quad \text{and} \tag{5.25}$$

$$\Upsilon_x^{(z)} = \begin{cases} M_{\mathrm{TX}}^{(z)} M_{\mathrm{RX}}^{(z)} & \text{w.p.} \quad \frac{\varphi_{\mathrm{TX}}}{2\pi} \frac{\varphi_{\mathrm{RX}}}{2\pi} \\ M_{\mathrm{TX}}^{(z)} m_{\mathrm{RX}}^{(z)} & \text{w.p.} \quad \frac{\varphi_{\mathrm{TX}}}{2\pi} (1 - \frac{\varphi_{\mathrm{RX}}}{2\pi}) \\ m_{\mathrm{TX}}^{(z)} M_{\mathrm{RX}}^{(z)} & \text{w.p.} \quad (1 - \frac{\varphi_{\mathrm{TX}}}{2\pi}) \frac{\varphi_{\mathrm{RX}}}{2\pi} \\ m_{\mathrm{TX}}^{(z)} m_{\mathrm{RX}}^{(z)} & \text{w.p.} \quad (1 - \frac{\varphi_{\mathrm{TX}}}{2\pi})(1 - \frac{\varphi_{\mathrm{RX}}}{2\pi}) \end{cases} \tag{5.26}$$

where the main lobe gain $M_s^{(z)}$ and the side lobe gain $m_s^{(z)}$ are set as

$$M_s^{(\mathsf{ISO})} = n_s \tag{5.27}$$

$$M_s^{(\mathsf{3GPP})} = 10^{0.8} n_s \tag{5.28}$$

$$m_s^{(z)} = 1/\sin^2\left(\frac{3\pi}{2\sqrt{n_s}}\right) \tag{5.29}$$

and n_s with $s \in \{\mathrm{TX}, \mathrm{RX}\}$ denotes the number of the transmit/receive antenna elements.

With the ISO element pattern, it is noted that the said simplified model becomes identical to the model considered in [35]. In this case, the side lobe gain $m_s^{(z)}$ in (5.29) is obtained from the array's 3 dB beamwidth[4] that equals $\sqrt{3/n_s}$.

With the 3GPP element pattern, by constrast, the main lobe gain in (5.28) is $10^{0.8} \approx 6.31$ times higher than in the ISO radiation case, due to its maximum 8 dBi directivity gain at each antenna element as discussed in Sections 4.2.1 and 5.2.1. The side lobe gain in (5.29) is computed in the same manner for both ISO and 3GPP element patterns, yet has the different physical meanings for each case as detailed next.

Following [35], the side lobe gain in (5.29) with the ISO element pattern corresponds to the *second maximum* lobe gain, as shown in Figure 5.8. On the contrary, (5.29) with the 3GPP element pattern is mostly below the second maximum lobe gain. This implicitly captures the 3GPP element pattern's side lobe reduction as shown in Figure 5.8.

Unlike the ISO element pattern, it is noted that (5.29) with the 3GPP element pattern approximates the *third maximum* lobe gain on average, but is not always identical to the third maximum value. In fact, due to the element-wise beam steering, the antenna gain under the 3GPP element pattern is not symmetrical about the steering angle, so each lobe's gain can only be ordered for a given steering angle, as further explained in [50].

Finally, utilizing the aligned and misaligned gains in Remark 5, we obtain the simplified SINR coverage probability.

Proposition 3 *(Simplified Coverage)* Using the simplified aligned and misaligned gains in Remark 5, the simplified SINR coverage probability $\hat{C}_{\mathrm{SINR}}(T)$ at the typical UE with a target SINR threshold $T > 0$ is given by

$$\begin{aligned}\hat{C}_{\mathrm{SINR}}(T) = \sum_{i\in\{L,\,N\}} \int_0^\infty f_{r_{x_o^i}}(r) \exp\left(-\frac{T r^{\alpha_i}\sigma^2}{\beta_i M_{TX}^{(z)} M_{RX}^{(z)}}\right) \\ \times \hat{\mathcal{L}}_{I_i^L}\left(\frac{T(\ell^i(r))^{-1}}{M_{TX}^{(z)} M_{RX}^{(z)}}\right) \hat{\mathcal{L}}_{I_i^N}\left(\frac{T(\ell^i(r))^{-1}}{M_{TX}^{(z)} M_{RX}^{(z)}}\right) \mathrm{d}r\end{aligned} \tag{5.30}$$

[4]Note that the previously defined $\theta_{3\mathrm{dB}}$ and $\phi_{3\mathrm{dB}}$ parameters were determined by the 3 dB beamwidth of the element radiation pattern, whereas φ_s is given by the 3 dB beamwidth of the array radiation pattern.

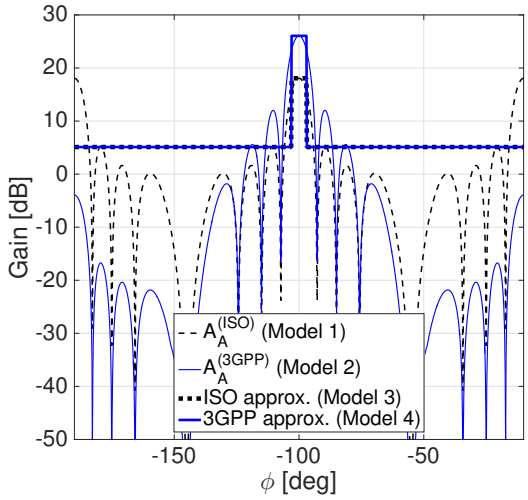

Figure 5.8: Comparison between the array radiation gains with the ISO and 3GPP element patterns and their piece-wise constant approximated gains given in Remark 5, with respect to the horizontal steering angle $\phi \in [-180°, 180°]$ while the vertical steering angle θ is fixed at 90°.

where $\hat{\mathcal{L}}_{I_i^j}(t)$ *is given in* (5.31).

Proof: See Theorem 1 in [35]. ■

In the next section, we will validate that this simplified SINR coverage expression becomes accurate for the 3GPP element pattern, as conjectured at the beginning of this subsection.

$$\hat{\mathcal{L}}_{I_i^j}(s) = \exp\Bigg(-2\pi\lambda_b \int_{\left(\frac{\beta_j}{\beta_i} r^{\alpha_i}\right)^{\frac{1}{\alpha_j}}}^{\infty} \Bigg[\frac{\varphi_{\mathrm{TX}}\varphi_{\mathrm{RX}}}{4\pi^2} F\left(M_{\mathrm{TX}}^{(z)} M_{\mathrm{RX}}^{(z)}\right) + \frac{\varphi_{\mathrm{TX}}}{2\pi}\left(1 - \frac{\varphi_{\mathrm{RX}}}{2\pi}\right) F\left(M_{\mathrm{TX}}^{(z)} m_{\mathrm{RX}}^{(z)}\right) + \left(1 - \frac{\varphi_{\mathrm{TX}}}{2\pi}\right)\frac{\varphi_{\mathrm{RX}}}{2\pi} F\left(m_{\mathrm{TX}}^{(z)} M_{\mathrm{RX}}^{(z)}\right) + \left(1 - \frac{\varphi_{\mathrm{TX}}}{2\pi}\right)\left(1 - \frac{\varphi_{\mathrm{RX}}}{2\pi}\right) F\left(m_{\mathrm{TX}}^{(z)} m_{\mathrm{RX}}^{(z)}\right) \Bigg] v p_j(v) \mathrm{d}v \Bigg) \tag{5.31}$$

where $F(x) = sxv^{-\alpha_i}\beta_i/(1 + sxv^{-\alpha_i}\beta_i)$.

Table 5.6: List of the channel-antenna configurations considered in Section 5.5.

Configuration	**Channel**	**Element radiation**	**Array radiation**
Model 1 [84]	NYU [21]	ISO	continuous main/side lobes
Model 2	NYU [21]	3GPP [90]	continuous main/side lobes with smaller side lobe radiations
Model 3 [35]	Rayleigh	–	piece-wise constant main/side lobes ($M^{(\mathsf{ISO})}$ or $m^{(\mathsf{ISO})}$)
Model 4	Rayleigh	–	piece-wise constant main/side lobes ($M^{(\mathsf{3GPP})}$ or $m^{(\mathsf{3GPP})}$)

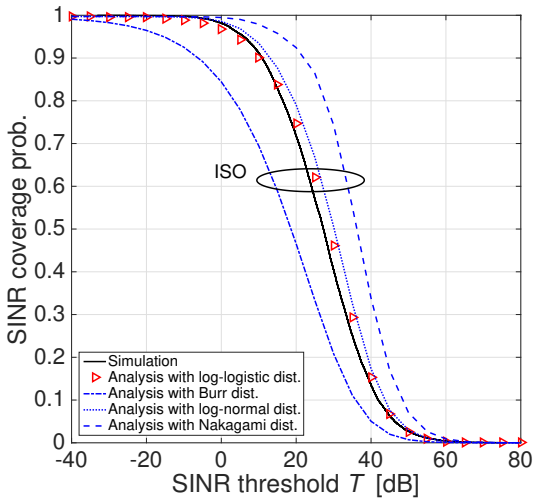

Figure 5.9: SINR coverage probability with the ISO element pattern under Model 1 for different misaligned gain fitting distributions: (i) the *log-logistic* distribution in Remark 3, (ii) the *Nakagami-m* distribution in (5.14), (iii) the *log-normal* distribution in (5.15), and (iv) the *Burr* distribution in (5.16). The aligned gain is fitted with the *exponential* distribution in Remark 1, and $\{n_{\mathrm{TX}}, n_{\mathrm{RX}}\} = \{256, 64\}$.

5.5 Comparisons of Coverage Evaluation in Cellular Scenarios

5.5.1 Numerical Results

In this section, by using the NYU mmWave network simulator [142], we validate our analytical mmWave SINR coverage expressions with the ISO element pattern in Proposition 1 and the expression with the 3GPP element pattern in Proposition 2, as well as their simplified SINR coverage expressions proposed in Proposition 3. For easier comparison, the channel-antenna configurations considered in this section are categorized as four models as summarized in Table 5.6. The antenna configurations are illustrated in Figure 5.8, and the channel configurations are detailed in Section 5.2.2 and Remark 5. Other simulation parameters are: carrier frequency $f = 28$ GHz, bandwidth $W = 500$ MHz, gNB density $\lambda_b = 100$ gNBs/km^2 and transmission power $P_{\mathrm{TX}} = 30$ dBm.

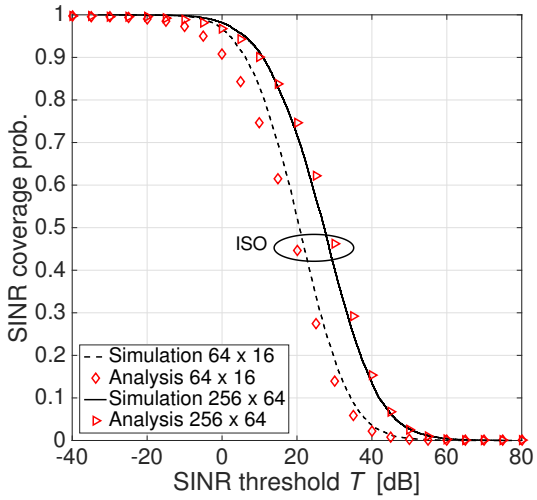

Figure 5.10: SINR coverage probability with the ISO element pattern under Model 1. The aligned gain is fit with the *exponential* distribution in Remark 1, and the misaligned gain is fitted with the *log-logistic* distribution in Remark 3, for $\{n_{\mathrm{TX}}, n_{\mathrm{RX}}\} = \{64, 16\}$ and $\{256, 64\}$.

Figures 5.9 and 5.10 show the SINR coverage probability with the ISO element pattern under Model 1. In Figure 5.9, the coverage probability obtained from the NYU network simulator fits well our proposed coverage expression in Proposition 1 that utilizes the aligned gain's *exponential* distribution in Remark 1 and the misaligned gain's *log-logistic* distribution in Remark 3. The proposed SINR coverage probability expression is also compared to the SINR coverage probabilities with the misaligned gain's *Nakagami-m* and *log-normal* distributions that are commonly used in stochastic geometric mmWave SINR coverage analysis [91, 133, 134]. It shows that both Nakagami-m and log-normal distributions given respectively in (5.14) and (5.15) underestimate the interference tail behaviors, therefore yielding empirical upper bounds for the SINR coverage probability. Another misaligned gain's *Burr* distribution given in (5.16) by contrast yields an empirical lower bound for the SINR coverage probability. All these bounds are too loose to approximate the simulated SINR coverage probability, emphasizing our appropriate choice of the misaligned gain's log-logistic distribution.

Figure 5.10, by comparing the curves with the antenna element configuration $\{n_{\mathrm{TX}}, n_{\mathrm{RX}}\} = \{64, 16\}$ and the curves with $\{n_{\mathrm{TX}}, n_{\mathrm{RX}}\} = \{256, 64\}$, shows that the increase in the number of antenna elements not only yields a higher SINR but also makes the SINR coverage probability expression in Proposition 1 more accurate. The latter is because the front-back ratio increases with the number of antenna elements [50, 79]. Following a similar reasoning as discussed after Remarks 2 and 4, this reduces the impact of the high-order statistics on the alignment and misaligned gains, and thereby Proposition 1 becomes more accurate.

Next, Figure 5.11 illustrates the SINR coverage probability with the 3GPP element pattern under Model 2. We observe that the simulated coverage probability fits well with our

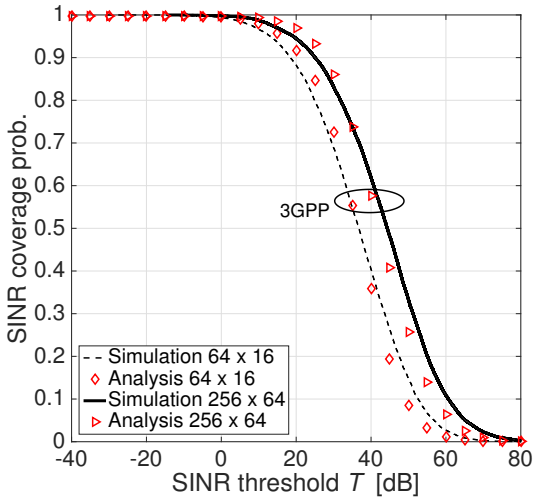

Figure 5.11: SINR coverage probability with the 3GPP element pattern under Model 2. The aligned and misaligned gains are fit independently with the *exponential-logarithmic* distributions in Remarks 2 and 4, respectively, for $\{n_{\mathrm{TX}}, n_{\mathrm{RX}}\} = \{64, 16\}$ and $\{256, 64\}$.

proposed coverage expression in Proposition 1 that utilizes the *exponential-logarithmic distributions* of aligned and misaligned gains in Remarks 2 and 4, respectively. As seen by comparing Figure 5.11 to Figure 5.10, the SINR coverage probability with the 3GPP element pattern is higher than the coverage probability with the ISO element pattern. This is because of the 3GPP element pattern's higher front-back ratio that provides higher directivity, thereby increasing the aligned gain. It also provides lower interference that decreases the misaligned gain, consequently yielding a higher SINR. These results highlight the presence of different performance trends as the network's density increases. This means that it is possible to accurately identify an optimal deployment density of the gNBs. We have further studied this aspect in [50].

Finally, Figure 5.12 illustrates the simplified SINR coverage probability expressions provided in Proposition 3 under Models 3 and 4 that are specified in Remark 5. As conjectured at the beginning of Section 5.4.2, the simplified SINR coverage probability expressions become more accurate approximations for the 3GPP element pattern than for the ISO element pattern. Precisely, the maximum difference between the simulated and the analytic SINR coverage probabilities are obtained as 7.7% with the 3GPP element pattern and as 9.5% with the ISO element pattern in Figure 5.12b. This originates from both aligned and misaligned gains' identical tail behaviors that follow an exponential-logarithmic distribution. These high-order behaviors are thus canceled out during the SINR calculation, and the first-order statistics thereby becomes dominant, from which the first-moment approximation used in the simplified SINR coverage expressions benefit. On the contrary, with ISO element pattern, the aligned gain and misaligned gains have different tail behaviors as

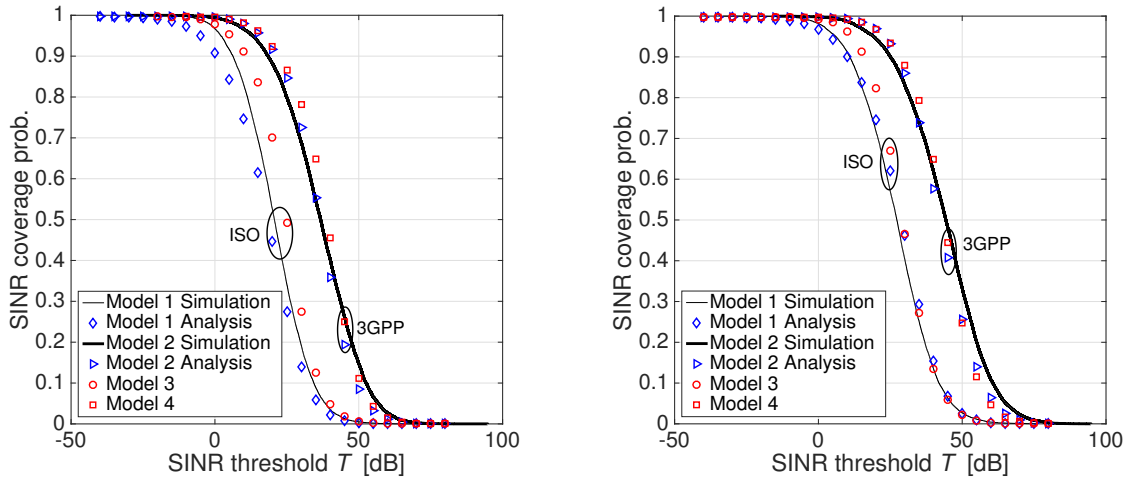

(a) For $\{n_{\mathrm{TX}}, n_{\mathrm{RX}}\} = \{64, 16\}$. **(b)** For $\{n_{\mathrm{TX}}, n_{\mathrm{RX}}\} = \{256, 64\}$.

Figure 5.12: Comparison between the SINR coverage probability expressions under Models 1 and 2 and their simplified expressions under Models 3 and 4. The simulated curves are obtained only under Models 1 and 2 without simplifying the channel-antenna configurations.

provided in Remarks 1 and 3, and the corresponding simplified SINR coverage probability expression therefore becomes less accurate.

Moreover, the figure describes the benefit of the non-simplified SINR coverage probability expressions provided in Propositions 1 and 2 respectively under Models 1 and 2. In contrast to the simplified expressions that are plausible only with the 3GPP element pattern, the non-simplified SINR coverage probability expressions well approximate the simulated SINR coverage probabilities with both 3GPP and ISO element patterns, so long as the number of antenna elements is sufficiently large, as seen by comparing Figures 5.12a and 5.12b. In addition, with a slight increase in complexity, these non-simplified SINR coverage probability expressions are more accurate than the simplified expressions, and so are appropriate for investigating ultra-reliable scenarios as considered in [129, 149–151], which prefer to maximize accuracy rather than improving analytical tractability. It is also noted again that the simplified aligned and misaligned gains in Remark 5 are only applicable for the SINR calculation. Thus, the non-simplified aligned and misaligned gains in Remarks 1-4 are still useful, for instance when deriving the mmWave interference distribution [4] or calculating the mmWave SNR under a noise-limited regime [4, 95].

5.5.2 Final Remarks and Open Challenges

In this study we have highlighted the impact of realistic mmWave channel behaviors and element patterns on the downlink SINR coverage probability in a large-scale mmWave network, via the NYU mmWave simulator [142] under the 3GPP element pattern model [92]. By introducing the aligned and misaligned gains, we have provided an analytical model

that captures such realistic channel-antenna gain characteristics, thereby deriving the SINR coverage probability expressions.

Especially for the 3GPP element pattern, arguably the most practical antenna configuration, we proposed a further simplified SINR coverage probability expression. This relies only on the exponentially distributed aligned and misaligned gains, which are known to be the simplest random variables for deriving the SINR coverage probability expressions.

With a slight increase in complexity, we have also provided non-simplified SINR coverage probability expressions as well as the corresponding aligned and misaligned gain distributions. These analytic expressions are versatile, and thus are expected to be exploited in more generic scenarios that particularly necessitate a higher accuracy, which could be an interesting topic for further research. Furthermore, with the proposed analytic framework, an extension of this work could be to investigate other mmWave network settings such as different carrier frequencies, channel/antenna models, and an uplink scenario. Besides, beyond the specific examples treated in the research activity, our proposed methodology approach can be applied to study other cases.

5.6 Coverage Evaluation in Vehicular Scenario

In addition to the cellular coverage evaluation, we develop a tractable framework based on stochastic geometry to evaluate both the coverage and the connectivity performance of an automotive node in a dynamic mmWave vehicular environment, based on a realistic measurement-based distance-dependent path loss model. In particular, this is the first contribution in which an analytical expression for the beam alignment probability and connection stability (i.e., the probability that the vehicle does not disconnect from its serving infrastructure over time) is evaluated considering a dynamic scenario.

With this studied framework we are able to show that an optimal value of throughput can be associated with a threshold for the density of base stations, above which the deployment of more gNBs results in a considerable increase of the system complexity while actually leading to worse communication performance.

5.6.1 Vehicular Scenario

5.6.1.1 Path Loss Models

The path loss characterization follows either the model presented in [152] (if a rural environment is considered) or that in [21] (if an urban scenario is considered). Since vehicles in the obstacle lane or urban buildings can block the link connecting the test VN to its serving gNB, it is necessary to distinguish between LoS and NLoS gNBs, respectively denoted with subscripts L and N throughout the end of the chapter. Moreover, for analytical tractability,

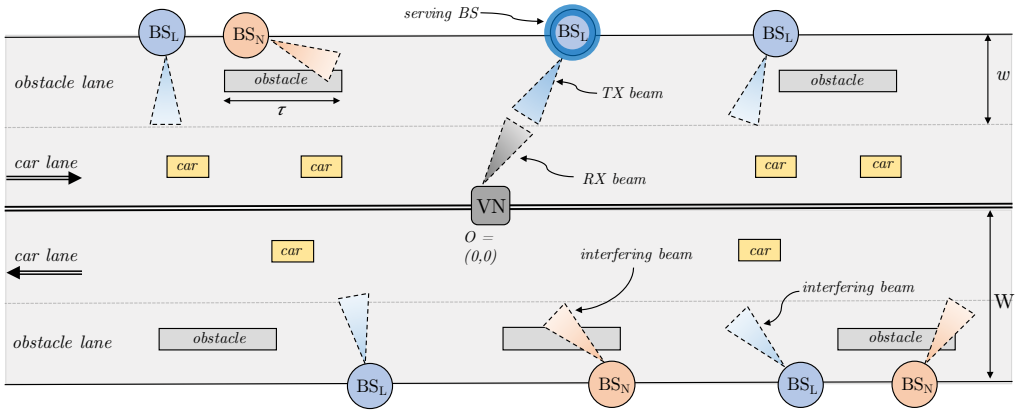

Figure 5.13: Illustration of the considered highway system model, composed of $N_l = 4$ lanes of width w, with one car lane and one obstacle lane in each traffic direction. The target Vehicular Node (VN) is placed at the center of the scenario, while LoS (NLoS) gNBs follow a PPP Φ_L (Φ_N) of density λ_L (λ_N).

in this work we neglect the outage condition induced by severe attenuation and incorporated in [21].

- *Rural path loss model.* When considering a rural highway scenario, gNB n is assumed to be in LoS (with probability $p_{n,L}^{(R)}$) if the ideal segment connecting the target VN and gNB n does not intersect with any of the segments of length τ_o describing the footprint of the vehicles in the obstacle lane. According to [152], this probability is independent of the distance from gNB n to O and can be approximated as $p_L^{(R)} \simeq e^{-\lambda_o \tau_o}$, for any n. Accordingly, a gNB will be in NLoS with probability $p_N^{(R)} = 1 - p_L^{(R)}$.

- *Distance-dependent urban path loss model.* When considering an urban highway scenario, gNB n is assumed to be in LoS (with probability $p_{n,L}^{(U)}(r)$) if the ideal segment connecting the test VN and gNB n (at distance r) does not intersect any building. According to [21], $p_{n,L}^{(U)}(r)$ is independent among different links and is a non-increasing function of r: the longer the link, the more likely to intersect one or more blockages. When obstacles are modeled as random shapes, it follows that $p_L^{(U)}(r) = e^{-a_{\text{LOS}} r}$, where the parameter $a_{\text{LOS}} = 0.0149$ m^{-1} is derived from the measurement campaign conducted in [21]. Again, a gNB is in NLoS with probability $p_N^{(U)}(r) = 1 - p_L^{(U)}(r)$.

By the thinning theorem of PPP [153], the PPPs of the LoS gNBs $\Phi_L \subseteq \Phi_b$ and the NLoS gNBs $\Phi_N \subseteq \Phi_b$ are independent and have density $\lambda_L^{(s)} = p_L^{(s)} \lambda_b$ and $\lambda_N^{(s)} = p_N^{(s)} \lambda_b$, respectively, with $s \in \{R, U\}$. Therefore, the path loss component $\ell_i(r)$ affecting the propagation of the test VN, at distance r from a gNB $\in \Phi_i$, for $i \in \{L, N\}$, is defined as

$$\ell_i(r) = C_i r^{-\alpha_i} \tag{5.32}$$

where α_i is the path loss exponent and C_i is the path loss gain at unit distance.

5.6.1.2 Antenna Model and Beam Tracking

As mentioned, isotropic transmission at mmWave frequencies incurs severe path loss. To overcome this problem, antenna arrays are typically deployed at both the gNBs and the VNs, to perform directional beamforming and benefit from the resulting antenna gain [154].

For the tractability of the analysis, following the model proposed in prior literature work (e.g., [91, 155]), the actual antenna array patterns are approximated by a sectored antenna model. We therefore assume that gNBs are equipped with a UPA of $[N_b \times M_b]$ elements, allowing to steer beams consisting of a main lobe with beamwidth ψ and a side lobe that covers the remainder of the antenna radiation pattern. Similarly, VNs are equipped with a UPA of $[N_{\text{VN}} \times M_{\text{VN}}]$ elements, allowing to steer beams consisting of a main lobe with beamwidth ϕ and a side lobe that covers the remainder of the antenna radiation pattern.

Moreover, we let G_{b_n} and g_{b_n} be the main lobe directivity gain (assumed constant for all angles in the main lobe) and the side lobe gain of the n-th gNB antenna, respectively. Similarly, we let G_{VN} and g_{VN} be the main and side lobe gains of the VN antenna. Then, we define $\Delta_1 = G_b \cdot G_{\text{VN}}$ as the overall antenna gain in case of perfect beam alignment between the test VN and its serving base station (i.e., gNB).

Also, the beam direction of an interfering link is modeled as a uniform random variable in $[0, 2\pi]$. Therefore, the effective interference antenna gain between an interfering gNB j and the test VN is a discrete random variable Δ_{I_j} described as

$$\Delta_{I_j} = \begin{cases} G_{b_j} \cdot G_{\text{VN}}, & \text{with probability } \theta_b/\pi \\ g_{b_j} \cdot g_{\text{VN}}, & \text{with probability } 1 - (\theta_b/\pi) \end{cases} \tag{5.33}$$

where θ_b is defined as the half beamwidth of the aggregate antenna radiation pattern.

As far as beam tracking is concerned, according to the procedure described in [156, 157], we assume that measurement reports are periodically exchanged among the nodes so that, at the beginning of every slot of duration T_S, VNs and gNBs identify the optimal directions for their respective beams. Such configuration is kept fixed for the whole slot duration, during which nodes may lose their alignment due to mobility. If connectivity is lost during a slot, it can only be recovered at the beginning of the subsequent slot, when the beam tracking procedure is performed again [154]. We also assume that, if the VN connects to gNB n, at the beginning of the slot the main lobes of the gNB's and VN's transmit beams are perfectly aligned [84]. This guarantees that, at every slot, the maximum gain Δ_1 is experienced between the VN and its serving gNB.

5.6.1.3 Channel Model

Available measurements at mmWaves in the Vehicle-to-Everything (V2X) or Vehicle-to-Vehicle (V2V) context are very limited, and realistic scenarios are indeed hard to simulate. In fact, the reflectivity and scattering from common objects and the poor diffraction and penetration capabilities of mmWaves are the main factors preventing the reuse of existing lower frequency channel models for an automotive mmWave scenario. Moreover, current models for mmWave cellular systems (e.g., [21]) present many limitations for their applicability to a V2X context, due to the more challenging propagation characteristics of highly mobile VNs [154]. It is thus necessary to make some assumptions related to the signal propagation.

The channel between the test VN and its serving gNB is described as a Rayleigh channel model[5] with mean μ, i.e., $|h_1|^2 \sim \text{Exp}(1/\mu)$ [54]. Similarly, to capture the effect of the interference on the communication performance, the channels between the interfering gNBs and the test VN are modeled as i.i.d. exponential random variables with mean μ [152].

We define the SINR measured between the test VN, attached to a gNB $\in \Phi_i$, for $i \in \{L, N\}$, at distance r_1, as

$$\text{SINR}_i = \frac{|h_1|^2 \Delta_1 \ell_i(r_1)}{(I_L + I_N) + \sigma^2} = \frac{|h_1|^2 \Delta_1 \ell_i(r_1)}{\left(\sum\limits_{k \in \Phi_L} |h_k|^2 \Delta_{I_k} \ell_L(r_k) + \sum\limits_{k \in \Phi_N} |h_k|^2 \Delta_{I_k} \ell_N(r_k) \right) + \sigma^2} \tag{5.34}$$

where $|h_n|^2$ and Δ_n are the small scale fading components and the overall antenna gains measured between gNB n and the test VN (at distance r_n), respectively, while $\ell_i(r_n)$ is the path loss component affecting the propagation between gNB $n \in \Phi_i$ and the VN. I_L and I_N represent the interference produced to the test VN by gNBs in Φ_L and Φ_N, respectively. Finally, σ^2 represents the thermal noise power, normalized with respect to the transmission power P_{TX}, which is assumed equal for all nodes.

5.6.2 Coverage and Connectivity Analysis

In this section, we analyze the coverage and the connectivity of a moving VN in the proposed scenario. The purpose is to exemplify some of the complex and interesting tradeoffs that are to be considered when designing solutions for mmWave automotive scenarios. First, we present the association rule for the VN and derive the expression of the PDF of the distance r between the VN and its serving gNB (LoS or NLoS). Second, we derive the expressions for the SINR coverage probability and the probability that the moving VN stays in the com-

[5]It has been observed in previous works (e.g., [35, 135]) that considering a general fading model such as Nakagami-m may not provide significant design insights and performance improvements compared to Rayleigh fading, while complicating the analysis significantly. Therefore, as a first step, in this study we consider only Rayleigh fading, and leave extensions to more general channel models as future work.

munication range of its serving gNB during one slot and, consequently, keeps connectivity. Finally, we analytically determine an expression for the average achievable throughput as a function of the vehicle speed V, the slot duration (or beam tracking periodicity) T_S and the beamwidth ψ.

5.6.2.1 Association Rule

According to the system model, every T_{S} both the VN and the gNBs estimate the surrounding channels and then adjust their antenna orientation accordingly, to exploit the maximum beamforming gain. We also assume that the measured channel information is perfect, neglecting any estimation error. Therefore, letting r_n be the distance between the VN and gNB n, the VN always connects to gNB $n^* \in \Phi_i$, $i \in \{L, N\}$, that provides the maximum average received power (i.e., the minimum path loss)

$$n^* = \underset{\forall i,\, \forall n}{\arg\max} \{\ell_i(r_n)\} \tag{5.35}$$

where $\ell_i(r_n)$ is as in Equation (5.32).

Lemma 1 *The probability density function of the distance r between the VN and the nearest LoS (NLoSs) gNB is*

$$f_i^{(s)}(r) = \frac{\partial}{\partial r}\left(1 - \exp\left(-2\lambda_b \int_0^{b(r)} p_i^{(s)}(x)\mathrm{d}x\right)\right), \tag{5.36}$$

where r is larger than the road width W, i.e., $r > W$, by construction, $s \in \{R, U\}$ (according to the simulated scenario[6]), $i \in \{L, N\}$ (according to the path loss state of the nearest gNB), and $b(r) = \sqrt{r^2 - W^2}$.

Proof: See Appendix A.3. ■

However, the test VN may not always perform association to the closest gNB, especially when considering a very dense urban environment in which the nearest infrastructure node may be in NLoS. On the contrary, the serving gNB can be either the nearest gNB in Φ_L or the nearest one in Φ_N [91]. Assuming that the test VN connects to a LoS (NLoS) gNB, there must be no NLoS (LoS) gNBs at distance greater than or equal to $A_N(r)$ ($A_L(r)$), which is defined as

$$A_i(r) = \left(\frac{C_{i^*}}{C_i} r^{\alpha_i}\right)^{\frac{1}{\alpha_{i^*}}} \tag{5.37}$$

[6]When considering a rural highway scenario, the path loss state (i.e., the probability of LoS/NLoS conditions) does not depend on the distance r between the VN and the gNB, therefore the expression in Equatiob (5.36) simplifies to $f_i^{(R)}(r) = \frac{2\lambda_i^{(R)} r}{b(r)} \exp\Big(-2\lambda_i^{(R)} b(r)\Big)$, $i \in \{L, N\}$. Similar simplifications apply for all the results referred to a rural environment presented throughout the section.

where i^* indicates the LoS/NLoS state other than i.

We can therefore compute the probability that the test VN is associated with either a LoS or NLoS gNB as follows.

Lemma 2 *The test VN connects to a gNB* $\in \Phi_i$*, for* $i \in \{L, N\}$*, with probability*

$$P_i^{(s)} = \int_W^\infty \exp\left(-2\lambda_b \int_0^{b(A_i(r))} p_{i^*}^{(s)}(x)\mathrm{d}x\right) f_i^{(s)}(r)\mathrm{d}r \tag{5.38}$$

where $s \in \{R, U\}$ *and* $b(A_i(r)) = \sqrt{A_i(r)^2 - W^2}$.

Proof: See Appendix A.4. ■

Lemma 3 *Given that the test VN connects to a gNB* $\in \Phi_i$*, for* $i \in \{L, N\}$*, the PDF* $\bar{f}_i^{(s)}(r)$*,* $s \in \{R, U\}$*, of the distance* r *between the vehicular node and the serving gNB is given by*

$$\bar{f}_i^{(s)}(r) = \exp\left(-2\lambda_b \int_0^{b(A_i(r))} p_{i^*}^{(s)}(x)dx\right) f_i^{(s)}(r) \tag{5.39}$$

Proof: The proof is based on the same rationale used to prove Lemma 2, and is therefore omitted here. ■

5.6.2.2 SINR Coverage Analysis

The SINR coverage probability $P_{cov}^{(s)}(\Gamma)$ is defined as the probability that the target VN experiences an SINR larger than a predefined threshold $\Gamma > 0$, i.e., $P_{cov}^{(s)}(\Gamma) = \mathbb{P}[\mathrm{SINR} > \Gamma]$. As previously defined in Equation (5.17), and by using the law of total probability, we get

$$P_{cov}^{(s)}(\Gamma) = \mathbb{P}[\underbrace{\mathrm{SINR} > \Gamma,\, n^* \in \Phi_L}_{\mathrm{SINR}_L > \Gamma}] + \mathbb{P}[\underbrace{\mathrm{SINR} > \Gamma,\, n^* \in \Phi_N}_{\mathrm{SINR}_N > \Gamma}] \tag{5.40}$$

where n^* is the serving gNB referred to the target VN. Based on the lemmas and the assumptions introduced in the previous sections, we present the main theorem on the SINR coverage probability.

Theorem 1 *The coverage probability* $P_{cov}^{(s)}(\Gamma)$ *for a target SINR threshold* $\Gamma > 0$ *is given by*

$$P_{cov}^{(s)}(\Gamma) = \sum_{i \in \{L, N\}} \int_W^\infty \exp\left(\frac{-\mu\sigma^2\Gamma r^{\alpha_i}}{\Delta_1 C_i}\right) \mathcal{L}_{I_i^L}^{(s)}\left(\frac{\mu\Gamma r^{\alpha_i}}{\Delta_1 C_i}\right) \mathcal{L}_{I_i^N}^{(s)}\left(\frac{\mu\Gamma r^{\alpha_i}}{\Delta_1 C_i}\right) \bar{f}_i^{(s)}(r)\mathrm{d}r, \tag{5.41}$$

where $\mathcal{L}_{I_i^j}^{(s)}(t)$ *is the Laplace transform of the interference from gNBs*$\in \Phi_j$*, for* $j \in \{L, N\}$*,*

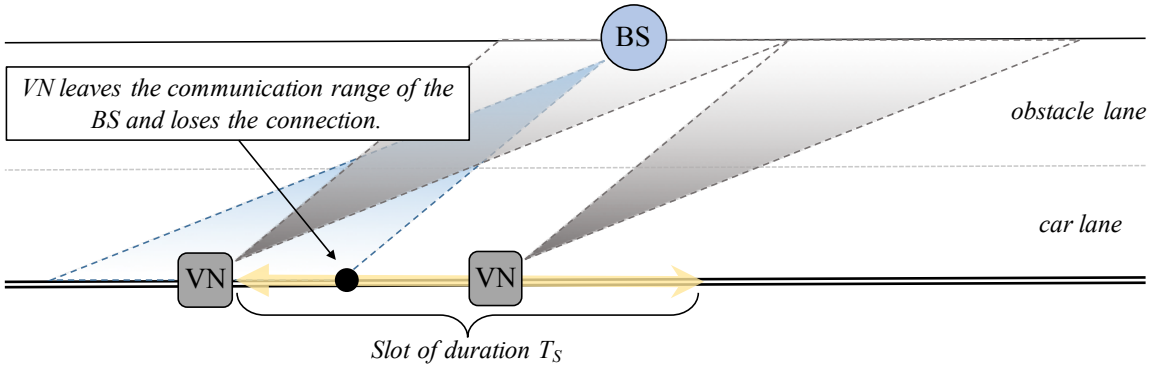

Figure 5.14: At the beginning of the slot of duration T_S, the VN is connected and aligned to its serving gNB. When moving at constant speed V during the slot, the VN leaves the communication range of the gNB. Since the beam direction cannot be updated during the slot, the link between the VN and the gNB will be lost until the beginning of the next slot.

to the test VN, and is expressed as

$$\mathcal{L}_{I_i^j}^{(s)}(t) = \exp\left(-2\lambda_b \int_{\left(\frac{C_j}{C_i} r^{\alpha_i}\right)^{\frac{1}{\alpha_j}}}^{\infty} \left[1 - \left(\frac{\frac{1}{\mu}(\theta_b/\pi)}{\frac{1}{\mu} + tv^{-\alpha_j} C_j G_b G_{\mathrm{VN}}} + \right.\right.\right. \\ \left.\left.\left. + \frac{\frac{1}{\mu}[1-(\theta_b/\pi)]}{\frac{1}{\mu} + tv^{-\alpha_j} C_j g_b g_{\mathrm{VN}}} \right) \right] p_j^{(s)}(v) \mathrm{d}v \right) \tag{5.42}$$

Proof: See Appendix A.5. ■

5.6.2.3 Connectivity Analysis

As we pointed out in Section 5.6.1.2, a directional beam pair needs to be determined to enable the transmission between two nodes, thus beam tracking heavily affects the connectivity performance of a V2X mmWave system. Assuming that perfect beam alignment is obtained at the beginning of every slot of duration T_S, the vehicle can be in either a connected (C) or an idle (I) state, depending on whether the endpoints experience an SINR larger than a predefined threshold Γ. Starting from state C, the VN can either maintain connectivity to the serving gNB for the whole slot duration, or lose the beam alignment and get disconnected. This second event is illustrated in Figure 5.14. Starting from state I, instead, the vehicle can either remain out-of-range for the whole slot, or enter the coverage range of a new gNB within T_{S} (*catch-up*). Even in this second case, however, the connection will be established only at the beginning of the following slot, when the beam alignment procedure is performed. Therefore, preservation of the connectivity during a slot requires that the VN is within the coverage range of the gNB at the beginning of the slot, with sufficient signal quality, and does not lose beam alignment throughout the slot duration T_S.

In this subsection, we analytically derive the expression of the probability P_C that the

moving VN does not disconnect from its serving infrastructure during a slot of duration T_S.

Theorem 2 *For $s \in \{R, U\}$, the probability that the VN is in the connected state C for the whole duration of a slot is given by*

$$P_C^{(s)} = P_{cov}^{(s)}(\Gamma) \cdot P_{NL}^{(s)} \tag{5.43}$$

where $P_{cov}^{(s)}(\Gamma)$ is the probability of being in state C at the beginning of the slot and $P_{\mathrm{NL}}^{(s)} = \mathbb{P}[T_L > T_S]$ represents the probability that the VN does not leave the communication range of the serving gNB during the slot.[7] *This can be expressed as a function of r as*

$$P_{\mathrm{NL}}^{(s)} = \mathbb{P}[T_L > T_S] = \mathbb{P}\left[r > \frac{VT_S}{\sin(\psi/2)}\left(\frac{W}{r}\sin(\eta) + \sqrt{1 - \left(\frac{W}{r}\right)^2}\cos(\eta)\right)\right] \tag{5.44}$$

where $\eta = \pi/2 - \psi/2$ and ψ is the beamwidth of the main lobe of the gNB.

Proof: See Appendix A.6. ■

The last expression can be easily solved via numerical computation by determining the value r^* for which the inequality in (5.44) is satisfied as an equality. Considering that the right-hand side of the inequality in (5.44) is monotonically decreasing in r, we hence have

$$P_{\mathrm{NL}}^{(s)} = \mathbb{P}[T_L > T_S] = \sum_{i \in \{L,\, N\}} \int_{r^*}^{\infty} \bar{f}_i^{(s)}(r)\mathrm{d}r \tag{5.45}$$

where $\bar{f}_i^{(s)}(r)$ is as in (5.39).

5.6.2.4 Throughput Analysis

In this subsection, we determine the expression for the average throughput B experienced by the target VN moving across the considered mmWave vehicular scenario. In particular, let $\mathbb{E}[T_{\mathrm{comm}}] \in \{0, T_S\}$ represent the average time (i.e., the portion of slot) during which the VN is within the coverage range of its serving infrastructure and properly aligned with it. In this case, the nodes are able to exchange data, on average, at a rate $\mathbb{E}[\gamma(r)]$ that depends on their distance r. The average achievable throughput during one slot is therefore defined as

$$B^{(s)}(r) = \mathbb{E}[\gamma(r)] \cdot \frac{\mathbb{E}[T_{\mathrm{comm}}]}{T_S}, \quad s \in \{R, U\}. \tag{5.46}$$

Notice that $B(r) = 0$ if the VN is disconnected at the beginning of the slot, while $B(r) = \mathbb{E}[\gamma(r)]$ if the VN is in the connected state for the whole duration of a slot (i.e., $\mathbb{E}[T_{\mathrm{comm}}] =$

[7] Notice that, according to (5.43), $P_{\mathrm{NL}}^{(s)}$ is to be interpreted as a *conditional* probability, i.e., the probability that the VN remains connected during a slot *given* that it is connected at the beginning (otherwise the endpoints would not be able to determine the optimal directions for their beams and no communication would be possible).

T_S). The average rate $\mathbb{E}[\gamma(r)]$ in Equation (5.46) can be computed using Lemma 4, while the average communication duration $\mathbb{E}[T_{\text{comm}}]$ is evaluated through Theorem 3.

Lemma 4 *Given the SINR coverage probability $P_{cov}(\Gamma)$, the average achievable rate experienced by the target VN, at distance r from its serving gNB, is given by the following expression*

$$\begin{aligned}\mathbb{E}[\gamma(r)] &= W_{\text{tot}}\mathbb{E}\{\log_2(1+SINR)\} = \frac{W_{\text{tot}}}{\log(2)}\int_0^\infty \mathbb{P}[SINR > e^t - 1]\mathrm{d}t \\ &= \frac{W_{\text{tot}}}{\log(2)}\int_0^\infty P_{cov}(e^t-1)\mathrm{d}t\end{aligned} \tag{5.47}$$

Proof: See [54, Theorem 3] and [158, Section V]. ■

Theorem 3 *Being $d(r)$ the maximum distance the VN can cover before leaving the communication range of its serving gNB and being VT_S the total distance covered by the VN, moving at speed V, within the slot of duration T_S, the average time (i.e., the portion of slot) in which the VN experiences a non-zero throughput is expressed as:*

$$\begin{aligned}\mathbb{E}[T_{\text{comm}}] &= (1-P_{\text{NL}})\cdot\mathbb{E}[T_{\text{comm,L}}] + P_{\text{NL}}\cdot\mathbb{E}[T_{\text{comm,NL}}] \\ &= (1-P_{\text{NL}})\cdot\left(\frac{1}{V}\cdot\frac{\int_0^{VT_S} F_d(VT_S) - F_d(u)\mathrm{d}u}{F_d(VT_S)}\right) + P_{\text{NL}}\cdot T_S,\end{aligned} \tag{5.48}$$

where $f_d(x)$ and $F_d(x)$ represent the PDF and CDF of the distance $d(r)$, respectively, and P_{NL} is as in Equation (5.44).

Proof: According to the analysis we developed in Appendix A.6, if the VN does not disconnect during the slot (with probability $P_{\text{NL}}^{(s)}$, i.e., with probability $\mathbb{P}[d(r) > VT_S]$) then $\mathbb{E}[T_{\text{comm,NL}}] = T_S$. Otherwise, the VN experiences a non-zero throughput only during the portion of the slot in which the alignment with the serving infrastructure is maintained, and therefore

$$\begin{aligned}\mathbb{E}[T_{\text{comm,L}}] &= \frac{\mathbb{E}\Big[d(r)\Big|d(r) < VT_S\Big]}{V} \overset{(a)}{=} \frac{1}{V}\cdot\frac{\int_0^{VT_S} x f_d(x)\mathrm{d}x}{\mathbb{P}[d<VT_S]} \\ &= \frac{1}{V}\cdot\frac{\int_0^{VT_S}\Big(\int_0^x \mathrm{d}u\Big)f_d(x)\mathrm{d}x}{\mathbb{P}[d<VT_S]} = \frac{1}{V}\cdot\frac{\int_0^{VT_S}\int_0^x f_d(x)\mathrm{d}u\mathrm{d}x}{\mathbb{P}[d<VT_S]} \\ &\overset{(b)}{=} \frac{1}{V}\cdot\frac{\int_0^{VT_S}\int_u^{VT_S} f_d(x)\mathrm{d}x\mathrm{d}u}{\mathbb{P}[d<VT_S]} \\ &= \frac{1}{V}\cdot\frac{\int_0^{VT_S}\Big(F_d(VT_S)-F_d(u)\Big)\mathrm{d}u}{F_d(VT_S)},\end{aligned} \tag{5.49}$$

Table 5.7: Notation and meaning of the main system parameters.

Parameter	Meaning
Φ_b, Φ_o, Φ_L, Φ_N	PPPs of gNBs, obstacles, LoS gNBs and NLoS gNBs
λ_L, λ_N	Density of LoS and NLoS gNBs
p_L, p_N	Probability of a gNB being in LoS (or NLoS) w.r.t. the test VN
$\ell_i(r)$	Path loss component of gNB $\in \Phi_i$, for $i \in \{L, N\}$, at distance r from the VN
$\Delta_1 = G_b \cdot G_{\text{VN}}$	Overall antenna gain (assuming perfect beam alignment)
Δ_{I_j}	Antenna gain between the test VN and interfering gNB j
$\lvert h_i\rvert^2 \sim \text{Exp}(1/\mu)$	Small scale fading component of the i-th gNB
$\bar{f}_i(r)$	PDF of the distance r from the test VN to the serving gNB $\in \Phi_i$, for $i \in \{L, N\}$
$P_i(r)$	Probability that the test VN connects to a gNB $\in \Phi_i$, for $i \in \{L, N\}$
P_{cov}	SINR Coverage probability
P_C	Connectivity probability
B	Achievable throughput within one slot

where step (a) derives from the definition of conditional expectation and from the fact that $d(r) < VT_S$, while step (b) has been obtained by changing the order of integration for the integrals in dx and du. ■

5.6.3 Numerical Results

In this section, after introducing our main simulation parameters, we provide some numerical results based on the analysis presented in Section 5.6.2, with the following objectives.

(i) Comparing the coverage and connectivity performance of vehicles considering both a rural and an urban path loss characterization, following the models of [21] and [152], respectively.

(ii) Evaluating the throughput performance of the VNs in a mmWave vehicular network. The validity of the proposed theoretical model will be assessed by comparing the analytical results representing Equation (5.46) with simulation outcomes.

(iii) Providing insights on the impact on the performance of V2X nodes in highly mobile mmWave networks of several automotive-specific features, e.g., the vehicle's speed, the beam tracking periodicity, the node density, the antenna configuration.

5.6.3.1 System Parameters

The parameters used to derive the results are summarized in Table 5.7.[8] In particular, we assume that the mmWave network is operated at $f_C = 28$ GHz, and the total available bandwidth is $W_{\text{tot}} = 1$ GHz. In addition, the mmWave channel follows the model presented in Section 5.6.1.3 where the Rayleigh parameter μ is set to 1. The gNBs are equipped with an antenna array of $[N_b \times M_b] = \{4, 16, 64\}$ elements. The resulting main lobe width ψ and beamforming gain G_b are proportional to the array size, since narrower beams can be steered and larger gains can be achieved when considering larger-scale arrays [79]. Therefore, we assume $\psi \simeq \{90°, 60°, 30°\}$ and $G_b \simeq \{20, 12, 6\}$ dB, according to the respective array dimension. On the other hand, the VN is equipped with $[N_{\text{VN}} \times M_{\text{VN}}] = 16$ elements, steering beams of width $\phi \simeq 60°$ and producing a gain $G_{\text{VN}} \simeq 12$ dB. Finally, the side lobe gain of both base stations and vehicular nodes is set to $g_b = g_{\text{VN}} = -10$ dB. The gNBs are positioned uniformly at random on both sides of the road according to a PPP with density λ_L and λ_N for LoS and NLoS gNBs, respectively. The road width is $2W = 14.8$ m, while the length is $L = 50$ km. As introduced in Section 5.6.1.2, perfect alignment between the VN, moving at constant speed $V = \{30, 60, 90, 100, 130\}$ km/h, and its serving infrastructure is guaranteed every $T_S = \{0.1, 0.3, 0.5, 1\}$ seconds. Conversely, interfering gNBs steer their beams through random angle configurations.

5.6.3.2 Coverage and Connectivity (Urban Path Loss Model)

Considering an urban path loss characterization, according to Theorem 2, the preservation of the connectivity during a slot requires both accurate alignment between the endpoints and satisfactory signal quality. The value of $P_{NL}^{(U)}$ therefore becomes particularly meaningful if weighed by the VN's coverage probability at the beginning of the slot. In Figure 5.15(a), we thus plot the SINR coverage probability, i.e., the probability that the VN is connected at the beginning of a synchronization slot, as expressed by Equation (5.41), for different transmit antenna configurations. We note that $P_{cov}^{(U)}(\Gamma)$ increases with the gNBs density λ_b because of the higher probability of having a gNB at shorter distance which can offer better signal quality. However, the gain progressively reduces with λ_b because of the increasing impact of the interference from the surrounding gNBs. Anyway, the increasing trend shown by $P_{cov}^{(U)}(\Gamma)$ proves that the reduction of the attachment distance is dominant over the increased interference. Finally, the figure shows that narrower beams result in higher SINR (and higher $P_{cov}^{(U)}(\Gamma)$) due to the higher gain achieved by beamforming, as expected.

In Figure 5.15(b), (c) and (d) we report the connectivity probability $P_C^{(U)}$ representing the probability, as expressed by Equation (5.43), that the VN is connected during an entire

[8] Although our system parameters are based on realistic system design considerations and therefore accurately reflect the specificities of different vehicular scenarios, the simulator described is fully customizable, thereby allowing future development of the 3GPP specifications on V2X and enhanced channel characterizations to be easily plugged in as they will be released.

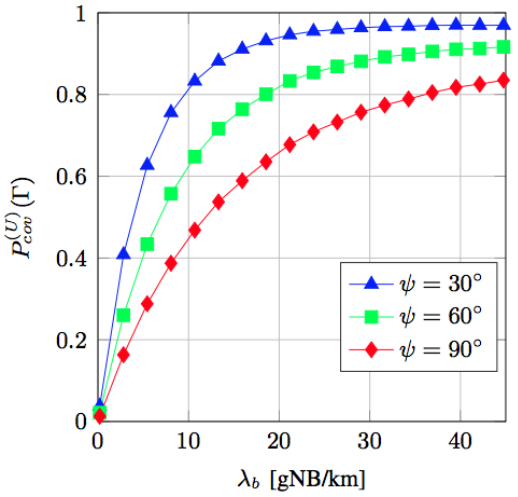

(a) $P_{cov}^{(U)}$, for different antenna configurations. SINR threshold $\Gamma = -5$ dB.

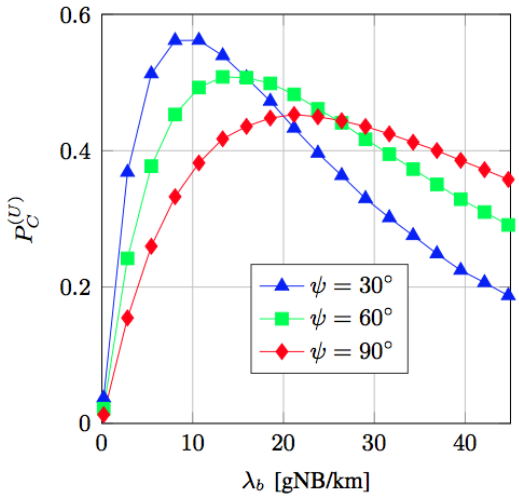

(b) $P_C^{(U)}$ with parameters $T_S = 300$ ms, $V = 100$ km/h, for different antenna configurations.

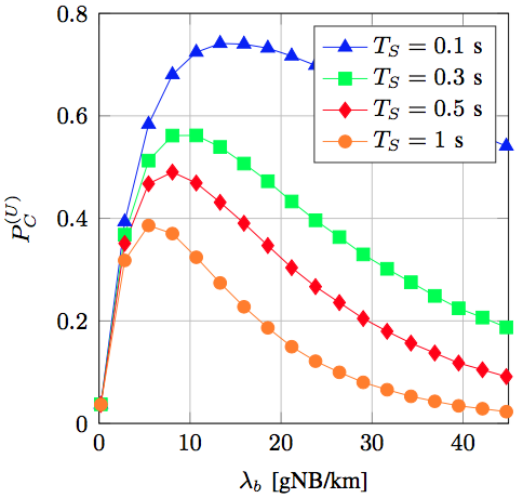

(c) $P_C^{(U)}$ with parameters $\psi = 30°$, $V = 100$ km/h, for different values of the slot duration.

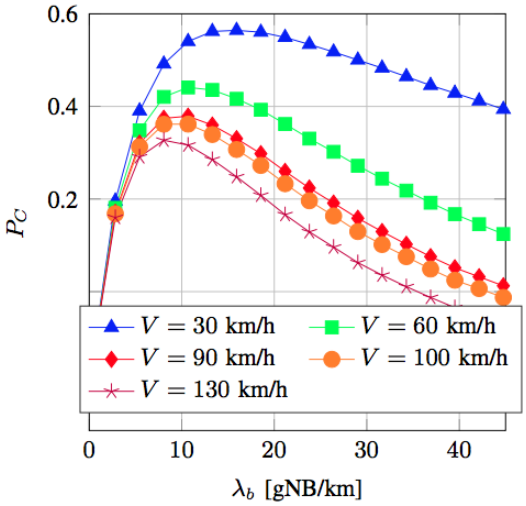

(d) $P_C^{(U)}$ with parameters $\psi = 30°$, $T_S = 300$ ms, for different values of the VN speed.

Figure 5.15: Coverage and connectivity probabilities ($P_{cov}^{(U)}$ and $P_C^{(U)}$, respectively) within a slot of duration T_S, when varying the gNBs density λ_b. An urban path loss model is considered. The curves are analytically obtained from Equations (5.41) and (5.43).

slot of duration T_S, i.e., the VN is still connected at the end of one slot given that it was connected at the beginning of the same slot, as a function of ψ, V and T_S. We observe that $P_C^{(U)} = P_{cov}^{(U)}(\Gamma) \cdot P_{NL}^{(U)}$ exhibits a maximum for a given density λ_b^*. In detail, we notice that $P_C^{(U)}$ increases with λ_b for sparse networks. In this region, the reduction of the attachment distance r to the serving gNB is more significant than the increase of the interference coming from the neighboring gNBs. Moreover, r is still sufficiently large to allow for a loose beam alignment (thanks to the widening of the beam's projection on the road's surface with the distance), so that the connectivity between the endpoints is maintained for a relatively large

number of slots. After a certain value of λ_b, $P_C^{(U)}$ starts decreasing. In this range, the coverage probability does not increase significantly, as depicted in Figure 5.15(a), while r keeps reducing and the resulting smaller beam projected on the highway lanes contributes to increasing the risk of losing connectivity during a slot.

Finally, as mentioned above, Figures 5.15(c) and (d) emphasize how more durable connectivity capabilities are guaranteed for smaller values of T_S and V, respectively.

5.6.3.3 Throughput Results (Urban Path Loss Model).

As mentioned in Section 5.6.2.4, a non-zero throughput B is experienced when the vehicle is within the coverage of its serving infrastructure and properly aligned with it. In Figure 5.16 we plot the results representing the average throughput measured by the target VN within a slot of duration T_S. While the analytical connectivity results presented in the previous paragraphs were exact, these throughput curves were obtained from an approximate theoretical framework. To assess the accuracy of the approximation, we report in the graphs also the simulation results obtained through a Monte Carlo approach, where multiple independent simulations are repeated to get different statistical quantities of interest. At each iteration, the simulator computes the path loss, according to the urban characterization proposed in [21], from each gNB to the test VN and (*i*) makes the optimal association decision according to a max-path loss policy, (*ii*) measures the SINR from the VN to its serving cell, and (*iii*) computes the data rate, according to Shannon's formula, for the fraction of time in which the nodes are properly aligned. Finally, the throughput is estimated by averaging over the total number of repetitions.

First, we observe that the numerical results closely follow the analytic curves representing Equation (5.46), thereby validating our theoretical framework. Moreover, it is interesting to observe that, in all considered configurations, the throughput exhibits a similar trend when varying the gNBs density λ_b and, most importantly, follows the behavior of the connectivity curves presented in Figure 5.15. An optimal value of $B^{(s)}$ can therefore be identified, meaning that there exists a density threshold λ_b^* above which the deployment of more gNBs results in a considerable increase of the system complexity while leading to worse communication performance. Moreover, B grows as T_S decreases, because the beam alignment is repeated more frequently, thus reducing the disconnection time. However, the overhead (which is not accounted for in this analysis) would also increase, thus limiting or even nullifying such a gain if T_S drops below a certain threshold.

5.6.4 Final Remarks and Open Challenges

In this last work, we proposed a stochastic geometry framework to characterize the coverage (i.e., downlink coverage) and the connectivity (i.e., beam alignment probability) performance of a dynamic mmWave vehicular network deployed along a multi-lane highway section.

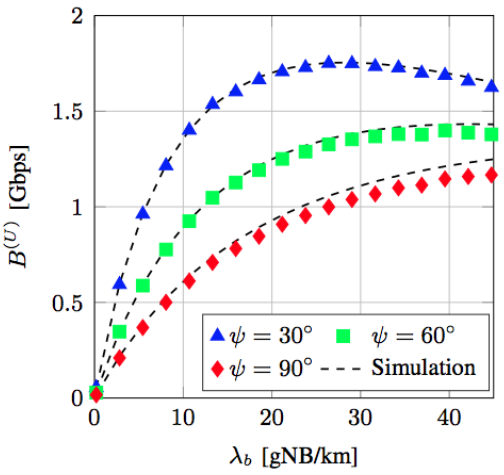

(a) $B^{(U)}$ with parameters $T_S = 300$ ms, $V = 130$ km/h, for different antenna configurations.

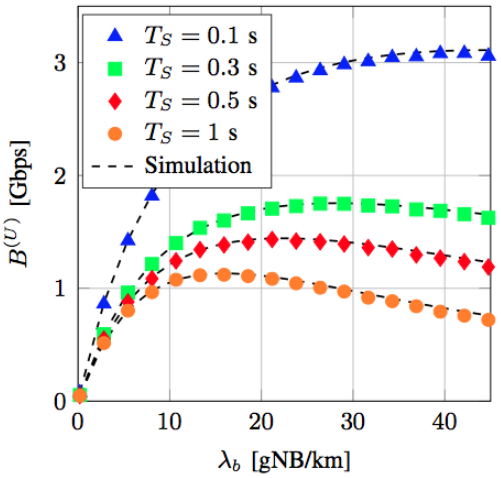

(b) $B^{(U)}$ with parameters $\psi = 30°$, $V = 130$ km/h, for different values of the slot duration.

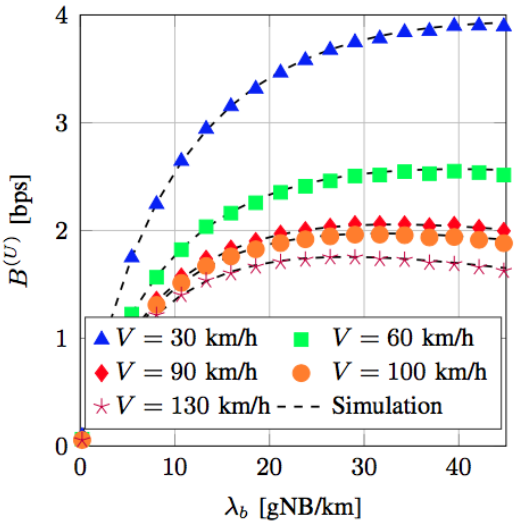

(c) $B^{(U)}$ with parameters $\psi = 30°$, $T_S = 300$ ms, for different values of the VN speed.

Figure 5.16: Average throughput (B) experienced within a slot of duration T_S, when varying the gNBsdensity λ_b. An urban path loss model is considered. The dashed lines are drawn from Monte Carlo simulations, the markers are obtained from Equation (5.46).

The key point is that, in order to compensate for the increased isotropic path loss experienced at high frequencies, next-generation mmWave automotive communication must provide mechanisms by which the vehicles and the infrastructure determine suitable directions of transmission to exchange data. In this context, our model characterizes the base stations as independent homogeneous LoS and NLoS one-dimensional Poisson processes and implements both a rural and a distance-dependent urban path loss model, in which the communication between the endpoints is impaired by large vehicles acting as obstructions, respectively. We derived expressions for the SINR coverage probability, the probability that

the vehicle does not disconnect from its serving cell over time, and the achievable throughput, as a function of the infrastructure density.

Most vehicular-related challenges are still largely unexplored, so that additional research is needed. As part of our future work, we aim at further validating the presented results considering innovative and original channel models specifically tailored to a next-generation V2X context. Moreover, it would be interesting to formally characterize space and time dependent target performance metrics to assess the connectivity performance of the nodes in the rapidly time-varying mmWave environment, while investigating realistic scenarios and models. Finally, a validation of the connectivity analysis including more sophisticated vehicular channel models, advanced deployment scenarios and more realistic movement traces for the vehicles represents another timely and relevant item for future research.

Chapter 6

Conclusions

In this thesis, we investigated how an accurate modeling of both the channel environment and the antenna radiation pattern strongly affect the results of any simulated millimeter wave (mmWave) cellular scenario. Starting from the models present in the literature we studied antenna and channel characterization for mmWave cellular networks focusing on both spectrum sharing and antenna optimization aspects. Our results are mostly based on simulations done using MATLAB scripts and the more complete ns-3 network simulator. In particular, in all the research activities we considered a complete scenario precisely designed to study the specific topic of our research. Even though the model we used in every chapter is different, because tailored to study a particular problem or condition, they all share some common mmWave features, such as directional transmission with beamforming and multipath channel modeling.

Although different conclusions have been discussed at the end of each chapter, there are also some common considerations that can be made. First of all, as already stressed in the entire thesis, in order to gather a fair comparison of different approaches, realistic and accurate channel and antenna models are fundamental. For example, we shown how the antenna propagation model strongly affects the Signal to Interference plus Noise Ratio (SINR) performance. Then, several approaches have been considered to perform spectrum sharing in the cellular environment. We considered dynamic and hybrid sharing schemes simulating dense and complete cellular networks following regulatory directives. Our results highlight the benefit of sharing the spectrum and according to the scenario considered, either the dynamic or the hybrid approach permits to improve both the spectral efficiency and also the fairness among the users of the network. Moreover, hybrid spectrum sharing offers advantages for the average user with respect to traditional fully licensed or fully pooled spectrum access schemes, in terms of increased throughput and spectral efficiency. Together with simulations, also a stochastic geometry analysis has been obtained which permits to gather details about the coverage SINR expression in dense scenarios. As examples, in the

thesis we reported some performance results for both cellular and vehicular environments. Another interesting aspect is that, considering aligned and misaligned gain distributions, we extend the coverage expression from the literature, thus capturing also the effects of a realistic antenna array radiation pattern.

We have highlighted in the thesis some of the important aspects that require further research and can be considered as future research activities (e.g., improvement in the stochastic geometry analysis or in the study of MIMO precoders). In particular, as the main future work, further research activities for the Machine Learning (ML) framework is extremely interesting in order to precisely understand the benefits of a learning tool used for solving complex cellular optimization problems.

6.1 Acknowledgments

The work in this thesis has been achieved thanks to the effort of collaborations from several research teams. Those are the mmWave team in NYU Wireless, the connectivity research team at the Aalborg University, the radio access team in Huawei Technology Milano and the 5G wireless research and standardization team in Nokia Bell Labs Paris.

Appendix A

Appendices

A.1 Appendix – Proof of Proposition 1

Consider the joint probability $\Pr\left(\text{SINR} \geq T, x_o \in \Phi_i\right) = \Pr\left(\text{SINR}_i \geq T\right)$ in Equation (5.18) when the typical User Equipment (UE) associates with a Next Generation Node Base (gNB) in state $i \in \{L, N\}$. Applying the SINR definition in (5.9) to (5.18), it is recast as follows

$$\Pr\left(\text{SINR}_i \geq T\right) = \mathbf{E}_{r^i_{x_o}, I^L_i, I^N_i}\left[\Pr\left(\frac{G_o^{(\mathsf{ISO})}\ell^i(r^i_{x_o})}{(I^L_i + I^N_i) + \sigma^2} \geq T\right)\right] \tag{A.1}$$

$$= \mathbf{E}_{r^i_{x_o}, I^L_i, I^N_i}\left[\Pr\left(G_o^{(\mathsf{ISO})} \geq \frac{T(I^L_i + I^N_i + \sigma^2)}{\ell^i(r^i_{x_o})}\right)\right] \tag{A.2}$$

$$= \mathbf{E}_{r^i_{x_o}, I^L_i, I^N_i}\left[F_{G_o}^{(\mathsf{ISO})}\left(\frac{T(I^L_i + I^N_i + \sigma^2)}{\ell^i(r^i_{x_o})}; \mu_o\right)\right] \tag{A.3}$$

The last step is because the innermost probability in (A.2) corresponds to $G_o^{(\mathsf{ISO})}$'s Complementary Cumulative Distribution Function (CCDF) $F_{G_o}^{(\mathsf{ISO})}(y; \mu_o)$ with y that equals $T(I^L_i + I^N_i + \sigma^2)/\ell^i(r^i_{x_o})$.

Next, applying $F_{G_o}^{(\mathsf{ISO})}(y; \mu_o) = \exp(-\mu_o y)$ in Remark 1 to Equation (A.3), we obtain

$$(\text{A.3}) = \mathbf{E}_{r^i_{x_o}, I^L_i, I^N_i}\left[\exp\left(\frac{-\mu_o T\sigma^2}{\ell^i(r^i_{x_o})}\right)\exp\left(\frac{-\mu_o T I^L_i}{\ell^i(r^i_{x_o})}\right)\exp\left(\frac{-\mu_o T I^N_i}{\ell^i(r^i_{x_o})}\right)\right] \tag{A.4}$$

$$= \mathbf{E}_{r^i_{x_o}}\left[e^{-\frac{\mu_o T\sigma^2}{\ell^i(r^i_{x_o})}}\mathbf{E}_{I^L_i}\left[e^{-\frac{\mu_o T I^L_i}{\ell^i(r^i_{x_o})}}\right]\mathbf{E}_{I^N_i}\left[e^{-\frac{\mu_o T I^N_i}{\ell^i(r^i_{x_o})}}\right]\right] \tag{A.5}$$

The last step is firstly because $r^i_{x_o}$ is independent of I^L_i and of I^N_i, according to Slyvnyak's theorem [145]. It is additionally because I^L_i and of I^N_i are mutually independent owing to the

Markov property for the Poisson Point Processes (PPPs) Φ_i^L and Φ_i^N [145]. The innermost two expectation terms in (A.5) can be represented using the Laplace transform $\mathcal{L}_X(s) := \mathbf{E}_X[e^{sX}]$. Then, the outermost expectation can be calculated using $r_{x_o}^i$'s Probability Density Function (PDF) $f_{r_{x_o}^i}$ in (5.20), yielding

$$(\text{A.5}) = \int_0^\infty f_{r_{x_o}^i}(r) \exp\left(\frac{-\mu_o T \sigma^2}{\ell^i(r)}\right) \mathcal{L}_{I_i^L}\left(\frac{\mu_o T}{\ell^i(r)}\right) \mathcal{L}_{I_i^N}\left(\frac{\mu_o T}{\ell^i(r)}\right) \mathrm{d}r \tag{A.6}$$

Lastly, in what follows we expand $\mathcal{L}_{I_i^j}(s)$ with $s = \mu_o T/\ell^i(r)$ in (A.6), i.e., the Laplace transform of the interference from the gNBs in Φ_j for $j \in \{L, N\}$ when $x_o \in \Phi_i$. Following the interference expression in Equation (5.9), its Laplace transform is represented as follows

$$\mathcal{L}_{I_i^j}(s) = \mathbf{E}_{\Phi_j, G_x}\left[\exp\left(-s \sum_{x \in \Phi_j} G_x^{(\mathsf{ISO})} \ell^j(r_x)\right)\right] \tag{A.7}$$

$$\overset{(a)}{=} \mathbf{E}_{\Phi_j}\left[\prod_{x \in \Phi_j} \mathbf{E}_{G_x}\left[\exp\left(-s G_x^{(\mathsf{ISO})} \ell^j(r_x)\right)\right]\right] \tag{A.8}$$

$$\overset{(b)}{=} \exp\left(-2\pi\lambda_b \int_{\left(\frac{\beta_j r^{\alpha_i}}{\beta_i}\right)^{\frac{1}{\alpha_j}}}^\infty \left(1 - \mathbf{E}_{G_x}\left[e^{-s G_x^{(\mathsf{ISO})} \ell^j(v)}\right]\right) v p_j(v) \mathrm{d}v\right) \tag{A.9}$$

step (a) follows from the fact that $G_x^{(\mathsf{ISO})}$ is independent of Φ_j and from independent and identically distributed (i.i.d.) $G_x^{(\mathsf{ISO})}$'s. Step (b) comes from applying the Probability Generating Functional (PGFL) of a Homogeneous Poisson Point Process (HPPP) [145]. Since the interfering gNB locations and $G_x^{(\mathsf{ISO})}$'s are independent, (A.9) is recast as follows

$$(\text{A.9}) = \exp\left(-2\pi\lambda_b \mathbf{E}_{G_x}\left[\int_{\left(\frac{\beta_j r^{\alpha_i}}{\beta_i}\right)^{\frac{1}{\alpha_j}}}^\infty \left(1 - e^{-\frac{\mu_o T G_x^{(\mathsf{ISO})} \ell^j(v)}{\ell^i(r)}}\right) v p_j(v) \mathrm{d}v\right]\right) \tag{A.10}$$

The innermost expectation can be calculated using $G_x{}^{(\mathsf{ISO})}$'s PDF $f_{G_x}^{(\mathsf{ISO})}(y; a, b)$ in Remark 3. Combining this result with (A.6) and (5.18) and applying the law of total probability completes the proof. ■

A.2 Appendix – Proof of Proposition 2

Replacing the exponentially distributed $G_o^{(\mathsf{ISO})}$ by the $G_o^{(\mathsf{3GPP})}$ in the joint probability calculation Equation (A.1), we get

$$\Pr\left(\mathrm{SINR}_i \geq T\right) = \mathbf{E}_{r^i_{x_o}, I^L_i, I^N_i}\left[\Pr\left(\frac{G_o^{(\mathsf{3GPP})}\ell^i(r^i_{x_o})}{(I^L_i + I^N_i) + \sigma^2} \geq T\right)\right] \tag{A.11}$$

$$= \mathbf{E}_{r^i_{x_o}, I^L_i, I^N_i}\left[F_{G_o}^{(\mathsf{3GPP})}\left(\frac{T(I^L_i + I^N_i + \sigma^2)}{\ell^i(r^i_{x_o})}; b_o, p_o\right)\right] \tag{A.12}$$

Similarly as before, the last step is because the innermost probability corresponds to $G_o^{(\mathsf{3GPP})}$'s CCDF $F_{G_o}^{(\mathsf{3GPP})}(y; b_o, p_o)$ with y that equals $T(I^L_i + I^N_i + \sigma^2)/\ell^i(r^i_{x_o})$.

Next, applying $F_{G_o}^{(\mathsf{3GPP})}(y; b_o, p_o) = \frac{\ln\left(1-(1-p_o)e^{-b_o y}\right)}{\ln p_o}$ in Remark 2 to (A.12), we obtain

$$(\text{A.12}) = \mathbf{E}_{r^i_{x_o}, I^L_i, I^N_i}\left[\frac{1}{\ln(p_o)}\ln\left(1-(1-p_o)\exp\left(\frac{-b_o T\sigma^2}{\ell^i(r^i_{x_o})}\right)\right.\right.$$
$$\left.\left.\times\exp\left(\frac{-b_o T I^L_i}{\ell^i(r^i_{x_o})}\right)\exp\left(\frac{-b_o T I^N_i}{\ell^i(r^i_{x_o})}\right)\right)\right] \tag{A.13}$$

$$\leq \mathbf{E}_{r^i_{x_o}}\left[\frac{1}{\ln(p_o)}\ln\left(1-(1-p_o)e^{-\frac{b_o T\sigma^2}{\ell^i(r^i_{x_o})}}\mathbf{E}_{I^L_i}\left[e^{-\frac{b_o T I^L_i}{\ell^i(r^i_{x_o})}}\right]\mathbf{E}_{I^N_i}\left[e^{-\frac{b_o T I^N_i}{\ell^i(r^i_{x_o})}}\right]\right)\right] \tag{A.14}$$

The last step is firstly because $r^i_{x_o}$ is independent of I^L_i and of I^N_i, according to Slyvnyak's theorem [145]. Additionally because I^L_i and of I^N_i are mutually independent owing to the Markov property for the PPPs Φ^L_i and Φ^N_i [145]. However, differently from the proof of Proposition 1, here we used Jensen's inequality to derive an upper bound of (A.13). This permits to bring the expectations inside the logarithm, thanks to the fact that CCDF of $G_o^{(\mathsf{3GPP})}$ is a concave function. Then, the outermost expectation can be calculated using $r^i_{x_o}$'s PDF $f_{r^i_{x_o}}$ in (5.20), yielding

$$(\text{A.14}) = \int_0^\infty \frac{f_{r^i_{x_o}}(r)}{\ln(p_o)}\ln\left(1-(1-p_o)\exp\left(\frac{-b_o T r^{\alpha_i}\sigma^2}{\beta_i}\right)\mathcal{L}_{I^L_i}\left(\frac{b_o T}{\ell^i(r)}\right)\mathcal{L}_{I^N_i}\left(\frac{b_o T}{\ell^i(r)}\right)\right)\mathrm{d}r. \tag{A.15}$$

To conclude the proof, the Laplace transforms are used as in equation (A.9) of the proof of Proposition 1, where the interfering gain $G_x^{(\mathsf{ISO})}$ is replaced with the respective $G_x^{(\mathsf{3GPP})}$. ■

A.3 Appendix – Proof of Lemma 1

Considering the Line of Sight (LoS) case, the Vehicular Node (VN) is at distance r from the closest LoS gNB if no other LoS gNBs lie at distance closer than r. Considering the highway scenario described and taking Figure A.1(a) as a reference, there must be no other LoS gNBs

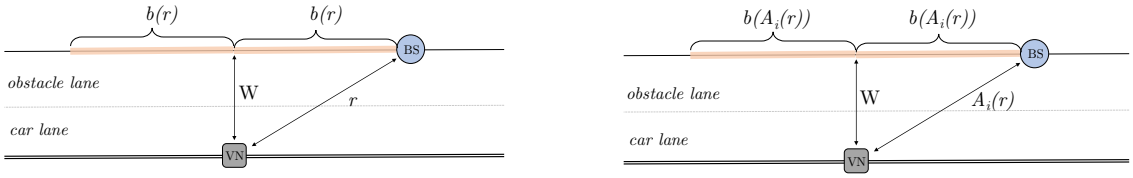

(a) The test VN is at distance r from the closest LoS (or Non Line of Sight (NLoS)) gNB, and $b(r) = \sqrt{r^2 - W^2}$.

(b) The test VN is at distance $A_i(r)$ from a gNB $\in \Phi_i$, for $i \in \{L, N\}$, and $b(A_i(r)) = \sqrt{A_i(r)^2 - W^2}$.

Figure A.1: Illustration of a half section of the highway of width W, as a support to the proof of Lemma 1 and Lemma 2.

within the interval $[-b(r), b(r)]$, with $b(r) = \sqrt{r^2 - W^2}$. Since the spatial distribution of the LoS gNBs is modeled as a 1-D Poisson process Φ_L with density $\lambda_L^{(s)}(r)$, we have

$$\begin{aligned} F_L^{(s)}(r) &= \mathbb{P}\Big[\text{No LoS gNBs within the interval } [-b(r), b(r)]\Big] \\ &= \exp\left(-\int_{-b(r)}^{b(r)} \lambda_L^{(s)}(x)\mathrm{d}x\right) \\ &\overset{(a)}{=} \exp\left(-2\int_{0}^{b(r)} \lambda_L^{(s)}(x)\mathrm{d}x\right) \\ &\overset{(b)}{=} \exp\left(-2\lambda_b\int_{0}^{b(r)} p_L^{(s)}(x)\mathrm{d}x\right) \end{aligned} \tag{A.16}$$

with $s \in \{R, U\}$. Step (a) follows from the symmetry of the scenario and (b) from the fact that $\lambda_L^{(s)}(x) = p_L^{(s)}(x)\lambda_b$. The PDF of r can be computed as

$$f_L^{(s)}(r) = \frac{\partial}{\partial r}\Big(1 - F_L^{(s)}(r)\Big) = \frac{\partial}{\partial r}\left(1 - \exp\left(-2\lambda_b\int_{0}^{b(r)} p_L^{(s)}(x)\mathrm{d}x\right)\right)$$

which gives Equation (5.36) for the LoS case. With a similar reasoning, it is also possible to prove the lemma for the NLoS case. ■

A.4 Appendix – Proof of Lemma 2

Let r_L and r_N be the random variables expressing the distance to the closest LoS and NLoS gNBs, respectively. For $s \in \{R, U\}$, consider the event in which the test VN connects to a LoS gNB, at distance r_L. Such an event requires the LoS gNB to have smaller path loss than that of the nearest NLoS gNB, at distance r_N. The probability $P_L^{(s)}$ of connecting to

the LoS gNB can therefore be expressed as

$$\begin{aligned} P_L^{(s)} &= \mathbb{P}\Big[C_L r_L^{-\alpha_L} > C_N r_N^{-\alpha_N}\Big] = \mathbb{P}\Big[r_N^{-\alpha_N} < \Big(C_L/C_N\Big) r_L^{-\alpha_L}\Big] \\ &= \mathbb{P}\Big[r_N^{\alpha_N} > \Big(C_N/C_L\Big) r_L^{\alpha_L}\Big] = \mathbb{P}\Big[r_N > \Big((C_N/C_L) r_L^{\alpha_L}\Big)^{\frac{1}{\alpha_N}}\Big] \\ &= \int_W^\infty \mathbb{P}\Big[r_N > A_L(r)\Big] f_L^{(s)}(r)\mathrm{d}r \end{aligned} \tag{A.17}$$

where the last step follows from the fact that $r > W$ by construction and that $f_L^{(s)}(r)$ is the PDF of r_L, as per Lemma 1. From Lemma 1 and considering the highway scenario represented in Figure A.1(b), $\mathbb{P}[r_N > A_L(r)]$ can be regarded as the probability that there are no NLoS gNBs within the interval $[-b(A_L(r)),\, b(A_L(r))]$, with

$$b\Big(A_L(r)\Big) = \sqrt{A_L(r)^2 - W^2} \tag{A.18}$$

and can be written as

$$\mathbb{P}[r_N > A_L(r)] = \exp\left(-2\lambda_b \int_0^{b(A_L(r))} p_N^{(s)}(x)\mathrm{d}x\right) \tag{A.19}$$

By substituting Equation (A.19) into Equation (A.17), we get Lemma 2 for the LoS scenario. The proof for the NLoS case follows the same line of reasoning. ■

A.5 Appendix – Proof of Theorem 1

Let $r_i^{n^*}$ be the random variable expressing the distance to the serving gNB $n^* \in \Phi_i$, for $i \in \{L, N\}$. The joint probability $\mathbb{P}[\mathrm{SINR} > \Gamma,\, n^* \in \Phi_i]$ in Equation (5.40) can be expressed as

$$\begin{aligned} \mathbb{P}\Big[\mathrm{SINR} > \Gamma,\, n^* \in \Phi_i\Big] &= \mathbf{E}_{r_i^{n^*}}\Big[\mathbb{P}[\mathrm{SINR}_i > \Gamma \mid r_i^{n^*}]\Big] \\ &\overset{(a)}{=} \mathbf{E}_{r_i^{n^*}}\left\{\mathbb{P}\left[\frac{|h_1|^2 \Delta_1 C_i r_i^{-\alpha_i}}{(I_L + I_N) + \sigma^2} > \Gamma \;\middle|\; r_i^{n^*}\right]\right\} \\ &= \int_W^\infty \mathbb{P}\left[\frac{|h_1|^2 \Delta_1 C_i r^{-\alpha_i}}{(I_L + I_N) + \sigma^2} > \Gamma \;\middle|\; r\right] \bar{f}_i^{(s)}(r)\mathrm{d}r \\ &= \int_W^\infty \mathbb{P}\left[|h_1|^2 > \frac{\Big[(I_L + I_N) + \sigma^2\Big]\Gamma r^{\alpha_i}}{\Delta_1 C_i} \;\middle|\; r\right] \bar{f}_i^{(s)}(r)\mathrm{d}r \end{aligned} \tag{A.20}$$

where (a) has been obtained by using the definition of SINR_i in Equation (5.34). Now, since $|h_1|^2$ is exponentially distributed with mean μ, the probability term inside Equation (A.20)

can be expressed as

$$\mathbb{P}\left[|h_1|^2 > \frac{\Big[(I_L+I_N)+\sigma^2\Big]\Gamma r^{\alpha_i}}{\Delta_1 C_i} \;\Big|\; r\right] = \mathbb{E}_{r,I_L,I_N}\left\{\mathbb{P}\left[|h_1|^2 > \frac{\Big[(I_L+I_N)+\sigma^2\Big]\Gamma r^{\alpha_i}}{\Delta_1 C_i} \;\Big|\; r, I_L, I_N\right]\right\}$$
$$= \mathbb{E}_{I_L,I_N}\left[\exp\left(\frac{-\mu\sigma^2\Gamma r^{\alpha_i}}{\Delta_1 C_i}\right)\exp\left(\frac{-\mu I_L\Gamma r^{\alpha_i}}{\Delta_1 C_i}\right)\exp\left(\frac{-\mu I_N\Gamma r^{\alpha_i}}{\Delta_1 C_i}\right) \;\Big|\; I_L, I_N\right]$$
$$\overset{(b)}{=} \exp\left(\frac{-\mu\sigma^2\Gamma r^{\alpha_i}}{\Delta_1 C_i}\right)\mathcal{L}^{(s)}_{I_i^L}\left(\frac{\mu\Gamma r^{\alpha_i}}{\Delta_1 C_i}\right)\mathcal{L}^{(s)}_{I_i^N}\left(\frac{\mu\Gamma r^{\alpha_i}}{\Delta_1 C_i}\right) \tag{A.21}$$

where (b) derives from the definition of Laplace transform $\mathcal{L}_{\mathcal{X}}(t) \triangleq \mathbf{E}[e^{-t\mathcal{X}}]$. By substituting Equation (A.21) into Equation (A.20), the coverage probability becomes

$$\mathbb{P}\Big[\text{SINR} > \Gamma,\, n^* \in \Phi_i\Big] = \int_W^\infty \exp\left(\frac{-\mu\sigma^2\Gamma r^{\alpha_i}}{\Delta_1 C_i}\right)\mathcal{L}^{(s)}_{I_i^L}\left(\frac{\mu\Gamma r^{\alpha_i}}{\Delta_1 C_i}\right)\mathcal{L}^{(s)}_{I_i^N}\left(\frac{\mu\Gamma r^{\alpha_i}}{\Delta_1 C_i}\right)\bar{f}_i^{(s)}(r)\mathrm{d}r \tag{A.22}$$

Given that the test VN is associated to gNB $n^* \in \Phi_i$, the Laplace transform of the interference from gNBs $\in \Phi_j$ to the test VN is obtained as follows

$$\mathcal{L}^{(s)}_{I_i^j}(t) \triangleq \mathbf{E}_{\Phi_j,h,\Delta_I}\Big[e^{-tI}\Big] = \mathbf{E}_{\Phi_j,h,\Delta_I}\left[\exp\left(-t\sum_{k\in\Phi_j}|h_k|^2\ell_j(r_k)\Delta_{I_k}\right)\right]$$
$$\overset{(a)}{=} \mathbf{E}_{\Phi_j}\left\{\prod_{k\in\Phi_j}\mathbf{E}_{h,\Delta_I}\left[\exp\Big(-t|h_k|^2 r_k^{-\alpha_j}C_j\Delta_{I_k}\Big)\right]\right\}$$
$$\overset{(b)}{=} \exp\left(-2\lambda_b\int_{\left(\frac{C_j}{C_i}r^{\alpha_i}\right)^{\frac{1}{\alpha_j}}}^\infty\Big\{1-\mathbf{E}_{h_k,\Delta_{I_k}}\Big[\exp\Big(-t|h_k|^2 v^{-\alpha_j}C_j\Delta_{I_k}\Big)\Big]\Big\}p_j^{(s)}(v)\mathrm{d}v\right) \tag{A.23}$$

where (a) follows from the i.i.d. distribution of the interferers channel parameters $|h_k|^2$ and from the further independence from the point process Φ_j, (b) derives from the symmetry of the scenario, and by applying the probability generating functional of the PPP [159]. Moreover, using the moment generating function of exponentially distributed $|h_k|^2$'s, that is

$$\mathbf{E}_{h_k}\Big[\exp\Big(-t|h_k|^2 v^{-\alpha_j}C_j\Delta_{I_k}\Big)\Big] = \frac{\frac{1}{\mu}}{\frac{1}{\mu}+tv^{-\alpha_j}C_j\Delta_{I_k}} \tag{A.24}$$

and from the consideration that Δ_{I_k} are discrete random variables with $\mathbb{P}[\Delta_I = G_b G_{\text{VN}}] = \theta_b/\pi$ and $\mathbb{P}[\Delta_I = g_b g_{\text{VN}}] = 1-(\theta_b/\pi)$, the expression for $\mathcal{L}^{(s)}_{I_i^j}(t)$ in (A.23) can be further

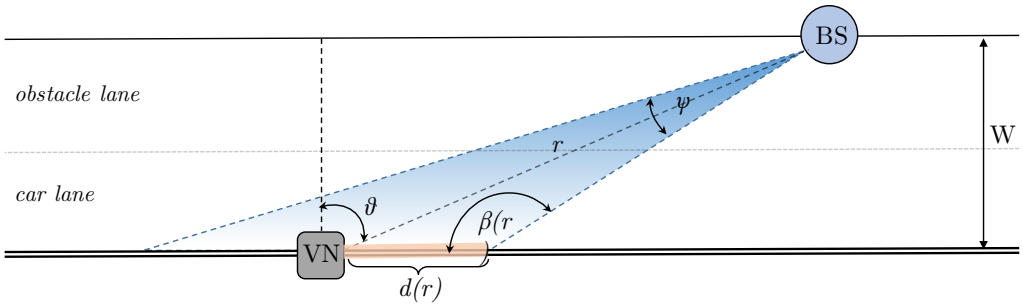

Figure A.2: Illustration of a half section of a highway of width W, as a support to the proof of Theorem 2.

written as

$$\mathcal{L}_{I_i^j}^{(s)}(t) = \exp\left(-2\lambda_b \int_{\left(\frac{C_j}{C_i} r^{\alpha_i}\right)^{\frac{1}{\alpha_j}}}^{\infty} \left[1 - \left(\frac{\frac{1}{\mu}(\theta_b/\pi)}{\frac{1}{\mu} + tv^{-\alpha_j} C_j G_b G_{\mathrm{VN}}} + \right.\right.\right. \\ \left.\left.\left. + \frac{\frac{1}{\mu}[1-(\theta_b/\pi)]}{\frac{1}{\mu} + tv^{-\alpha_j} C_j g_b g_{\mathrm{VN}}} \right) \right] p_j^{(s)}(v) \mathrm{d}v \right) \tag{A.25}$$

By combining Equations (A.22) and (A.25), the proof is concluded. ■

A.6 Appendix – Proof of Theorem 2

Suppose that, at the beginning of a slot of duration T_S, the target VN is connected with a gNB at distance r (w.p. $P_{cov}^{(s)}(\Gamma)$). According to the considerations we made, the main lobe center of the gNB's transmit beam points at its associated VN, as illustrated in Figure A.2. According to the *law of sines*, the quantity $d(r)$ that represents the maximum distance that the node can cover before leaving the communication range of its serving gNB is defined as

$$d(r) \triangleq \frac{r \sin(\psi/2)}{\sin(\beta(r))} \tag{A.26}$$

where ψ is the beamwidth of the gNB's main lobe and, from the trigonometric identities, $\beta(r) = \eta + \theta(r)$, with $\eta = \pi/2 - \psi/2$ and $\theta(r) = \arccos(W/r)$. Notice that $d(r)$ increases with r due to the resulting wider geometric projection of the gNB's beam onto the road surface. That being said, the probability that the VN does not disconnect from its serving infrastructure can be viewed as the probability that the VN does not cover a distance greater than $d(r)$ within the slot. The distance covered by the VN, moving at speed V, within the

slot of duration T_S is VT_S, therefore

$$\begin{aligned}
P_{NL} &= \mathbb{P}[T_L > T_S] = \mathbb{P}\left[VT_S < d(r)\right] \\
&= \mathbb{P}\left[VT_S < \frac{r\sin(\psi/2)}{\sin(\beta(r))}\right] \\
&= \mathbb{P}\left[r > \frac{VT_S\sin(\beta(r))}{\sin(\psi/2)}\right] \\
&= \mathbb{P}\left[r > \frac{VT_S\sin\Big(\overbrace{\pi/2-\psi/2}^{\eta}+\overbrace{\arccos(W/r)}^{\theta(r)}\Big)}{\sin(\psi/2)}\right] \\
&\overset{(a)}{=} \mathbb{P}\left[r > \frac{VT_S}{\sin(\psi/2)}\Big(\sin(\eta)\cos(\arccos(W/r)) + \cos(\eta)\sin(\arccos(W/r))\Big)\right] \\
&\overset{(b)}{=} \mathbb{P}\left[r > \frac{VT_S}{\sin(\psi/2)}\left(\frac{W}{r}\sin(\eta) + \sqrt{1-\left(\frac{W}{r}\right)^2}\cos(\eta)\right)\right]
\end{aligned} \tag{A.27}$$

where (a) derives from the trigonometric addition formula

$$\sin(\eta+\theta(r)) = \sin(\eta)\cos(\theta(r)) + \cos(\eta)\sin(\theta(r)) \tag{A.28}$$

and (b) from the trigonometric identities

$$\cos\Big(\arccos(x)\Big) = x \tag{A.29}$$

$$\sin\Big(\arccos(x)\Big) = \sqrt{1-x^2} \tag{A.30}$$

The expressions in (A.27) and (5.44) coincide, concluding the proof. ■

List of Publications

All the research activities presented in this thesis has in part appeared in my articles reported below.

Journal Papers

[**J1**] **M. Rebato**, F. Boccardi, M. Mezzavilla, S. Rangan, and M. Zorzi, "Hybrid Spectrum Sharing in mmWave Cellular Networks," IEEE Transactions on Cognitive Communications and Networking, vol. 3, no. 2, pp. 155–168, June 2017. doi: 10.1109/TCCN.2017.2707551

[**J2**] M. Giordani, **M. Rebato**, A. Zanella, and M. Zorzi, "Coverage and connectivity analysis of millimeter wave vehicular networks," Ad Hoc Networks, vol. 80, pp. 158 – 171, 2018. doi: 10.1016/j.adhoc.2018.08.007.

[**J3**] **M. Rebato**, J. Park, P. Popovski, E. De Carvalho, and M. Zorzi, "Stochastic Geometric Coverage Analysis in mmWave Cellular Networks With Realistic Channel and Antenna Radiation Models," IEEE Transactions on Communications, vol. 67, no. 5, pp. 3736– 3752, May 2019. doi: 10.1109/TCOMM.2019.2895850

[**J4**] **M. Rebato**, L. Rose and M. Zorzi, "Tilt Angle Optimization in Dynamic-TDD mmWave Cellular Scenarios", submitted to IEEE Communication Letter.

Conference and Workshop Papers

[**C1**] **M. Rebato**, J. Park, P. Popovski, E. de Carvalho, and M. Zorzi, "Stochastic Geometric Coverage Analysis in mmWave Cellular Networks with a Realistic Channel Model," in Proc. IEEE Glob. Commun. Conf. Mobile Wireless Netw. (Globecom MWN), Singapore, Dec. 2017.

[**C2**] M. Giordani, **M. Rebato**, A. Zanella, and M. Zorzi, "Poster: Connectivity analysis of millimeter wave vehicular networks," in 2017 IEEE Vehicular Networking Conference (VNC), Nov 2017, pp. 41–42.

[**C3**] **M. Rebato**, L. Resteghini, C. Mazzucco, and M. Zorzi, "Study of Realistic Antenna Patterns in 5G mmWave Cellular Scenarios," in IEEE ICC 2018 Communications QoS, Reliability, and Modeling Symposium, Kansas City, USA, May 2018.

[**C4**] **M. Rebato**, M. Polese, and M. Zorzi, "Multi-Sector and Multi-Panel Performance in 5G mmWave Cellular Networks," in IEEE Global Communications Conference (GLOBECOM), Dec 2018.

[**C5**] **M. Rebato** and M. Zorzi, "A Spectrum Sharing Solution for the Efficient Use of mmWave Bands in 5G Cellular Scenarios," in 2018 IEEE International Symposium on Dynamic Spectrum Access Networks (DySPAN), Oct 2018.

[**C6**] **M. Rebato**, L. Rose, and M. Zorzi, "Performance Assessment of MIMO Precoding on Realistic mmWave Channels," in 2019 IEEE International Conference on Communications Workshops (ICC Workshops), May 2019.

[**C7**] P. Testolina, M. Lecci, **M. Rebato**, A. Testolin, J. Gambini, R. Flamini, C. Mazzucco, and M. Zorzi, "Eenabling Simulation-Based optimization through machine learning: A case study on antenna design," in IEEE Global Communications Conference: Wireless Communications (Globecom2019 WC), Waikoloa, USA, Dec. 2019.

Bibliography

[1] Nokia, "5G use cases and requirements," 2016, white Paper Product code C401-0120031-WP-201608-1-EN.

[2] I.-R. M.-T. P. REQ], "Minimum Requirements Related to Technical Performance for IMT–2020 Radio Interface(s), document ITU-R M.2410-0, International Telecommunication Union Recommendations," Tech. Rep., Nov. 2017.

[3] 3GPP TR 38.802, "Study on New Radio (NR) Access Technology - Physical Layer Aspects - Release 14," Tech. Rep., 2017.

[4] M. Rebato, M. Mezzavilla, S. Rangan, F. Boccardi, and M. Zorzi, "Understanding Noise and Interference Regimes in 5G Millimeter-Wave Cellular Networks," in *22th European Wireless Conference*, May 2016.

[5] M. Rebato, "Simulation analysis of algorithms for interference management in 5G cellular networks using spatial spectrum sharing," *Master Thesis*, 2015.

[6] M. Rebato, M. Mezzavilla, S. Rangan, and M. Zorzi, "Resource Sharing in 5G mmWave Cellular Networks," in *IEEE Conference on Computer Communications Workshops (INFOCOM WKSHPS)*, April 2016, pp. 271–276.

[7] M. Rebato, F. Boccardi, M. Mezzavilla, S. Rangan, and M. Zorzi, "Hybrid Spectrum Access for mmWave Networks," in *2016 Mediterranean Ad Hoc Networking Workshop (Med-Hoc-Net)*, June 2016.

[8] Ericsson, "5G radio access," February 2015, white Paper Uen 284 23-3204 Rev B.

[9] H. Shokri-Ghadikolaei, C. Fischione, G. Fodor, P. Popovski, and M. Zorzi, "Millimeter Wave Cellular Networks: A MAC Layer Perspective," *IEEE Transactions on Communications*, vol. 63, no. 10, pp. 3437–3458, Oct 2015.

[10] S. Rangan, T. S. Rappaport, and E. Erkip, "Millimeter-Wave Cellular Wireless Networks: Potentials and Challenges," *Proceedings of the IEEE*, vol. 102, no. 3, pp. 366–385, March 2014.

[11] T. S. Rappaport, S. Sun, R. Mayzus, H. Zhao, Y. Azar, K. Wang, G. N. Wong, J. K. Schulz, M. Samimi, and F. Gutierrez, "Millimeter Wave Mobile Communications for 5G Cellular: It Will Work!" *IEEE Access*, vol. 1, pp. 335–349, 2013.

[12] S. Rajagopal, S. Abu-Surra, Z. Pi, and F. Khan, "Antenna Array Design for Multi-Gbps mmWave Mobile Broadband Communication," in *Global Telecommunications Conference (GLOBECOM 2011), 2011 IEEE*, Dec 2011.

[13] E. G. Larsson, O. Edfors, F. Tufvesson, and T. L. Marzetta, "Massive MIMO for next generation wireless systems," *IEEE Communications Magazine*, vol. 52, no. 2, pp. 186–195, February 2014.

[14] L. Lu, G. Li, A. Swindlehurst, A. Ashikhmin, and R. Zhang, "An Overview of Massive MIMO: Benefits and Challenges," *Selected Topics in Signal Processing, IEEE Journal of*, vol. 8, no. 5, pp. 742–758, Oct 2014.

[15] B. Van Veen and K. Buckley, "Beamforming: a versatile approach to spatial filtering," *ASSP Magazine, IEEE*, vol. 5, no. 2, pp. 4–24, April 1988.

[16] T. Wu, T. Rappaport, and C. Collins, "The Human Body and Millimeter-Wave Wireless Communication Systems: Interactions and Implications," in *IEEE International Conference on Communications (ICC)*, June 2015, pp. 2423–2429.

[17] T. S. Rappaport, R. W. Heath Jr., R. C. Daniels, and J. N. Murdock, *Millimeter Wave Wireless Communications*. Pearson Education, 2014.

[18] Y. Azar, G. Wong, K. Wang, R. Mayzus, J. Schulz, H. Zhao, F. Gutierrez, D. Hwang, and T. Rappaport, "28 GHz Propagation Measurements for Outdoor Cellular Communications Using Steerable Beam Antennas in New York City," in *IEEE International Conference on Communications (ICC)*, June 2013, pp. 5143–5147.

[19] H. Zhao, R. Mayzus, S. Sun, M. Samimi, J. Schulz, Y. Azar, K. Wang, G. Wong, F. Gutierrez, and T. Rappaport, "28 GHz Millimeter Wave Cellular Communication Measurements for Reflection and Penetration Loss in and Around Buildings in New York City," in *IEEE International Conference on Communications (ICC)*, June 2013, pp. 5163–5167.

[20] M. Samimi, K. Wang, Y. Azar, G. Wong, R. Mayzus, H. Zhao, J. Schulz, S. Sun, F. Gutierrez, and T. Rappaport, "28 GHz Angle of Arrival and Angle of Departure

Analysis for Outdoor Cellular Communications Using Steerable Beam Antennas in New York City," in *IEEE 77th Vehicular Technology Conference (VTC Spring)*, June 2013.

[21] M. Akdeniz, Y. Liu, M. Samimi, S. Sun, S. Rangan, T. Rappaport, and E. Erkip, "Millimeter Wave Channel Modeling and Cellular Capacity Evaluation," *IEEE Journal on Selected Areas in Communications*, vol. 32, no. 6, pp. 1164–1179, June 2014.

[22] P. Kyosti and et al., "WINNER II channel model," *Technical Report IST-WINNER D1.1.2 ver 1.1*, Sept. 2007.

[23] M. K. Samimi and T. S. Rappaport, "3-D statistical channel model for millimeter-wave outdoor mobile broadband communications," in *IEEE International Conference on Communications (ICC)*, June 2015, pp. 2430–2436.

[24] M. Rebato, F. Boccardi, M. Mezzavilla, S. Rangan, and M. Zorzi, "Hybrid Spectrum Sharing in mmWave Cellular Networks," *IEEE Transactions on Cognitive Communications and Networking*, vol. 3, no. 2, pp. 155–168, June 2017.

[25] M. Rebato and M. Zorzi, "A Spectrum Sharing Solution for the Efficient Use of mm-Wave Bands in 5G Cellular Scenarios," in *2018 IEEE International Symposium on Dynamic Spectrum Access Networks (DySPAN)*, Oct 2018.

[26] R. Baldemair, T. Irnich, K. Balachandran, E. Dahlman, G. Mildh, Y. Selen, S. Parkvall, M. Meyer, and A. Osseiran, "Ultra-Dense Networks in Millimeter-Wave Frequencies," *IEEE Communications Magazine*, vol. 53, no. 1, pp. 202–208, January 2015.

[27] S. Larew, T. Thomas, M. Cudak, and A. Ghosh, "Air Interface Design and Ray Tracing Study for 5G Millimeter Wave Communications," in *IEEE Globecom Workshops (GC Wkshps)*, Dec 2013, pp. 117–122.

[28] L. Anchora, M. Mezzavilla, L. Badia, and M. Zorzi, "Simulation Models for the Performance Evaluation of Spectrum Sharing Techniques in OFDMA Networks," in *Proceedings of the 14th ACM International Conference on Modeling, Analysis and Simulation of Wireless and Mobile Systems*, ser. MSWiM '11. New York, NY, USA: ACM, 2011, pp. 249–256.

[29] P. Karunakaran, T. Wagner, A. Scherb, and W. Gerstacker, "Sensing for Spectrum Sharing in Cognitive LTE-A Cellular Networks," in *IEEE Wireless Communications and Networking Conference (WCNC)*, April 2014, pp. 565–570.

[30] L. Badia, R. Del Re, F. Guidolin, A. Orsino, and M. Zorzi, "A Tunable Framework for Performance Evaluation of Spectrum Sharing in LTE Networks," in *IEEE 14th Inter-*

national Symposium and Workshops on a World of Wireless, Mobile and Multimedia Networks (WoWMoM), June 2013.

[31] W. Feng, Y. Li, D. Jin, and L. Zeng, "Inter-Network Spatial Sharing with Interference Mitigation Based on IEEE 802.11ad WLAN System," in *Globecom Workshops (GC Wkshps)*, Dec 2014, pp. 752–758.

[32] R. Cai, Q. Chen, X. Peng, and D. Liu, "Spatial Sharing Algorithm in mmWave WPANs with Interference Sense Beamforming Mechanism," in *IEEE Military Communications Conference, MILCOM 2013*, Nov 2013, pp. 163–168.

[33] G. Li, T. Irnich, and C. Shi, "Coordination Context-Based Spectrum Sharing for 5G Millimeter-Wave Networks," in *9th International Conference on Cognitive Radio Oriented Wireless Networks and Communications (CROWNCOM)*, June 2014, pp. 32–38.

[34] J. Luo, J. Eichinger, Z. Zhao, and E. Schulz, "Multi-Carrier Waveform Based Flexible Inter-Operator Spectrum Sharing for 5G Systems," in *IEEE International Symposium on Dynamic Spectrum Access Networks (DYSPAN)*, April 2014, pp. 449–457.

[35] A. K. Gupta, J. G. Andrews, and R. W. Heath, "On the Feasibility of Sharing Spectrum Licenses in mmWave Cellular Systems," *IEEE Trans. Commun.*, vol. 64, no. 9, pp. 3981–3995, Sep. 2016.

[36] H. ElSawy, E. Hossain, and D. I. Kim, "Hetnets with Cognitive Small Cells: User Offloading and Distributed Channel Access Techniques," *IEEE Communications Magazine*, vol. 51, no. 6, pp. 28–36, June 2013.

[37] T. Frisanco, P. Tafertshofer, P. Lurin, and R. Ang, "Infrastructure Sharing and Shared Operations for Mobile Network Operators from a Deployment and Operations View," in *IEEE Network Operations and Management Symposium (NOMS)*, April 2008, pp. 129–136.

[38] Cisco, "Cisco Visual Networking Index: Global Mobile Data Traffic Forecast Update, 2016–2021," *White Paper*, March 2017.

[39] Radio spectrum policy group, "Strategic spectrum roadmap towards 5G for Europe, RSPG Second Opinion on 5G networks, RSPG18-005 FINAL," Tech. Rep., 2018.

[40] F. Guidolin, M. Nekovee, L. Badia, and M. Zorzi, "A study on the coexistence of fixed satellite service and cellular networks in a mmWave scenario," in *IEEE International Conference on Communications (ICC)*, June 2015, pp. 2444–2449.

[41] M. Massaro, "Next generation of radio spectrum management: Licensed shared access for 5G," *Telecommunications Policy*, vol. 41, no. 5, pp. 422 – 433, 2017.

[42] R. Umar, A. U. H. Sheikh, M. Deriche, M. Shoaib, and M. Hadi, "Multi-operator spectrum sharing in next generation wireless communications networks: A short review and roadmap to future," in *International Symposium on Wireless Systems and Networks (ISWSN)*, Nov 2017.

[43] S. Bhattarai, J. M. J. Park, B. Gao, K. Bian, and W. Lehr, "An Overview of Dynamic Spectrum Sharing: Ongoing Initiatives, Challenges, and a Roadmap for Future Research," *IEEE Transactions on Cognitive Communications and Networking*, vol. 2, no. 2, pp. 110–128, June 2016.

[44] R. H. Tehrani, S. Vahid, D. Triantafyllopoulou, H. Lee, and K. Moessner, "Licensed Spectrum Sharing Schemes for Mobile Operators: A Survey and Outlook," *IEEE Communications Surveys and Tutorials*, vol. 18, no. 4, pp. 2591–2623, Fourth quarter 2016.

[45] F. Boccardi, H. Shokri-Ghadikolaei, G. Fodor, E. Erkip, C. Fischione, M. Kountouris, P. Popovski, and M. Zorzi, "Spectrum Pooling in MmWave Networks: Opportunities, Challenges, and Enablers," *IEEE Communications Magazine*, vol. 54, no. 11, pp. 33–39, November 2016.

[46] A. Lertsinsrubtavee, N. Malouch, and S. Fdida, "Hybrid spectrum sharing through adaptive spectrum handoff for cognitive radio networks," in *IFIP Networking Conference*, June 2014, pp. 1–9.

[47] A. Merwaday, M. Yuksel, T. Quint, I. Güvenç, W. Saad, and N. Kapucu, "Incentivizing spectrum sharing via subsidy regulations for future wireless networks," *Computer Networks*, vol. 135, pp. 132–146, 2018.

[48] Y. Luo, L. Gao, and J. Huang, "Spectrum broker by geo-location database," in *IEEE Global Communications Conference (GLOBECOM)*, Dec 2012, pp. 5427–5432.

[49] Allegato B alla delibera n. 89/18/CONS, "Consultazione pubblica sulle procedure per l'assegnazione e le regole per l'utilizzo delle frequenze disponibili nelle bande 694-790 MHz, 3600-3800 MHz e 26.5-27.5 GHz per sistemi terrestri di comunicazioni elettroniche al fine di favorire la transizione verso la tecnologia 5G, ai sensi della legge 27 dicembre 2017, n. 205," Tech. Rep., 2018.

[50] M. Rebato, L. Resteghini, C. Mazzucco, and M. Zorzi, "Study of Realistic Antenna Patterns in 5G mmWave Cellular Scenarios," in *IEEE ICC 2018 Communications QoS, Reliability, and Modeling Symposium*, Kansas City, USA, May 2018.

[51] R. Jain, D. M. Chiu, and W. Hawe, "A Quantitative Measure of Fairness and Discrimination for Resource Allocation in Shared Computer Systems," *DEC Research Report TR-301*, 1984.

[52] Z. Pi and F. Khan, "An introduction to millimeter-wave mobile broadband systems," *IEEE Communications Magazine*, vol. 49, no. 6, pp. 101–107, June 2011.

[53] F. Boccardi, R. W. Heath, A. Lozano, T. L. Marzetta, and P. Popovski, "Five disruptive technology directions for 5G," *IEEE Communications Magazine*, vol. 52, no. 2, pp. 74–80, February 2014.

[54] J. G. Andrews, F. Baccelli, and R. K. Ganti, "A Tractable Approach to Coverage and Rate in Cellular Networks," *IEEE Transactions on Communications*, vol. 59, no. 11, pp. 3122–3134, Nov 2011.

[55] E. Perahia, C. Cordeiro, M. Park, and L. L. Yang, "IEEE 802.11ad: Defining the Next Generation Multi-Gbps Wi-Fi," in *7th IEEE Consumer Communications and Networking Conference*, Jan 2010.

[56] E. Perahia and M. X. Gong, "Gigabit Wireless LANs: An Overview of IEEE 802.11ac and 802.11ad," *SIGMOBILE Mob. Comput. Commun. Rev.*, vol. 15, no. 3, pp. 23–33, Nov. 2011. [Online]. Available: http://doi.acm.org/10.1145/2073290.2073294

[57] W. Roh, J. Y. Seol, J. Park, B. Lee, J. Lee, Y. Kim, J. Cho, K. Cheun, and F. Aryanfar, "Millimeter-wave beamforming as an enabling technology for 5G cellular communications: theoretical feasibility and prototype results," *IEEE Commun. Mag*, vol. 52, no. 2, pp. 106–113, Feb. 2014.

[58] A. Osseiran, F. Boccardi, V. Braun, K. Kusume, P. Marsch, M. Maternia, O. Queseth, M. Schellmann, H. Schotten, H. Taoka, H. Tullberg, M. A. Uusitalo, B. Timus, and M. Fallgren, "Scenarios for 5G mobile and wireless communications: the vision of the METIS project," *IEEE Communications Magazine*, vol. 52, no. 5, pp. 26–35, May 2014.

[59] NGMN Alliance, "5G white paper," *Next Generation Mobile Networks, White paper*, February 2015.

[60] F. Gómez-Cuba, S. Rangan, and E. Erkip, "Scaling Laws for Infrastructure Single and Multihop Wireless Networks in Wideband Regimes," in *IEEE International Symposium on Information Theory (ISIT)*, June 2014, pp. 76–80.

[61] A. Ghosh, T. A. Thomas, M. C. Cudak, R. Ratasuk, P. Moorut, F. W. Vook, T. S. Rappaport, G. R. MacCartney, S. Sun, and S. Nie, "Millimeter-wave enhanced local area systems: A high-data-rate approach for future wireless networks," *IEEE Journal on Selected Areas in Communications*, vol. 32, no. 6, pp. 1152–1163, June 2014.

[62] J. G. Andrews, "Seven ways that HetNets are a cellular paradigm shift," *IEEE Communications Magazine*, vol. 51, no. 3, pp. 136–144, March 2013.

[63] H. Ishii, Y. Kishiyama, and H. Takahashi, "A novel architecture for LTE-B: C-plane/U-plane split and Phantom Cell concept," in *IEEE Globecom Workshops*, Dec 2012, pp. 624–630.

[64] H. Elshaer, M. N. Kulkarni, F. Boccardi, J. G. Andrews, and M. Dohler, "Downlink and Uplink Cell Association with Traditional Macrocells and Millimeter Wave Small Cells," *IEEE Transactions on Wireless Communications*, vol. 15, no. 9, pp. 6244–6258, Sept 2016.

[65] ITU-R, "Final acts WRC-15," Tech. Rep., Dec. 2015.

[66] T. A. Weiss and F. K. Jondral, "Spectrum pooling: an innovative strategy for the enhancement of spectrum efficiency," *IEEE Communications Magazine*, vol. 42, no. 3, pp. S8–14, Mar 2004.

[67] METIS, "Deliverable 5.1, intermediate description of spectrum needs and usage principles," Tech. Rep., 2013.

[68] T. Irnich, J. Kronander, Y. Selén, and G. Li, "Spectrum sharing scenarios and resulting technical requirements for 5G systems," in *IEEE 24th International Symposium on Personal, Indoor and Mobile Radio Communications (PIMRC Workshops)*, Sept 2013, pp. 127–132.

[69] A. K. Gupta, A. Alkhateeb, J. G. Andrews, and R. W. Heath, "Gains of restricted secondary licensing in millimeter wave cellular systems," *IEEE Journal on Selected Areas in Communications*, vol. 34, no. 11, pp. 2935–2950, Nov 2016.

[70] G. Zheng and Q. Guan, "Routing and spectrum sharing in geo-location database assisted secondary multi-hop networks," in *IEEE International Conference on Communications (ICC)*, June 2014, pp. 1669–1674.

[71] M. Matinmikko, H. Okkonen, M. Palola, S. Yrjola, P. Ahokangas, and M. Mustonen, "Spectrum sharing using licensed shared access: the concept and its workflow for lte-advanced networks," *IEEE Wireless Communications*, vol. 21, no. 2, pp. 72–79, April 2014.

[72] 3GPP TR 36.889 v1.0.1, "Study on licensed-assisted access to unlicensed spectrum," Tech. Rep., 2015.

[73] A. Mukherjee, J. F. Cheng, S. Falahati, H. Koorapaty, D. H. Kang, R. Karaki, L. Falconetti, and D. Larsson, "Licensed-Assisted Access LTE: coexistence with IEEE 802.11 and the evolution toward 5G," *IEEE Communications Magazine*, vol. 54, no. 6, pp. 50–57, June 2016.

[74] F. M. Abinader, E. P. L. Almeida, F. S. Chaves, A. M. Cavalcante, R. D. Vieira, R. C. D. Paiva, A. M. Sobrinho, S. Choudhury, E. Tuomaala, K. Doppler, and V. A. Sousa, "Enabling the coexistence of LTE and Wi-Fi in unlicensed bands," *IEEE Communications Magazine*, vol. 52, no. 11, pp. 54–61, Nov 2014.

[75] 3GPP, "Liaison from 3GPP on LWA and LWIP," Tech. Rep., Mar 2016.

[76] A. Galanopoulos, F. Foukalas, and T. A. Tsiftsis, "Efficient Coexistence of LTE With WiFi in the Licensed and Unlicensed Spectrum Aggregation," *IEEE Transactions on Cognitive Communications and Networking*, vol. 2, no. 2, pp. 129–140, June 2016.

[77] H. Shokri-Ghadikolaei, F. Boccardi, C. Fischione, G. Fodor, and M. Zorzi, "On the value of Beamforming and Coordination for Spectrum Sharing in mmWave Cellular Networks," *IEEE Journal on Selected Areas in Communications*, vol. 34, no. 11, pp. 2902–2917, Nov 2016.

[78] F. Fund, S. Shahsavari, S. S. Panwar, E. Erkip, and S. Rangan, "Spectrum and infrastructure sharing in millimeter wave cellular networks: An economic perspective," *CoRR*, vol. abs/1605.04602, 2016. [Online]. Available: http://arxiv.org/abs/1605.04602

[79] D. Tse and P. Viswanath, *Fundamentals of Wireless Communication*. New York, NY, USA: Cambridge University Press, 2005.

[80] H. Kim, G. de Veciana, X. Yang, and M. Venkatachalam, "Distributed α-Optimal User Association and Cell Load Balancing in Wireless Networks," *IEEE/ACM Transactions on Networking*, vol. 20, no. 1, pp. 177–190, Feb 2012.

[81] P. Coucheney, C. Touati, and B. Gaujal, "Fair and Efficient User-Network Association Algorithm for Multi-Technology Wireless Networks," in *IEEE INFOCOM*, April 2009, pp. 2811–2815.

[82] Q. Ye, B. Rong, Y. Chen, M. Al-Shalash, C. Caramanis, and J. G. Andrews, "User Association for Load Balancing in Heterogeneous Cellular Networks," *IEEE Transactions on Wireless Communications*, vol. 12, no. 6, pp. 2706–2716, June 2013.

[83] C. Kim, R. Ford, and S. Rangan, "Joint interference and user association optimization in cellular wireless networks," in *48th Asilomar Conference on Signals, Systems and Computers*, Nov 2014, pp. 511–515.

[84] M. Rebato, J. Park, P. Popovski, E. de Carvalho, and M. Zorzi, "Stochastic Geometric Coverage Analysis in mmWave Cellular Networks with a Realistic Channel Model," in *Proc. IEEE Glob. Commun. Conf. Mobile Wireless Netw. (Globecom MWN)*, Singapore, Dec. 2017.

[85] M. Rebato, M. Polese, and M. Zorzi, "Multi-Sector and Multi-Panel Performance in 5G mmWave Cellular Networks," in *IEEE Global Communications Conference (GLOBECOM)*, Dec 2018.

[86] M. Rebato, L. Rose, and M. Zorzi, "Performance Assessment of MIMO Precoding on Realistic mmWave Channels," in *IEEE International Conference on Communications Workshops (ICC Workshops)*, May 2019.

[87] ——, "Tilt Angle Optimization in Dynamic-TDD mmWave Cellular Scenarios," 2019, *submitted to IEEE Communication Letter*.

[88] P. Testolina, M. Lecci, M. Rebato, A. Testolin, J. Gambini, R. Flamini, C. Mazzucco, and M. Zorzi, "Enabling Simulation-Based Optimization Through Machine Learning: A Case Study on Antenna Design," in *IEEE Global Communications Conference: Wireless Communications (Globecom2019 WC)*, Waikoloa, USA, Dec. 2019.

[89] V. Rabinovich and N. Alexandrov, *Antenna Arrays and Automotive Applications*. Springer-Verlag, New York, NY, USA, 2013.

[90] 3GPP TR 38.901 v14.2.0, "Technical Specification Group Radio Access Network; Study on Channel Model for Frequencies from 0.5 to 100 GHz," Tech. Rep., 2016.

[91] T. Bai and R. W. Heath, "Coverage and Rate Analysis for Millimeter-Wave Cellular Networks," *IEEE Transactions on Wireless Communications*, vol. 14, no. 2, pp. 1100–1114, Feb 2015.

[92] 3GPP TR 37.840 v12.1.0, "Technical Specification Group Radio Access Network; Study of Radio Frequency (RF) and Electromagnetic Compatibility (EMC) requirements for Active Antenna Array System (AAS) base station," Tech. Rep., 2013.

[93] 3GPP TR 36.873 v12.4.0, "Technical Specification Group Radio Access Network; Study on 3D channel model for LTE," Tech. Rep., 2017.

[94] ANSYS HFSS software simulating high-frequency electromagnetic fields. [Online]. Available: http://www.ansys.com/Products/Electronics/ANSYS-HFSS

[95] H. Shokri-Ghadikolaei, C. Fischione, and E. Modiano, "Interference model similarity index and its applications to millimeter-wave networks," *IEEE Transactions on Wireless Communications*, vol. 17, no. 1, pp. 71–85, Jan 2018.

[96] A. Thornburg, T. Bai, and R. W. Heath, "Interference statistics in a random mmwave ad hoc network," in *2015 IEEE International Conference on Acoustics, Speech and Signal Processing (ICASSP)*, April 2015, pp. 2904–2908.

[97] M. Mezzavilla, M. Zhang, M. Polese, R. Ford, S. Dutta, S. Rangan, and M. Zorzi, "End-to-End Simulation of 5G mmWave Networks," *IEEE Communication Surveys & Tutorials*, 2018. [Online]. Available: https://arxiv.org/abs/1705.02882

[98] 3GPP TS 37.340 (Rel. 15), "Evolved Universal Terrestrial Radio Access (E-UTRA) and NR; Multi-connectivity," Tech. Rep., 2018.

[99] M. Polese, M. Mezzavilla, and M. Zorzi, "Performance Comparison of Dual Connectivity and Hard Handover for LTE-5G Tight Integration," in *Proceedings of the 9th EAI International Conference on Simulation Tools and Techniques (SIMUTOOLS)*, 2016, pp. 118–123.

[100] Y. Huo, X. Dong, and W. Xu, "5G Cellular User Equipment: From Theory to Practical Hardware Design," *IEEE Access*, vol. 5, pp. 13 992–14 010, July 2017.

[101] Y. Huo, X. Dong, W. Xu, and M. Yuen, "Cellular and WiFi Co-design for 5G User Equipment," in *2018 IEEE 5G World Forum (5GWF)*, July 2018, pp. 256–261.

[102] H. Yang and T. L. Marzetta, "Performance of Conjugate and Zero-Forcing Beamforming in Large-Scale Antenna Systems," *IEEE J. Sel. Areas Commun.*, vol. 31, no. 2, pp. 172–179, February 2013.

[103] J. Hoydis, S. ten Brink, and M. Debbah, "Massive MIMO in the UL/DL of Cellular Networks: How Many Antennas Do We Need?" *IEEE J. Sel. Areas Commun.*, vol. 31, no. 2, pp. 160–171, February 2013.

[104] D. L. Colon, F. H. Gregorio, and J. Cousseau, "Linear precoding in multi-user massive MIMO systems with imperfect channel state information," in *XVI Workshop on Information Processing and Control (RPIC)*, Oct 2015.

[105] X. Gao, O. Edfors, F. Rusek, and F. Tufvesson, "Linear Pre-Coding Performance in Measured Very-Large MIMO Channels," in *IEEE Vehicular Technology Conference (VTC Fall)*, Sept 2011.

[106] M. E. Hassan, A. E. Falou, and C. Langlais, "Performance assessment of linear precoding for multi-user massive MIMO systems on a realistic 5G mmWave channel," in *IEEE Middle East and North Africa Communications Conference (MENACOMM)*, April 2018.

[107] 3GPP TS 38.104, "Base Station radio transmission and reception," Tech. Rep., Sept. 2018.

[108] 3GPP TS 38.211, "Physical Channels and Modulation," Tech. Rep., Sept. 2018.

[109] 3GPP TS 38.214, " Physical layer procedures for data," Tech. Rep., Sept. 2018.

[110] M. Joham, W. Utschick, and J. A. Nossek, "Linear transmit processing in MIMO communications systems," *IEEE Trans. Signal Process.*, vol. 53, no. 8, pp. 2700–2712, Aug 2005.

[111] C. B. Peel, B. M. Hochwald, and A. L. Swindlehurst, "A vector-perturbation technique for near-capacity multiantenna multiuser communication-part I: channel inversion and regularization," *IEEE Trans. Commun.*, vol. 53, no. 1, pp. 195–202, Jan 2005.

[112] L. Rose and M. Maso, "Receiver-Centric Inter-Cell Interference Cancellation in D2D-Assisted Networks," in *IEEE Globecom Workshops*, Dec 2016.

[113] A. Müller, A. Kammoun, E. Björnson, and M. Debbah, "Efficient linear precoding for massive MIMO systems using truncated polynomial expansion," in *IEEE 8th Sensor Array and Multichannel Signal Processing Workshop (SAM)*, June 2014, pp. 273–276.

[114] V. Angelakis, S. Papadakis, V. A. Siris, and A. Traganitis, "Adjacent Channel Interference in 802.11a is Harmful: Testbed Validation of a Simple Quantification Model," *Comm. Mag.*, vol. 49, no. 3, pp. 160–166, Mar. 2011.

[115] A. Khoryaev, A. Chervyakov, M. Shilov, S. Panteleev, and A. Lomayev, "Performance analysis of dynamic adjustment of TDD uplink-downlink configurations in outdoor picocell LTE networks," in *IV International Congress on Ultra Modern Telecommunications and Control Systems*, Oct 2012, pp. 914–921.

[116] S. Guo, X. Hou, and H. Wang, "Dynamic TDD and interference management towards 5G," in *IEEE Wireless Communications and Networking Conference (WCNC)*, April 2018.

[117] M. Rebato, J. Park, P. Popovski, E. De Carvalho, and M. Zorzi, "Stochastic Geometric Coverage Analysis in mmWave Cellular Networks With Realistic Channel and Antenna Radiation Models," *IEEE Transactions on Communications*, vol. 67, no. 5, pp. 3736–3752, May 2019.

[118] D. Figueiredo, P. Matos, N. Cota, and A. Rodrigues, *Adjacent channel interference.* Dordrecht: Springer Netherlands, 2006, pp. 186–192.

[119] 3GPP TR 37.842, "Technical Specification Group Radio Access Network; Evolved Universal Terrestrial Radio Access (E-UTRA) and Universal Terrestrial Radio Access (UTRA); Radio Frequency requirement background for Active Antenna System Base Station," Tech. Rep., 2017.

[120] A. Alkhateeb, "DeepMIMO: A Generic Deep Learning Dataset for Millimeter Wave and Massive MIMO Applications," in *Proc. of Information Theory and Applications Workshop (ITA)*, San Diego, CA, Feb 2019.

[121] M. Arnold, S. Dörner, S. Cammerer, S. Yan, J. Hoydis, and S. ten Brink, "Enabling FDD Massive MIMO through Deep Learning-based Channel Prediction," Tech. Rep., Jan 2019, extended version of the conference paper submitted to SPAWC2019. [Online]. Available: https://arxiv.org/pdf/1901.03664.pdf

[122] O. Simeone, "A Very Brief Introduction to Machine Learning With Applications to Communication Systems," *IEEE Transactions on Cognitive Communications and Networking*, vol. 4, no. 4, pp. 648–664, Dec 2018.

[123] T. J. O'Shea and J. Hoydis, "An Introduction to Deep Learning for the Physical Layer," *IEEE Transactions on Cognitive Communications and Networking*, vol. 3, no. 4, pp. 563–575, Dec 2017.

[124] M. Zorzi, A. Zanella, A. Testolin, M. De Filippo De Grazia, and M. Zorzi, "Cognition-Based Networks: A New Perspective on Network Optimization Using Learning and Distributed Intelligence," *IEEE Access*, vol. 3, pp. 1512–1530, 2015.

[125] A. Testolin, M. Zanforlin, M. De Filippo De Grazia, D. Munaretto, A. Zanella, M. Zorzi, and M. Zorzi, "A machine learning approach to QoE-based video admission control and resource allocation in wireless systems," in *13th Annual Mediterranean Ad Hoc Networking Workshop (MED-HOC-NET)*, June 2014, pp. 31–38.

[126] H. Sun, X. Chen, Q. Shi, M. Hong, X. Fu, and N. D. Sidiropoulos, "Learning to Optimize: Training Deep Neural Networks for Interference Management," *IEEE Transactions on Signal Processing*, vol. 66, no. 20, pp. 5438–5453, Oct 2018.

[127] 3GPP, "Study on scenarios and requirements for next generation access technologies," 3rd Generation Partnership Project (3GPP), Technical Report (TR) 38.913, 07 2018, version 15.0.0.

[128] C. M. Bishop, *Pattern Recognition and Machine Learning (Information Science and Statistics)*. Berlin, Heidelberg: Springer-Verlag, 2006.

[129] M. Giordani, M. Rebato, A. Zanella, and M. Zorzi, "Coverage and connectivity analysis of millimeter wave vehicular networks," *Ad Hoc Networks*, vol. 80, pp. 158 – 171, 2018.

[130] M. Giordani, M. Rebato, A. Zanella, and M. Zorzi, "Poster: Connectivity analysis of millimeter wave vehicular networks," in *2017 IEEE Vehicular Networking Conference (VNC)*, Nov 2017, pp. 41–42.

[131] 3GPP TR 38.803, "TR for Study on New Radio Access Technology: RF and co-existence aspects," Tech. Rep., 2017.

[132] H. Wang, K. Huang, and T. A. Tsiftsis, "Base Station Cooperation in Millimeter Wave Cellular Networks: Performance Enhancement of Cell-Edge Users," *IEEE Transactions on Communications*, vol. 66, no. 11, pp. 5124–5139, Nov 2018.

[133] J. G. Andrews, T. Bai, M. N. Kulkarni, A. Alkhateeb, A. K. Gupta, and R. W. Heath, "Modeling and Analyzing Millimeter Wave Cellular Systems," *IEEE Trans. Commun.*, vol. 65, no. 1, pp. 403–430, Jan. 2017.

[134] M. Di Renzo, "Stochastic Geometry Modeling and Analysis of Multi-Tier Millimeter Wave Cellular Networks," *IEEE Trans. Wireless Commun.*, vol. 14, no. 9, pp. 5038–5057, Sept 2015.

[135] J. Park, S. L. Kim, and J. Zander, "Tractable Resource Management With Uplink Decoupled Millimeter-Wave Overlay in Ultra-Dense Cellular Networks," *IEEE Trans. Wireless Commun.*, vol. 15, no. 6, pp. 4362–4379, June 2016.

[136] Y. Li, J. G. Andrews, F. Baccelli, T. D. Novlan, and C. Zhang, "Design and Analysis of Initial Access in Millimeter Wave Cellular Networks," *IEEE Trans. Wireless Commun.*, vol. 16, no. 10, pp. 6409–6425, Oct. 2017.

[137] J. Kim, J. Park, S. Kim, S. L. Kim, K. W. Sung, and K. S. Kim, "Millimeter-Wave Interference Avoidance via Building-Aware Associations," *IEEE Access*, vol. 6, pp. 10 618–10 634, Feb. 2018.

[138] M. N. Kulkarni, E. Visotsky, and J. G. Andrews, "Correction Factor for Analysis of MIMO Wireless Networks With Highly Directional Beamforming," *IEEE Wireless Communications Letters*, vol. 7, no. 5, pp. 756–759, Oct 2018.

[139] M. D. Renzo, W. Lu, and P. Guan, "The Intensity Matching Approach: A Tractable Stochastic Geometry Approximation to System-Level Analysis of Cellular Networks," *IEEE Transactions on Wireless Communications*, vol. 15, no. 9, pp. 5963–5983, Sept 2016.

[140] X. Yu, J. Zhang, M. Haenggi, and K. B. Letaief, "Coverage Analysis for Millimeter Wave Networks: The Impact of Directional Antenna Arrays," *IEEE Journal on Selected Areas in Communications*, vol. 35, no. 7, pp. 1498–1512, July 2017.

[141] N. Deng and M. Haenggi, "A Novel Approximate Antenna Pattern for Directional Antenna Arrays," *IEEE Wireless Communications Letters*, 2018.

[142] M. Mezzavilla, S. Dutta, M. Zhang, M. R. Akdeniz, and S. Rangan, "5G MmWave Module for the ns-3 Network Simulator," in *Proceedings of the 18th ACM International Conference on Modeling, Analysis and Simulation of Wireless and Mobile Systems*, ser. MSWiM '15. New York, NY, USA: ACM, 2015, pp. 283–290.

[143] R. Ford, M. Zhang, S. Dutta, M. Mezzavilla, S. Rangan, and M. Zorzi, "A Framework for End-to-End Evaluation of 5G mmWave Cellular Networks in ns-3," in *Proceedings of the Workshop on ns-3*, ser. WNS3 '16. New York, NY, USA: ACM, 2016, pp. 85–92.

[144] T. S. Rappaport, Y. Xing, G. R. MacCartney, A. F. Molisch, E. Mellios, and J. Zhang, "Overview of Millimeter Wave Communications for Fifth-Generation (5G) Wireless Networks – With a Focus on Propagation Models," *IEEE Trans. Antennas Propag.*, vol. 65, no. 12, pp. 6213–6230, Dec 2017.

[145] M. Haenggi, *Stochastic Geometry for Wireless Networks*. Cambridge Univ. Press, 2013.

[146] R. Tahmasbi and S. Rezaei, "A Two-parameter Lifetime Distribution with Decreasing Failure Rate," *Comput. Stat. Data Anal.*, vol. 52, no. 8, pp. 3889–3901, Apr. 2008.

[147] S. Bennett, "Log-Logistic Regression Models for Survival Data," *J. R. Stat. Soc. Ser. C. Appl. Stat.*, vol. 32, no. 2, pp. 165–171, 1983.

[148] I. W. Burr, "Cumulative Frequency Functions," *The Annals of Mathematical Statistics*, vol. 13, no. 2, pp. 215–232, 1942.

[149] P. Popovski, J. J. Nielsen, C. Stefanovic, E. de Carvalho, E. G. Ström, K. F. Trillingsgaard, A. Bana, D. Kim, R. Kotaba, J. Park, and R. B. Sørensen, "Wireless Access for Ultra-Reliable Low-Latency Communication (URLLC): Principles and Building Blocks," *IEEE Netw.*, vol. 32, no. 2, pp. 16–23, Mar. 2018.

[150] M. Bennis, M. Debbah, and H. V. Poor, "Ultrareliable and Low-Latency Wireless Communication: Tail, Risk, and Scale," *Proceedings of the IEEE*, vol. 106, no. 10, pp. 1834–1853, Oct 2018.

[151] J. Park, D. Kim, P. Popovski, and S.-L. Kim, "Revisiting Frequency Reuse towards Supporting Ultra-Reliable Ubiquitous-Rate Communication," *Proc. IEEE WiOpt Wksp. SpaSWiN, Paris, France*, May 2017.

[152] A. Tassi, M. Egan, R. J. Piechocki, and A. Nix, "Modeling and Design of Millimeter-Wave Networks for Highway Vehicular Communication," *IEEE Transactions on Vehicular Technology*, vol. 66, no. 12, pp. 10 676–10 691, Dec 2017.

[153] F. Baccelli and B. Blaszczyszyn, "Stochastic Geometry and Wireless Networks: Volume I Theory," *Foundations and Trends in Networking*, vol. 3, no. 3–4, pp. 249–449, 2010.

[154] M. Giordani, A. Zanella, and M. Zorzi, "Millimeter wave communication in vehicular networks: Challenges and opportunities," in *6th International Conference on Modern Circuits and Systems Technologies (MOCAST)*, May 2017.

[155] E. Turgut and M. C. Gursoy, "Coverage in Heterogeneous Downlink Millimeter Wave Cellular Networks," *IEEE Transactions on Communications*, vol. 65, no. 10, pp. 4463–4477, Oct 2017.

[156] M. Giordani, M. Mezzavilla, S. Rangan, and M. Zorzi, "An Efficient Uplink Multi-Connectivity Scheme for 5G Millimeter-Wave Control Plane Applications," *IEEE Transactions on Wireless Communications*, vol. 17, no. 10, pp. 6806–6821, Oct 2018.

[157] M. Polese, M. Giordani, M. Mezzavilla, S. Rangan, and M. Zorzi, "Improved Handover through Dual Connectivity in 5G mmWave mobile networks," *IEEE Journal on Selected Areas in Communications*, vol. 35, no. 9, pp. 2069–2084, Sept 2017.

[158] S. Akoum, O. E. Ayach, and R. W. Heath, "Coverage and capacity in mmWave cellular systems," in *Conference Record of the Forty Sixth Asilomar Conference on Signals, Systems and Computers (ASILOMAR)*, Nov 2012, pp. 688–692.

[159] S. N. Chiu, D. Stoyan, W. S. Kendall, and J. Mecke, *Stochastic geometry and its applications*. John Wiley & Sons, 2013.